ST. PETERSBURG STATE POLYTECHNICAL UNIVERSITY JOURNAL

Physics and Mathematics

VOLUME 14, No.2, 2021

ST. PETERSBURG STATE POLYTECHNICAL UNIVERSITY JOURNAL.
PHYSICS AND MATHEMATICS

НАУЧНО-ТЕХНИЧЕСКИЕ ВЕДОМОСТИ

САНКТ-ПЕТЕРБУРГСКОГО ГОСУДАРСТВЕННОГО ПОЛИТЕХНИЧЕСКОГО УНИВЕРСИТЕТА

Физико-математические науки

Том 14, №2
2021

НАУЧНО-ТЕХНИЧЕСКИЕ ВЕДОМОСТИ САНКТ-ПЕТЕРБУРГСКОГО ГОСУДАРСТВЕННОГО ПОЛИТЕХНИЧЕСКОГО УНИВЕРСИТЕТА. ФИЗИКО-МАТЕМАТИЧЕСКИЕ НАУКИ

Contents

Condensed matter physics

Simulation of physical processes

Nuclear physics

Radiophysics

Theoretical physics

Mechanics

Содержание

Condensed matter physics

DIELECTRIC PROPERTIES OF (R)-3-QUINUCLIDINOL IN THE POROUS MATRIX OF ALUMINUM OXIDE

S.V. Baryshnikov[1], A.Yu. Milinskiy[1], E.V. Stukova[2], A.A. Antonov[1]

[1] Blagoveshchensk State Pedagogical University,
Blagoveshchensk, Russian Federation;

[2] Amur State University,
Blagoveshchensk, Russian Federation

The paper presents findings of an investigation of the linear and nonlinear dielectric properties of (R)-3-quinuclidinol embedded in porous aluminum oxide (pores of size 300 nm), in comparison with the properties of bulk (R)-3-quinuclidinol. A decrease in the Curie temperature in the nanocomposite, both upon heating and cooling, in comparison with a bulk sample is revealed. A decrease in the phase transition temperature allows for interpretation on the basis of the known theoretical models for ferroelectric small particles.

Keywords: (R)-3-quinuclidinol, aluminum oxide, ferroelectric, dielectric constant, nanocomposite, phase transition

ДИЭЛЕКТРИЧЕСКИЕ СВОЙСТВА (R)-3-ХИНУКЛИДИНОЛА В ПОРИСТОЙ МАТРИЦЕ ОКСИДА АЛЮМИНИЯ

С.В. Барышников[1], А.Ю. Милинский[1], Е.В. Стукова[2], А.А. Антонов[1]

[1] Благовещенский государственный педагогический университет,
г. Благовещенск, Российская Федерация;

[2] Амурский государственный университет,
г. Благовещенск, Российская Федерация

Представлены результаты исследований линейных и нелинейных диэлектрических свойств (R)-3-хинуклидинола, внедренного в пористый оксид алюминия (размер пор − 300 нм), в сравнении со свойствами объемного (R)-3-хинуклидинола. Выявлено понижение температуры Кюри в нанокомпозите как при нагреве, так и охлаждении, по сравнению с объемным образцом. Понижение температуры фазового перехода допускает интерпретацию на основе известных теоретических моделей для сегнетоэлектрических малых частиц.

Ключевые слова: (R)-3-хинуклидинол, оксид алюминия, сегнетоэлектрик, диэлектрическая проницаемость, нанокомпозит, фазовый переход

Introduction

Ferroelectric materials have unique properties and wide application in practice. Spontaneous polarization and high permittivity, as well as their dependence on exposure (electric fields, mechanical stress, etc.) makes ferroelectrics a popular solution for the development of various functional electronic devices. Recently, there is a constant search for polar materials with high permittivity ε', spontaneous polarization P_s and Curie temperature T_C; moreover, such materials are cheap and environmentally friendly due to the absence of heavy metals in their structure.

Recently, researchers found ferroelectric properties of organic salts $C_6H_{16}NHal$, where halogens include Cl, Br and I [1−3]: diisopropylammonium chloride (DIPAC) with Curie temperature of 440 K and spontaneous polarization of 8.2 $\mu C/cm^2$; diisopropylammonium bromide (DIPAB) with Curie temperature of 426 K and spontaneous polarization of 23 $\mu C/cm^2$; diisopropylammonium iodide (DIPAI) with Curie temperature of 378 K and spontaneous polarization of 5.17 $\mu C/cm^2$.

Thanks to promising practical application of organic ferroelectrics in nanoelectronics, there is a considerable interest towards the studies of the molecular size influence on the material properties. Ferroelectric phase transitions in the nanocomposites obtained based on DIPAC, DIPAB and DIPAI, and nanoporous matrices were studied in papers [4−7].

Papers [8, 9] reported a discovery of ferroelectric properties of homochiral organic crystals of (R)-3- and (S)-3-quinuclidinol ($C_7H_{13}NO$). These crystals exist in two mirror-isometric (enantiomorphic) forms: homochiral (R)-3- and (S)-3-quinuclidinols. At room temperature, they crystallize in enantiomorphically polar point group 6 (C6) demonstrating a mirror image in the vibrational spectra. The Curie temperature determined using the differential thermal analysis method (DTA) for the single-crystalline samples was $T_{C1} \approx 398$ K upon heating and $T_{C2} \approx 360$ K upon cooling [8]. Dielectric permittivity at the phase transition has a dramatic jump anomaly changing approximately from 5 up to 17. Spontaneous polarization at $T \approx 300$ K equals approximately 7 $\mu C/cm^2$, coercive field is 15 kV/cm. It was also discovered that their racemate (Rac)-3-quinuclidinol is crystallizing in a centrosymmetric point group 2/m (C2h) which is not ferroelectric.

This discovery shows great significance homochirality plays in occurrence of the ferroelectric state in organic ferroelectrics. As it was found in paper [9], the phase transition temperatures decrease down to $T_{C1} \approx 338$ K upon heating and $T_{C2} \approx 324$ K upon cooling for (R)-3-quinuclidinol substrate-supported films (150 nm thick).

This article presents the results of studying dielectric properties of (R)-3-quinuclidinol embedded in porous aluminum oxide Al_2O_3 with 300 nm pores. For a comparison, we also studied similar identical properties in comparison with the properties of bulk polycrystalline (R)-3-quinuclidinol.

Samples and experiment procedure

To obtain the nanocomposites, we used the (R)-3-quinuclidinol produced by the Acros Organics company (Belgium). According to the sample certificate, the phase temperatures amounted to $T_{C1} \approx 390$ K upon heating and $T_{C2} \approx 364$ K upon cooling. The samples for the study were represented by aluminum oxide films 50 μm thick with the pores 300 nm in diameter. Fig. 1 shoes the photographs of the films obtained using a scanning electron microscope. To fill the aluminum oxide films with the ferroelectric, a saturated (R)-3-quinuclidinol solution in methanol was used. The oxide sample was placed in the solution heated up to 320 K and then cooled down slowly. The remaining methanol was removed by means of vacuum drying. After three repetitions of the described procedure, the pore occupancy measured by the change in the films weight using AND BM-252G balances (accuracy of 10^{-6} g) amounted to 53−55%.

Dielectric properties of bulk and nanostructured (R)-3-quinuclidinol were measured at the frequency of 100 kHz and operating voltage of 0.7 V using E7-25 LCR meter. To electrode the sample surface, we used Gallium−Indium paste. The temperature was determined with the accuracy of 0.1 K be means of TC-6621 electronic
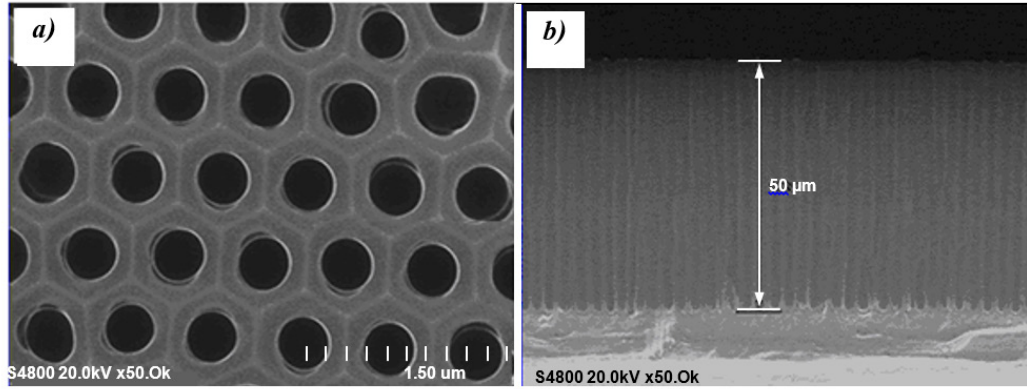
Fig. 1. Photomicrograph of Al$_2$O$_3$ film: a — surface, b — end view

thermometer based on a chromel–alumel thermocouple. In the course of the measurements, the samples were heated from 300 to 440 K, and then cooled down. The rate of temperature change equaled 1 DPM (degrees per minute).

To study the non-linear properties, we applied 2 kHz frequency sine-curve voltage to the sample with a series resistor. To determine the amplitude of the multiple frequency signals, we applied sine-curve voltage with the frequency of several kilohertz and the field intensity of approximately 10^2 V/mm to the sample with a series resistor. To determine the ferroelectric domain, we used third harmonic coefficient ($\gamma_{3\omega} = U_{3\omega}/U_{\omega}$). Papers [10, 11] describe the methodology of investigating ferroelectrics by means of non-linear dielectric spectroscopy in more detail.

Experimental results and discussion

As a result of the studying dielectric characteristics of the considered (R)-3-quinuclidinol samples in bulk and (R)-3-quinuclidinol embedded in an aluminum oxide film, we analyzed temperature dependences $\varepsilon'(T)$ (Fig. 2). The ferroelectric-to-paraelectric phase transition occurs at the temperature of 390 K which corresponds to the maximum of permittivity on the temperature dependence $\varepsilon'(T)$. For the bulk sample, when the temperature increases, there is an anomaly ε' at 390 K which corresponds to the transition from the ferroelectric phase to the paraelectric one. Upon cooling, the phase transition temperature depends on the temper-

ature up to which the sample was heated to, as well as the cooling rate. If a sample was heated up to 420 K with the cooling rate 1 K/min, it is equal to 372 K. For effective permittivity of the (R)-3-quinuclidinol/Al$_2$O$_3$ nanocomposite (measured in the same conditions), the anomalies in the neighborhood of the phase transitions are very diffuse and shifted in the lower temperatures domain. As a comparison of the results for the bulk and nanostructured (R)-3-quinuclidinol shows, for the (R)-3-quinuclidinol in the pores of the Al$_2$O$_3$ films, the transition temperature decreasres by 10 K upon heating and by 25 K upon cooling.

At the next stage of the research, in order to determine the temperature interval of the ferroelectric phase in the nano-sized (R)-3-quinuclidinol with more accuracy, we measured the non-linear dielectric characteristics of the bulk and nanostructured (R)-3-quinuclidinol. The phase transition temperatures were determined by temperature dependences of the third harmonic coefficient $\gamma_{3\omega}$ in the heating-cooling cycle (Fig. 3). In the course of heating, both samples have great values of the $\gamma_{3\omega}$ coefficient starting from room temperature and up to 391 K (for the bulk sample) and 380 K (for the nanocomposite). Above this temperatures, the third harmonic coefficient changes insignificantly which can be attributed to the transition of the samples into the paraelectric state. Upon cooling, the $\gamma_{3\omega}$ coefficient begins to grow at around 372 and 347 K for the bulk and the nanocomposite (R)-3-quinuclidinol respectively.

9
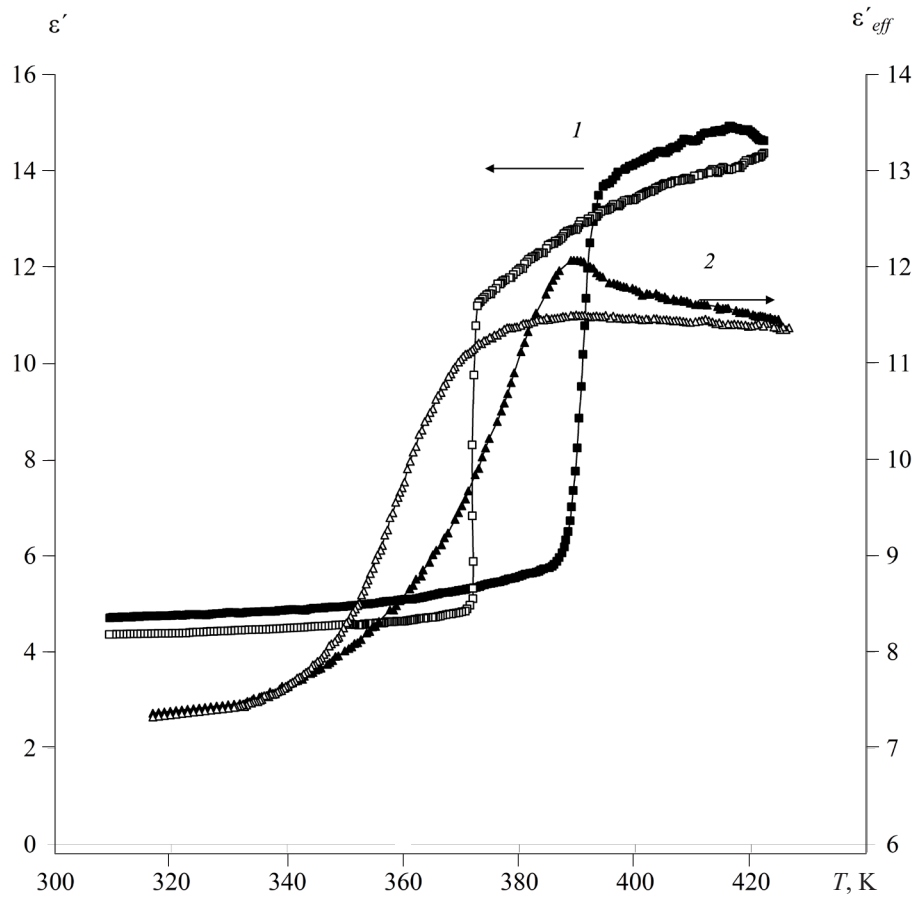
Fig. 2. Dependence $\varepsilon'(T)$ for bulk (*1*) and Al_2O_3 nanocomposite (*2*) (R)-3-quinuclidinol samples at the frequency of 100 kHz (black symbols for heating, white symbols for cooling)

A change in the Curie temperature for ferroelectrics located in nanoporous matrices can occur due to several factors. It is primarily connected with size effects observed for isolated nanoparticles. As the size of the particles decreases, the share of surface atoms grows. Free energy F of nanoparticles is a sum of the volume (F_V) and surface (F_s) contributions:

$$F = F_V + F_s.$$

The decrease of the phase transition temperature of the (R)-3-quinuclidinol embedded in the pores of aluminum oxide agrees with the conclusion of the theoretical models developed on the basis of the phenomenological Landau theory and Ising model [12−14]. These models predict that the temperature of the structural phase transition for small isolated particles of spherical and cylindrical shape shifts deeper into the ferroelectric phase as the size of the particles decreases. The conclusions of these models were also experimentally verified for separate small particles of such ferroelectrics as barium titanate (see paper [15] and its references).

For matrix nanocomposites, unlike for separate ferroelectric particles, we need to account for the interaction between the matrix inclusions. In this case, the change in the surface energy is determined as

$$\tilde{F}_S = F_S + \sum \int_{S_i} \sigma_i dS_i + \sum \int_{S_i} \varphi_i \delta_i dS_i,$$

where σ_i is the surface tension; S_i is the particle surface; φ_i is the electric potential; δ_i is the surface-charge density.

The summand σdS may considerably contribute to the total energy of the system with

10
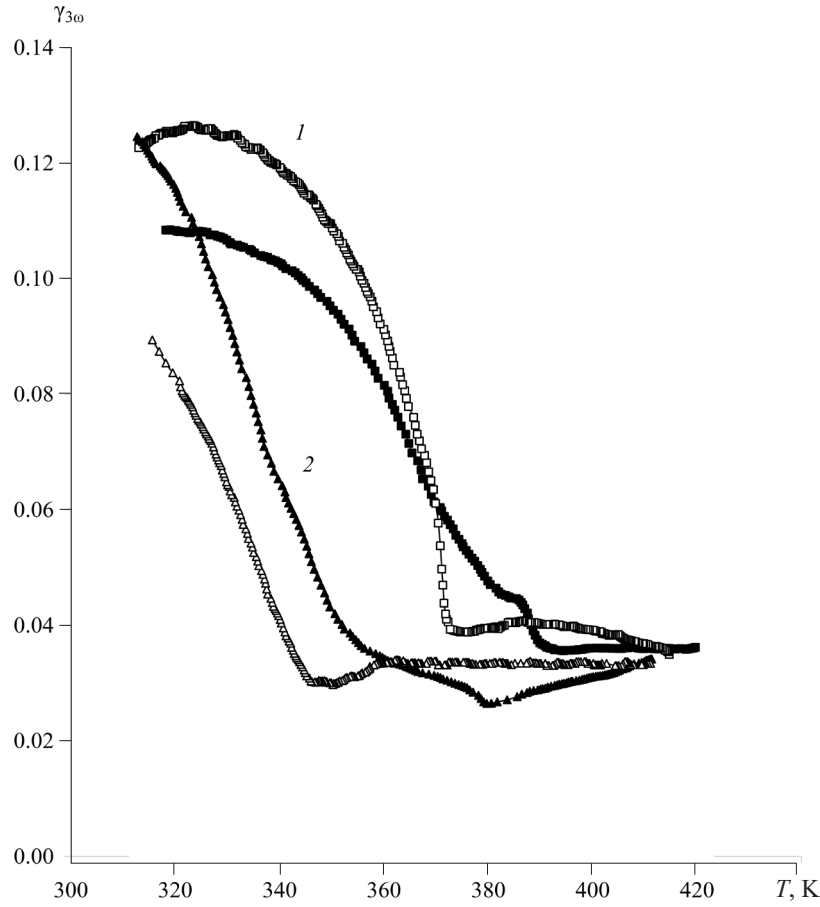
Fig. 3. Temperature dependences of the third harmonic coefficient for bulk (*1*)
and Al_2O_3 nanocomposite (*2*) (R)-3-quinuclidinol samples in the heating-cooling cycles
(black symbols for heating, white symbols for cooling)

well developed surface of the phase interface. Formation of a double electric layer at the phase interface as a result electron emission or spontaneous polarization screening leads to emergence of surface conductance and Maxwell-Wagner polarization. The depolarization field depending on permittivity, conductance, shape and size of the particles additionally contributes into the size effect which results in decreased Curie temperature.

Moreover, paper [16] indicated that electric interaction between ferroelectric particles in neighboring pores could influence the phase transition shift in the matrix nanocomposites. However, in our case, the electric interaction between the particles in neighboring pores plays no significant role due to the small value of the spontaneous polarization of (R)-3-quinuclidi-

nol ($P_s \approx 7$ μC/cm^2) and a considerable distance between the neighboring pores (around 200 nm). Taking mechanical stress for the nanoparticles into account in the measurements is essential in terms of retaining polar properties of the ferroelectric. In this case, pressure under the curved surface is defined by the surface tension tensor μ. The dependence of the polar properties of ferroelectric particles on surface tension was evaluated in paper [17−19]. Thus, paper [19] shows that at $\mu = 0.5 - 50$ N/m, the effect of the transition temperature shift due to electrostriction begins working at the nanoparticle radius of curve $R = 5 - 50$ nm, which is significantly less than the size of the pores in the composite of interest.

Therefore, a decrease in the ferroelectric phase transition temperature of (R)-3-quinuclidinol in porous matrices of aluminum oxide discovered in

this article is due to the influence of size effects characteristic of free particles.

Conclusion

The results of the study of (R)-3-quinuclidinol embedded in porous aluminum oxide presented in this article revealed a decrease in the Curie temperature in the nanocomposite, both upon heating and cooling, in comparison with the bulk sample. A decrease in the phase transition temperature allows interpretation based on the known theoretical models for ferroelectric small particles.

REFERENCES

1. **Fu D.-W., Zhang W., Cai H.-L., et al.,** Diisopropyl ammonium chloride: a ferroelectric organic salt with a high phase transition temperature and practical utilization level of spontaneous polarization, Advanced Materials. 23 (47) (2011) 5658−5662.

2. **Fu D.-W., Cai H.-L., Liu Y., et al.,** Diisopropyl ammonium bromide is a high-temperature molecular ferroelectric crystal, Science. 339 (6118) (2013) 425−428.

3. **Piecha A., Gągor A., Jakubas R., Szklarz P.,** Room-temperature ferroelectricity in diisopropyl ammonium bromide, CrystEngComm. 15 (5) (2013) 940−944.

4. **Baryshnikov S.V., Charnaya E.V., Milinskiy A.Yu., et al.,** Impact of nanoconfinement on the diisopropyl ammonium chloride ($C_6H_{16}ClN$) organic ferroelectric, Phase Transitions. 91 (3) (2018) 293−300.

5. **Milinskiy A.Yu., Baryshnikov S.V., Charnaya E.V., et al.,** Dielectric properties of an organic ferroelectric of bromide diisopropyl ammonium embedded into the pores of nanosized Al_2O_3 films, Journal of Physics: Condensed Matter. 31 (48) (2019) 485704.

6. **Nguyen H.T., Baryshnikov S.V., Milinskiy A.Yu., et al.,** Linear and nonlinear dielectric properties of nanocomposites based on the organic ferroelectric of diisopropyl ammonium bromide, Phase Transitions. 92 (10) (2019) 899−906.

7. **Milinskiy A.Y., Baryshnikov S.V., Charnaya E.V., et al.,** Phase transitions in bulk and confined organic ferroelectric DIPAI, Results in Physics. 17 (2020) 103069.

8. **Li P.-F., Liao W.-Q., Tang Y.-Y., et al.,** Organic enantiomeric high-T_C ferroelectrics, PNAS. 116 (13) (2019) 5878−5885.

9. **Li P.-F., Tang Y.-Y., Wang Z.-X., et al.,** Anomalously rotary polarization discovered in homochiral organic ferroelectrics, Nature Communications. 7 (2016) 13635.

10. **Ikeda S., Kominami H., Koyama K., Wada Y.J.,** Nonlinear dielectric constant and ferroelectric-to-paraelectric phase transition in copolymers of vinylidene fluoride and trifluoroethylene, Applied Physics. 62 (8) (1987) 3339−3342.

11. **Yudin S.G., Blinov L.M., Petukhova N.N., Palto S.P.,** Ferroelectric phase transition in Langmuir − Blodgett films of copper phthalocyanine, Journal of Experimental and Theoretical Physics. Letters. 70 (9) (1999) 633−640.

12. **Zhong W.L., Wang Y.G., Zhang P.L., Qu D.B.,** Phenomenological study of the size effect on phase transition in ferroelectric particles, Phys. Rev. B. 50 (2) (1994) 698−703.

13. **Wang, C.L., Xin Y., Wang X.S., Zhong W.L.,** Size effects of ferroelectric particles described by the transverse Ising model, Phys. Rev. B. 62 (17) (2000) 11423−11427.

14. **Uskov A.V., Charnaya E.V., Pirozerskii A.L., Bugaev A.S.,** The transverse Ising model of the ferroelectric phase transition in a system of coupled small particles, Ferroelectrics. 482 (1) (2015) 70−81.

15. **Sedykh P., Michael D.,** Ferroelectric phase transition in barium titanate nanoparticles, Phys. Rev. B. 79 (13) (2009) 134119.

16. **Pirozerskii, A.L. Charnaya E.V.,** Ising model for a ferroelectric phase transition in a system of interacting small particles, Physics of the Solid State. 52 (3) (2010) 620−624.

17. **Shchukin V.A., Bimberg D.,** Spontaneous ordering of nanostructures on crystal surfaces, Re-

views of Modern Physics. 71 (4) (1999) 1125−1171.

18. **Morozovska A.N., Glinchuk M.D., Eliseev E.A.,** Phase transitions induced by confinement of ferroic nanoparticles, Phys. Rev. B. 76 (1) (2007) 014102.

19. **Morozovska A.N., Eliseev E.A., Glinchuk M.D.,** Size effects and depolarization field influence on the phase diagrams of cylindrical ferroelectric nanoparticles, Physica B: Condensed Matter. 387 (1−2) (2006) 358−366.

THE AUTHORS

BARYSHNIKOV Sergey V.

Blagoveschensk State Pedagogical University

104 Lenin St., Blagoveshchensk, 675000, Russian Federation

svbar2003@list.ru

MILINSKIY Alexey Yu.

Blagoveshchensk State Pedagogical University

104 Lenin St., Blagoveshchensk, 675000, Russian Federation

a.milinskiy@mail.ru

STUKOVA Elena V.

Amur State University

21 Ignatievskoe Ave., Blagoveshchensk, 675027, Russian Federation

lenast@bk.ru

ANTONOV Anton A.

Blagoveshchensk State Pedagogical University

104 Lenin St., Blagoveshchensk, 675000, Russian Federation

antonov.lit@bgpu.ru

СПИСОК ЛИТЕРАТУРЫ

1. **Fu D.-W., Zhang W., Cai H.-L., Ge J.-Z., Zhang Y., Xiong R.-G.** Diisopropyl ammonium chloride: a ferroelectric organic salt with a high phase transition temperature and practical utilization level of spontaneous polarization // Advanced Materials. 2011. Vol. 23. No. 47. Pp. 5658−5662.

2. **Fu D.-W., Cai H.-L., Liu Y., Ye Q., Zhang W., Zhang Y., Chen X.-Y., Giovannetti G., Capone M., Li J., Xiong R.-G.** Diisopropyl ammonium bromide is a high-temperature molecular ferroelectric crystal // Science. 2013. Vol. 339. No. 6118. Pp. 425−428.

3. **Piecha A., Gągor A., Jakubas R., Szklarz P.** Room-temperature ferroelectricity in diisopropyl ammonium bromide // CrystEngComm. 2013.

Vol. 15. No. 5. Pp. 940−944.

4. **Baryshnikov S.V., Charnaya E.V., Milinskiy A.Yu., Parfenov V.A., Egorova I.V.** Impact of nanoconfinement on the diisopropyl ammonium chloride ($C_6H_{16}ClN$) organic ferroelectric // Phase Transitions. 2018. Vol. 91. No. 3. Pp. 293−300.

5. **Milinskiy A.Yu., Baryshnikov S.V., Charnaya E.V., Egorova I.V., Nguyen H.T.** Dielectric properties of an organic ferroelectric of bromide diisopropyl ammonium embedded into the pores of nanosized Al_2O_3 films // Journal of Physics: Condensed Matter. 2019. Vol. 31. No. 48. P. 485704.

6. **Nguyen H.T., Baryshnikov S.V., Milinskiy A.Yu., Charnaya E.V., Egorova I.V.** Linear and nonlinear dielectric properties of nanocomposites

based on the organic ferroelectric of diisopropyl ammonium bromide // Phase Transitions. 2019. Vol. 92. No. 10. Pp. 899−906.

7. **Milinskiy A.Y., Baryshnikov S.V., Charnaya E.V., Egorova I.V., Sarnatskii V.M.** Phase transitions in bulk and confined organic ferroelectric DIPAI // Results in Physics. 2020. Vol. 17. June. P. 103069.

8. **Li P.-F., Liao W.-Q., Tang Y.-Y., Qiao W., Zhao D., Ai Y., Yao Y.-F., Xiong R.-G.** Organic enantiomeric high-T_C ferroelectrics // Proceedings of the National Academy of Sciences (PNAS). 2019. Vol. 116. No. 13. Pp. 5878−5885.

9. **Li P.-F., Tang Y.-Y., Wang Z.-X., Ye H.-Y., You Y.-M., Xiong R.-G.** Anomalously rotary polarization discovered in homochiral organic ferroelectrics // Nature Communications. 2016. Vol. 7. P. 13635.

10. **Ikeda S., Kominami H., Koyama K., Wada Y.J.** Nonlinear dielectric constant and ferroelectric-to-paraelectric phase transition in copolymers of vinylidene fluoride and trifluoroethylene // Applied Physics. 1987. Vol. 62. No. 8. Pp. 3339−3342.

11. **Юдин С.Г., Блинов Л.М., Петухова Н.Н., Палто С.П.** Сегнетоэлектрический фазовый переход в пленках Ленгмюра − Блоджетт фталоцианина меди // Письма в ЖЭТФ. 1999. Т. 70. Вып. 9. С. 625−631.

12. **Zhong W.L., Wang Y.G., Zhang P.L., Qu D.B.** Phenomenological study of the size effect on phase transition in ferroelectric particles // Phys.

Rev. B. 1994. Vol. 50. No. 2. Pp. 698−703.

13. **Wang, C.L., Xin Y., Wang X.S., Zhong W.L.** Size effects of ferroelectric particles described by the transverse Ising model // Phys. Rev. B. 2000. Vol. 62. No. 17. Pp. 11423−11427.

14. **Uskov A.V., Charnaya E.V., Pirozerskii A.L., Bugaev A.S.** The transverse Ising model of the ferroelectric phase transition in a system of coupled small particles // Ferroelectrics. 2015. Vol. 482. No. 1. P. 70−81.

15. **Sedykh P., Michael D.** Ferroelectric phase transition in barium titanate nanoparticles // Phys. Rev. B. 2009. Vol. 79. No. 13. P. 134119.

16. **Пирозерский А.Л., Чарная Е.В.** Модель Изинга сегнетоэлектрического фазового перехода в системе взаимодействующих малых частиц // Физика твердого тела. 2010. Т. 52. Вып. 3. С. 572−576.

17. **Shchukin V.A., Bimberg D.** Spontaneous ordering of nanostructures on crystal surfaces // Rev. Mod. Phys. 1999. Vol. 71. No. 4. Pp. 1125−1171.

18. **Morozovska A.N., Glinchuk M.D., Eliseev E.A.** Phase transitions induced by confinement of ferroic nanoparticles // Phys. Rev. B. 2007. Vol. 76. No. 1. P. 014102.

19. **Morozovska A.N., Eliseev E.A., Glinchuk M.D.** Size effects and depolarization field influence on the phase diagrams of cylindrical ferroelectric nanoparticles // Physica B. Condensed Matter. 2006. Vol. 387. No. 1−2. Pp. 358−366.

СВЕДЕНИЯ ОБ АВТОРАХ

БАРЫШНИКОВ Сергей Васильевич − *доктор физико-математических наук, профессор кафедры физического и математического образования Благовещенского государственного педагогического университета, г. Благовещенск, Российская Федерация.*

675000, Российская Федерация, г. Благовещенск, ул. Ленина, 104
svbar2003@list.ru

МИЛИНСКИЙ Алексей Юрьевич − *кандидат физико-математических наук, доцент кафедры физики Благовещенского государственного педагогического университета, г. Благовещенск, Российская Федерация.*

675000, Российская Федерация, г. Благовещенск, ул. Ленина, 104
a.milinskiy@mail.ru

СТУКОВА Елена Владимировна — *доктор физико-математических наук, профессор, заведующая кафедрой физики Амурского государственного университета, г. Благовещенск, Российская Федерация.*

675027, Российская Федерация, г. Благовещенск, Игнатьевское шоссе, 21

lenast@bk.ru

АНТОНОВ Антон Анатольевич — *кандидат физико-математических наук, доцент кафедры физического и математического образования Благовещенского государственного педагогического университета, г. Благовещенск, Российская Федерация.*

675000, Российская Федерация, г. Благовещенск, ул. Ленина, 104

antonov.lit@bgpu.ru

PHASE TRANSITIONS AND DIFFUSE REFLECTANCE SPECTRA OF BARIUM TITANATE-ZIRCONATE SOLID SOLUTIONS

M.M. Mikhailov[1], O.A. Alekseeva[1], S.A. Yuryev[1], A.N. Lapin[1], E.Yu. Koroleva[2]

[1] Tomsk State University of Control Systems and Radioelectronics,
Tomsk, Russian Federation;

[2] Peter the Great St. Petersburg Polytechnic University,
St. Petersburg, Russian Federation

The composition, structure, particle size distribution, diffuse reflectance spectra, integral absorption coefficients of solar radiation and dielectric properties of $BaTi(1-x)Zr(x)O_3$ powders synthesized from micro powders $BaCO_3$, ZrO_2 and TiO_2 at $x = 0 - 0.3$ have been studied. Changes in the integral absorption coefficient of the powders at different concentrations of zirconium cations were found to be within 34 %. Dielectric studies conducted over the wide ranges of temperature and frequency showed the presence of two phase transitions, one of them undergoing near the room temperatures. This fact makes it possible to consider these powders as pigments for thermal control coatings at operating temperatures of space crafts.

Keywords: barium titanate-zirconate, thermal control coating, phase transition, diffuse reflectance spectrum

ФАЗОВЫЕ ПЕРЕХОДЫ И СПЕКТРЫ ДИФФУЗНОГО ОТРАЖЕНИЯ ТВЕРДЫХ РАСТВОРОВ ТИТАНАТА-ЦИРКОНАТА БАРИЯ

М.М. Михайлов[1], О.А. Алексеева[1], С.А. Юрьев[1], А.Н. Лапин[1], Е.Ю. Королева[2]

[1] Томский государственный университет систем управления и радиоэлектроники,
г. Томск, Российская Федерация;

[2] Санкт-Петербургский политехнический университет Петра Великого,
Санкт-Петербург, Российская Федерация

Исследованы состав, структура, гранулометрический состав, спектры диффузного отражения, интегральные коэффициенты поглощения солнечного излучения и диэлектрические свойства порошков $BaTi(1-x)Zr(x)O_3$, синтезированных из микропорошков $BaCO_3$, ZrO_2 и TiO_2 при концентрации замещающих катионов циркония в диапазоне значений x от 0 до 0,3. Установлены изменения интегрального коэффициента поглощения исследованных порошков при различной концентрации замещающих катионов циркония в пределах 34 %. Диэлектрические исследования, проведенные в широком температурном и частотном диапазонах, выявили существование двух фазовых переходов в исследованных соединениях. Определены температуры фазовых переходов; установлено, что низкотемпературный фазовый переход происходит при комнатных температурах, что позволяет рассматривать данные

порошки в качестве пигментов для термостабилизирующих покрытий космических аппаратов при рабочих температурах.

Introduction

There is now currently a growing interest to the studies of thermal control coatings, which can be used to maintain the temperature of the objects they are applied to stable [1, 2]. So-called intelligent coatings draw the most attention, since they are capable of modifying their functional physical properties in response to small environment changes. Such coatings are very promising in terms of thermal control applications, in particular space craft device, where their ability to change emittance and radiated power in response to the change in the environment or the absorbed energy allows stabilizing the temperature of the space craft working points.

Solid solutions with phase transitions (PT) accompanied by rearrangement of the crystalline structure can be used as pigments for thermal control coatings (TCC) of reflecting type; the PT are located in the range of operating temperatures of the unit. Solid solutions of barium titanate $BaTiO_3$ are solid solutions of this type with its barium or titanium cations partially substituted by cations of other elements. The Curie temperature for barium titanate $BaTiO_3$ is 120°C. Barium titanate has cubic structure above this temperature. As temperature T decreases, there is a structural transition into phases with tetragonal ($5 \leq T \leq 120$°C), rhombic ($-90 \leq T \leq +5$ °C) and rhombohedric ($T < -90$ °C) lattices. The electric [3], dielectric [4] and optical [5] properties change as well. The most significant modification of the indicated properties is observed in the neighborhood of the Curie point (in the transition from the cubic to the tetragonal syngony): there is a variance by several times in dielectric permittivity ε and by five orders of magnitude in electrical conductivity σ [3]. Optical properties can change as well [6].

The change of electrical properties in the domain of phase transitions leads to significant changes [6] of the barium titanate emittance, which depends on the carrier density, in a temperature range from the values characteristic of quasi-metallic state (0.10) to the value specific to dielectrics (0.96). In case the coating is heating up to the PT temperature, its emissivity increases dramatically, which results in thermal radiation rising and the coating temperature decreasing. In the opposite situation, i.e. when the coating temperature is below the operating one, there is an abrupt drop in emittance. This leads to a reduction of thermal radiation and, respectively, to the temperature rising back to the previous level. This is the basis of thermal stabilization in the operation area of the object with the thermal control coating on its surface.

For practical purposes, there is a need for coatings, which can operate at lower temperatures than that barium titanate can provide. A partial substitution of barium or titanium cations with other positive ions A or B forming solid solutions of $Ba_{1-x}A_xTiO_3$ or $BaTi_{1-x}B_xO_3$ type allows the Curie temperature to shift into lower value ranges [7]. The value of the shift and PT characteristics are defined by the type of the substituting element and its concentration. If we vary the type and concentration of the substituting elements A or B, as well as the conditions of the pigment production, we can control the phase transitions of the coatings produced on the basis of such compounds [8−10].

The objectives of this study included a solid-phase synthesis of the $BaTi_{1-x}Zr_xO_3$ com-

pound at various values of x, as well as finding its phase and particle-size distribution, phase transition temperature and other essential physical properties characterizing its ability to reflect solar radiation (there is a need for materials promising in terms of producing reflective coatings for space crafts).

In favor of the set goal, we subjected the synthesized samples to X-ray phase and particle-size distribution analysis, studied their dielectric properties, obtained and analyzed their diffuse reflectance spectra and integral absorption coefficients.

Samples and test procedure

This paper presents a solid-phase synthesis of solid $BaTi_{1-x}Zr_xO_3$ solution based on $BaCO_3$, ZrO_2 and TiO_2 micro powders at concentration of substituting zirconium cations in the range of $0-0.3$.

The samples were produced by means of solid-phase synthesis from manufactured micro-sized $BaCO_3$, ZrO_2 and TiO_2 powders. For each concentration of substituting zirconium cations, we prepared a mixture of the initial $BaCO_3$, ZrO_2 and TiO_2 powders in such a way as to meet the set barium atoms/$Ti_{1-x}Zr_x$ compound ratio of 1:1 for the obtained $BaTi_{1-x}Zr_xO_3$ compound at each value of x in compliance with the molecular masses of the initial $BaCO_3$, ZrO_2 and TiO_2 powders. The barium carbonate micropowder was dissolved in distilled water agitated by ultrasonic waves; then we added the silicon dioxide and titanium dioxide micropowders to the solution. The obtained compound was mixed in a magnetic stirrer for 1 h. The mixture was dried at 150°C, ground in an agate mortar and subject to double heating under atmosphere: first it was heated at 800°C for 2 h, then (after completely cooled down) it was heated at 1200°C for 2 h. The rate of temperature elevation on average amounted to 50°C/min, of cooling -9°C/min.

We studied the samples of $BaTi_{1-x}Zr_xO_3$ with six different concentration of substituting cations in the range from 0 to 30%: $x = 0.01$; 0.03; 0.10; 0.15; 0.20; 0.30. We studied particle-size distribution of $BaTi_{1-x}Zr_xO_3$ powders using Shimadzu SALD-2300 laser diffraction particle size ana-

lyzer. We employed Shimadzu XRD 6000 X-ray diffractometer to perform X-ray phase analysis (XRD).

For dielectric measurements, we pressed the powders under 10 MPa pressure into tablets 1 cm wide and 1 mm thick. We used gold contacts with a chromium sublayer as electrodes for better adhesion. In the course of the measurement, the samples were heated at 120°C for 30 min first to remove the adsorbed water.

We measured dielectric properties using a broad-band spectrometer Novocontrol BDS80 in the frequency range from 0.1 Hz to 10 MHz, with the scanning field amplitude of 10 V/cm; relative measurement error of impedance and capacity is approximately $3\cdot10^{-5}$. The measurements were performed in a heating/cooling mode, the temperature change rate amounted to $1-2$°C/min, measurement temperatures ranged from -50 to 150°C.

To measure diffuse reflectance spectra, the $BaTi_{1-x}Zr_xO_3$ samples were pressed into supports 24 mm wide and 2 mm tall under the pressure of 1 MPa with hold time of 2 mm. For diffuse reflectance spectra, we used Shimadzu UV-3600 Plus spectrophotometer with an integrating sphere attachment (ISR-603) in a wavelength range from 200 to 2200 nm and resolution of 5 nm.

Test results and their discussion

X-ray phase analysis data. A diffraction spectra analysis of the synthesized barium titanate powders with partially substituted cations showed that the peaks of intensity correspond to $BaTiO_3$ or $BaTi_{1-x}Zr_xO_3$ compounds. As an example, Fig. 1 demonstrates an X-ray diagram of $BaZr_{0.1}Ti_{0.9}O_3$ powder ($x = 0.1$). Aside from the basic compound, the synthesized powders contained phases of $ZrTiO_4$ and $BaZrO_3$, as well as residual unreacted initial powders used in the synthesis: $BaCO_3$, ZrO_2 and TiO_2. A study of the obtained X-ray diagrams allowed us to conclude that the basic phase of the produced powders had a tetragonal structure.

Based on the obtained diffraction data, we calculated the content of various compounds in the synthesized $BaTi_{1-x}Zr_xO_3$ powders (Table 1). The yield of the main phase for all obtained sam-
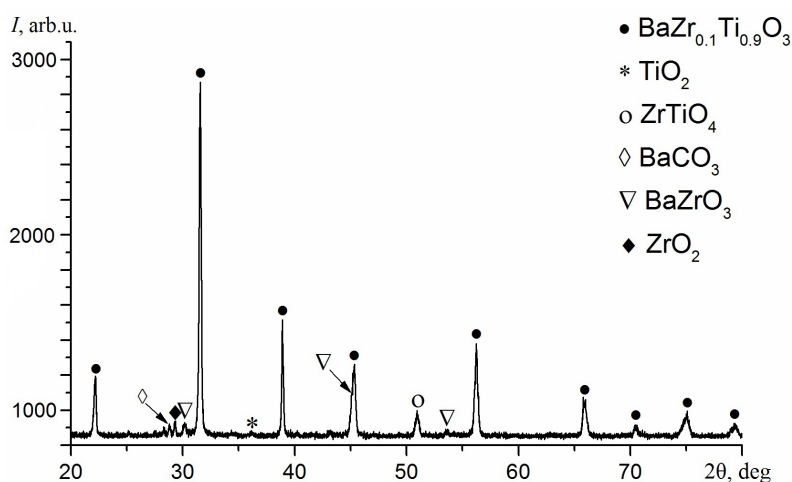
Fig. 1. X-ray diagram of $BaZr_{0.1}Ti_{0.9}O_3$ powder

Table 1

Percentage of different compounds in the synthesized
$BaTi_{1-x}Zr_xO_3$ powders at $x = 0.01 - 0.30$

x	Compound composition, %					
	$BaTi_{1-x}Zr_xO_3/BaTiO_3$	ZrO_2	TiO_2	$ZrTiO_4$	$BaCO_3$	$BaZrO_3$
0.01	84.9	0.2	6.7	3.7	3.6	0.9
0.03	85.1	0.8	7.0	3.3	3.4	0.4
0.05	90.3	1.3	2.8	2.2	1.9	1.5
0.10	80.6	3.9	6.2	3.0	3.1	3.3
0.15	78.9	5.0	5.1	2.5	2.3	6.2
0.20	67.6	11.4	6.2	2.0	2.0	10.8
0.30	62.0	10.8	7.2	2.6	2.4	15.0

N o t e. The presented results were obtained on the basis of the X-ray phase analysis data.

ples containing from 0 to 0.3 of the substituting zirconium cations is in the range between 62.0 and 90.3%. The highest yield of the main phase (90.3%) is observed at the substituting zirconium cations concentration $x = 0.05$, while the lowest one (62%) — at $x = 0.30$. The content of $BaZrO_3$ and ZrO_2 phases grows with the increase in the substituting cations density. The percentage of the remaining non-essential phases in the synthesized solid solutions depends on the concentration of the substituting cations insignificantly and at various concentrations of $x = 0.01-0.30$ vary as follows:

TiO_2 — from 2.8 to 7.2 %,

$ZrTiO_4$ — from 2 to 3.7 %,

$BaCO_3$ — from 1.9 to 3.6 %.

Particle-size analysis data. The particle-size research showed that the synthesized powders contain particle of the size from 0.2 to 12 μm. The function of particles distribution for the $BaTi_{1-x}Zr_xO_3$ powders has a form of a curve with two peaks corresponding to the particle sizes of 0.51−0.53 μm and 2.30−2.67 μm respectively. With the change of the zirconium cations percentage from 1 to 30%, there is no significant shift of the distribution peaks (within the range of 0.02 and 0.37 μm for the first and the second peaks respectively), just as there is no considerable change in the intensity of the said peaks (up to 20% for the first peak and up to 10% for

the second one). The median particle size in the $BaTi_{1-x}Zr_xO_3$ powders ranges from 1.911 to 2.990 μm. The maximum median particle size is observed in the $BaTiO_3$ powder (2.196 μm) at the zirconium cation concentration equal to 0.15 (2.199 μm). The minimum median particle size (1.911 μm) corresponds to the maximum zirconium cation concentration equal to 0.03. The modal particle diameter (diameter with the highest incidence rate of grain sizes or a prevailing fraction) for all the powders under study was identical and equal to 2.234 μm.

Dielectric properties study. We can see two peaks on the permittivity temperature dependences of all the samples: a more prominent one is observed at the temperature range of 109−117°C and a less prominent one − at 27−47°C (Fig. 2). Note that the temperature values corresponding to the maximum permittivity during heating are lower than that during cooling down (see Fig. 2 for an example); for a high temperature peak in the range of 109−117°C the thermal lag is around 5°C. The respective data for the remaining values of x are similar.

In the entire temperature test range, we obtained and analyzed the frequency dependences of the real and imaginary components of permittivity $\varepsilon'(\omega)$, $\varepsilon''(\omega)$ for the solid $BaTi_{1-x}Zr_xO_3$

solutions. To describe the relaxation contributions, we used the Cole−Cole distribution, which allows describing the spectra extending over a wider range than Debye relaxation. As a model function, we applied a sum of DC conductivity, several relaxation processes and high-frequency conductivity contributions:

$$\varepsilon^*(\omega) = \varepsilon_\infty + \sum_{i=1}^{n} CC_i + j\frac{\sigma_{DC}}{\omega\varepsilon_0} =$$

$$= \varepsilon_\infty + \sum_{i=1}^{n} \frac{\Delta\varepsilon_i}{1 + (i\omega\tau_i)^{\alpha_i}} + j\frac{\sigma_{DC}}{\omega\varepsilon_0},$$

where CC_i is the relaxation process contribution described by the empirical Cole−Cole formula; ε_∞ is the phonon modes and electric polarizability contribution; $\Delta\varepsilon = \varepsilon - \varepsilon_\infty$; τ, s, is the most probable time (relaxation frequency ω), $\tau = 2\pi/\omega$; σ_{DC}, S/m, is the DC conductivity; α is the relaxation time distribution ($0 < \alpha < 1$).

The best way of approximating the frequency dependences was finding the sum of the contributions made by three relaxation processes; the processes differ in the most probable relaxation frequencies: one of the processes was observed in the frequency range of $f = 0.1−1$ Hz and had a monotone temperature dependence of the $\Delta\varepsilon$
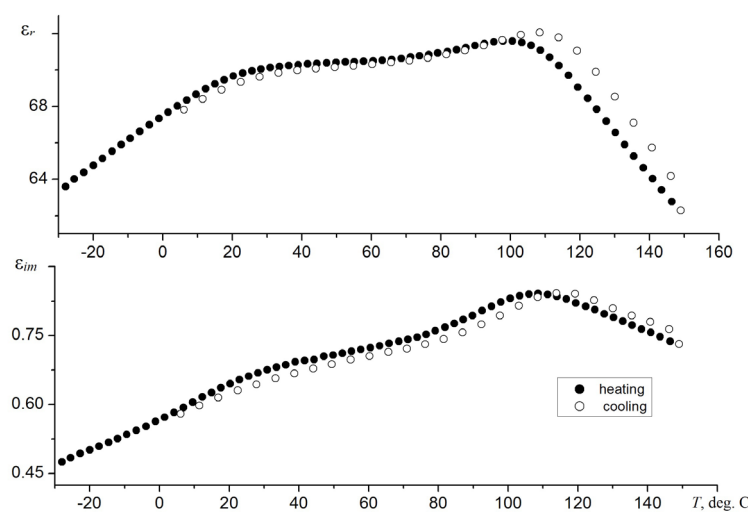
Fig. 2. Heating/cooling permittivity temperature dependences
of the solid $BaZr_{0.1}Ti_{0.9}O_3$ solution; test frequency $f = 1.4$ kHz

a)   *b)*
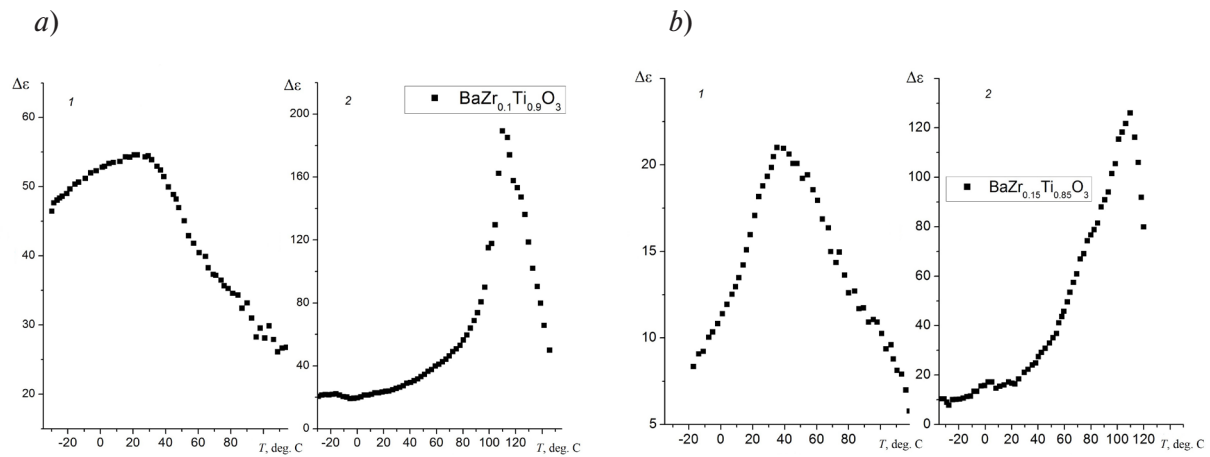
Fig. 3. Temperature dependences of the $\Delta\varepsilon$ parameter for relaxation processes *1* and *2* (see text)
in solid solutions $BaZr_{0.1}Ti_{0.9}O_3$ (*a*) and $BaZr_{0.15}Ti_{0.85}O_3$ (*b*)

Table 2

**Temperature values corresponding to peaks on $\Delta\varepsilon(T)$ dependences
for relaxation processes *1* and *2* in the studied $BaTi_{1-x}Zr_xO_3$ samples**

x value	Peak temperature, °C	
	Process *1*	Process *2*
0.01	31.6	118.5
0.03	36.9	115.6
0.10	27.4	112.4
0.15	35.9	111.2
0.20	42.1	109.6
0.30	27.8	113.9

N o t e. The presented results are obtained on the basis of dielectric measurements data. Processes *1* and *2* differ
in the temperature ranges where their peaks were observed.

parameter; two other processes with different relaxation frequencies lying in the range of $f = 10^3 - 10^4$ Hz had peaks on the $\Delta\varepsilon(T)$ dependences at the temperature of around 27°C (process *1*) and around 109°C (process *2*) (Fig. 3). As an example, Fig. 3 presents the corresponding data for two studied samples.

Thus, we were able to identify the relaxation processes responsible for the phase transitions in the material under study. We used temperature dependences of the $\Delta\varepsilon$ parameter to determine the phase transition temperatures for each compound (Table 2). The peak temperatures $\Delta\varepsilon(T)$ for process *2* in all the samples was close to the temperature of the ferroelectric transition from the cubic into tetragonal phase in pure $BaTiO_3$ ($T_C = 120$°C) and solid solutions of $BaTi_{1-x}Zr_xO_3$ with low zirconium concentration. A small decrease in the temperature of this transition agrees with the phase diagram of the solid $BaTi_{1-x}Zr_xO_3$ solutions, according to which at low zirconium content the temperature of this transition decreases in these solutions [11].

The peaks of $\Delta\varepsilon(T)$ for relaxation process 1 in the samples of $BaTi_{1-x}Zr_xO_3$ are observed at temperatures close to the respective value of the transition between two ferroelectric phases of pure $BaTiO_3$ ($T = 5$°C) with the orthorhombic and tetragonal crystalline structures. The observed increase in the temperature of this transition agrees with the phase diagram of the solid $BaTi_{1-x}Zr_xO_3$

21

solutions in the range of small zirconium concentrations.

However, we should note that the temperature values of both phase transitions in all six samples vary insignificantly with the change of the assumed zirconium concentration in solutions and show no dependence on x [12]. This is probably due to the fact the main contribution to the dielectric response of the obtained solutions is made by the phase of the solid $BaTi_{1-x}Zr_xO_3$ solutions with low and approximately identical zirconium concentration of $x < 0.1$ for all the samples.

Diffuse reflectance spectra and integral absorption coefficient. A study of the diffuse reflectance spectra in the solar range of the synthesized powders necessary for finding the optimal concentration of the zirconium cations to obtain the $BaTi_{1-x}Zr_xO_3$ powder with high reflectance and low absorption coefficient as is of particular interest.

The diffuse reflectance spectra of the $BaTi_{1-x}Zr_xO_3$ powders were registered in the UV, visible and near infrared ranges. Fig. 4 presents the diffuse reflectance spectra of the synthesized powders with the concentration of substituting zirconium cations in the range from 0 to 30%.

For all concentrations of substituting zirconium cations, the reflectance coefficient of the $BaTi_{1-x}Zr_xO_3$ powders varies in the range of 85–96% in the area from the main absorption edge to 2200 nm. Qualitatively, the form of ρ spectra is practically identical for all the powders under study, at 1400 and 2040 nm wavelengths, there are absorption bands visible due to OH-groups located at the surface of the powder grains and granules of $BaTi_{1-x}Zr_xO_3$ [13]. In the area of the main absorption edge, as the zirconium concentration grows, we can observe a minor deterioration in reflectance.

It follows from the diffuse reflectance spectra shown in Fig. 4 that $BaTi_{1-x}Zr_xO_3$ powder has the highest reflectance in the visible and near infrared ranges at the zirconium concentration of $x = 0.05$, and the lowest reflectance at the concentration of $x = 0.15$. The difference in the reflection coefficient for different zirconium concentrations in one wavelength reaches 10%.

The integral absorption coefficient of solar radiation as was calculated based on the diffuse reflection coefficient using the following formula:

$$a_s = 1 - R_s = 1 - \frac{\int_{\lambda_1}^{\lambda_2} \rho_\lambda I_\lambda d\lambda}{\int_{\lambda_1}^{\lambda_2} I_\lambda d\lambda} = 1 - \frac{\sum_{i=1}^{n} \rho_\lambda}{n},$$
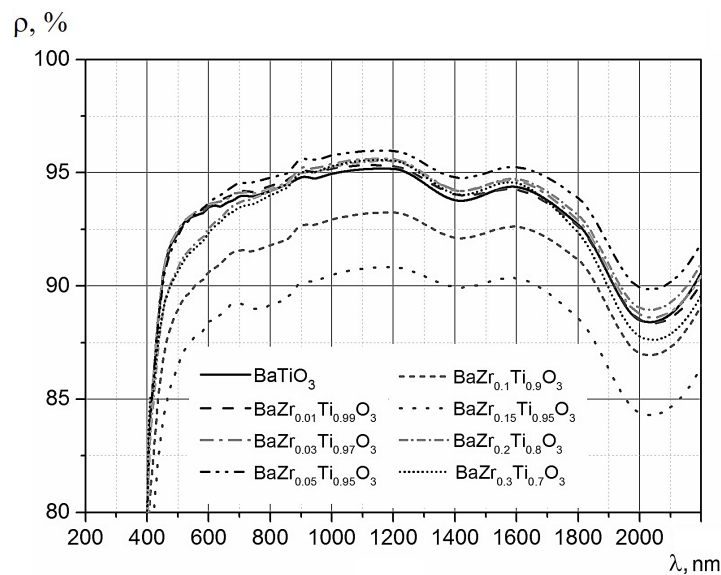
Fig. 4. Diffuse reflectance spectra of solid $BaTi_{1-x}Zr_xO_3$ solutions with different content of substituting zirconium cations
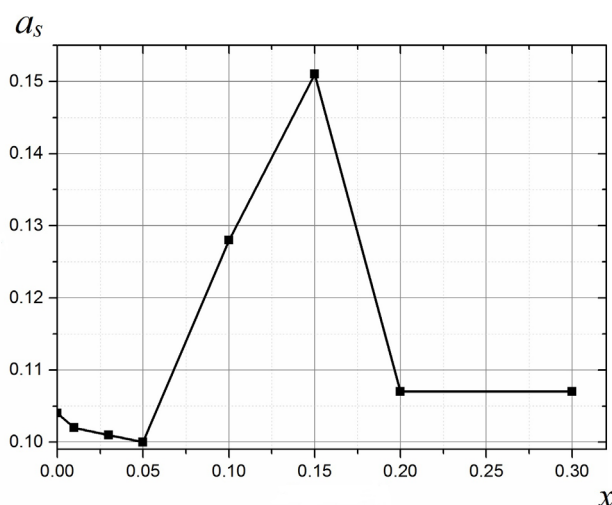
Fig. 5. Dependence of the integral absorption coefficient of solar radiation
on zirconium content in the solid $BaTi_{1-x}Zr_xO_3$ solution

Table 3

**Values of the integral absorption coefficient of solar radiation
for the $BaTi_{1-x}Zr_xO_3$ powders at different values of x**

x	0.00	0.01	0.03	0.05	0.10	0.15	0.20	0.30
a_s	0.104	0.102	0.101	0.100	0.128	0.151	0.107	0.107

N o t e. The presented results are obtained by means of calculations on the basis of the diffuse solar radiation reflectance spectra.

where R_s is the integral absorption coefficient of solar radiation calculated as the arithmetic mean value of the reflection coefficient over 24 points located in equal-energy areas of the solar radiation spectrum according to the international standards [14, 15]; ρ_λ is the spectral reflectivity; I_λ is the solar radiation spectrum; λ_1, λ_2, µm, are the boundary values of the solar spectrum range (in the area of 0.2–2,5 µm the sun radiates 98% of the total energy); n is the number of equal-energy areas of the solar spectrum given by the standard tables [14, 15].

As you can see from Table 3, all synthesized powders have rather low integral absorption coefficients of solar radiation in the range from 0.100 to 0.151 and can fall into the class of "solar reflectors". The $BaTi_{1-x}Zr_xO_3$ powder with 5% of zirconium cations ($x = 0.05$) possesses the smallest value of a_s (0.100), while the powder with 15% of zirconium ($x = 0.15$) has the greatest value.

Fig. 5 presents a dependence of a_s on the percentage of the substituting zirconium cations in the range from 0 to 30% ($x = 0–0.30$). As the zirconium cations concentration in the $BaTi_{1-x}Zr_xO_3$ compounds increases, the integral absorption coefficient of solar radiation changes based on a rather complex dependence with a minimum and a maximum. The highest values of as are observed at 10 and 15 % zirconium concentrations.

Conclusion

We used the solid-phase synthesis method with a two-step heating to produce $BaTi_{1-x}Zr_xO_3$ powders from a mixture of micron-sized $BaCO_3$, ZrO_2 and TiO_2 powders at concentration of substituting zirconium cations in the range of 0–30 weight % ($x = 0.01–0.30$). We studied the dependences of the particle-size distribution, phase composition, diffuse reflectance spectra in the

23

UV, visible and near infrared ranges, and the integral absorption coefficient of solar radiation as on the zirconium cations concentration. The established maximum yield of the main powder phase amounts to 90.3%. The form of the diffuse reflectance of the synthesized $BaTi_{1-x}Zr_xO_3$ micro powders varies insignificantly depending on the zirconium concentration; however, the qualitative changes reach 10%. The integral absorption coefficient of the studied powders at different zirconium concentration varied within 34%. The conducted dielectric research of the pressed powders revealed two peaks on the permittivity temperature dependences associated with the phase transitions. We determined the temperatures of these phase transitions for all compositions and revealed that the low temperature transition in the solutions under study was observed at room temperatures. This fact makes these compounds a promising material for production of pigments for thermal control coatings at operating temperatures of space crafts.

REFERENCES

1. **Li Q., Fan D., Xuan Y.,** Thermal radiative properties of plasma sprayed thermochromic coating, Journal of Alloys and Compounds. 583 (25 February) (2014) 516−522.

2. **Green N.W., Kim W., Low N., et al.,** Electrostatic discharges from conductive thermal coatings, IEEE Transactions on Plasma Science. 47 (8-2) (2019) 3759−3765.

3. **Yamamoto T., Sato Y., Tanaka T., et al.,** Electron transport behaviors across single grain boundaries in n-type $BaTiO_3$, $SrTiO_3$ and ZnO, Journal of Materials Science. 40 (4) (2005) 881− 887.

4. **Lee J.H., Nersisyan H.H., Lee H.H., Won C.W.,** Structural change of hydrothermal $BaTiO_3$ powder, Journal of Materials Science. 39 (4) (2004) 1397−1401.

5. **Rout S.K.,** Phase formation and dielectric studies of some BaO-TiO_2-ZrO_2 based perovskite system, A thesis in physics (Materials Science), April 2006, Department of Physics, National Institute of Technology, Rourkela-769 008 (A Deemed University) Orissa, India, 2006.

6. **Wang H., Cao X., Liu F., et al.,** Synthesis and electrochemical properties of transparent nanostructured $BaTiO_3$ film electrodes, Open Journal of Inorganic Chemistry. 5 (2) (2015) 30−39.

7. **Mikhailov M.M., Ul'yanitskii V.Yu., Vlasov V.A., et al.,** Thermostabilizing $BaTiO_3$ coatings synthesized by detonation spraying method, Surface Coating Technology. 319 (15 June) (2017) 70−75.

8. **Ho C., Fu S.-L.,** Effects of zirconium on the structural and dielectric properties of (Ba, Sr) TiO_3 solid solution, Journal of Materials Science. 25 (11) (1990) 4699−4703.

9. **Son S.Y., Kim B.S., Oh S.H., et al.,** Electrical properties of (Ba, Sr) TiO_3 on (Sr, Ca) RuO_3 electrode, Journal of Materials Science. 34 (24) (1999) 6115−6119.

10. **Saburi O., Wakino K., Fuzikawa N.,** Semiconductors based on barium titanate, Tokyo, 1977.

11. **Gorev M., Bondarev V., Flerov I., et al.,** Heat capacity study of double perovskite-like compounds $BaTi_{1-x}Zr_xO_3$, Physics of the Solid State. 47 (12) (2005) 2304−2308.

12. **Shvartsman V.V., Zhai J., Kleemann W.,** The dielectric relaxation in solid solutions $BaTi_{1-x}Zr_xO_3$, Ferroelectrics. 379 (1) (2009) 77−85.

13. **Cronemeyer D.C.,** Infrared absorption of reduced rutile TiO_2 single crystals, Physical Review. 113 (5) (1959) 1222−1226.

14. ASTM E490 − 00a Standard Solar Constant and Zero Air Mass Solar Spectral Irradiance Tables. 2005. https://www.astm.org/Standards/E490.htm

15. ASTM E903 − 96 Standard Test Method for Solar Absorptance, Reflectance, and Transmittance of Materials Using Integrating Spheres. 2005. https://www.astm.org/DATABASE.CART/HISTORICAL/E903-96.htm

THE AUTHORS

MIKHAILOV Mikhail M.

Tomsk State University of Control Systems and Radioelectronics

40, Lenin Ave. Tomsk, 634050, Russian Federation

membrana2010@mail.ru

ALEKSEEVA Olga A.

Tomsk State University of Control Systems and Radioelectronics

40, Lenin Ave. Tomsk, 634050, Russian Federation

blackhole2010@yandex.ru

YURYEV Semen A.

Tomsk State University of Control Systems and Radioelectronics

40, Lenin Ave. Tomsk, 634050, Russian Federation

semyon.yuryev@tusur.ru

LAPIN Alexey N.

Tomsk State University of Control Systems and Radioelectronics

40, Lenin Ave. Tomsk, 634050, Russian Federation

alexey.lapin@tusur.ru

KOROLEVA Ekaterina Yu.

Peter the Great St. Petersburg Polytechnic University

29 Politechnicheskaya St., St. Petersburg, 195251, Russian Federation

e.yu.koroleva@mail.ioffe.ru

СПИСОК ЛИТЕРАТУРЫ

1. **Li Q., Fan D., Xuan Y.** Thermal radiative properties of plasma sprayed thermochromic coating // Journal of Alloys and Compounds. 2014. Vol. 583. 25 February. Pp. 516−522.

2. **Green N.W., Kim W., Low N., Zhou Ch., Andersen A., Linton T., Martin E.** Electrostatic discharges from conductive thermal coatings // IEEE Transactions on Plasma Science. 2019. Vol. 47. No. 8. Part 2. Pp. 3759−3765.

3. **Yamamoto T., Sato Y., Tanaka T., Hayashi K., Ikuhara Y., Sakuma T.** Electron transport behaviors across single grain boundaries in n-type $BaTiO_3$, $SrTiO_3$ and ZnO // Journal of Materials Science. 2005. Vol. 40. No. 4. Pp. 881−887.

4. **Lee J.H., Nersisyan H.H., Lee H.H., Won C.W.** Structural change of hydrothermal $BaTiO_3$ powder // Journal of Materials Science. 2004. Vol. 39. No. 4. Pp. 1397−1401.

5. **Rout S.K.** Phase formation and dielectric studies of some $BaO\text{-}TiO_2\text{-}ZrO_2$ based perovskite system. A thesis in physics (Materials Science). April 2006. Department of Physics. National Institute of Technology. Rourkela-769 008 (A Deemed University) Orissa, India. 166 p.

6. **Wang H., Cao X., Liu F., Guo S., Ren X., Yang S.** Synthesis and electrochemical properties of transparent nanostructured $BaTiO_3$ film electrodes // Open Journal of Inorganic Chemistry. 2015. Vol. 5. No. 2. Pp. 30−39.

7. **Mikhailov M.M., Ul'yanitskii V.Yu., Vlasov V.A., Sokolovskiy A.N., Lovitskii A.A.** Thermostabilizing $BaTiO_3$ coatings synthesized by detonation spraying method // Surface and Coating Technology. 2017. Vol. 319. 15 June. Pp. 70−75.

8. **Ho C., Fu S.-L.** Effects of zirconium on the structural and dielectric properties of (Ba, Sr) TiO_3

solid solution // Journal of Materials Science. 1990. Vol. 25. No. 11. Pp. 4699−4703.

9. **Son S.Y., Kim B.S., Oh S.H., Choi D.K., Yoo C.C., Lee S.I., Dai Z.R., Ohuchi F.S.** Electrical properties of (Ba, Sr)TiO$_3$ on (Sr, Ca)RuO$_3$ electrode // Journal of Materials Science. 1999. Vol. 34. No. 24. Pp. 6115−6119.

10. **Сабури О., Вакино К., Фудзикава Н.** Полупроводники на основе титаната бария. Пер. с японского яз. М.: Энергоиздат, 1982. 53 с.

11. **Горев М.В., Бондарев В.С., Флёров И.Н., Сью Ф., Саварио Ж.-М.** Исследования теплоемкости двойных перовскитоподобных соединений BaTi$_{1-x}$Zr$_x$O$_3$ // Физика твердого тела. 2005. Т. 47. № 12. С. 2212−2216.

12. **Shvartsman V.V., Zhai J., Kleemann W.** The dielectric relaxation in solid solutions BaTi$_{1-x}$Zr$_x$O$_3$ // Ferroelectrics. 2009. Vol. 379. No. 1. Pp. 77−85.

13. **Cronemeyer D.C.** Infrared absorption of reduced rutile TiO$_2$ single crystals // Physical Review. 1959. Vol. 113. No. 5. Pp. 1222−1226.

14. ASTM E490 − 00a standard solar constant and zero air mass solar spectral irradiance tables. 2005. https://www.astm.org/Standards/E490.htm

15. ASTM E903 − 96 standard test method for solar absorptance. Reflectance, and transmittance of materials using integrating spheres. 2005. https://www.astm.org/DATABASE.CART/HISTORICAL/E903-96.htm

СВЕДЕНИЯ ОБ АВТОРАХ

МИХАЙЛОВ Михаил Михайлович — *доктор физико-математических наук, профессор, заведующий лабораторией радиационного и космического материаловедения Томского государственного университета систем управления и радиоэлектроники, г. Томск, Российская Федерация.*

634050, Российская Федерация, г. Томск, пр. Ленина, 40

membrana2010@mail.ru

АЛЕКСЕЕВА Ольга Александровна — *кандидат физико-математических наук, старший научный сотрудник лаборатории радиационного и космического материаловедения Томского государственного университета систем управления и радиоэлектроники, г. Томск, Российская Федерация.*

634050, Российская Федерация, г. Томск, пр. Ленина, 40

kblackhole2010@yandex.ru

ЮРЬЕВ Семен Александрович — *кандидат технических наук, старший научный сотрудник лаборатории радиационного и космического материаловедения Томского государственного университета систем управления и радиоэлектроники, г. Томск, Российская Федерация.*

634050, Российская Федерация, г. Томск, пр. Ленина, 40

semyon.yuryev@tusur.ru

ЛАПИН Алексей Николаевич — *кандидат технических наук, старший научный сотрудник лаборатории радиационного и космического материаловедения Томского государственного университета систем управления и радиоэлектроники, г. Томск, Российская Федерация.*

634050, Российская Федерация, г. Томск, пр. Ленина, 40

alexey.lapin@tusur.ru

КОРОЛЕВА Екатерина Юрьевна — *кандидат физико-математических наук, старший научный сотрудник научно-образовательного центра «Физика нанокомпозитных материалов электронной техники» Санкт-Петербургского политехнического университета Петра Великого, Санкт-Петербург, Российская Федерация.*

195251, Российская Федерация, г. Санкт-Петербург, Политехническая ул., 29
e.yu.koroleva@mail.ioffe.ru

THE ANOMALOUS RISE OF CAPACITANCE OF C$_{60}$ FULLERITE FILMS AT LOW FREQUENCIES: A CAUSE ANALYSIS

D.I. Dolzhenko, I.B. Zakharova, N.T. Sudar

Peter the Great St. Petersburg Polytechnic University,
St. Petersburg, Russian Federation

A known physical fact of the anomalous rise of dielectric permittivity ε of C$_{60}$ fullerite films at ac low frequencies (below 1 kHz) has not had a convincing explanation up to now. Our study was aimed at elucidating the causes of that anomaly. The p-Si/C$_{60}$/InGa-eutectic structure was made and a frequency dependence of its capacitance was measured. Relying on the experimental result, a versatile analysis of the phenomenon was carried out. It was shown that the anomalous rise of ε value in the low-frequency region resulted from oxygen intercalation of fullerite with formation of C$_{60}$/O$_{2}$ molecular groups exhibited significant dipole momenta. The presence of such groups produced a dramatic difference between dielectric permittivity of the crystallites' surface areas and that of their volumes. As a result, the difference led to an apparent increase in the dielectric permittivity ε of the structure under study.

Keywords: C$_{60}$ fullerite, polycrystalline film, permittivity, Frohlich's equation, oxygen intercalation

АНАЛИЗ ПРИЧИН АНОМАЛЬНОГО ПОВЫШЕНИЯ ЕМКОСТИ ПЛЕНОК ФУЛЛЕРИТА C$_{60}$ НА НИЗКИХ ЧАСТОТАХ

Д.И. Долженко, И.Б. Захарова, Н.Т. Сударь

Санкт-Петербургский политехнический университет Петра Великого,
Санкт-Петербург, Российская Федерация

Известный экспериментальный факт аномального возрастания диэлектрической проницаемости ε пленок фуллерита C$_{60}$ на низких частотах (ниже 1 кГц) переменного электрического тока не имеет до настоящего времени убедительного объяснения. Данное исследование было нацелено на выяснение причин указанной аномалии. Была изготовлена структура p-Si/C$_{60}$/эвтектика InGa и измерена частотная зависимость ее емкости. На основании полученных экспериментальных данных проведен многосторонний анализ явления. Показано, что возможной причиной аномального повышения ε в низкочастотной области является интеркаляция фуллерита молекулами кислорода с образованием молекулярных групп C$_{60}$/O$_{2}$, обладающих значительным дипольным моментом. Наличие таких групп вызывает кардинальное различие между значениями диэлектрической проницаемости поверхностных областей кристаллитов и таковой для области их объема, что, в свою очередь, приводит к кажущемуся подъему диэлектрической проницаемости исследуемой структуры.

Ключевые слова: фуллерит C$_{60}$, поликристаллическая пленка, диэлектрическая проницаемость, уравнение Фрёлиха, интеркаляция кислорода

Introduction

Fullerene thin films are currently believed to be promising candidates for organic electronics [1 − 3]. A major focus is investigations into the properties of fullerene C_{60}, since its molecules have the greatest symmetry and stability. A characteristic feature of fullerene in condensed phase (fullerite) is that impurity atoms can be intercalated into its crystal lattice [4]. Impurity atoms in the face-centered cubic (fcc) lattice of C_{60} fullerite fill octahedral and tetrahedral voids between the host molecules, interacting with them with a potentially pronounced effect on the physical properties of fullerite films [5].

Intercalation of fullerite by oxygen atoms is a particularly intriguing subject. The electron affinity of C_{60} molecules is significantly higher than that of oxygen molecules, estimated at about 2.67 eV [6], while for oxygen it amounts to about 0.45 eV [7]. Therefore, it can be expected that oxygen acts as an electron donor, and fullerite as an electron acceptor. It is hypothesized in [8] that partial transfer of an electron from a donor to an acceptor generates a dipole moment in the C_{60}/O_2 molecule, which is what likely causes a significant increase in the dielectric permittivity for C_{60} films at frequencies below 10^3 Hz. However, the actual physical mechanism behind this phenomenon is not considered in [8].

Electrode polarization is often the cause of the abnormal increase in capacitance at low AC frequencies, occurring in dielectrics with noticeable electrical conductivity given poor contact between the sample and the electrode. A thin layer forms at the interface in these conditions, characterized by a significant electrical impedance [9]. Obviously, this reason is not related to the physical properties of the actual fullerite films.

Other reasons for the anomalous increase in the capacitance of dielectrics in the low-frequency region are also discussed in the literature. For example, the Maxwell − Wagner polarization is observed in inhomogeneous dielectrics with conducting impurities [10]; for polycrystalline dielectrics, this can be attributed to the difference between the permittivities (and conductivities) of the external and internal regions of crystallites, i.e., the grain-interlayer model [3, 10].

The goal of this study consists in understanding the potential role of the described effects and assessing the degree to which they influence the dielectric permittivity of C_{60} fullerite films.

Experimental procedure

The sample was a C_{60} fullerite film deposited on a cold substrate made of p-type silicon of KDB-1 grade by thermal spraying. The thickness L of the film, measured with an MII-4 interference microscope, was 250±50 nm.

A close focus was on ensuring reliable contacts between the fullerite sample and the electrodes.

The C_{60} film produced by this method had a polycrystalline structure with the size D of crystallites equal to 100 − 200 nm [11]. The crystallites forming the film were randomly arranged on the silicon substrate in several layers. Before the experiments, the C_{60} films deposited on the substrates were exposed to an air atmosphere for a long time in order to ensure reliable contact of the film with the silicon substrate, since the latter was used as one of the electrodes.

The second electrode was a needle probe made of a liquid indium-gallium eutectic [12]. Such an electrode provided reliable electrical contact with the fullerite film, without mechanical damage, due to interaction of the surface tension forces of the eutectic and gravitational forces.

An E7-20 LCR meter was used to measure the capacitance C and the tangent tgδ of the dielectric loss angle in the frequency range from 25 Hz to 1 MHz. The amplitude of the test AC voltage was 0.04 V. All measurements were carried out at room temperature $T = 293$ K in a darkened measuring cell. The given section of the C_{60} film was subjected to electroforming prior to dielectric measurements: a constant voltage $U = 30$ V was applied to the electrodes for several tens of

minutes. Electroforming considerably increased the stability of the readings and the reproducibility of the results for repeated measurements in this section of the film [11].

The area S of the contact spot of the needle electrode with the fullerite film was calculated based on the data for the capacitance C of the given structure measured at a frequency of 1 MHz. It was assumed that the dielectric permittivity of the film at this frequency was close to the value of the high-frequency dielectric permittivity ε_∞ of C_{60} fullerite. According to the data given in literature [13], $\varepsilon_\infty = 2.6$. Therefore, with a capacitance $C = 8.2$ pF, the area of the contact spot turns out to be $S \approx 0.09$ mm². This value of S was subsequently used to calculate the dielectric permittivity spectrum in the entire investigated frequency range.

Experimental results and discussion

The goal posed at the first stage of the study was to find out whether the increase in capacitance in the low-frequency region is due to the phenomenon of electrode polarization. According to the data given in [9], the correction for electrode effects in low-frequency measurements, defined as the difference between the measured capacitance C and the true capacitance C_{true} (appearing in the absence of electrode polarization), depends on the material conductivity σ and the frequency f, at which the measurement is carried out, so that

$$C - C_{true} \sim \sigma^2 / f^2. \tag{1}$$

Since the photoconductivity of C_{60} fullerite is observed in the visible spectral range, the conductivity of the given structure could be increased by exposure to light. For this purpose, we used a white LED with a color temperature of 4000 K, producing a luminous flux of 250 lm. The light was focused on the contact spot of the indium-gallium electrode with the fullerite film using a special lens. The structure's conductivity increased from $7 \cdot 10^{-7}$ S/cm (value in the dark) to $3 \cdot 10^{-5}$ S/cm upon illumination.

Fig. 1 shows the low-frequency dependences for the capacitance of the given structure in the dark (curve *1*) and under LED lighting (curve *2*), i.e., at different concentrations of free charge carriers determining the conductivity in it. Apparently, the curves on the graph practically coincide, although the value of the capacitance should have increased by about four orders of magnitude, in accordance with Eq. (1). Furthermore, the assumed dependence should have been linear in the case of electrode polarization in the considered coordinates $C(1/f^2)$ but this did not happen either.

Thus, analysis of the experiment carried out at the first stage of the study allows eliminating electrode polarization as the cause of the anomalous increase in capacitance in the low-frequency region of the spectrum. In other words, the increase in capacitance we have observed should not be regarded as an artifact, that is, it is not associated with the specific experimental conditions or the peculiarities of electrical contacts.

At the second stage of the study, we considered the deep mechanisms underlying the increase in the capacitance of the structure at low frequencies.

As noted above, fullerite films obtained by thermal spraying are polycrystalline. Oxygen molecules quickly penetrate into the film, diffusing along the crystallite interfaces; as a result, the near-interface regions of the crystallites are saturated with oxygen to a greater extent than their bulk. For this reason, the conductivity and dielectric permittivity of the surface layers of crystallites and their bulk are different [3]. Consequently, the dielectric dispersion in such structures is best described by the theory of multilayer dielectric systems, characterized by an abnormally high dielectric permittivity in the low-frequency region [9].

Fig. 2, a shows the dependence of the dielectric permittivity on the frequency f. The values of ε' were calculated with the equation for a plane capacitor based on capacitance measurements. Evidently, the dielectric permittivity increases rapidly and monotonically with a decrease in the frequency of the applied AC voltage. For example, $\varepsilon' \approx 3$ at a frequency of 10^3 Hz, reaching $\varepsilon' \approx 300$ at 30 Hz.

The dependence of the dielectric loss angle
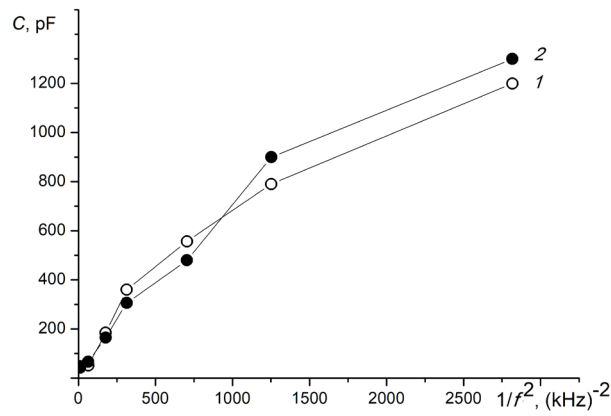
Fig. 1. Low-frequency dependences for capacitance of a p-Si/C$_{60}$/InGa
eutectic structure in the dark (1) and under LED lighting (2).
Luminous flux (250 lm) focused on the contact spot of the C$_{60}$/InGa eutectic at $T = 293$ K

a)

b)
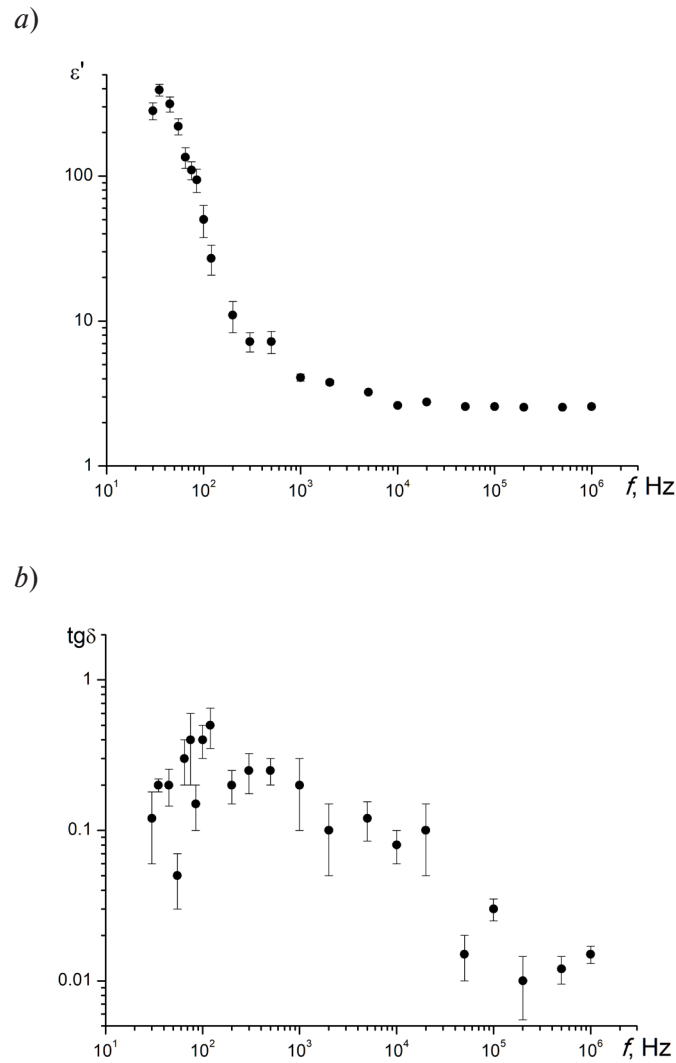
Fig. 2. Dependences of dielectric permittivity (a) and dielectric loss angle tangent (b)
for p-Si/C$_{60}$/InGa eutectic structure; $T = 293$ K

tangent tgδ (f) (Fig. 2, b) bears a non-monotonic character. The value of tgδ ≈ 0.01 at frequencies above 10^5 Hz, however, it gradually increases with decreasing frequency, reaching a maximum value of about 0.8 at $f \approx 10^2$ Hz, subsequently decreasing to about 0.1. It is impossible to accurately determine the position of this maximum on the frequency scale due to the significant scatter of data in measurements of tgδ. Notably, a broad maximum was also observed in [8] for the frequency curve tanδ in the region of 1 kHz during measurements of C_{60} fullerite films. The appearance of the maximum was attributed to intercalation of fullerite with oxygen and formation of dipole groups in the C_{60}/O_2 molecule.

According to the grain-interlayer model, the set of links that are internal crystallite regions (grains) and their surface regions (interlayers) is considered as a homogeneous structure with a common relaxation time τ corresponding to the relaxation time of an individual link, while the value of τ is calculated by the Debye equations for dipole orientation polarization.

As polar molecular groups C_{60}/O_2 are accumulated in the interlayers, their dielectric permittivity turns out to be higher than that of grains, and the conductivity of these groups is lower [9]. Therefore, the low-frequency dielectric permittivity ε_1 of the oxidized near-surface crystallite layer (interlayer) can be estimated using the relation

$$\varepsilon' = \varepsilon_1 D/d, \qquad (2)$$

where ε' is the dielectric permittivity of the C_{60} film, determined experimentally; d is the thickness of the oxidized near-surface crystallite layer (interlayer).

The thickness d can only be estimated approximately. According to the data in [14], the value of d should not exceed 15 nm. Consequently, given a crystallite size of $D = 150$ nm, we obtain that the dielectric permittivity ε_1 of the interlayer lies in the range from 10 to 30 at a frequency of 35 Hz with d in the range from 5 to 15 nm.

Let us estimate the values of the dipole moment of the C_{60}/O_2 molecule and the concentra-

tions of these molecules at which the given value of ε_1 is attainable. We use the Fröhlich equation relating the macroscopic dielectric permittivity to the dipole moment of the molecule

$$\frac{(\varepsilon_1 - \varepsilon_\infty)(2\varepsilon_1 + \varepsilon_\infty)}{\varepsilon_1(\varepsilon_\infty + 2)^2} = \frac{Ngp^2}{9\varepsilon_0 k_B T}, \qquad (3)$$

where N is the number of polar molecules of C_{60}/O_2 (dipoles) per unit volume of the interlayer; p, D, is their dipole moment; T, K, is the temperature, kB, JK^{-1}, is the Boltzmann constant; ε_0, F/m, is the vacuum permittivity; g is a parameter accounting for the local ordering of molecules;

$$g = 1 + z\langle\cos\gamma\rangle.$$

Here z is the coordination number ($z = 12$ for the fcc lattice), $\langle\cos\gamma\rangle$ is the average cosine of the angle between the molecule at the point of reference and its nearest neighbors ($\langle\cos\gamma\rangle = 0.7$ was taken in the calculations).

Let us calculate the value of N bearing in mind that there are two C_{60} molecules for each fcc cell. Suppose that all C_{60} molecules in the near-surface layer of the compound are oxidized; then the number of dipoles per unit volume of this layer is equal to

$$N = 2\frac{V_{ox}}{(a \cdot D)^3}, \qquad (4)$$

where V_{ox}, nm³, is the volume of the oxidized layer in one crystallite, a, nm, is the edge length of the fcc cell of C_{60} ($a = 1.417$ nm [14]).

We obtain for these conditions that $N \approx 2.5 \cdot 10^{26}$ m⁻³. This value of the concentration of polar groups seems reasonable, since, according to the data in [14], the relative oxygen content in the oxidized layer is C : O = 10 : 1.

According to the data in [8], the value of the dipole moment p of the C_{60}/O_2 molecule is 0.9 D. The authors estimated it assuming that the fraction ξ of the charge transferred from the donor (intercalated oxygen O_2) to the acceptor (C_{60} fullerite molecule) was 4%. This value of ξ was
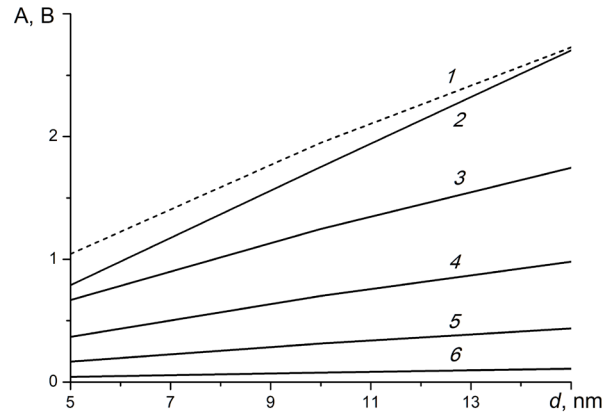
Fig. 3. Dependences of left (A) (straight line *1*) and right-hand (B) (straight lines *2 − 6*) sides of the Fröhlich equation (3) on the thickness of oxidized near-surface crystallite layer (interlayer) at different values of the dipole moment of the C_{60}/O_2 molecule, *p*, D: 5 (*2*), 4 (*3*), 3 (*4*), 2 (*5*), 1 (*6*)

determined by the authors from the condition of the best agreement between the calculation results and experiment. Nevertheless, it is pointed out in [15] that a substantially larger fraction of the charge can be transferred. According to the estimates in that study, the value of ξ can reach 49%.

We should note that estimating the dipole moments of the given molecular groups should account for the fact tha interaction of oxygen with fullerene molecules produces various forms of oxidized fullerene $C_{60}O_n$. For example, the so-called 'open' and 'closed' epoxides can evolve, as well as other isomers, where the oxygen atoms can be attached to different sites of the fullerene molecule. An oxygen atom in the 'open' epoxide, $C_{60}O$ (5-6, pentagon-hexagon), is attached to two carbon atoms at the border of the corresponding faces. The oxygen atom in the 'closed' one, $C_{60}O$ (6-6, hexagon-hexagon), is located above the double bond at the border of two hexagons [16]. As already mentioned, the oxygen atoms in other isomers can be attached to various sites of the fullerene molecule.

Evidently, all the formed $C_{60}O_n$ molecules are characterized by different lengths of chemical bonds and the degree of electron density transfer from donor to acceptor, and, as a consequence, different dipole moments.

In view of the above, let us find the values of the interlayer thickness *d* and the dipole moment *p* for which relation (3) can be satisfied. Calculating its left-hand side for various values of *d*, we use expression (2), taking $\varepsilon' = 300$ and $D = 150$ nm. We denote this left-hand side as A (*d*), and the right-hand, which includes the previously estimated parameters *N* and *g*, as B (*d*). We consider the dipole moment of the C_{60}/O_2 molecule as a parameter, varying its values.

These dependences are shown in Fig. 3. Apparently, the condition A = B can be fulfilled only at the thickness of the oxidized layer $d \approx 15$ nm (which is consistent with the known experimental results), but at significant dipole moments of the C_{60}/O_2 molecules, amounting to 4−5 D, when the relative fraction δ of the transferred electron charge exceeds 22%, according to the data in [8].

Conclusion

We have considered the frequency dependence of the dielectric properties of the p-Si/C_{60}/InGa eutectic structure. We have confirmed that the molecular groups C_{60}/O_2 evolving in the external regions of the crystallites of the C_{60} fullerite possessing a substantial dipole moment can be regarded as a physical mechanism governing the anomalously high increase in the capacity of the given structure at a low frequency. The conductivity and dielectric permittivity of the surface

layers of crystallites and their bulk are different, producing an apparent increase in the dielectric permittivity of the given structure. Therefore, the dielectric permittivity in such structures can be described based on the theory of multilayer dielectric systems.

Acknowledgment

The authors would like to express their gratitude to V.F. Borodzyulya for assistance with experiments.

REFERENCES

1. **Sachdeva S., Singh D., Tripathi S.K.,** Optical and electrical properties of fullerene C_{70} for solar cell applications, Optical Materials. 101 (March) (2020) 109717.

2. **Pascual J., Delgado J.L., Tena-Zaera R.,** Physicochemical phenomena and application in solar cells of perovskite: Fullerene films, The Journal of Physical Chemistry Letters. 9 (11) (2018) 2893−2902.

3. **Dolzhenko D.I., Borodzyulya V.F., Zakharova I.B., Sudar' N.T.,** The influence of space-charge-limited current on the dielectric properties of polycrystalline films of fullerite C_{60}, Technical Physics. 66 (1) (2021) 53−58.

4. **Assink R.A., Schirber J.E., Loy D.A., et al.,** Intercalation of molecular species into the interstitial sites of fullerene, Journal of Materials Research. 7 (8) (1992) 2136−2143.

5. **Yagotintsev K.A., Stetsenko Yu.E., Gal'tsov N.N., et al.,** Effect of impurity oxygen molecules on the structural and thermodynamic properties of fullerite C_{60}, Low Temperature Physics. 36 (3) (2010) 266−271.

6. **Brink C., Andersen L.H., Hvelplund P., et al.,** Laser photodetachment of C_{60}^- and C_{70}^- ions cooled in a storage ring, Chemical Physics Letters. 233 (1−2) (1995) 52−56.

7. **Gurvich L.V., Karachevcev G.V., Kondratiev V.N., et al.,** Energii razryva khimicheskikh sviazey. Potentsial ionizatsii i srodstvo k elektronu. Spravichnik. [Chemical bound energies. Ionization potential and electron affinity, Reference book], Nauka, Moscow, 1974 (in Russian).

8. **Pevzner B., Hebard A.F., Dresselhaus M.S.,** Role of molecular oxygen and other impurities in the electrical transportand dielectric properties of C_{60} films, Physical Review B. 55 (24) (1997) 16439−16449.

9. **Blythe A.R., Blythe T, Bloor D.,** Electrical properties of polymers, Cambridge University Press, Cambridge, 2005.

10. **Koops C.G.,** On the dispersion of resistivity and dielectric constant of some semiconductors at audio frequencies, Physical Review. 83 (1) (1951) 121−124.

11. **Zakharova I.B., Dolzhenko D.I., Borodzyulya V.F., Sudar' N.T.,** The electroforming effect in polycrystalline fullerene C_{60} films, Technical Physics Letters. 45 (2) (2019) 142−144.

12. **Borodzyulya V.F., Moshnikov B.A., Permiakov H.V.,** Measuring probe and method of its manufacture. Pat. RU 2654385 C1. Russia, G 01 Q 60/00, 70/16, B 82 Y 35/00. No. 2017 11 4837. Date of filing: 26.04. 2017. Published 17.05.2018. Proprietors: Borodzyulya V.F., Moshnikov B.A., Permiakov H.V., Bul. No. 14. 2018.

13. **Mondal P., Lunkenheimer P., Loidl A.,** Dielectric relaxation, ac and dc conductivities in the fullerenes C_{60} and C_{70}, Zeitschrift für Physik. B: Condensed Matter. 99 (1) (1995) 527−533.

14. **Makarova T.L., Vul' A.Ya., Zakharova I.B., Zubkova T.I.,** Oriented growth of oxygen-free C_{60} crystallites on silicon substrates, Physics of the Solid State. 41 (2) (1999) 319−323.

15. **Dattani R., Gibson K.F., Few S., et al.,** Fullerene oxidation and clustering in solution induced by light, Journal of Colloid and Interface Science. 446 (15 May) (2015) 24−30.

16. **Creegan K.M., Robbins J.L., Robbins W.K., et al.,** Synthesis and characterization of $C_{60}O$, the first fullerene epoxide, Journal of the American Chemical Society. 114 (3) (1992) 1103−1105.

THE AUTHORS

DOLZHENKO Dmitry I.
Peter the Great St. Petersburg Polytechnic University
29 Politechnicheskaya St., St. Petersburg, 195251, Russian Federation
ddi.dev.94@gmail.com

ZAKHAROVA Irina B.
Peter the Great St. Petersburg Polytechnic University
29 Politechnicheskaya St., St. Petersburg, 195251, Russian Federation
zakharova@rpht.spbstu.ru

SUDAR Nicolay T.
Peter the Great St. Petersburg Polytechnic University
29 Politechnicheskaya St., St. Petersburg, 195251, Russian Federation
sudar53@mail.ru

СПИСОК ЛИТЕРАТУРЫ

1. **Sachdeva S., Singh D., Tripathi S.K.** Optical and electrical properties of fullerene C_{70} for solar cell applications // Optical Materials. 2020. Vol. 101. March. P. 109717.

2. **Pascual J., Delgado J.L., Tena-Zaera R.** Physicochemical phenomena and application in solar cells of perovskite: Fullerene films // The Journal of Physical Chemistry Letters. 2018. Vol. 9. No. 11. Pp. 2893−2902.

3. **Долженко Д.И., Бородзюля В.Ф., Захарова И.Б., Сударь Н.Т.** Влияние тока, ограниченного объемным зарядом, на диэлектрические свойства поликристаллических пленок фуллерита C_{60} // Журнал технической физики. 2021. Т. 91. Вып. 1. С. 58−63.

4. **Assink R.A., Schirber J.E., Loy D.A., Morosin B., Carlson G.A.** Intercalation of molecular species into the interstitial sites of fullerene // Journal of Materials Research. 1992. Vol. 7. No. 8. Pp. 2136−2143.

5. **Яготинцев К.А., Стеценко Ю.Е., Гальцов Н.Н., Легченкова И.В., Прохватилов А.И.** Влияние примесных молекул кислорода на структурные и термодинамические свойства фуллерита C_{60} // Физика низких температур. 2010. Т. 36. № 3. С. 335−342.

6. **Brink C., Andersen L.H., Hvelplund P., Mathur D., Voldstad J.D.** Laser photodetachment of C_{60}^- and C_{70}^- ions cooled in a storage ring // Chemical Physics Letters. 1995. Vol. 233. No. 1−2. Pp. 52−56.

7. **Гурвич Л.В., Карачевцев Г.В., Кондратьев В.Н., Лебедев Ю.А., Медведев В.А., Потапов В.К., Ходеев Ю.С.** Энергии разрыва химических связей. Потенциалы ионизации и сродство к электрону. М.: Наука, 1974. 351 с.

8. **Pevzner B., Hebard A.F., Dresselhaus M.S.** Role of molecular oxygen and other impurities in the electrical transport and dielectric properties of C_{60} films // Physical Review B. 1997. Vol. 55. No. 24. Pp. 16439−16449.

9. **Блайт Э.Р., Блур Д.** Электрические свойства полимеров. М.: Физматлит, 2008. 376 с.

10. **Koops C.G.** On the dispersion of resistivity

and dielectric constant of some semiconductors at audio frequencies // Physical Review. 1951. Vol. 83. No. 1. Pp. 121−124.

11. **Захарова И.Б., Долженко Д.И., Бородзюля В.Ф., Сударь Н.Т.** Эффект электроформовки в поликристаллических пленках фуллерена C_{60} // Письма в Журнал технической физики. 2019. Т. 45. Вып. 4. С. 21−23.

12. **Бородзюля В.Ф., Мошников В.А., Пермяков Н.В.** Измерительный зонд и способ его изготовления. Пат. RU 2654385 C1. Россия. G 01 Q 60/00, 70/16, B 82 Y 35/00. Заявка № 2017 11 4837. Заявл. 26.04.2017. Опубл. 17.05.2018. Патентообладатели: Бородзюля В.Ф., Мошников В.А., Пермяков Н.В. Бюл. № 14. 2018. 2 с.

13. **Mondal P., Lunkenheimer P., Loidl A.** Dielectric relaxation, ac and dc conductivities in the fullerenes C_{60} and C_{70} // Zeitschrift für Physik. B: Condensed Matter. 1995. Vol. 99. No. 1. Pp. 527−533.

14. **Макарова Т.Л., Захарова И.Б., Зубкова Т.И., Вуль А.Я.** Ориентированный рост бескислородных кристаллитов C_{60} на кремниевых подложках // Физика твердого тела. 1999. Т. 41. № 2. С. 354−359.

15. **Dattani R., Gibson K.F., Few S., Borg A.J., Dimaggio P.A., Nelson J., Kazarian S.G., Cabral J.T.** Fullerene oxidation and clustering in solution induced by light // Journal of Colloid and Interface Science. 2015. Vol. 446. 15 May. Pp. 24−30.

16. **Creegan K.M., Robbins J.L., Robbins W.K., Millar J.M., Sherwood R.D., Tindall P.J., Jones D.R.** Synthesis and characterization of $C_{60}O$, the first fullerene epoxide // Journal of the American Chemical Society. 1992. Vol. 114. No. 3. Pp. 1103−1105.

СВЕДЕНИЯ ОБ АВТОРАХ

ДОЛЖЕНКО Дмитрий Игоревич — *аспирант Высшей школы прикладной физики и космических технологий Санкт-Петербургского политехнического университета Петра Великого, Санкт-Петербург, Российская Федерация.*

195251, Российская Федерация, г. Санкт-Петербург, Политехническая ул., 29
ddi.dev.94@gmail.com

ЗАХАРОВА Ирина Борисовна — *доктор физико-математических наук, доцент инженерно-физической школы Санкт-Петербургского политехнического университета Петра Великого, Санкт-Петербург, Российская Федерация.*

195251, Российская Федерация, г. Санкт-Петербург, Политехническая ул., 29
zakharova@rpht.spbstu.ru

СУДАРЬ Николай Тобисович — *доктор физико-математических наук, профессор Высшей школы прикладной физики и космических технологий Санкт-Петербургского политехнического университета Петра Великого, Санкт-Петербург, Российская Федерация.*

195251, Российская Федерация, г. Санкт-Петербург, Политехническая ул., 29
sudar53@mail.ru

Simulation of physical processes

STABILITY OF AN ELASTIC ORTHOTROPIC CANTILEVER PLATE

M.V. Sukhoterin[1], T.P. Knysh[1], E.M. Pastushok[1], R.A. Abdikarimov[2]

[1] Admiral Makarov State University of Maritime and Inland Shipping,
St. Petersburg, Russian Federation;

[2] Tashkent Financial Institute,
Tashkent, Republic of Uzbekistan

The paper studies the stability of an elastic orthotropic rectangular cantilever plate under compressive forces applied to the face opposite to the seal. The aim of the study was to obtain the range of critical forces and the relevant shapes of the supercritical equilibrium. The deflection function was chosen as a sum of two hyperbolic-trigonometric series with the addition of special compensating terms for the free terms of the Fourier cosine series to the symmetric solution. For the square ribbed plate, the first three critical loads of the symmetric solution and the first critical load of the antisymmetric solution were obtained. The authors present 3D images of the respective equilibrium forms. The results obtained can be used to study the stability of cantilever elements of various structures.

Keywords: orthotropic cantilever plate, stability, Fourier series, critical load, equilibrium form

УСТОЙЧИВОСТЬ УПРУГОЙ ОРТОТРОПНОЙ КОНСОЛЬНОЙ ПЛАСТИНКИ

М.В. Сухотерин[1], Т.П. Кныш[1], Е.М. Пастушок[1], Р.А. Абдикаримов[2]

[1] Государственный университет морского и речного флота
имени адмирала С.О. Макарова, Санкт-Петербург, Российская Федерация;
[2] Ташкентский финансовый институт,
г. Ташкент, Республика Узбекистан

В работе исследуется устойчивость упругой ортотропной прямоугольной консольной пластинки под действием сжимающих усилий, приложенных к грани, противоположной заделке. Целью исследования является получение спектра критическиих усилий и соответствующих форм закритического равновесия. Функция прогибов выбирается в виде суммы двух гиперболо-тригонометрических рядов с добавлением к симметричному решению специальных компенсирующих слагаемых для свободных членов разложения функций в ряды Фурье по косинусам. Выполнение всех условий краевой задачи приводит к бесконечной однородной системе линейных алгебраических уравнений относительно неизвестных коэффициентов рядов. Поиск критических нагрузок (собственных чисел), дающих нетривиальное решение этой системы, осуществляется перебором величины сжимающей нагрузки в сочетании с методом последовательных приближений. Для квадратной ребристой пластинки получены первые три критические нагрузки симметричного решения и первая критическая нагрузка антисимметричного решения. Представлены 3D-изображения соответствующих форм равновесия. Результаты работы могут быть использованы для исследования устойчивости консольных элементов различных конструкций.

Ключевые слова: ортотропная консольная пластина, устойчивость, ряд Фурье, критическая нагрузки, форма равновесия

Introduction

Cantilever plates are used in various fields of technology: in civil and mechanical engineering, shipbuilding and aviation, in instrumentation and control engineering [1] (ferromagnetic plates). Cantilever plates are used in nanotechnology as key sensor components for nanoscale transistors [2], where they are exposed to magnetic fields in the plane of the plate. Cantilever plates are also used in different smart structures [3, 4].

The stability of orthotropic cantilever plates has received insufficient attention this far due to the complexity of the basic differential equation of the problem and the boundary conditions. Reliable numerical analytical methods need to be developed to solve this problem. If we assume the plate material to be perfectly elastic, then there is an infinite number of critical loads that change the form of the plate equilibrium. This eigenvalue problem is similar to the problem on determining the frequency spectrum of free vibrations of a plate [5]. It is primarily interesting from a mathematical standpoint. In practice, only the first critical load (assumed to be load to failure) is computed for planar elements of standard metal structures; however, elastic plates can work in the supercritical region in the presence of structural bending limiters and a rapid increase in the compressive load, acquiring subsequent forms of equilibrium, including antisymmetric ones. Failure may not occur at the first critical load; therefore, it is of practical importance to determine a certain range of critical loads and the corresponding forms of equilibrium.

The stability problem is solved in this study in a linear statement within the theory of thin rigid plates. A more complex nonlinear problem arises for stability of flexible plates; however, linear solutions are used as reference to check the accuracy of the given approximate method.

The stability of anisotropic and isotropic rectangular plates was investigated in [6 − 16] by different means. The methods for solving the buckling problems of anisotropic plates and shells considered in [6 − 9] are also applicable to cantilever plates.

The stability of an isotropic cantilever plate was described in [10, 11] for the cases when a compressive load was applied to a face parallel to the clamped edge [10], and when it was applied to a side face [11]. The first critical loads were found from the condition of the minimum potential energy. Lateral buckling under the action of a concentrated force was also considered in [12] using finite element modeling (FEM). FEM was used in [1] to analyze buckling in ferromagnetic cantilever plates in a magnetic field accounting for plastic deformations.

Anisotropic cantilever nanoplates exposed to in-plane magnetic fields were characterized in [2]. The analytical solution to the linear problem was constructed by a simplex method using trigonometric series. The range of critical forces was obtained for isotropic and orthotropic plates.

FEM and an approximate analytical approach are used in [13] to study the influence that the stiffness of the mid-surface has on the bending of the cantilever plate.

Refs. [14, 15] are dedicated to the stability of an isotropic cantilever plate under the action of compressive forces applied to two parallel free edges [14] or to all three free edges [15]. Two hyperbolic trigonometric series produced an infinite system of linear algebraic equations containing a compressive load as a parameter. Numerical results were obtained for critical loads.

Notably, while FEM has become widespread, it brings the challenge of verifying whether boundary conditions are satisfied. Such verification is fraught with great difficulties, since this numerical method operates arrays of numbers rather than analytical expressions (which can be

substituted into the boundary conditions). FEM is not a universal method for solving mechanical problems and has other drawbacks: insufficient accuracy of solving high-order partial differential equations, computational 'locking' on a refined grid, associated with rounding errors when solving a huge system of linear algebraic equations, 'viewing' of singular points of the solution (stress raisers). The method itself often needs to be verified by purely analytical or numerical analytical methods.

An exact solution to the stability problem has been obtained in our study using hyperbolic trigonometric series with respect to both variables. Satisfying all the conditions of the problem produced an infinite homogeneous system of linear algebraic equations for the coefficients of these series. If the determinant of the system is equal to zero, this yields nontrivial values of the coefficients. However, the procedure for obtaining and solving this equation turns out to be incredibly cumbersome.

We propose a method searching through the load values followed by an iterative process for determining the coefficients. The initial coefficients of the first functional series were given as an arbitrary decreasing sequence; the values of the remaining coefficients were computed next, and they are all refined during the iterative process. The load was selected so that the process converged to nontrivial solutions, that is, adjacent iterations (with nonzero coefficients) did not differ from each other. This load was taken as critical. This method was successfully used in our earlier studies [14, 15].

Problem statement

Let uniform compressive forces with intensity TY be applied to the free edge $Y = b$ of a thin orthotropic rectangular cantilever plate of constant thickness h (Fig. 1). We assume that the main directions of elasticity are parallel to the sides of the plate.

The differential equation of plate stability takes the dimensionless form [16]:

$$D_x \frac{\partial^4 w}{\partial x^4} + 2D_{xy} \frac{\partial^4 w}{\partial x^2 \partial y^2} + \qquad (1)$$

$$+ D_y \frac{\partial^4 w}{\partial y^4} + T_y \frac{\partial^2 w}{\partial y^2} = 0, \qquad (1)$$

where w is the relative deflection ($w = W/b$, $W(X, Y)$ is the deflection function of the plate's mid-surface); x, y are the dimensionless coordinates ($x = X/b$, $y = Y/b$); D_x, D_y, D_{xy} are the relative stiffnesses in the principal directions, $D_x = D_1/D$, $D_y = D_2/D$, $D_{xy} = D_3/D$ (D is the cylindrical stiffness of the corresponding isotropic plate of the same thickness, D_1, D_2, D_3 are the principal stiffnesses) T_y is the intensity of relative compressive forces ($T_y = T_Y b^2/D$).

The value D is expressed as

$$D = Eh^3 / \left[12 \left(1 - v^2 \right) \right],$$

where E is Young's modulus of the given plate, v is its Poisson's ratio.

The main stiffnesses follow the expressions

$$D_1 = E_1 h^3 / \left[12 \left(1 - v_1 v_2 \right) \right],$$
$$D_2 = E_2 h^3 / \left[12 \left(1 - v_1 v_2 \right) \right],$$
$$D_3 = D_1 v_2 + 2 D_r,$$

where E_1, E_2, v_1, v_2 are the principal elastic constants; Dr is the torsional stiffness, $D_r = G h^3/12$ (G is the shear modulus).

The relative dimensions of the plate are $\gamma \times 1$, where $\gamma = a/b$.

The boundary conditions are written as follows [16, 17]:
on the face $y = 0$,

$$w = 0, \quad \frac{\partial w}{\partial y} = 0; \qquad (2)$$

on the face $y = 1$,

$$\frac{\partial^2 w}{\partial y^2} + v_1 \frac{\partial^2 w}{\partial x^2} = 0,$$

$$D_y \frac{\partial^3 w}{\partial y^3} + \left(D_{xy} + 2\bar{D}_r \right) \frac{\partial^3 w}{\partial x^2 \partial y} + \qquad (3)$$

$$+ T_y \frac{\partial w}{\partial y} = 0;$$

39
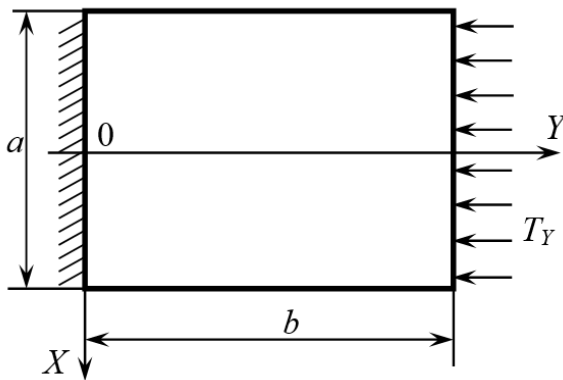
Fig. 1. Loading diagram of cantilever
plate (thickness h);
T_y is the intensity of uniform compressive forces

on the faces $x = \pm\gamma/2$,

$$\frac{\partial^2 w}{\partial x^2} + \nu_2 \frac{\partial^2 w}{\partial y^2} = 0,$$

$$D_x \frac{\partial^3 w}{\partial x^3} + \left(D_{xy} + 2\bar{D}_r\right)\frac{\partial^3 w}{\partial x \partial y^2} = 0; \tag{4}$$

at points $(\pm\gamma/2, 1)$,

$$\frac{\partial^2 w}{\partial x \partial y} = 0. \tag{5}$$

Eqs. (2) here are the geometric conditions for rigidly clamped edges (the section does not move or rotate). Eqs. (3), (4) prohibit bending moments and shear forces on the free faces. Condition (5) excludes torques at the corner points of the free part of the boundary. Note that the second condition (3) for shear forces on a face along which a compressive load is applied is complemented with a term accounting for the action of this load in the deflected state of this face. This was pointed out by Alfutov in [17].

Problem (1) − (5) always has a trivial (zero) solution for the deflection function. This corresponds to a stable undeformed state of the plate. Aside from the trivial solution, the problem can also have nontrivial solutions for certain loads Ty, when the plate acquires a new form of equilibrium upon loss of stability. Plates with high elastic-

ity can 'pass' the critical state several times with increasing load, changing the form of the subsequent equilibrium. This refers to plates made of novel highly elastic materials, including nanoplates (graphene).

Construction of the symmetric solution

We represent the sought deflection function as a sum of two series:

$$w_1(x, y) = \sum_{k=1,3,\ldots}^{\infty} \left(\begin{array}{c} A_k \,\mathrm{ch}\,\alpha_k x + \\ + B_k \,\mathrm{ch}\,\beta_k x \end{array}\right) \sin \lambda_k y, \quad (6)$$

$$w_2(x, y) = $$
$$= \sum_{s=1}^{\infty} (-1)^s \left(\begin{array}{c} C_s \,\mathrm{sh}\,\xi_s \tilde{y} + \\ + H_s \,\mathrm{sh}\,\eta_s \tilde{y} + \\ + E_s \,\mathrm{ch}\,\xi_s \tilde{y} + \\ + F_s \,\mathrm{ch}\,\eta_s \tilde{y} \end{array}\right) \cos \mu_s x, \quad (7)$$

where A_k, B_k, C_s, H_s, E_s, F_s, α_k, β_k, ξ_s, η_s are undetermined coefficients; $\lambda_k = k\pi/2$; $\mu_s = 2\pi_s/\gamma$; $\tilde{y} = y - 1$.

Notably, both of these functions satisfy the boundary condition (5).

We require that functions (6), (7) satisfy the differential equation (1). This gives biquadratic equations of the following form for the coefficients α_k, β_k, ξ_s, η_s:

$$D_x \alpha_k^4 - 2D_{xy}\alpha_k^2\lambda_k^2 + D_y\lambda_k^4 - T_y\lambda_k^2 = 0,$$
$$D_x \mu_s^4 - 2D_{xy}\xi_s^2\mu_s^2 + D_y\xi_s^4 + T_y\xi_s^2 = 0 \tag{8}$$

(the equations for the coefficients β_k and η_s are similar).

These equations each have four roots, however, based on the properties of hyperbolic functions, it is sufficient to take one pair of roots from each of the quartets:

$$\alpha_k = \lambda_k \sqrt{\frac{D_{xy} + \sqrt{D_{xy}^2 - D_x D_y + \dfrac{D_x T_y}{\lambda_k^2}}}{D_x}}, \quad (9)$$

$$\beta_k = \lambda_k \sqrt{\dfrac{D_{xy} - \sqrt{D_{xy}^2 - D_x D_y + \dfrac{D_x T_y}{\lambda_k^2}}}{D_x}},$$

$$\xi_s = \sqrt{\dfrac{2D_{xy}\mu_s^2 - T_y + R_s}{2D_y}},\qquad (9)$$

$$\eta_s = \sqrt{\dfrac{2D_{xy}\mu_s^2 - T_y - R_s}{2D_y}},$$

where

$$R_s = \sqrt{\dfrac{T_y^2 - 4D_{xy}\mu_s^2 T_y +}{+\,4\mu_s^4\left(D_{xy}^2 - D_x D_y\right)}}.$$

We now require that the sum of functions (6), (7) satisfy boundary conditions (2) − (4). Then we obtain the following system of equations:

$$C_s \,\mathrm{sh}\,\xi_s + H_s \,\mathrm{sh}\,\eta_s - \\ -\,E_s \,\mathrm{ch}\,\xi_s - F_s \,\mathrm{ch}\,\eta_s = 0, \qquad (10)$$

$$\sum_{s=1}^{\infty}(-1)^s \begin{pmatrix} C_s\xi_s \,\mathrm{ch}\,\xi_s + \\ +H_s\eta_s \,\mathrm{ch}\,\eta_s - \\ -E_s\xi_s \,\mathrm{sh}\,\xi_s - \\ -F_s\eta_s \,\mathrm{sh}\,\eta_s \end{pmatrix}\cos\mu_s x + \\ +\sum_{k=1,3,\dots}^{\infty}\lambda_k\left(A_k \,\mathrm{ch}\,\alpha_k x + B_k \,\mathrm{ch}\,\beta_k x\right) = 0, \qquad (11)$$

$$\sum_{s=1}^{\infty}(-1)^s \begin{bmatrix} E_s\left(\xi_s^2 - \nu_1\mu_s^2\right) + \\ +\,F_s\left(\eta_s^2 - \nu_1\mu_s^2\right) \end{bmatrix}\cos\mu_s x - \\ -\sum_{k=1,3,\dots}^{\infty}(-1)^{\tilde k}\begin{bmatrix} A_k\left(\nu_1\alpha_k^2 - \lambda_k^2\right)\mathrm{ch}\,\alpha_k x + \\ +\,B_k\left(\nu_1\beta_k^2 - \lambda_k^2\right)\mathrm{ch}\,\beta_k x \end{bmatrix} = 0, \qquad (12)$$

$$C_s\xi_s\left[T_y + D_y\xi_s^2 - \left(D_{xy} + 2\bar{D}_r\right)\mu_s^2\right] + \\ +\,H_s\eta_s\left[T_y + D_y\eta_s^2 - \left(D_{xy} + 2\bar{D}_r\right)\mu_s^2\right] = 0, \qquad (13)$$

$$-\sum_{s=1}^{\infty}\begin{bmatrix} C_s\left(\mu_s^2 - \nu_2\xi_s^2\right)\mathrm{sh}\,\xi_s\tilde{y} + \\ +\,H_s\left(\mu_s^2 - \nu_2\eta_s^2\right)\mathrm{sh}\,\eta_s\tilde{y} + \\ +\,E_s\left(\mu_s^2 - \nu_2\xi_s^2\right)\mathrm{ch}\,\xi_s\tilde{y} + \\ +\,F_s\left(\mu_s^2 - \nu_2\eta_s^2\right)\mathrm{ch}\,\eta_s\tilde{y} \end{bmatrix} + \\ +\sum_{k=1,3,\dots}^{\infty}\begin{bmatrix} A_k\left(\alpha_k^2 - \nu_2\lambda_k^2\right)\mathrm{ch}\,\tilde{\alpha}_k + \\ +\,B_k\left(\beta_k^2 - \nu_2\lambda_k^2\right)\mathrm{ch}\,\tilde{\beta}_k \end{bmatrix}\sin\lambda_k y = 0, \qquad (14)$$

$$A_k\alpha_k\left[D_x\alpha_k^2 - \left(D_{xy} + 2\bar{D}_r\right)\lambda_k^2 +\right]\mathrm{sh}\,\tilde{\alpha}_k + \\ +\,B_k\beta_k\left[D_x\beta_k^2 - \left(D_{xy} + 2\bar{D}_r\right)\lambda_k^2\right]\mathrm{sh}\,\tilde{\beta}_k = 0. \qquad (15)$$

Here, $\tilde{\alpha}_k = \alpha_k\gamma/2$, $\tilde{\beta}_k = \beta_k\gamma/2$, $\tilde{k} = (k+1)/2$.

Note that the signs of the sum are omitted in Eqs. (10), (13), and (15), since the trigonometric series vanishes when all its coefficients are equal to zero.

Summation in the series in Eqs. (11), (12), (14) is carried out over different indices, so we expand the hyperbolic functions in them into Fourier series. We use the well-known expansions in $\cos(\mu_s x)$ for Eqs. (11) and (12):

$$\mathrm{ch}\,\alpha_k x = \\ = \mathrm{sh}\,\tilde{\alpha}_k\left[\dfrac{1}{\tilde{\alpha}_k} + \dfrac{4\alpha_k}{\gamma}\sum_{s=1}^{\infty}(-1)^s\dfrac{\cos\mu_s x}{\alpha_k^2 + \mu_s^2}\right], \\ \mathrm{ch}\,\beta_k x = \qquad (16) \\ = \mathrm{sh}\,\tilde{\beta}_k\left[\dfrac{1}{\tilde{\beta}_k} + \dfrac{4\beta_k}{\gamma}\sum_{s=1}^{\infty}(-1)^s\dfrac{\cos\mu_s x}{\beta_k^2 + \mu_s^2}\right];$$

then these equations (after permutation of the summation signs in the double series) take the form

$$\sum_{s=1}^{\infty}(-1)^s\begin{pmatrix} C_s\xi_s \,\mathrm{ch}\,\xi_s + \\ +H_s\eta_s \,\mathrm{ch}\,\eta_s - \\ -\,E_s\xi_s \,\mathrm{sh}\,\xi_s - \\ -\,F_s\eta_s \,\mathrm{sh}\,\eta_s \end{pmatrix}\cos\mu_s x + \\ +\,\varphi_0 + \sum_{s=1}^{\infty}(-1)^s\,\varphi_s\cos\mu_s x = 0, \qquad (17)$$

$$\sum_{s=1}^{\infty}(-1)^s\begin{bmatrix} E_s\left(\xi_s^2-\nu_1\mu_s^2\right)+ \\ +F_s\left(\eta_s^2-\nu_1\mu_s^2\right)\end{bmatrix}\cos\mu_s x+$$

$$+m_0+\sum_{s=1}^{\infty}(-1)^s m_s\cos\mu_s x=0, \quad (18)$$

where

$$\varphi_0=\sum_{k=1,3,\dots}^{\infty}\lambda_k\left(A_k\frac{\operatorname{sh}\tilde\alpha_k}{\tilde\alpha_k}+B_k\frac{\operatorname{sh}\tilde\beta_k}{\tilde\beta_k}\right),$$

$$\varphi_s=\frac{4}{\gamma}\sum_{k=1,3,\dots}^{\infty}\lambda_k\left(A_k\frac{\alpha_k\operatorname{sh}\tilde\alpha_k}{\alpha_k^2+\mu_s^2}+B_k\frac{\beta_k\operatorname{sh}\tilde\beta_k}{\beta_k^2+\mu_s^2}\right),$$

$$m_0=-\sum_{k=1,3,\dots}^{\infty}(-1)^{\tilde k}\begin{bmatrix} A_k\left(\nu_1\alpha_k^2-\lambda_k^2\right)\dfrac{\operatorname{sh}\tilde\alpha_k}{\tilde\alpha_k}+ \\ +B_k\left(\nu_1\beta_k^2-\lambda_k^2\right)\dfrac{\operatorname{sh}\tilde\beta_k}{\tilde\beta_k}\end{bmatrix},$$

$$m_s=-\frac{4}{\gamma}\sum_{k=1,3,\dots}^{\infty}(-1)^{\tilde k}\begin{bmatrix} A_k\left(\nu_1\alpha_k^2-\lambda_k^2\right)\times \\ \times\dfrac{\alpha_k\operatorname{sh}\tilde\alpha_k}{\alpha_k^2+\mu_s^2}+ \\ +B_k\left(\nu_1\beta_k^2-\lambda_k^2\right)\times \\ \times\dfrac{\beta_k\operatorname{sh}\tilde\beta_k}{\beta_k^2+\mu_s^2}\end{bmatrix}. \quad (19)$$

To transform Eq. (14), we use the expansions

$$\operatorname{sh}\xi_s\tilde y=-2\sum_{k=1,3,\dots}^{\infty}\frac{(-1)^{\tilde k}\xi_s+\lambda_k\operatorname{sh}\xi_s}{\lambda_k^2+\xi_s^2}\sin\lambda_k y,$$

$$\operatorname{ch}\xi_s\tilde y=2\operatorname{sh}\xi_s\sum_{k=1,3,\dots}^{\infty}\frac{\lambda_k}{\lambda_k^2+\xi_s^2}\sin\lambda_k y \quad (20)$$

(the expressions for $\operatorname{sh}(\eta_s\tilde y)$ and $\operatorname{ch}(\eta_s\tilde y)$ are the same if ξ_s is substituted with η_s) and permute the summation signs in the double series obtained:

$$\sum_{k=1,3,\dots}^{\infty}b_k\sin\lambda_k y+$$

$$+\sum_{k=1,3,\dots}^{\infty}\begin{bmatrix} A_k\left(\alpha_k^2-\nu_2\lambda_k^2\right)\operatorname{ch}\tilde\alpha_k+ \\ +B_k\left(\beta_k^2-\nu_2\lambda_k^2\right)\operatorname{ch}\tilde\beta_k\end{bmatrix}\sin\lambda_k y=0, \quad (21)$$

where

$$b_k=2\sum_{s=1}^{\infty}\begin{bmatrix} \dfrac{\mu_s^2-\nu_2\xi_s^2}{\lambda_k^2+\xi_s^2}\times \\ \times\left\{C_s\begin{bmatrix}(-1)^{\tilde k}\xi_s+ \\ +\lambda_k\operatorname{sh}\xi_s\end{bmatrix}-\right\}+ \\ -E_s\lambda_k\operatorname{ch}\xi_s \\ +\dfrac{\mu_s^2-\nu_2\eta_s^2}{\lambda_k^2+\eta_s^2}\times \\ \times\left\{H_s\begin{bmatrix}(-1)^{\tilde k}\eta_s+ \\ +\lambda_k\operatorname{sh}\eta_s\end{bmatrix}-\right\} \\ -F_s\lambda_k\operatorname{ch}\eta_s\end{bmatrix}. \quad (22)$$

Since the free terms φ_0 and m_0 from cosine series expansion appeared in Eqs. (17), (18), we should introduce an auxiliary deflection function w_3, which can compensate for these free terms, satisfying Eqs. (1) − (3), (5) of the problem together with the main solution.

We select this function in the form

$$w_3(y)=\sum_{k=1,3,\dots}^{\infty}g_k\sin\lambda_k y+\frac{1}{2}My^2-\Phi y, \quad (23)$$

where the coefficients g_k, M, Φ are found from conditions (2) − (4):

$$\sum_{k=1,3,\dots}^{\infty}g_k\lambda_k^2\left(D_y\lambda_k^2-T_y\right)\sin\lambda_k y+MT_y=0,$$

$$\sum_{k=1,3,\dots}^{\infty}g_k\lambda_k-\Phi+\varphi_0=0, \quad (24)$$

$$\sum_{k=1,3,\dots}^{\infty}(-1)^{\tilde k}\lambda_k^2 g_k+M+m_0=0.$$

We expand the constant $M\cdot T_y$ in the first equation in (25) in a sine Fourier series:

$$MT_y=MT_y\sum_{k=1,3,\dots}^{\infty}\frac{2}{\lambda_k}\sin\lambda_k y. \quad (25)$$

Then we obtain the following expressions:

$$g_k = \frac{-2MT_y}{\lambda_k^3 \left(D_y\lambda_k^2 - T_y\right)},$$

$$M = \frac{-m_0}{1 - 2\sum\limits_{k=1,3,\ldots}^{\infty} \frac{(-1)^{\tilde{k}}T_y}{\lambda_k\left(D_y\lambda_k^2 - T_y\right)}}, \qquad (26)$$

$$\Phi = \varphi_0 + \sum\limits_{k=1,3,\ldots}^{\infty} g_k\lambda_k.$$

The residual of the function w_3 with respect to the bending moment M_x on the faces $x = \pm\gamma/2$ (the first condition (4)) is expressed as

$$\nu_2\left(M - \sum\limits_{k=1,3,\ldots}^{\infty} g_k\lambda_k^2 \sin\lambda_k y\right) =$$
$$= \sum\limits_{k=1,3,\ldots}^{\infty} b_k^* \sin\lambda_k y, \qquad (27)$$

where the coefficient

$$b_k^* = \frac{2\nu_2 M D_y \lambda_k}{D_y\lambda_k^2 - T_y} =$$
$$= \frac{-2\nu_2 D_y\lambda_k m_0\big/\left(D_y\lambda_k^2 - T_y\right)}{1 - 2T_y\sum\limits_{k=1,3,\ldots}^{\infty} \frac{(-1)^{\tilde{k}}}{\lambda_k\left(D_y\lambda_k^2 - T_y\right)}} \qquad (28)$$

is added to Eq. (21).

Then system of equations (10) − (15) takes the following final form after the external summation signs are removed, taking into account Eqs. (17), (18), (21), (27):

$$C_s \operatorname{sh}\xi_s + H_s \operatorname{sh}\eta_s -$$
$$- E_s \operatorname{ch}\xi_s - F_s \operatorname{ch}\eta_s = 0, \qquad (29)$$

$$C_s\xi_s \operatorname{ch}\xi_s + H_s\eta_s \operatorname{ch}\eta_s -$$
$$- E_s\xi_s \operatorname{sh}\xi_s - F_s\eta_s \operatorname{sh}\eta_s = -\varphi_s, \qquad (30)$$

$$E_s\left(\xi_s^2 - \nu_1\mu_s^2\right) + F_s\left(\eta_s^2 - \nu_1\mu_s^2\right) = -m_s, \qquad (31)$$

$$C_s\xi_s\left[D_y\xi_s^2 - \left(D_{xy} + 2\bar{D}_r\right)\mu_s^2 + T_y\right] +$$
$$+ H_s\eta_s\left[D_y\eta_s^2 - \left(D_{xy} + 2\bar{D}_r\right)\mu_s^2 + T_y\right] = 0, \qquad (32)$$

$$A_k\left(\alpha_k^2 - \nu_2\lambda_k^2\right)\operatorname{ch}\tilde{\alpha}_k +$$
$$+ B_k\left(\beta_k^2 - \nu_2\lambda_k^2\right)\operatorname{ch}\tilde{\beta}_k = -\left(b_k + b_k^*\right), \qquad (33)$$

$$A_k\alpha_k\left[D_x\alpha_k^2 - \left(D_{xy} + 2\bar{D}_r\right)\lambda_k^2\right]\operatorname{sh}\tilde{\alpha}_k +$$
$$+ B_k\beta_k\left[D_x\beta_k^2 - \left(D_{xy} + 2\bar{D}_r\right)\lambda_k^2\right]\operatorname{sh}\tilde{\beta}_k = 0. \qquad (34)$$

The set (29) − (34) is an infinite homogeneous system of linear algebraic equations with respect to the coefficients A_k, B_k, C_s, H_s, E_s, F_s.

Notice that the right-hand sides φ_s and ms of Eqs. (30), (31) contain the coefficients A_k, B_k under the sum sign (see Eqs. (19)), while the terms on the right-hand side of Eqs. (33) contain, respectively, the coefficients C_s, H_s, E_s, F_s, and also A_k, B_k under the sum signs (see Eqs. (22, 28)). It is extremely complicated to represent a homogeneous system in standard form, to compose and expand the corresponding determinant of the system, to find its roots giving nontrivial solutions; therefore, here we propose a method for enumerating the parameter T_y (the 'shooting' method) combined with the method of sequential approximations for determining the coefficients A_k, B_k, C_s, H_s, E_s, F_s.

To organize the iterative process, the resolving system is divided into two subsystems:

(29) − (32), where the principal coefficients are assumed to be C_s, H_s, E_s, F_s;

(33), (34), where the principal coefficients are assumed to be A_k, B_k.

First, the right-hand side of Eq. (33) is substituted with an initial arbitrary decreasing sequence (in this case, $1/\lambda_k$), then the subsystem of equations (33), (34) is solved for the selected value of the compressive load T_y. The initial coefficients A_{k0}, B_{k0} found are substituted into subsystem (29) − (32), from which the coefficients C_{s0}, H_{s0}, E_{s0}, F_{s0} are found, used then together with A_{k0}, B_{k0} to form the right-hand side of Eq. (33) and a new solution A_{k1}, B_{k1} of systems (33), (34). Next, the first-approximation coefficients C_{s1}, H_{s1}, E_{s1}, F_{s1} are computed, followed by the iterative process of refining the problem coefficients.

If the corresponding coefficients of the series

coincide in absolute value (up to 4–5 significant digits) for the given load starting from some iteration, then this is exactly the nonzero solution of the homogeneous system (29) − (34): its determinant is equal to zero. This (critical) load determines a new form of equilibrium after loss of stability (it corresponds to the minimum potential energy of the plate).

Construction of an antisymmetric solution

We also represent the sought solution as the sum of two series, where odd functions with respect to the variable x appear:

$$w_1(x, y) = \sum_{k=1,3,\dots}^{\infty} \left(\begin{matrix} A_k \operatorname{sh} \alpha_k x + \\ + B_k \operatorname{sh} \beta_k x \end{matrix} \right) \sin \lambda_k y, \quad (35)$$

$$w_2(x, y) = $$
$$= \sum_{s=1,3,\dots}^{\infty} (-1)^{\tilde{s}} \left(\begin{matrix} C_s \operatorname{sh} \xi_s \tilde{y} + \\ + H_s \operatorname{sh} \eta_s \tilde{y} + \\ + E_s \operatorname{ch} \xi_s \tilde{y} + \\ + F_s \operatorname{ch} \eta_s \tilde{y} \end{matrix} \right) \sin \mu_s x. \quad (36)$$

Here $\tilde{s} = (s+1)/2$, $\mu_s = \pi s / \gamma$; the coefficients λ_k, α_k, β_k, ξ_s, η_s have the same values as before.

Satisfying all the boundary conditions of the problem, we arrive at a system similar to (29) − (34), but with the sines and cosines interchanged in the last two equations:

$$C_s \operatorname{sh} \xi_s + H_s \operatorname{sh} \eta_s - \\ - E_s \operatorname{ch} \xi_s - F_s \operatorname{ch} \eta_s = 0, \quad (37)$$

$$C_s \xi_s \operatorname{ch} \xi_s + H_s \eta_s \operatorname{ch} \eta_s - \\ - E_s \xi_s \operatorname{sh} \xi_s - F_s \eta_s \operatorname{sh} \eta_s = -\varphi_s, \quad (38)$$

$$E_s \left(\xi_s^2 - \nu_1 \mu_s^2 \right) + F_s \left(\eta_s^2 - \nu_1 \mu_s^2 \right) = -m_s, \quad (39)$$

$$C_s \xi_s \left[D_y \xi_s^2 - \left(D_{xy} + 2\bar{D}_r \right) \mu_s^2 \right] + \\ + H_s \eta_s \left[D_y \eta_s^2 - \left(D_{xy} + 2\bar{D}_r \right) \mu_s^2 \right] = 0, \quad (40)$$

$$A_k \left(\alpha_k^2 - \nu_2 \lambda_k^2 \right) \operatorname{sh} \tilde{\alpha}_k + \\ + B_k \left(\beta_k^2 - \nu_2 \lambda_k^2 \right) \operatorname{sh} \tilde{\beta}_k = -b_k, \quad (41)$$

$$A_k \alpha_k \left[D_x \alpha_k^2 - \left(D_{xy} + 2\bar{D}_r \right) \lambda_k^2 \right] \operatorname{ch} \tilde{\alpha}_k + \\ + B_k \beta_k \left[D_x \beta_k^2 - \left(D_{xy} + 2\bar{D}_r \right) \lambda_k^2 \right] \operatorname{ch} \tilde{\beta}_k = 0, \quad (42)$$

where

$$\varphi_s = -\frac{4}{\gamma} \sum_{k=1,3,\dots}^{\infty} \lambda_k \left(\begin{matrix} A_k \dfrac{\alpha_k \operatorname{ch} \tilde{\alpha}_k}{\alpha_k^2 + \mu_s^2} + \\ + B_k \dfrac{\beta_k \operatorname{ch} \tilde{\beta}_k}{\beta_k^2 + \mu_s^2} \end{matrix} \right),$$

$$m_s = \frac{4}{\gamma} \sum_{k=1,3,\dots}^{\infty} (-1)^{\tilde{k}} \left[\begin{matrix} A_k \left(\nu_1 \alpha_k^2 - \lambda_k^2 \right) \times \\ \times \dfrac{\alpha_k \operatorname{ch} \tilde{\alpha}_k}{\alpha_k^2 + \mu_s^2} + \\ + B_k \left(\nu_1 \beta_k^2 - \lambda_k^2 \right) \times \\ \times \dfrac{\beta_k \operatorname{ch} \tilde{\beta}_k}{\beta_k^2 + \mu_s^2} \end{matrix} \right],$$

$$b_k = -2 \sum_{s=1,3,\dots}^{\infty} \left[\begin{matrix} \dfrac{\mu_s^2 - \nu_2 \xi_s^2}{\lambda_k^2 + \xi_s^2} \times \\ \times \left\{ C_s \left[\begin{matrix} (-1)^{\tilde{k}} \xi_s + \\ + \lambda_k \operatorname{sh} \xi_s \end{matrix} \right] - \\ - E_s \lambda_k \operatorname{ch} \xi_s \right\} + \\ + \dfrac{\mu_s^2 - \nu_2 \eta_s^2}{\lambda_k^2 + \eta_s^2} \times \\ \times \left\{ H_s \left[\begin{matrix} (-1)^{\tilde{k}} \eta_s + \\ + \lambda_k \operatorname{sh} \eta_s \end{matrix} \right] - \\ - F_s \lambda_k \operatorname{ch} \eta_s \right\} \end{matrix} \right]. \quad (43)$$

Here we used the sine expansion of hyperbolic functions of the variable x in Fourier series:

$$\operatorname{sh} \alpha_k x = -\frac{4\alpha_k}{\gamma} \operatorname{ch} \tilde{\alpha}_k \sum_{s=1,3,\dots}^{\infty} (-1)^{\tilde{s}} \frac{\sin \mu_s x}{\alpha_k^2 + \mu_s^2},$$

$$\operatorname{sh} \beta_k x = -\frac{4\beta_k}{\gamma} \operatorname{ch} \tilde{\beta}_k \sum_{s=1,3,\dots}^{\infty} (-1)^{\tilde{s}} \frac{\sin \mu_s x}{\beta_k^2 + \mu_s^2}. \quad (44)$$

Computations for ribbed plate

As an example, we consider a square plate with closely spaced stiffening ribs placed parallel to the coordinate axes at an equal distance from each other (Fig. 2).

Formulas for calculating the stiffnesses for such a ribbed plate are given in [16]:

$$D_1 = D_2 = D + \frac{E_R I_R}{d}, \ D_3 = D, \qquad (45)$$

where D is the cylindrical stiffness of the plate itself; E_R, I_R are, respectively, Young's modulus and the moment of inertia of the ribs relative to the midline; d is the distance between the ribs.

Then the relative stiffnesses take the form

$$D_x = D_y = 1 + \bar{D}, \ D_{xy} = 1$$
$$\left(\bar{D} = E_R I_R / dD \right), \qquad (46)$$

and the discriminant of the biquadratic equation (8) (and the similar equation for φ_s and ψ_s) is negative:

$$D_{xy}^2 - D_x D_y = -\left(\bar{D}^2 + 2\bar{D} \right) < 0, \qquad (47)$$

producing complex roots α_k, β_k, φ_s and ψ_s.

The transformations of complex expressions carried out prove that the sought solution is obtained in real form. Computations with the Maple system confirmed this.

We assume that the plate and the ribs are made of the same material. We take Poisson's ratio $\nu = 0.3$, rib width $b_R = h$, rib height $h_R = 3h$, rib width to rib spacing ratio $b_R/d = 0.1$. Then the moment of inertia of the rib and its relative stiffness are expressed as

$$I_R = \frac{b_R h_R^3}{12} - \frac{h^4}{12} = \frac{26}{12} h^4,$$

$$\bar{D} = \frac{E_R I_R}{dD} = \frac{26 E h^4 12 \left(1 - \nu^2 \right)}{12 \cdot 10 h E h^3} =$$
$$= 2{,}6 \left(1 - \nu^2 \right) = 2{,}366.$$

Numerical results

Critical loads and forms of equilibrium were determined according to the above algorithm using Maple software.

The following parameters of the computational process were used:

T_y is the intensity of the relative compressive load applied to the face $y = 1$; $\nu = 0.3$ is Poisson's ratio; $\gamma = a/b$ is the ratio of the sides of the plate; N is the number of terms in the series; N_s is the number of iterations.

The coefficients of series (7), (8) or (36), (37) were printed out at each iteration in order to control the process of successive approximations. After finding the critical value, the deflection function was computed and a $3D$ image of the corresponding form of the plate equilibrium was printed. There were 59 terms retained in a series, a larger number of terms did not significantly affect the accuracy of the computations. The number of iterations was assumed to be 25. The run time for each loading scenario was no more than two minutes. The strategy of enumerating the load was chosen to account for the behavior of the sought coefficient values and did not take much time.

The first three critical loads found for symmetric forms and the first critical loads for the antisymmetric form of equilibrium for square plates (ribbed, with low anisotropy, isotropic) are
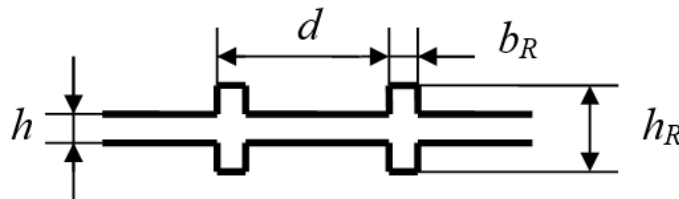
Fig. 2. View of ribbed panel

45

a) *b)*

c)
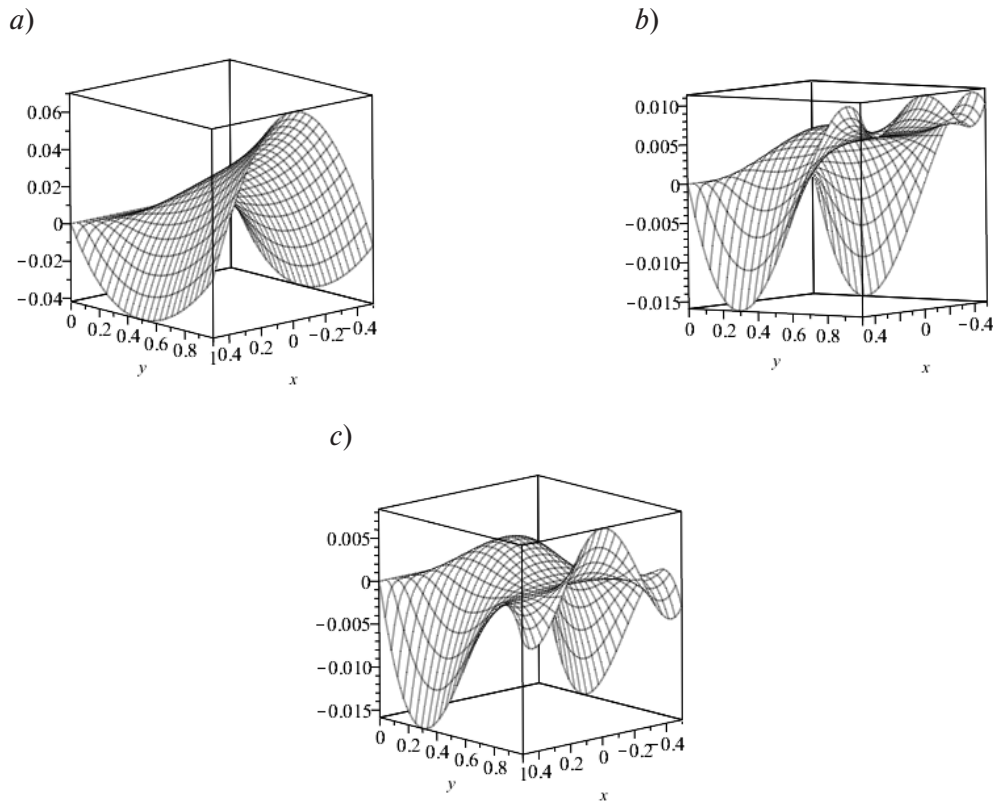
Fig. 3. First (*a*), second (*b*) and third (*c*) symmetrical forms of equilibrium
for a ribbed square plate at $T_{cr1} = 7.824$, $T_{cr2} = 64.933$ and $T_{cr3} = 100.970$ respectively
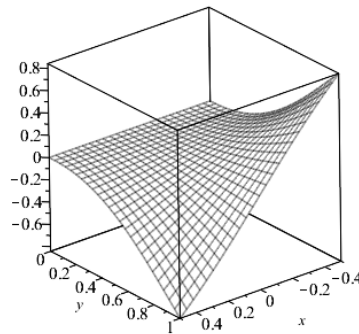
Fig. 4. First antisymmetric form of equilibrium for a ribbed square plate at $T_{cr1} = 25.6765$

shown in Table, and the corresponding 3*D* forms of equilibrium of a ribbed plate are shown in Figs. 3, 4. Importantly, the number of iterations had to be increased to 200 for finding the first antisymmetric critical load due to the weak convergence of the process.

Discussion of computational results

The variation method was used in [10] to find the first critical load for an isotropic square can-

tilever plate $p_{cr} = 2.4571 \cdot D/a^2$. In this study, the first critical load was computed for comparison for a plate with low anisotropy $\overline{D} = 0.005$, which amounted to $2.1164 \cdot D/a^2$. These values are comparable. We should note that energy methods typically yield overestimated results.

The numerical results in [2] were obtained for the stability of elastic isotropic and orthotropic cantilever nanoplates in a magnetic field using the simplex superposition method based on the

Computed range of critical loads T_y for square cantilever plates

Type of plate	$\overline{D}$	$T_y = T_Y b^2/D$			
		Symmetrical solution			Antisymmetrical solution
		T_{cr1}	T_{cr2}	T_{cr3}	T_{cr1}
Ribbed	2.366	7.8235	64.933	100.970	25.676
With low anisotropy	0.005	2.1164	20.525	58.721	7.835
Isotropic	0	2.1057	20.457	58.597	8.080

Notations: $\overline{D}$ is the relative stiffness of the ribs, T_Y is the intensity of uniform compressive forces, b is the plate length, D is the cylindrical stiffness of the isotropic plate.

nonlocal elasticity theory. Stability computations were performed to verify the method for a very thin ($h/a = 1/1000$) isotropic cantilever plate but within the framework of the linear Kirchhoff theory. In particular, for a plate with the aspect ratio $\gamma = 2$ subjected to a uniform compressive load applied to the face $y = 1$, the first relative critical values of symmetric forms of equilibrium amounted to (converting these data to the notation we adopted) 2.4174 and 20.5173 versus the values of 2.1594 and 20.663 that we obtained for a standard thin plate ($h/a <1/5$).

The significant discrepancy (10.7%) for the first critical load can be explained by the large difference in the relative plate thicknesses. Notably, the range of the first six critical loads is given in [2], and the corresponding forms of equilibrium are obtained. This is perhaps the only work on determining the spectrum of eigenvalues and forms in the problem on stability of cantilever plates. On the other hand, however, the buckling in a clamped plate subjected to shear forces along the edge was considered in [18] within the framework of the linear theory; a range of 10 first critical loads and the corresponding 3D forms of equilibrium of plates with different aspect ratios were obtained.

The method proposed in this paper for studying the stability of an elastic orthotropic rectangular cantilever plate allows finding the range of critical loads and the corresponding forms of equilibrium with high accuracy, increasing the number of terms in the series, the number of iterations and the length of the mantissa in the computations.

Conclusion

We have obtained a numerical analytical solution to the stability problem for an elastic rectangular orthotropic cantilever plate. Hyperbolic trigonometric series were used to reduce the problem to an infinite system of linear algebraic equations with respect to unknown coefficients, containing a compressive load as a parameter. An efficient iterative process for finding critical loads has been constructed. A range of critical forces was obtained for a specific example of a ribbed plate; if necessary, it can be expanded by computational means using the Maple environment for numerical analysis. The corresponding 3D forms of equilibrium are given. Finding the critical loads will allow avoiding failure in cantilever elements or understanding their behavior in supercritical regions, offering application for nanotechnology and smart structures.

REFERENCES

1. **Gao Y.,** Analysis on the magneto-elastic-plastic buckling/snapping of cantilever rectangular ferromagnetic plates, Acta Mechanica Solida Sinica. 20 (2007) 180−188.

2. **Wang W., Rong D., Xu C., et al.,** Accurate buckling analysis of magnetically affected canti-

lever nanoplates subjected to in-plane magnetic fields, Journal of Vibration Engineering & Technologies. 8 (4) (2020) 505−515.

3. **Kim J., Varadan V.V., Varadan V.K., Bao X.Q.,** Finite element modeling of a smart cantilever plate and comparison with experiments, Smart Materials and Structures. 5 (2) (1996) 165−170.

4. **Gohari S., Sharifi S., Vrcelj Z.,** A novel explicit solution for twisting control of smart laminated cantilever composite plates/beams using inclined piezoelectric actuators, Composite Structures. 161 (1 February) (2017) 477−504.

5. **Sukhoterin M.V., Baryshnikov S.O., Aksenov D.A.,** Free vibration analysis of rectangular cantilever plates using the hyperbolic-trigonometric series, American Journal of Applied Sciences. 13 (12) (2016) 1442−1451.

6. **Tsiatas G.C., Yiotis A.J.,** A BEM-based meshless solution to buckling and vibration problems of orthotropic plates, Engineering Analysis with Boundary Elements. 37 (3) (2013) 579−584.

7. **Papkov S.O., Banerjee J.R.,** A new method for free vibration and buckling analysis of rectangular orthotropic plates, Journal of Sound and Vibration. 339 (17 March) (2015) 342−358.

8. **Manukhin V.A., Korshunov V.A., Viryacheva N.N.,** O rabotosposobnosti tonkikh plastin posle poteri ustoychivosti [On serviceability of thin plates after buckling], Transactions of the CRI named after acad. A.N. Krylov. (89.2(373)) (2015) 151−160 (in Russian).

9. **Semenov A.A., Moskalenko L.P., Karpov V.V., Sukhoterin M.V.,** Buckling of cylindrical panels strengthened with an orthogonal grid of stiffeners, Bulletin of Civil Engineers. 83 (6) (2020) 117−125 (in Russian).

10. **Xiang-Sheng C.,** The bending stability and vibration of cantilever rectangular plates, Applied Mathematics and Mechanics (English Edition, China). 8 (7) (1987) 673−683.

11. **Xiang-Sheng C.,** On several problems for lateral instability of cantilever plates, Applied Mathematics and Mechanics (English Edition, China). 9 (8) (1988) 787−792.

12. **Jiang L., Wu S., Zheng H.,** Lateral buckling analysis for rectangular cantilever plate subjected to a concentrated load, Advanced Materials Research. 671−674 (2013) 1596−1599.

13. **Yakoob J.A., Hasan I.J.** Study the increasing of the cantilever plate stiffness by using stiffeners, International Journal of Scientific & Engineering Research. 6 (4) (2015) 1678−1687.

14. **Baryshnikov S.O., Sukhoterin M.V., Knysh T.P.,** Stability of external cantilever elements of deep-sea vehicles, Vestnik Gosudarstvennogo Universiteta Morskogo i Rechnogo Flota Imeni Admirala S.O. Makarova. 12 (2 (60)) (2020) 347−358 (in Russian).

15. **Baryshnikov S.O., Sukhoterin M.V., Knysh T.P., Pizhurina N.F.,** Buckling of stabilizers deep-sea vehicles, Marine Intellectual Technologies. 48 (2-1) (2020) 83−90 (in Russian).

16. **Lekhnitskii S.G.,** Anisotropic plates, Gordon and Breach, London, 1968.

17. **Alfutov N.A.,** Stability of elastic structures, Series: Foundations of Engineering Mechanics, Eds.: Babitsky V.I., Wittenburg J., Springer, Berlin, Germany, 2000.

18. **Ullah S., Zhou J., Zhang J., et al.,** New analytic shear buckling solution of clamped rectangular plates by a two-dimensional generalized finite integral transform method, International Journal of Structural Stability and Dynamics. 20 (02) (2020) 2071002.

THE AUTHORS

SUKHOTERIN Mikhail V.
Admiral Makarov State University of Maritime and Inland Shipping
5/7 Dvinskaya St., St. Petersburg, 198135, Russian Federation
sukhoterinmv@gumrf.ru

KNYSH Tatiana P.

Admiral Makarov State University of Maritime and Inland Shipping

5/7 Dvinskaya St., St. Petersburg, 198135, Russian Federation

knyshtp@gumrf.ru

PASTUSHOK Elena M.

Admiral Makarov State University of Maritime and Inland Shipping

5/7 Dvinskayia St., St. Petersburg, 198135, Russian Federation

pastushokem@gumrf.ru

ABDIKARIMOV Rustamkhan A.

Tashkent Financial Institute

60A, A. Temur St., Tashkent, 100000, Republic of Uzbekistan

rabdikarimov@mail.ru

СПИСОК ЛИТЕРАТУРЫ

1. **Gao Y.** Analysis on the magneto-elastic-plastic buckling/snapping of cantilever rectangular ferromagnetic plates // Acta Mechanica Solida Sinica. 2007. Vol. 20. No. 2. Pp. 180−188.

2. **Wang W., Rong D., Xu C., Zhang Ju., Xu X., Zhou Z.** Accurate buckling analysis of magnetically affected cantilever nanoplates subjected to in-plane magnetic fields // Journal of Vibration Engineering & Technologies. 2020. Vol. 8. No. 4. Pp. 505−515.

3. **Kim J., Varadan V.V., Varadan V.K., Bao X.Q.** Finite element modeling of a smart cantilever plate and comparison with experiments // Smart Materials and Structures. 1996. Vol. 5. No. 2. Pp. 165−170.

4. **Gohari S., Sharifi S., Vrcelj Z.** A novel explicit solution for twisting control of smart laminated cantilever composite plates/beams using inclined piezoelectric actuators // Composite Structures. 2017. Vol. 161. 1 February. Pp. 477−504.

5. **Sukhoterin M.V., Baryshnikov S.O., Aksenov D.A.** Free vibration analysis of rectangular cantilever plates using the hyperbolic-trigonometric series // American Journal of Applied Sciences. 2016. Vol. 13. No. 12. Pp. 1442−1451.

6. **Tsiatas G.C., Yiotis A.J.** A BEM-based meshless solution to buckling and vibration problems of orthotropic plates // Engineering Analysis with Boundary Elements. 2013. Vol. 37. No. 3. Pp. 579−584.

7. **Papkov S.O., Banerjee J.R.** A new method for free vibration and buckling analysis of rectangular orthotropic plates // Journal of Sound and Vibration. 2015. Vol. 339. 17 March. Pp. 342−358.

8. **Манухин В.А., Коршунов В.А., Вирячева Н.Н.** О работоспособности тонких пластин после потери устойчивости // Труды ЦНИИ им. акад. А.Н. Крылова. 2015. Т. 89. № 2. С. 151−160.

9. **Семенов А.А., Москаленко Л.П., Карпов В.В., Сухотерин М.В.** Устойчивость цилиндрических панелей, подкрепленных ортогональной сеткой ребер // Вестник гражданских инженеров. 2020. Т. 83. № 6. С. 117−125.

10. **Xiang-Sheng C.** The bending stability and vibration of cantilever rectangular plates // Applied Mathematics and Mechanics (English Edition, China). 1987. Vol. 8. No. 7. Pp. 673−683.

11. **Xiang-Sheng C.** On several problems for lateral instability of cantilever plates // Applied Mathematics and Mechanics (English Edition, China). 1988. Vol. 9. No. 8. Pp. 787−792.

12. **Jiang L., Wu S., Zheng H.** Lateral buckling analysis for rectangular cantilever plate subjected to a concentrated loads // Advanced Materials Research. 2013. Vols. 671−674. Pp. 1596−1599.

13. **Yakoob J.A., Hasan I.J.** Study the increasing of the cantilever plate stiffness by using stiffeners // International Journal of Scientific & Engineering Research. 2015. Vol. 6. No. 4. Pp. 1678−1687.

14. **Барышников С.О., Сухотерин М.В., Кныш Т.П.** Устойчивость внешних консольных элементов глубоководных аппаратов // Вестник государственного университета морского и речного флота им. адмирала С.О. Ма-

карова. 2020. Т. 12. № 2. С. 347—358.

15. **Барышников С.О., Сухотерин М.В., Кныш Т.П., Пижурина Н.Ф.** Устойчивость стабилизаторов глубоководных аппаратов // Морские интеллектуальные технологии. 2020. Т. 48. № 2-1. С. 83—90.

16. **Лехницкий С.Г.** Анизотропные пластинки. Москва-Ленинград: Гостехиздат, 1947. 355 с.

17. **Алфутов Н.А.** Основы расчета на устойчивость упругих систем. М.: Машиностроение, 1991. 334 с.

18. **Ullah S., Zhou J., Zhang J., Zhou C., Wang H., Zhong Y., Wang B., Li R.** New analytic shear buckling solution of clamped rectangular plates by a two-dimensional generalized finite integral transform method // International Journal of Structural Stability and Dynamics. 2020. Vol. 20. No. 02. P. 2071002.

СВЕДЕНИЯ ОБ АВТОРАХ

СУХОТЕРИН Михаил Васильевич — *доктор технических наук, член-корреспондент РАЕ, заведующий кафедрой Государственного университета морского и речного флота имени адмирала С.О. Макарова, Санкт-Петербург, Российская Федерация.*

198135, Российская Федерация, г. Санкт-Петербург, Двинская ул., 5/7
sukhoterinmv@gumrf.ru

КНЫШ Татьяна Петровна — *кандидат физико-математических наук, заместитель начальника управления информатизации Государственного университета морского и речного флота имени адмирала С.О. Макарова, Санкт-Петербург, Российская Федерация.*

198135, Российская Федерация, г. Санкт-Петербург, Двинская ул., 5/7
knyshtp@gumrf.ru

ПАСТУШОК Елена Михайловна — *доцент Государственного университета морского и речного флота имени адмирала С.О. Макарова, Санкт-Петербург, Российская Федерация.*

198135, Российская Федерация, г. Санкт-Петербург, Двинская ул., 5/7
pastushokem@gumrf.ru

АБДИКАРИМОВ Рустамхан Алимханович — *доктор физико-математических наук, профессор Ташкентского финансового института, г. Ташкент, Республика Узбекистан.*

100000, Республика Узбекистан, г. Ташкент, ул. А. Темур, 60А
rabdikarimov@mail.ru

NUMERICAL DYNAMICS SCENARIOS OF A VARIABLE IN WIDTH GAS SUSPENSION LAYER ACCELERATED BY A PASSING SHOCK WAVE

D.V. Sadin

Military Space Academy named after A.F. Mozhaysky,
St. Petersburg, Russian Federation

The behavior of the interaction between a shock wave and a gas suspension layer with curved boundaries has been studied using the hybrid large-particle method, the wave running over the layer. The conducted research made it possible to reveal two-dimensional effects of double refraction (von Neumann effects), focusing or divergence of the refracted shock wave, and baroclinic instability at the gas-suspension interface with the formation of mushroom-shaped or ring-shaped vortex structures. The features of the flow nonequilibrium were brought out. These features were associated with a decrease in the intensity of the passing shock wave and the splitting of the initial separation of the media into two contact discontinuities: a jump in porosity and a contact discontinuity in the gas phase.

Keywords: hybrid large-particle method, gas suspension layer, shock wave, baroclinic instability

ЧИСЛЕННЫЕ СЦЕНАРИИ ДИНАМИКИ НЕРАВНОМЕРНОГО ПО ШИРИНЕ СЛОЯ ГАЗОВЗВЕСИ, УСКОРЯЕМОГО ПРОХОДЯЩЕЙ УДАРНОЙ ВОЛНОЙ

Д.В. Садин

Военно-космическая академия имени А.Ф. Можайского,
Санкт-Петербург, Российская Федерация

В работе изучены закономерности взаимодействия ударной волны со слоем газовзвеси, имеющим искривленные границы; при этом волна набегает на указанный слой. Использован гибридный метод крупных частиц. Проведенное исследование позволило обнаружить двумерные эффекты двойного преломления (эффекты фон Неймана), фокусировки или расхождения преломленной ударной волны, бароклинной неустойчивости на поверхности раздела газа и взвеси с образованием грибовидных или кольцевых вихревых структур. Выявлены особенности неравновесности течения, связанные с уменьшением интенсивности проходящей ударной волны и расщеплением начального раздела сред на два контактных разрыва: скачок пористости и контактный разрыв в газовой фазе.

Ключевые слова: гибридный метод крупных частиц, неравномерный слой газовзвеси, ударная волна, преломление

Introduction

Studies of shock wave propagation in inhomogeneous media (uneven distribution of physical-chemical and thermodynamic parameters, including those at the media interface) are relative in various scientific and technical applications. This topic is encountered in the course of solving gas dynamics problems, which imply spatial change in the ratio of specific heats, molecular weight or temperature. The phenomena of shock-inhomogeneity interaction are notable for their complex topology of reflection, refraction and diffraction of the shock waves, as well as the development of the Richtmyer – Meshkov instability [1 – 6].

In the recent decades, the research on the shock wave dynamics in inhomogeneous relaxing multiphase media (gas with particles, fluid with bubbles) have been attracting more and more attention. The work in this direction are connected with the study of gas suspension cloud accelerating in the passing shock wave [7, 8], dispersion of a cloud of particles [9, 10], deformation of boundaries and instability development [11, 12], splitting and escape of gas–particle mixtures [13, 14]. Along with the common qualitative patterns emerging in inhomogeneous flows of "pure" gas, the presence of fine disperse inclusions can lead to unobvious results, for instance, to formation of "abnormal" shock-wave structures at the subsonic carrier-gas flow regime [14, 15].

Due to significant labor intensity of experiments and obtaining quantitative results, mathematical modeling is the most effective method of research. Multiscale solutions are an important feature of problem statements for nonequilibrium flows of heterogeneous media. If the relaxation scale (time of phase relaxation) is significantly less than the gas-dynamic scale of the time the disturbance travels between the grid points and cells (the condition by Courant – Friedrichs – Lewy), then such problems are regarded as stiff. Application of traditional explicit difference schemes of source terms calculation is impractical due to the

unacceptably small time step, which is limited by the characteristic time scale for the fast solution component. To overcome this obstacle of numerical integration of the equations of gas-dispersion media dynamics, researchers propose schemes with explicit spatial approximation of derivatives and implicit scheme for source terms calculation (interphase interactions) [16 – 20]. The other approach consists in construction of fully-implicit schemes represented within vector and scalar runs [21 – 23].

The type and properties of the differential equation system, for example, its hyperbolicity, influence the choice of difference or finite-volume schemes. For two-speed and two-temperature formulations with general pressure or two pressures, the laws of conservation for some models are of hyperbolic or of composite type depending on the phase speed difference [24 – 26]. This places restrictions on the applicability of discrete models based on characteristic representation of the initial equations system, for instance, Godunov type schemes or grid-characteristic methods.

Modification of schemes used in the problems of computational fluid dynamics, for heterogeneous flows modeling in general encounters the problem of nonconservativity (nondivergence notation) of conservation laws due to the Archimedes force caused by the change in the tube of gas flow: $p \nabla \alpha_1$ (p is the gas pressure, α_1 is its volume fraction). To eliminate this difficulty in the schemes, which require divergent notation of discrete conservation laws, an artificial technique is used: the variable $p \nabla \alpha_1$ is transposed to the right-hand side of the conservation laws and united with the source terms (interphase interactions) [17].

The objectives of this article include a detailed numerical analysis between a shock wave and a gas suspension layer of uneven width taking into account relaxation processes, as well as testing the capabilities of the hybrid large-particle method [20, 27] in terms of solving this class of problems.

Mathematical model and calculation method

Consider conservation laws of a calorically perfect gas and solid incompressible particles in the frame of multi-fluid dynamics [28] formulated as [20]:

$$\frac{\partial \rho_i}{\partial t} + \nabla \cdot \left(\rho_i \mathbf{v}_i \right) = 0,$$

$$\frac{\partial}{\partial t} \left(\rho_1 \mathbf{v}_1 \right) + \nabla \left(\rho_1 \mathbf{v}_1 \mathbf{v}_1 \right) + \alpha_1 \nabla p = -\mathbf{F}_\mu,$$

$$\frac{\partial}{\partial t} \left(\rho_2 \mathbf{v}_2 \right) + \nabla \left(\rho_2 \mathbf{v}_2 \mathbf{v}_2 \right) + \alpha_2 \nabla p = \mathbf{F}_\mu,$$ (1)

$$\frac{\partial}{\partial t} \left(\rho_2 e_2 \right) + \nabla \cdot \left(\rho_2 e_2 \mathbf{v}_2 \right) = Q_T,$$

$$\frac{\partial}{\partial t} \left(\rho_1 E_1 + \rho_2 K_2 \right) +$$
$$+ \nabla \cdot \left(\rho_1 E_1 \mathbf{v}_1 + \rho_2 K_2 \mathbf{v}_2 \right) +$$
$$+ \nabla \cdot \left[p \left(\alpha_1 \mathbf{v}_1 + \alpha_2 \mathbf{v}_2 \right) \right] = -Q_T,$$

$$\rho_i = \rho_i^\circ \alpha_i \ \ (i = 1, \ 2), \ \alpha_1 + \alpha_2 = 1,$$
$$E_1 = e_1 + \mathbf{v}_1^2 / 2, \ \ K_2 = \mathbf{v}_2^2 / 2,$$
$$E_2 = K_2 + e_2,$$

where ∇ is the gradient operator; α_i, ρ_i, kg/m³, $\mathbf{v}_i$, m/s, E_i, e_i, J/kg, p, Pa, are the volume fraction, reduced density, velocity vector, total and inner energy of ith phase unit mass, gas pressure; $\mathbf{F}_\mu$, N/м³, is the viscous component of the interphase interaction force; Q, W·m⁻³, is the gas-particles heat transfer power per unit volume; t, s, is the time; here and elsewhere, subscripts 1 and 2 refer respectively to the parameters of the carrier and dispersion phases, and the superscripts denoted by a circle refers to the true values of the density.

Equations of state of the calorically perfect gas and incompressible solid particles are the closing relation for system (1):

$$p = \left(\gamma_1 - 1 \right) \rho_1^\circ e_1, \ e_1 = c_v T_1,$$

$$e_2 = c_2 T_2, \ \left\{ \gamma_1, c_v, c_2, \rho_2^\circ \right\} \equiv \text{const},$$

where T_1, T_2, K, are the temperatures of the carrier phase and the particles; γ_1, c_v, J/(kg·K), is the ratio of specific heats and specific heat of the gas at constant volume; c_2, J/(kg·K) is the specific heat of the particles.

Force and thermal interphase interactions $\mathbf{F}_\mu$, Q_T are determined using criterion relations [28].

For the calculations, we used the hybrid large-particle method of the second order of accuracy in space and time [27]. We used two approaches to regularize the numerical solution. At the first stage of the algorithm, we added artificial dissipation with nonlinear Christensen type correction into the scheme. In contrast to the linear or quadratic artificial viscosity, the proposed numerical viscosity does not reduce the order of approximation and becomes zero in arbitrary resolution grids for smooth solutions. Based on the obtained preliminary values of the required functions, at the second stage, there were fluxes forming by means of hybridization: a quasilinear combination of the central and upwind approximations weighted by a limiter. At the same time, discrete analogs of the conservation laws remain true. We increased the order of accuracy with respect to time using the Runge − Kutta method with two stages. We applied an non-iterations scheme to calculate the interphase interactions without splitting them into gas-dynamic and relaxation stages by means of linearization and implicitly taking into account the linear part of the source terms.

The method has several positive computational properties including K-stability [18] (independence of the time step on the size of the computational grid and intensity of the interphase interactions). The scheme is non-dissipative for smooth solutions, demonstrates monotonicity and high resolution for structurally complex flows. The algorithm is distinguished by universality of solving an extended class of problems with dominating convection of both hyperbolic and composite types [20, 27].

The time step is determined from the Courant − Friedrichs − Lewy condition for "pure" gas:

$$\tau^k = \text{CFL} \frac{h}{\max\limits_{\forall n} \left(\left| v_{1,n}^k \right| + a_n^k \right)},$$

where CFL is the fixed Courant number, a_n^k is sonic speed through the gas phase in point $\left(x_n, t^k\right)$.

Problem statement

Flat shock tube *1* is filled with nonturbulent air *2*. Inside the shock tube, there is a layer of gas suspension *3* with cylindrical convex *4* or a concave *5* with diameter $D = 5$ cm (Fig. 1). A shock wave *6* of constant intensity is moving from left to right with the Mach number M = 1.22. We consider variants of the problems with cylindrical curvature of the gas suspension layer on its left (at $x = 3D$) or right (at $x = 4D$) boundary (Fig. 1,*a* and *b*, respectively).

At the initial instant, the shock front is located in plane $x_s = 1.5D$. At $t = 0$, the gas suspension layer is a still mixture of air ($\gamma_1 = 1.4$) and monodispersed incompressible spherical particles with the density $\rho_2^\circ = 2500$ kg/m³, volume fraction $\alpha_2 = 0.001$ and specific heat $c_2 = 710$ J/(km·K) in the conditions of thermodynamical equilibrium ($T_1 = T_2 = 293,23$ K) and at the pressure $p = 101325$ Pa.

We set boundary reflection conditions at the walls and soft boundary conditions of the continuation of the solution at the input (at $x = 0$) and the output (at $x = 9D$) from the domain of computation. To exclude (minimize) the influence of the boundedness of the computational domain on the solution in the neighborhood of the right boundary $8.5D < x \leq 9D$ (Fig. 1), we used an increasing step grid. The problems were solved numerically using the hybrid large-particle method with the Courant number CFL = 0.4 up to the line of symmetry at a uniformly spaced grid with the step $h/D = 0.0025$. For homogeneity of the algorithm in the domain of the "pure" gas, volume concentration of particles is taken to be negligible ($\alpha_2 = 10^{-10}$).

Numerical results and discussion

Interaction between the passing shock wave and the limited gas suspension layer with curved boundaries is accompanied by a number of nonlinear physical phenomena: breakdown of a discontinuity at the media interface, their deformation, development of instability and formation of vortex structures.

Depending on the difference in the effective acoustic impedance

$$\delta R = \rho_+ a_+ - \rho_- a_-$$

(plus on the right and minus on the left) from the gas-suspension contact (in this expression

$$a = \sqrt{p / \left[\left(\rho_1 + \rho_2\right)\alpha_1\right]}$$

is the effective speed of sound of the mixture of gas *1* and particles *2*), there two configurations manifesting: with two shock waves at $\delta R > 0$ or a passing shock wave and a rarefaction wave at $\delta R < 0$.

For all variants of the problem under consideration, at the left (*L*) and the right (*R*) boundaries of the layer, the δR values amount to:
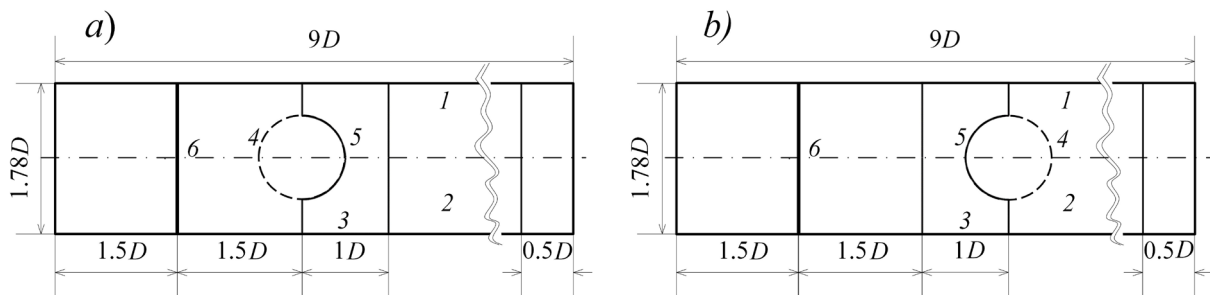
Fig. 1. Computational schemes of the problems with left (*a*)
or right (*b*) boundary curvature of the gas suspension layer
1 – flat shock tube filled with nonturbulent air (*2*); *3* – gas suspension layer;
4 – cylindrical convex; *5* – concave; *6* – shock wave of constant intensity

$$\delta R_L = 238.423 \, \text{kg}/\left(\text{m}^2 \cdot \text{s}\right),$$

$$\delta R_R = -238.423 \, \text{kg}/\left(\text{m}^2 \cdot \text{s}\right).$$

The physical cause of the instability and vortex formation at the contact interface is baroclinic instability, which is incongruence of the density and pressure gradients. Indeed, in a one-velocity approximation, at the initial point of time the vorticity variable

$$\omega = \nabla \times \mathbf{v} = 0,$$

while a transfer equation for the vorticity has the form

$$\frac{\partial \omega}{\partial t} + \left(\mathbf{v} \cdot \nabla\right)\omega =$$

$$= \frac{\nabla \rho \times \nabla p}{\rho^2} + \left(\omega \cdot \nabla\right)\mathbf{v} - \omega\left(\nabla \cdot \mathbf{v}\right).$$

Consequently, if $t > 0$, in case of differently-directed gradients of density and pressure ($\nabla \rho \times \nabla p \neq 0$), there is a vortex motion of the gas-particles mixture appearing in the neighborhood of curved contact boundaries.

Another considerable factor is connected with the nonequilibrium of the gas suspension dynamics (a difference in the velocities and temperatures of the gas and the particles), which is characterized by dimensionless time of the dynamic $\overline{t}_1^{(\mu)}$, $\overline{t}_2^{(\mu)}$ and thermal $\overline{t}_1^{(T)}$, $\overline{t}_2^{(T)}$ phase relaxations [18]:

$$\overline{t}_1^{(\mu)} = \frac{1}{18}\frac{\rho_1^{\circ}d^2}{\mu_1 \alpha_2}\frac{a_{10}}{D}, \quad \overline{t}_2^{(\mu)} = \frac{1}{18}\frac{\rho_2^{\circ}d^2}{\mu_1 \alpha_1}\frac{a_{10}}{D};$$

$$\overline{t}_1^{(T)} = \frac{d^2\rho_1^{\circ}c_p}{4\lambda_1 \alpha_2}\frac{a_{10}}{D}, \quad \overline{t}_2^{(T)} = \frac{d^2\rho_2^{\circ}c_2}{4\lambda_2 \alpha_1}\frac{a_{10}}{D},$$

where d is the particle diameter, a_{10} is the initial speed of sound in the carrier phase.

Numerical scenarios of dust layer dynamics for a fine particles suspension. Let us consider in detail the indicated scenarios for fine particles of $d = 0.1$ μm diameter and a dust layer with a cylindrical concave or a thickening of the layer at the left (Fig. 2) or the right (Fig. 3) boundary. The flows are visualized in the form of numerical schlieren images of the gradient function of the reduced density of the mixture $s(\nabla \rho)$ [29]. The results are presented for four successive characteristic moments in time: breakdown of a discontinuity at the left boundary of the suspension (Fig. 2, *a*, *e* and Fig. 3, *a*, *e*), shock wave passing inside the suspension (Fig. 2, *b*, *f* and Fig. 3, *b*, *f*), shock-wave refraction at the right boundary (Fig. 2, *c*, *g* and Fig. 3, *c*, *g*) and development of an instability along with vortex motion at the media interface (Fig. 2, *d*, *h* and Fig. 3, *d*, *h*). Axial and transverse coordinates are based on the diameter D of the initial layer curvature: $x' = x/D$ and $y' = y/D$. The time is calculated in the dimensionless form: $t' = \alpha_{10}\, t/D$.

The beginning of the interaction of the primary shock wave s_1 is accompanied by a breakdown of a discontinuity on straight (Fig. 3) or curved (Fig. 2) surfaces of the dust layer c_1. Since the difference in the effective acoustic impedance $\delta R_L = 238.423$ kg/(m²·s), i.e. is greater than zero, the reflection takes place in a form of a straight s_3 (Fig. 3, *a*, *e*) or curved $s_3 - s_3'$ (Fig. 2, *a*, *e*) shock wave. On interaction with the inhomogeneity, a rarefaction wave r_1 (Fig. 2, *a*) or a convex shock wave (Fig. 2, *e*) is forming. In the case of a concave on the left (Fig. 2, *a*), there is a passing shock wave s_2 forming along with von Neumann's double refraction, or a disc s_2' in case of the layer thickening (Fig. 2, *e*).

In successive moments of time, the curved shock wave $s_2 - s_2'$ moves inside the two-phase medium layer (Fig. 2, *b*, *f*), and when it is running over the right boundary c_2, it breaks down into a passing shock wave s_4 and a reflected rarefaction wave r_2 in the opposite direction (Fig. 2, *c*, *g*). The splitting character of the shock wave s_4 through the layer in the case of the cylindrical concave (Fig. 3, *c*) or the focusing effect F of the transverse shock waves s_4' reflecting from the symmetry line (Fig. 3, *g*) serve as the distinctive features of the breakdown of the discontinuity at the right curved boundary.

For the concave/convex layer cases, the vector product of the gradients of mixture density and pressure $\nabla \rho \times \nabla p$ has opposite directions, which
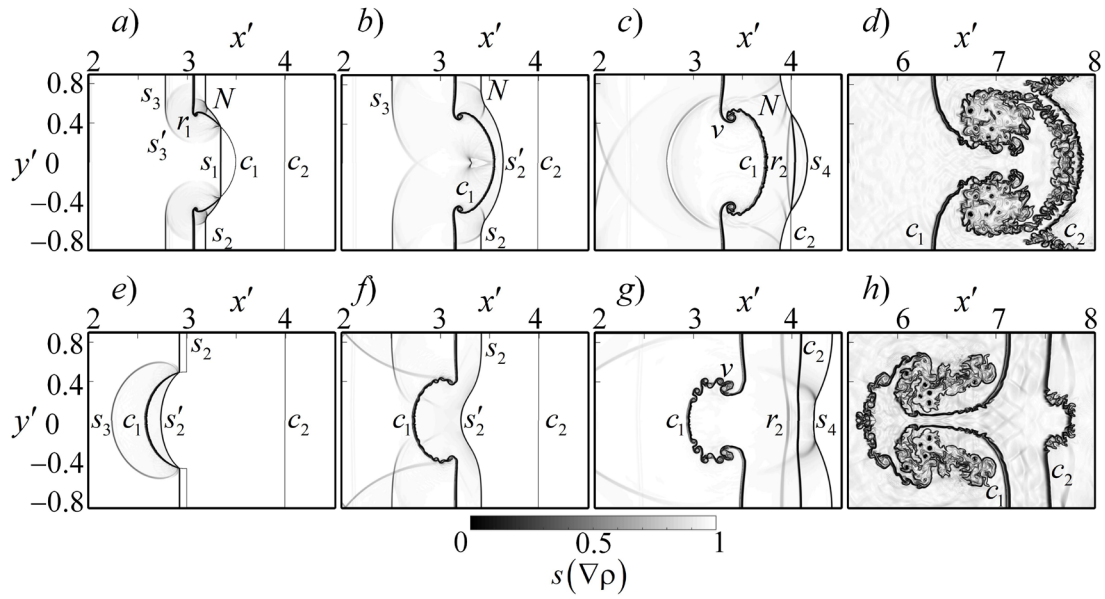
Fig. 2. Interaction of a shock wave with a concave ($a - d$) or a convex ($e - h$) at the left boundary of a gas suspension layer ($d = 0.1$ μm). Numerical schlieren images of the gradient function of the mixture density are presented in successive moments of time:
1.51 (a), 1.85 (b), 2.54 (c), 13.73 (d), 1.17 (e), 1.85 (f); 3.09 (g), 13.73 (h).
Grid size above the symmetry line 3600 × 356; N is von Neumann's double refraction; c_1, c_2 — are left and right surfaces of dustи; s_1, s_2, s_2', s_3, s_3', s_4 are shock waves; r_1, r_2 are rarefaction waves; v are vortices
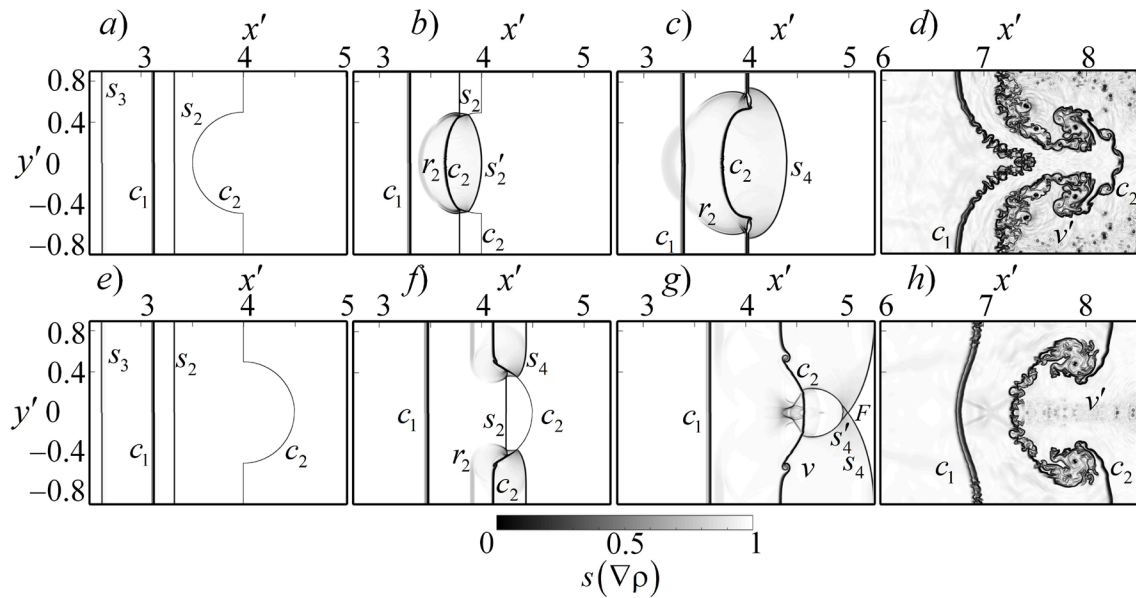
Fig. 3. Diagrams similar to those in Fig. 2, but for the right boundary of the gas suspension layer; in addition, numerical schlieren images of the gradient function of the mixture density are presented partially in other successive moments of time:
1.72 (a); 2.40 (b); 2.75 (c); 13.73 (d); 1.72 (e), 3.09 (f), 3.78 (g), 13.73 (h).
F is the focusing effect of transverse shock waves; s_4', v' are separated vortices
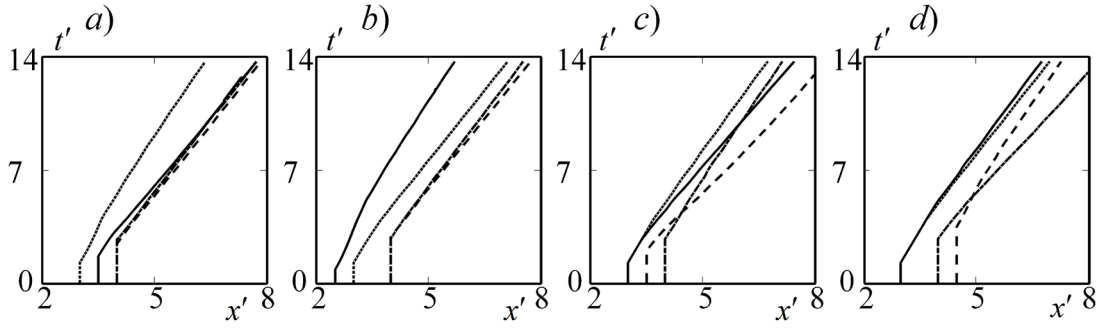
Fig. 4. Trajectories of the left and the right boundaries of the gas suspension layer
(the solid and dashed lines, respectively) along the symmetry line ($y'=0$),
as well as on the shock tube wall ($y'=0,89$) (the densely dotted and dashdotted lines, respectively)
for the concave/convex cases of the respective left (*a* and *b*) and right (*c* and *d*) boundaries

causes the formation of differently-directed vortices (Fig. 2 and 3, *c*, *g*). Subsequently, there are mushroom-shaped (Fig. 2, *h*) and ring-shaped (Fig. 3, *d*) vortex structures *t*. Note the emergence of small separated vortices in the gas phase peripherally down the stream (Fig. 3, *d*) or in the neighborhood of the symmetry line (Fig. 3, *h*).

Dynamics of the layer for the variants of the problems under consideration is shown in Fig. 4 in a form of a trajectory of set point at the interface of the media. The agreed notations are as follows: solid and dashed lines correspond to the trajectories of the left and the right boundaries along the symmetry line (at $y'=0$), while densely dotted and dashdotted curves show the time changes of the positions of the left and the right contact surfaces on the shock tube wall (at $y'=0,89$).

The dust layer boundaries are deformed with compression along the symmetry line for the variant of concave interaction on the left (Fig. 4, *a*), while the cylindrical convex, on the contrary, leads to a delay of the contact surface in the center of the shock tube from the peripheral movement of the suspension (Fig. 4, *b*). In case of the initial curvature of the right edge of the gas suspension layer, we can observe the characteristic points trajectories intersecting (Fig. 4, *c* and *d*). For instance, the right boundary of the layer in the neighborhood of the wall (the dashdotted line) eventually falls back (Fig. 4, *c*) or goes ahead of (Fig. 4, *d*) the positions of the layer boundaries

along the symmetry line (the solid and dashed lines).

The scenarios of interest occur for fine gas suspension particles, which have short equalization period in terms of velocity and phase temperature, i.e.

$$\bar{t}_1^{(\mu)}10^4 = 2.551, \bar{t}_2^{(\mu)}10^4 = 5.302;$$

$$\bar{t}_1^{(T)}10^4 = 8.303, \ \bar{t}_2^{(T)}10^4 = 0.277,$$

while the relaxation zones are subgrid.

Numerical scenarios of dust layer dynamics for a suspension of larger particles. Let us now consider the interaction of a shock wave with a gas suspension layer of particles with the diameter of $d = 10$ μm on the example the problem with the initial width reduction (concave) at the left surface.

The calculation results in the successive moments of time are presented in Fig. 5 as numerical schlieren images and as the mixture density distributions based on its value after the shock wave $\rho' = \rho/\rho_s$.

Due to significant phase relaxation time equal to

$$\bar{t}_1^{(\mu)} = 2.551, \bar{t}_2^{(\mu)} = 5.302;$$

$$\bar{t}_1^{(T)} = 8.303, \ \bar{t}_2^{(T)} = 0.277,$$

the gas suspension layer dynamics have a num-
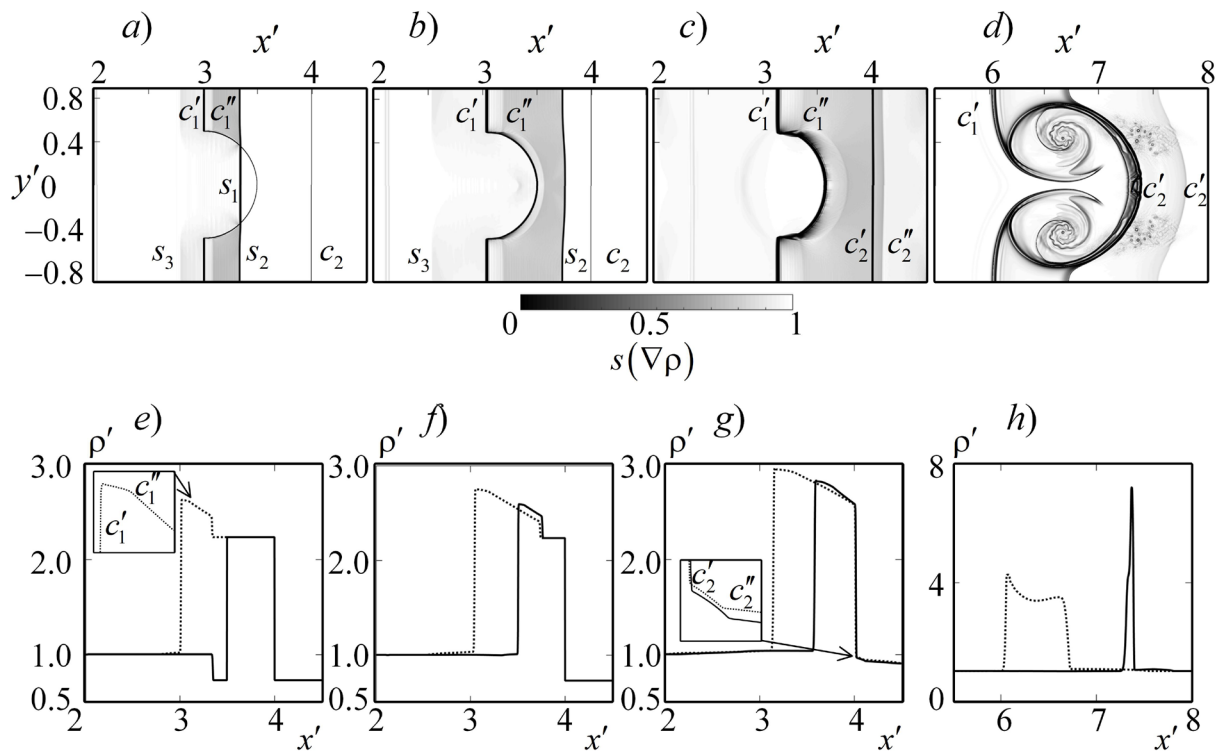
Fig. 5. Interaction of a shock wave with a concave on the left boundary of the gas suspension layer ($d = 10$ μm). Numerical schlieren images of the gradient function of the mixture density ($a - d$) and the relative density profiles of the mixture ($e - h$) at the symmetry line (solid curves) and on the wall (dashed lines) are presented in successive dimensionless moments of time: 1.51 (a, e), 1.85 (b, f), 2.54 (c, g), 13.73 (d, h)

ber of significant features. When a shock wave s_1 strikes the left boundary of the disperse medium, there forms a passing shock wave s_2 of decreasing intensity and a reflected weak compressive shock wave s_3.

Since the gas carrier phase is ahead of the disperse particles driven by it, the initial separation of the media splits into two contact discontinuities. The first one is a jump in porosity, and the second one is contact discontinuity in the gas phase c_1'' (Fig. 5, a, b and e, f). A similar situation also occurs at the right gas suspension boundary with the media interface c_2' and the interface surface of the gases c_2'' (Fig. 5, c and g).

The interfacial friction and heat transfer are considerable factors affecting the suppression of small vortices. Bu the end of computations, the layer is deforming with significant compression along the symmetry line (Fig. 5, g) and generates a large ring-shaped gas-dispersion vortex structure (Fig. 5, d).

Conclusion

We used the method of numerical modeling to study the behavior of the interaction between a shock wave running over a gas suspension layer with curved boundaries. Depending on the difference in the effective acoustic impedance, there are two types of discontinuity breakdown manifesting at the interface of the media: two shock waves or a rarefaction wave and a shock wave. The presence of a convex or a concave in the gas suspension layer generates two-dimensional effects of von Neumann double refraction, focusing or divergence of the passing shock wave. The incongruence of the density and pressure gradients causes an instability to form at the gas-suspension interface and generates mushroom-shaped and ring-shaped vortex structures. The nonequilibrium factor of the flow at increasing size of disperse particles adds considerable features: a shock wave moves through the gas suspension layer with decreasing intensity, while the initial separation of

the media splits into two contact discontinuities: a jump in porosity and a contact discontinuity in the gas phase.

The results of the numerical modeling proved reliability, stability and high resolution capacity of the hybrid large-particle method.

REFERENCES

1. **Abd-El-Fattah A.M., Henderson L.F.,** Shock waves at a fast-slow gas interface, Journal of Fluid Mechanics. 86 (1) (1978) 15−32.

2. **Abd-El-Fattah A.M., Henderson L.F.,** Shock waves at a slow-fast gas interface, Journal of Fluid Mechanics. 89 (1) (1978) 79−95.

3. **Voinovich P.A., Zhmakin A.I., Fursenko A.A.,** Numerical simulation of the interaction of shock waves in spatially inhomogeneous gases, Sov. Phys. Tech. Phys. 33 (1988) 748−753.

4. **Georgievskiy P.Yu., Levin V.A., Sutyrin O.G.,** Spatial effects of interaction of a shock with a lateral low-density gas channel, Technical Physics Letters. 44 (10) (2018) 905−908.

5. **Ranjan D., Oakley J., Bonazza R.,** Shock-bubble interactions, Annual Review of Fluid Mechanics. 43 (2011) 117−140.

6. **Wang M., Si T. & Luo X.,** Experimental study on the interaction of planar shock wave with polygonal helium cylinders, Shock Waves. 25 (4) (2015) 347−355.

7. **Kiselev V.P., Kiselev S.P., Vorozhtsov E.V.,** Interaction of a shock wave with a particle cloud of finite size, Shock Waves. 16 (1) (2006) 53−64.

8. **Tukmakov D.A.,** Numerical study of intense shock waves in dusty media with a homogeneous and two-component carrier phase, Computer Research and Modeling. 12 (1) (2020) 141−154 (in Russian).

9. **Davis S.L., Dittmann T.B., Jacobs G.B., Don W.S.,** Dispersion of a cloud of particles by a moving shock: effects of the shape, angle of rotation, and aspect ratio, J. Appl. Mech. Tech. Phys. 54 (6) (2013) 900−912.

10. **Volkov K.N., Emel'yanov V.N., Karpenko A.G., Teterina I.V.,** Simulation of unsteady gas-particle flow induced by the shock wave interaction with a particle layer, Numerical Methods and Programming. 21 (1) (2020) 96−114.

11. **Georgievskiy P.Yu., Levin V.A., Sutyrin O.G.,** Shock focusing upon interaction of a shock with a cylindrical dust cloud, Technical Physics Letters. 42 (9) (2016) 936−939.

12. **Sadin D.V., Davidchuk V.A.,** Interaction of a plane shock wave with regions of varying shape and density in a finely divided gas suspension, J. Eng. Phys. Thermophys. 93 (2) (2020) 474−483.

13. **Nigmatulin R.I., Gubajdullin D.A., Tukmakov D.A.,** Shock-wave dispersion of gas−particle mixtures, Doklady Physics. 61 (2) (2016) 70−73.

14. **Sadin D.V., Lyubarskii S.D., Gravchenko Yu.A.,** Features of an underexpanded pulsed impact gas-dispersed jet with a high particle concentration, Technical Physics. 62 (1) (2017) 18−23.

15. **Sadin D.V., Guzenkov V.O., Lyubarskii S.D.,** Numerical study of the structure of a finely disperse unsteady two-phase jet, Journal of Applied Mechanics and Technical Physics. 46 (2) (2005) 224−229.

16. **Sadin D.V.,** A method for computing heterogeneous wave flows with intense phase interaction, Computational Mathematics and Mathematical Physics. 38 (6) (1998) 987−993.

17. **Saurel R., Abgrall R.,** A multiphase Godunov method for compressible multifluid and multiphase flows, Journal of Computational Physics. 150 (2) (1999) 425−467.

18. **Sadin D.V.,** On stiff systems of partial differential equations for motion of heterogeneous media, Mathematical Models and Computer Simulations. 14 (11) (2002) 43−53 (in Russian).

19. **Saurel R., Petitpas F., Berry R.A.,** Simple and efficient relaxation methods for interfaces separating compressible fluids, cavitating flows and shocks in multiphase mixtures, Journal of Computational Physics. 228 (5) (2009) 1678−1712.

20. **Sadin D.V.,** TVD scheme for stiff problems of wave dynamics of heterogeneous media of non-hyperbolic nonconservative type, Computational Mathematics and Mathematical Physics. 56 (12) (2016) 2068−2078.

21. **Frepoli C., Mahaffy J.H., Ohkawa K.,** Notes

on the implementation of a fully-implicit numerical scheme for a two-phase three-field flow model, Nuclear Engineering and Design. 225 (12) (2003) 191–217.

22. **Nascimento J.C.S., Santos A., Pires A.P.,** A fully-implicit solution for the single-pressure two-fluid model with sharp discontinuities, Computers and Fluids. 175 (15) (2018) 214–229.

23. **Bulovich S.V.,** An implicit economical algorithm for numerical integration of the equation system describing a multiphase flow state with common pressure, St. Petersburg Polytechnical State University Journal. Physics and Mathematics. 13 (4) (2020) 47–60.

24. **Klebanov L.A., Kroshilin A.E., Nigmatulin B.I., Nigmatulin R.I.,** On hyperbolicity, stability and correctness of the Cauchy problem for a differential equations system of the two-speed motion of two-phase media, Journal of Applied Mathematics and Mechanics. 46 (1) (1982) 83–95 (in Russian).

25. **Drew D.A.,** Mathematical modelling of two-phase flow, Annual Review of Fluid Mechanics. 15 (1983) 261–291.

26. **Hudson J., Harris D.,** A high resolution scheme for Eulerian gas–solid two-phase isentropic flow, Journal of Computational Physics. 216 (2) (2006) 494–525.

27. **Sadin D.V.,** A modification of the large-particle method to a scheme having the second order of accuracy in space and time for shockwave flows in a gas suspension, Bulletin of the South Ural State University. Ser. Mathematical Modelling, Programming & Computer Software (Bulletin SUSU MMCS). 12 (2) (2019) 112–122 (in Russian).

28. **Nigmatulin R.I.,** Dynamics of multiphase media, Vol. 1, 2; Hemisphere Publ. Corp., New York, United States, 1990.

29. **Quirk J.J., Karni S.,** On the dynamics of a shock-bubble interaction, Journal of Fluid Mechanics. 318 (10 July) (1996) 129–163.

THE AUTHOR

SADIN Dmitriy V.
Military Space Academy named after A.F. Mozhaysky
13, Zhdanovskaya St., St. Petersburg, 197198, Russian Federation
sadin@yandex.ru

СПИСОК ЛИТЕРАТУРЫ

1. **Abd-El-Fattah A.M., Henderson L.F.** Shock waves at a fast-slow gas interface // Journal of Fluid Mechanics. 1978. Vol. 86. No. 1. Pp. 15–32.

2. **Abd-El-Fattah A.M., Henderson L.F.** Shock waves at a slow-fast gas interface // Journal of Fluid Mechanics. 1978. Vol. 89. No. 1. Pp. 79–95.

3. **Войнович П.А., Жмакин А.И., Фурсенко А.А.** Моделирование взаимодействия ударных волн в газах с пространственными неоднородностями параметров // Журнал технической физики. 1988. Т. 58. № 7. С. 1259–1267.

4. **Георгиевский П.Ю., Левин В.А., Сутырин О.Г.** Пространственные эффекты при взаимодействии ударной волны с продольным каналом газа пониженной плотности // Письма в Журнал технической физики. 2018. Т. 44. № 20. С. 5–13.

5. **Ranjan D., Oakley J., Bonazza R.** Shock-bubble interactions // Annual Review of Fluid Mechanics. 2011. Vol. 43. Pp. 117–140.

6. **Wang M., Si T., Luo X.** Experimental study on the interaction of planar shock wave with polygonal helium cylinders // Shock Waves. 2015. Vol. 25. No. 4. Pp. 347–355.

7. **Kiselev V.P., Kiselev S.P., Vorozhtsov E.V.** Interaction of a shock wave with a particle cloud of finite size // Shock Waves. 2006. Vol. 16. No. 1. Pp. 53–64.

8. **Тукмаков Д.А.** Численное исследование интенсивных ударных волн в запыленных сре-

дах с однородной и двухкомпонентной несущей фазой // Компьютерные исследования и моделирование. 2020. Т. 12. № 1. С. 141—154.

9. **Дэвис С.Л., Диттман Т.Б., Якобс Дж.Б., Дон В.С.** Дисперсия облака частиц в ударной волне. Влияние формы, угла поворота и геометрических параметров облака на динамику потока и дисперсию // Прикладная механика и техническая физика. 2013. Т. 54. № 6. С. 45—59.

10. **Волков К.Н., Емельянов В.Н., Карпенко А.Г., Тетерина И.В.** Влияние двумерных эффектов на взаимодействие ударной волны с облаком частиц // Вычислительные методы и программирование. 2020. Т. 21. № 3. С. 207—224.

11. **Георгиевский П.Ю., Левин В.А., Сутырин О.Г.** Фокусировка ударной волны при взаимодействии ударной волны с цилиндрическим облаком пыли // Письма в Журнал технической физики. 2016. Т. 42. № 18. С. 17—24.

12. **Садин Д.В., Давидчук В.А.** Взаимодействие плоской ударной волны с областями различной формы и плотности в мелкодисперсной газовзвеси // Инженерно-физический журнал. 2020. Т. 93. № 2. С. 489—498.

13. **Нигматулин Р.И., Губайдуллин Д.А., Тукмаков Д.А.** Ударно-волновой разлет газовзвесей // Доклады Академии наук. 2016. Т. 466. № 4. С. 418—421.

14. **Садин Д.В., Любарский С.Д., Гравченко Ю.А.** Особенности недорасширенной импульсной импактной газодисперсной струи с высокой концентрацией частиц // Журнал технической физики. 2017. Т. 87. №1. С. 22—26.

15. **Садин Д.В., Гузенков В.О., Любарский С.Д.** Численное исследование структуры нестационарной двухфазной тонкодисперсной струи // Прикладная механика и техническая физика. 2005. Т. 46. № 2. С. 91—97.

16. **Садин Д.В.** Метод расчета волновых гетерогенных течений с интенсивным межфазным взаимодействием // Журнал вычислительной математики и математической физики. 1998. Т. 38. № 6. С. 1033—1039.

17. **Saurel R., Abgrall R.** A multiphase Godunov method for compressible multifluid and multiphase flows // Journal of Computational Physics. 1999. Vol. 150. No. 2. Pp. 425—467.

18. **Садин Д.В.** О жесткости систем дифференциальных уравнений в частных производных, описывающих движения гетерогенных сред // Математическое моделирование. 2002. Т. 14. № 11. С. 43—53.

19. **Saurel R., Petitpas F., Berry R.A.** Simple and efficient relaxation methods for interfaces separating compressible fluids, cavitating flows and shocks in multiphase mixtures // Journal of Computational Physics. 2009. Vol. 228. No. 5. Pp. 1678—1712.

20. **Садин Д.В.** TVD-схема для жестких задач волновой динамики гетерогенных сред негиперболического неконсервативного типа // Журнал вычислительной математики и математической физики. 2016. Т. 56. № 12. С. 2098—2109.

21. **Frepoli C., Mahaffy J.H., Ohkawa K.** Notes on the implementation of a fully-implicit numerical scheme for a two-phase three-field flow model // Nuclear Engineering and Design. 2003. Vol. 225. No. 12. Pp. 191—217.

22. **Nascimento J.C.S., Santos A., Pires A.P.** A fully-implicit solution for the single-pressure two-fluid model with sharp discontinuities // Computers and Fluids. 2018. Vol. 175. No. 15. Pp. 214—229.

23. **Булович С.В.** Неявный экономичный алгоритм численного интегрирования системы уравнений для описания состояния многофазного потока с общим давлением // Научно-технические ведомости СПбГПУ. Физико-математические науки. 2020. Т. 13. № 4. С. 47—60.

24. **Клебанов Л.А., Крошилин А.Е., Нигматулин Б.И., Нигматулин Р.И.** О гиперболичности, устойчивости и корректности задачи Коши для системы дифференциальных уравнений двухскоростного движения двухфазных сред // Прикладная математика и механика. 1982. Т. 46. № 1. С. 83—95.

25. **Drew D.A.** Mathematical modelling of two-phase flow // Annual Review of Fluid Mechanics. 1983. Vol. 15. Pp. 261—291.

26. **Hudson J., Harris D.** A high resolution scheme for Eulerian gas—solid two-phase isentropic flow // Journal of Computational Physics. 2006. Vol. 216. No. 2. Pp. 494—525.

27. **Садин Д.В.** Модификация метода крупных частиц до схемы второго порядка точности

по пространству и времени для ударно-волновых течений газовзвеси // Вестник Южно-Уральского государственного университета. Серия: Математическое моделирование и программирование. 2019. Т. 12. № 2. С. 112—122.

28. **Нигматулин Р.И.** Динамика многофазных сред. Ч. 1, 2. М.: Наука, 1987.

29. **Quirk J.J., Karni S.** On the dynamics of a shock-bubble interaction // Journal of Fluid Mechanics. 1996. Vol. 318. 10 July. Pp. 129—163.

СВЕДЕНИЯ ОБ АВТОРЕ

САДИН Дмитрий Викторович — *доктор технических наук, профессор Военно-космической академии имени А.Ф. Можайского, Санкт-Петербург, Российская Федерация.*

197198, Российская Федерация, г. Санкт-Петербург, Ждановская ул., 13
sadin@yandex.ru

THE DYNAMIC CHARACTERISTICS OF A RESONATOR OF THE GIROSCOPE BASED ON ELASTIC WAVES IN SOLIDS: FINITE-ELEMENT MODELING

S.A. Shevchenko, O.I. Konotopov

JSC "Command Devices Research Institute",
St. Petersburg, Russian Federation

In the paper, the eigenfrequencies of a hemispherical resonator of the Coriolis vibratory gyroscope have been studied by the finite element method (FEM) using ANSYS Mechanical. Consideration was given to the feasibility of various FE used in the ANSYS to solve the problem of determining the eigenfrequencies. The specifics of working with shell and solid-state elements were established. The results of analytical and numerical solutions of the mentioned problem were compared. The presence of "mathematical" frequency split caused by the used FEM and the unsymmetrical mesh of the FEM was noted, and the need to take this split into account when introducing the defect distribution function into the model was pointed out. The technique for finding the frequency split value resulted by added defect in the presence of "mathematical" frequency split component was demonstrated.

Keywords: Coriolis vibratory gyroscopes, hemispherical resonator, eigenfrequency split, finite element method

ПРИМЕНЕНИЕ КОНЕЧНО-ЭЛЕМЕНТНОГО МОДЕЛИРОВАНИЯ ДЛЯ ИССЛЕДОВАНИЯ ДИНАМИЧЕСКИХ ХАРАКТЕРИСТИК РЕЗОНАТОРА ТВГ

С.А. Шевченко, О.И. Конотопов

АО «НИИ командных приборов»,
Санкт-Петербург, Российская Федерация

В статье методом конечных элементов (МКЭ) исследованы собственные частоты полусферического резонатора твердотельного волнового гироскопа (ТВГ) с использованием программного комплекса ANSYS Mechanical. Рассмотрена применимость различных КЭ, использующихся в ANSYS, для решения задачи определения собственных частот. Установлены особенности работы с оболочечными и твердотельными элементами. Проведено сравнение результатов аналитического и численного решений задачи по определению собственных частот резонатора. Отмечено наличие «математического» расщепления частоты, вызванного применяемым МКЭ и несимметричностью КЭ-сетки, а также необходимость учета данного расщепления при внесении в модель функции распределения дефекта. Представлен способ нахождения величины расщепления от внесенного дефекта при наличии составляющей «математического» расщепления.

Ключевые слова: твердотельный волновой гироскоп, полусферический резонатор, расщепление частоты, метод конечных элементов

Introduction

Various types of gyroscopes find their application in modern guidance, position control and stabilization systems. Gyroscopes are employed in shipbuilding, air- and spacecraft industries, as well as rocket engineering. Production of Coriolis vibratory gyroscopes (CVGs) is a promising direction of gyroscopic technology development. New generations of optic, vibratory, wave solid-state and other gyroscopes are taking over the traditional gyroscopic devices [1, 2]. Manufacture and application of the new types of gyroscopes are associated with the need for miniaturization alongside with meeting the accuracy, reliability and service life requirements.

Effect of inertia of elastic waves is the cornerstone of modern CVGs operation [3]. When the object with a CVG installed rotates, the device registers the standing wave precession emerging due to constant oscillations of the sensory organ − resonator. Measuring the angular displacement of the wave makes it possible to calculate the angular velocity in inertial space used in production of angular velocity and displacement sensors [4]. The CVG design often includes thin cylindrical and hemispherical resonators, which are classic shells with mode shapes convenient for application.

We further consider a hemispherical resonator design (Fig. 1), its primary geometrical parameters, as well as the properties of its material (Table 1).

Resonator Q-factor is one of the main properties characterizing the device operation. Therefore, low viscosity materials are used for the production of resonators. Fused quartz is a material with one of the lowest levels of viscosity. For instance, metals have the respective parameter at a 2−3 orders higher level, thus producing resonators with inferior performance specifications [4], and, consequently, fail to provide high accuracy. Note that fused quartz possesses the same isotropy of elastic characteristics, which is essential for the material of CVG sensory organs. We selected the values of physical and mechanical characteristics of fused quartz taken for the calculations presented in the article in compliance with the state standard GOST 15130-86.

There are strict accuracy requirements imposed upon gyroscopic systems, particularly on CVGs. Currently, due to rather high development of electronic devices, the factors defining the accuracy of a CVG are geometrical and physical properties of its elastic element (the resonator), which are obtained in the process of its production. In other words, the accuracy parameters of CVGs are most influenced by various errors resulting from the production of the elastic element (circumferentially varying thickness, out-of-roundness, surface roughness, circumferentially varying thickness of the metallic film, etc.), as well as by imperfection of the physical characteristics of the material applied

Table 1

Main characteristics of the hemispherical resonator

Material	Fused quartz KU-1
Elastic modulus, GPa	73.6
Poisson's ratio	0.17
Density, kg/m^3	2210
Outer radius of hemisphere, mm	15.25
Wall thickness of hemisphere, mm	0.90
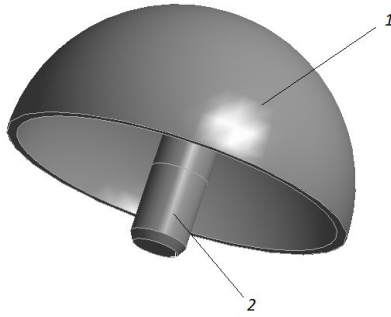
Fig. 1. Geometrical model
of the hemispherical resonator:
1 − thin hemispherical shell, *2* − stem

(anisoelasticity, anisodamping, inhomogeneous density, internal defects, etc.). The indicated imperfections cause the effect of eigenfrequencies and modes split in the resonator due to its axial symmetry perturbation. The effect manifests itself in the non-ideal resonator spectrum obtaining two closely spaced frequencies instead of one with two close eigenmodes excitation, which leads to a change in the operation regime of the device. With its operation frequency splitting, the resonator Q-factor decreases, which leads to a drift of the gyroscope, and consequently, to a drop of the CVG accuracy characteristics. To estimate the influence of the errors and defects of the CVG manufacturing process on its operating frequency split value, the design stage includes various mathematical methods, one of them being the finite element method (FEM).

Many works are devoted to the approaches of calculating the eigenvalues of thin shells of different shape, as well as to the studies on the eigenfrequency split (see, for example, articles [5—8] and thesis [11]). Along with the widespread analytical calculations, the authors of the mentioned sources also use FEM. For instance, paper [8] reports good, compared to the analytical methods, agreement of the results obtained via FEM. Noteworthy is that the listed works, with the exception of [11], do not mention the resonator eigenfrequency split caused by the application of FEM itself and apparently attributable to the error in the method of calculating the eigenfrequencies (it is the block Lanczos method [9, 10]

in the present paper) and imperfection of the FE mesh. We will further denote this split as "mathematical".

Out of all considered papers, thesis [11] provides the most detailed study of the resonator frequency split using FEM. The author notes that it is impossible to divide the "mathematical" (in [11] referred to as "parasitic") split from the one caused by manufacturing defects and proposes to minimize the value of the "mathematical" split by means of constructing a finite element mesh according to the author's methodology. However, just like the other indicated works, the thesis pays insufficient attention to the influence of the phase angle between the harmonics of various defects while investigating their simultaneous impact on the resonator frequency split. Noteworthy, the authors often describe a change in the wall thickness of the resonator as harmonic function with respect to the middle surface, while technologically, in the manufacturing process, the outside surface of the resonator is usually of better quality than that of the inside one. Therefore, describing the change of the thickness via a circumferential harmonic function with respect to coordinate surface of the resonator formed by the outside radius of the hemisphere is of certain interest as well.

The purpose of the present paper is to produce a finite-element model (FEM model) of the CVG resonator designed to determine the values of the operating eigenfrequency of the resonator with sufficient accuracy and verify a possibility of taking into account circumferentially varying thickness of the resonator wall in the frequency split calculations.

To build a FEM model, we used ANSYS Mechanical software [12]. In this paper, we considered two separate modeling problems:

calculation of the exact value of the operating eigenfrequency of the resonator;

estimation of the influence of various factors on the resonator operating eigenfrequency split, for example, circumferentially varying thickness.

Problem statement

The performed study originated from a problem of calculating the oscillation eigenfrequen-

cies of a thin hemispherical shell. It is appropriate to apply Hamilton's variational principle [13]:

$$\delta I =$$
$$= \delta \int_{t_0}^{t_1} L\left(q_1, \ldots, q_n,\ \dot{q}_1, \ldots, \dot{q}_n,\ t\right) dt = 0,$$

where δI is the change in the desired functional, $L = T - W$ (T, W are kinetic energy of the studied elementary volume of the shell and potential energy of elastic strains respectively).

We can write the kinetic and potential energy expressions in the general form as

$$T = \frac{1}{2}\int_{\sigma} \rho V^2 d\sigma,$$

$$W = \frac{1}{2}\int_{\sigma} \left(\sigma_{11}\varepsilon_{11} + \sigma_{22}\varepsilon_{22} + \sigma_{33}\varepsilon_{33} + \right.$$
$$\left. + \sigma_{12}\varepsilon_{12} + \sigma_{13}\varepsilon_{13} + \sigma_{23}\varepsilon_{23}\right) d\sigma,$$

where ρ, kg/cm^3, is the material density; $\mathbf{V}$, m/s^2, is the absolute velocity vector of an arbitrary point of the elastic body; σ_{11}, σ_{22}, σ_{33}, Pa, are normal stresses of the specified element of the elastic body; ε_{11}, ε_{22}, ε_{33} are the respective normal strains; σ_{12}, σ_{13}, σ_{23}, Pa, are shear stresses of the specified element of the elastic body; ε_{12}, ε_{13}, ε_{23} are the respective shear strains; σ, m^3, is the volume of the specified element of the elastic body.

The expressions for T and W applicable to the calculations of the resonator eigenfrequency can be found in a number of works; however, the expressions can differ in the fact that either stress or strain tensor components are neglected in them. Thus, in this work, in order to compare the expected frequency values obtained via FEM, we used the expressions in the formulation of the thin shell theory presented, in particular, in book [14]:

$$T = \frac{1}{2}\int_0^{2\pi}\int_0^{\frac{\pi}{2}} \rho h V^2 A_1 A_2 d\theta d\varphi,$$

$$W = \frac{Eh}{2\left(1-\nu^2\right)}\int_0^{2\pi}\int_0^{\frac{\pi}{2}} \left[\left(\varepsilon_1 + \varepsilon_2\right)^2 - \right.$$

$$\left. - 2\left(1-\nu\right)\left(\varepsilon_1\varepsilon_2 - \left(\frac{\omega}{2}\right)^2\right)\right] A_1 A_2 d\theta d\varphi + \rightarrow$$

$$\rightarrow + \frac{Eh^3}{24\left(1-\nu^2\right)}\int_0^{2\pi}\int_0^{\frac{\pi}{2}} \left[\left(\kappa_1 + \kappa_2\right)^2 - \right.$$

$$\left. - 2\left(1-\nu\right)\left(\kappa_1\kappa_2 - \tau^2\right)\right] A_1 A_2 d\theta d\varphi,$$

where h, m, is the thickness of the hemispherical shell; A_1, A_2 are Lamé parameters; ν is Poisson's ratio of the material; E, MPa, is the elastic modulus of the material; ε_1, ε_2 are parameters characterizing tensile strain of the mid-surface; κ_1, κ_2 are parameters characterizing bending strain of the mid-surface; ω, τ are parameters characterizing shear and torsional strains respectively; θ, φ, deg, — zenith and azimuth angles respectively.

The use of the Ritz method [15] reduces the eigenfrequencies problem to the algebraic eigenvalue problem:

$$\left(A - \lambda^2 B\right)\mathbf{C} = 0,$$

where A, B are matrices connected with the kinetic and potential matrices, as well as with the coordinate functions; $\mathbf{C}$ is a column-vector of unknown coefficients; λ is a column-vector of the eigenfrequencies values.

It is important to note that the relations in the shells theory formulation specified above comply with the main assumptions of the Kirchhoff – Love theory of thin shells [16]:

plane section normal to the mid-surface remains normal to the mid-surface after deformation;

normal stress along the axis normal to the mid-surface is not considered due to its smallness;

the thickness of the shell does not change during a deformation.

In addition, the calculation implies an assumption of small strains and, respectively, of neglecting the geometrical non-linearity.

The problem statement will further include not only Solid type elements, but also the Shell type elements. Modeling Shell type elements in ANSYS software also entails the abovementioned Kirchhoff – Love assumptions, with the exception of the first one. In this case, a defor-

mation-related change in the angle between the plane section and the mid-surface is admissible. This formulation corresponds to the Mindlin — Reissner shell variant [17], which is better known as Timoshenko shell in Russian literature [18].

Selection of optimal resonator FE models

The operation of the resonator is characterized by the numerical value of the operating eigenfrequency and the respective mode shape. The values of the eigenfrequency and the mode shape are defined by the following factors:

Dimensions of the resonator (radius and thickness of the hemisphere);

dimensions and mounting mode of the stem;

physical and mechanical properties of the selected material.

Traditionally, the CVG operation is based on coupled vibrations in two gyroscopically connected elliptical modes corresponding to its operating frequency [4, 19] (Fig. 2).

Nonideality of the geometrical parameters of the resonator entails a perturbation of the axial symmetry, which causes the splitting effect of its oscillation eigenfrequencies. The effect manifests itself in the non-ideal resonator spectrum obtaining two closely spaced frequencies instead of one with two close eigenmodes excitation, which leads to a change in the operation regime of the device and to an unacceptable reduction in accuracy [7]. Therefore, the developed FE model needs to possess an appropriate sensitivity level

to register the frequencies split corresponding to its admissible value for the product under study. In other words, to estimate the resonator characteristics which influence the accuracy parameters of CVG, we need to pay attention not only to finding the exact value of the oscillation eigenfrequency of the selected design, but more so to the dependence on the variation of its studied deviations from the ideal system.

Because of this, we propose applying various models to solve two separate problems: to find the exact operating eigenfrequency of the resonator oscillations and to determine how circumferentially varying thickness influence the frequency split value.

The required accuracy of the estimated eigenfrequency value (for the first problem) and the value of the frequency split depending on the defect dimensions (for the second problem) can serve as the criteria defining the quality of the developed models. Let us note that the accuracy of determining the eigenfrequency value of up to 1 Hz is sufficient for the primary analysis. We took the admissible error of the split calculation (for the second problem) equal to $1 \cdot 10^{-4}$ Hz, which is one order higher than the admissible value of frequency split for fused quarz hemispherical resonators after balancing.

Since we can use various types elements to build FE models, we compared the models built with some types of Shell and Solid elements. The objective was to find an optimal balance between
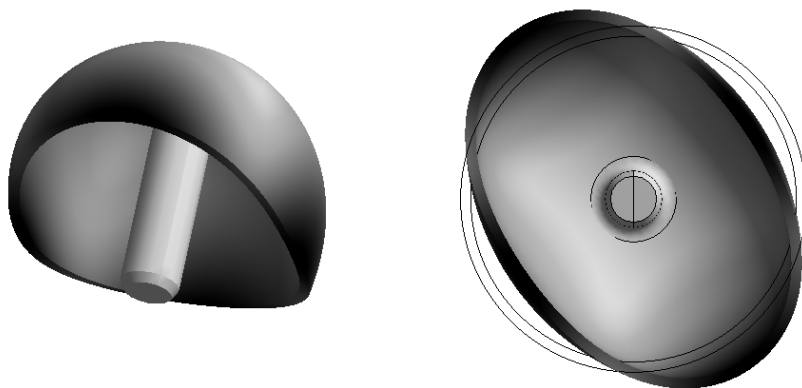
Fig. 2. Elliptical mode shape of the resonator corresponding to its operating frequency (two planes demonstrated, the second one illustrating the deviation from the circular mode shape in the oscillations plane)

the labor cost of the computation and its accuracy.

First model (FEM I). The hemisphere was meshed into SHELL181 type elements, i.e. into shell elements of the 1st order, which had 4 nodes with six degrees of freedom in each (linear translations in three axes and rotation about these axes);

Second model (FEM II). The hemisphere was meshed into SHELL281 type elements, i.e. into shell elements of the 2nd order, which had 8 nodes with six degrees of freedom in each (linear translations in three axes and rotation about these axes);

Third model (FEM III). The hemisphere was meshed into SOLID186 type elements, i.e. into solid elements of the 2nd order, which had 20 nodes with three degrees of freedom in each (linear translations in three axes);

Fourth model (FEM IV). The hemisphere was divided into SOLID187 type elements, i.e. into solid elements of the 2nd order, which had 10 nodes with three degrees of freedom in each (linear translations in three axes).

To improve the accuracy of the obtained results, we needed to meshed the initial geometry of the object into a regular finite-element mesh. Such a mesh is distinguished by its structured nature and the order of the predominantly regular-shaped elements used.

In all for FE models, we meshed the stem using SOLID185 elements of the 1st order to reduce the computational time, as the degree of meshing the resonator stem has no influence of the values of its eigenfrequencies corresponding to the second (elliptical) mode shape. We meshed the rounding area from the stem to the hemisphere using SOLID186 elements (Fig. 3). We should note that the absence of the indicated influence is due to the stem design, in particular, to its diameter and length. The chosen design parameters provide sufficient offset of the resonator frequencies caused by the bend of the stem from the operating elliptical frequency. In case of near values of the indicated frequencies, there may be negative effects considered in paper [20].

In the course of the calculations aimed at obtaining the model of the desired accuracy and minimal computational time, we set the minimal necessary number of the elements and nodes of the hemisphere. In case of shell models, the size
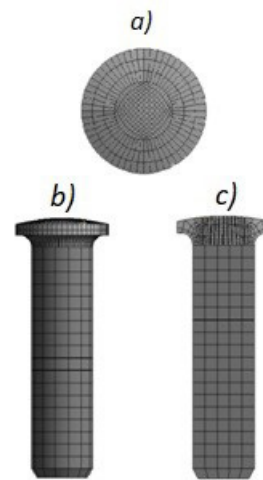
Fig. 3. Finite element mesh of rounding area (*a*) and resonator stem (*b*, *c*). Meshing into SOLID186 and SOLID185 elements respectively; *b*, *c* − the stem and its longitudinal section

of hemisphere elements varied in the range from 0.9000 to 0.1125 mm. The mesh of SHELL281 finite elements is shown in Fig. 4, *a*, *b*.

When studying the stress-strain state of the shell or plate type structural elements using SOLID type finite elements, to obtain acceptable result, we need to provide sufficient number of elements over the thickness in the FE model. Therefore, this paper considers different options of the model with the number of the elements over the thickness ranging from one to eight. Fig. 4, *c*, *d* shows an example of meshing the hemisphere into SOLID186 elements.

Fig. 5, 6 shows dependences of the resonator eigenfrequency values on the number of nodes employed in the models. The obtained diagrams help determine the optimal number of nodes which provide the value of Δ, the change on the value of the obtained solution with the growing number of nodes, less than 0.01%.

Analysis of the diagrams in Fig. 5 corresponding to the models with shell elements allows us to conclude that the value of the eigenfrequency sets at the level of 4808−4809 Hz. The diagrams are given for the model with the mid-surface as a reference plane. In FEM I, $\Delta = 0.005$ %, while in FEM II, II $\Delta = 0.006$ %. The difference of the obtained frequency values between two models reaches no more than 0.6 Hz. We can see here,

a)

b)

c)

d)
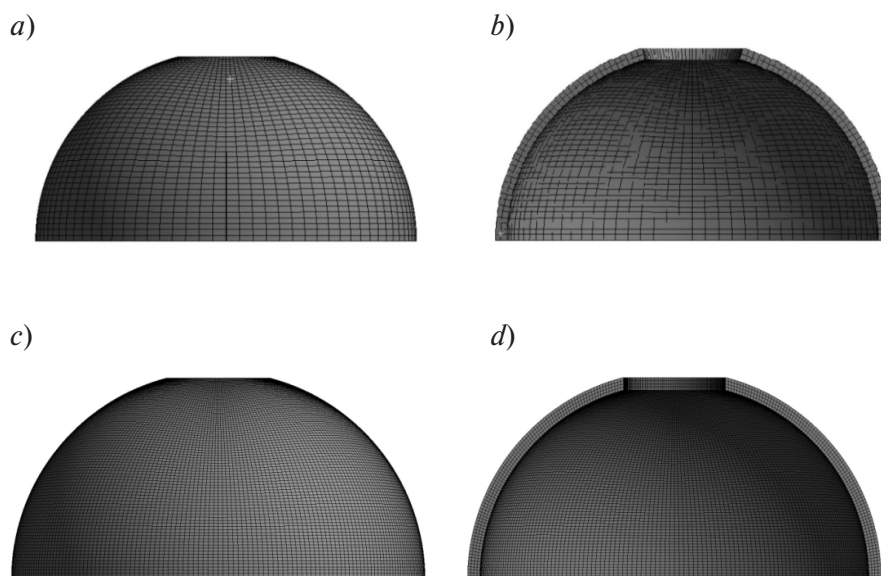
Fig. 4. Meshing of hemisphere (*a*, *c*) and its cross-section (*b*, *d*)
into SHELL281 (*a*, *b*) and SOLID186 (*c*, *d*) elements

a)

b)
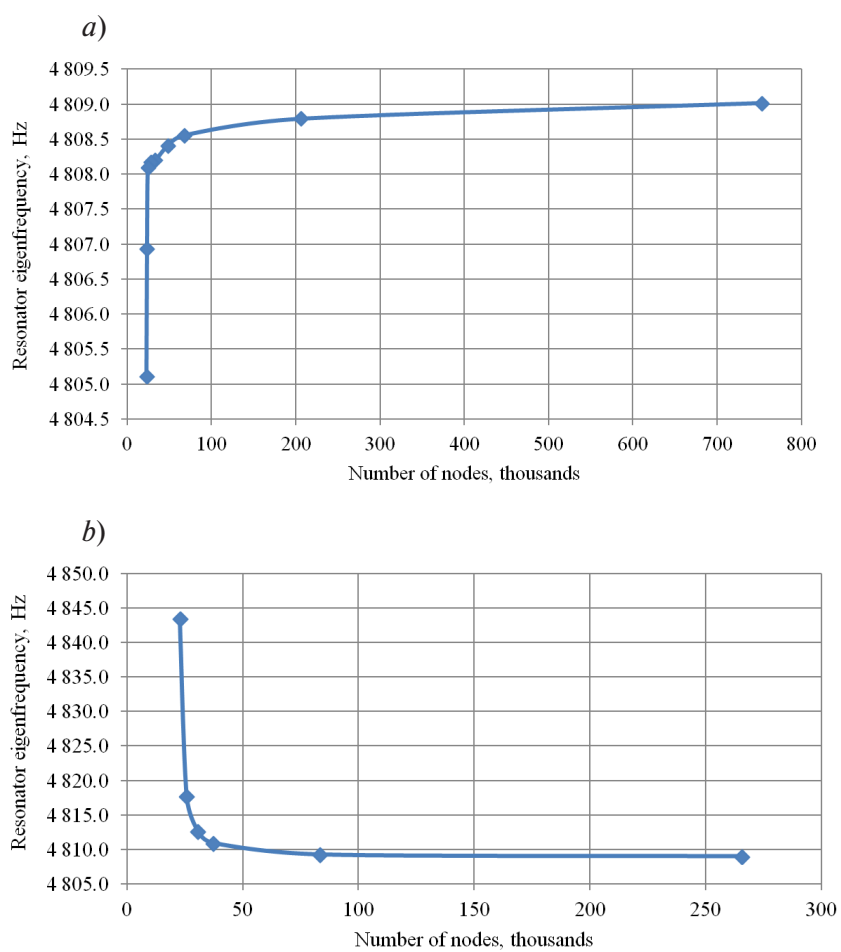
Fig. 5. Computational diagrams of resonator eigenfrequencies dependences on the number
of nodes applied in FEM I (SHELL281) (*a*) and FEM II (SHELL181) (*b*)

a)

b)
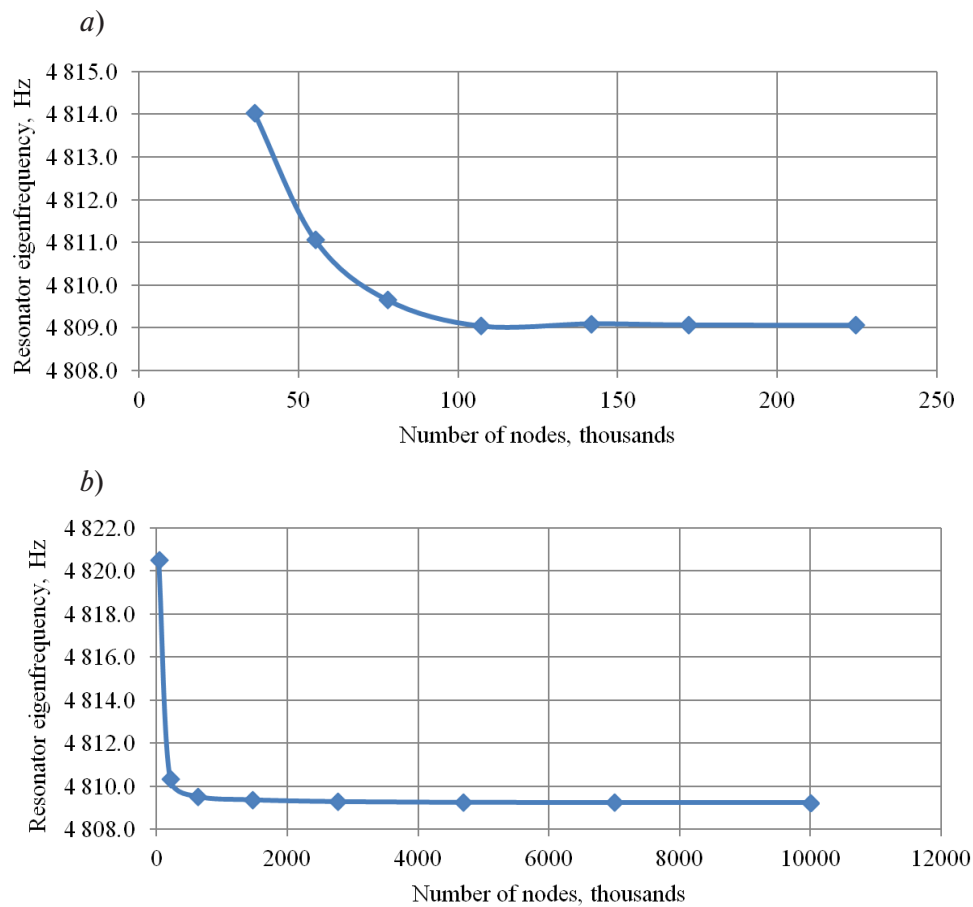
Fig. 6. Computational dependences similar to the ones in Fig. 5,
but for FEM III (SOLID186) (*a*) and FEM IV (SOLID187) (*b*)

that the use of the 2nd order elements (SHELL281) is preferable, as we need only 50 thousand nodes for the steady-state solution in this case, while no less than 83 thousand nodes are required for the 1st order elements.

Note that convergence of the results to the steady-state value of eigenfrequency in the models using shell elements occurs from different directions (from the highest/lowest value to the steady-state value). The problem with the SHELL181 type elements converges to a steady-state solution from the greater values, which corresponds to the classical behavior of the numerical problem convergence diagrams. However, the use of SHELL281 elements produces a reverse effect. This is probably due to the applied type of the contact interaction (SHELL-SOLID) of the hemisphere and the stem. The bodies contact along a line, which leads to local loading along the faces of solid elements. More-

over, if we exclude the stem from the model and apply a boundary condition like a fixed support along the corresponding face of the hemisphere, we can observe the "stiff" characteristic of the diagram for SHELL281 element as well.

Analysis of the solid model diagrams (Fig. 6) shows that the desired eigenfrequency value remains constant starting from a certain level of the model discretization. The difference of the obtained frequency values between SOLID186 and SOLID187 elements is no more than 0.6 Hz. The values of Δ, obtained from mesh convergence, were 0.0002 % in both FEM III and FEM IV. However, to obtain the results close in accuracy, we required 1.5 times more FEM nodes in case of SOLID187 elements. Because of this, it is feasible to apply SOLID186 for computations. In general, we can conclude that meshing into four elements over the thickness of the hemisphere wall is optimal for the eigenfrequencies analysis

providing the accuracy of up to 0.1 Hz. Note that for the primary estimate of the eigenfrequency values (up to 1 Hz accuracy), it is sufficient to divide the hemisphere thickness only into two elements. The difference from the steady-state solution in this case is 0.44 Hz.

Results of the operating resonator eigenfrequency calculations

Simultaneously with the finite elements methods, for a comparison we performed an analytical calculation using the simplified expressions for a hemisphere shell obtained by Rayleigh [21], and the Goldenweiser's thin shells theory [22] with specifications as to the tensile property of the mid-surface. The results of all the obtained values of the eigenfrequency in the second mode shape are given in Table 2.

Note that in the present paper, when comparing the obtained data, we took the result of the steady-state calculation using solid elements as the exact solution. This is due to the fact that the solid element models imply solving the elasticity theory problem without any simplifications. In addition, the accuracy of the result is defined by the degree of the model discretization and the mathematical error of the very method of solving the eigenvalues problem.

As we can see from Table 2, the result of determining the eigenfrequency of the resonator obtained using the considered shell and solid finite elements models shows comparable values. Moreover, among the calculation results obtained using analytical methods, the Goldenweiser's value is the most accurate one.

In the course of solving the second problem

set above, i.e. to determine the split of the resonator eigenfrequencies, we used SHELL281 (FEM I) type elements to analyze the influence of circumferentially varying thickness on the dynamic behavior of the resonator. The use of shell elements allows us to set the change in the thickness of the hemisphere quite easily with no changes of its geometry, as well as to reduce the estimated time while saving the sufficient accuracy of the calculations.

Influence of defects on the value of the operating resonator frequency split

Features of introducing various defects into the resonator FEM. To determine the split of the operating frequency of the resonator in the presence of any defect, we need to introduce a distribution function of this defect into the model. In a real resonator, the distribution of such defects as circumferentially varying thickness and inhomogeneous density over the azimuth or zenith angle is random. However, researchers often use a harmonic dependence of the defect distribution in modeling as the simplest in respect of calculations:

$$x(\alpha) = x_0 + X \cdot \sin(m\alpha + \beta),$$

where x_0, m, is the nominal value of the parameter (hemisphere thickness, material density); X, m, is the amplitude; m is the number of the defect harmonic; α, β, deg, are the initial angle and phase respectively.

The number of the harmonic is chosen arbitrarily depending on the simulated defect function; nonetheless, let us note that the fourth

Table 2
Values of the operating eigenfrequency of the resonator oscillations (second mode) calculated via different methods

Calculation method	Frequency, Hz
Rayleigh	5277.60
Goldenweiser's thin shells	4814.20
Finite elements SHELL type SOLID type	4809.02 4809.08
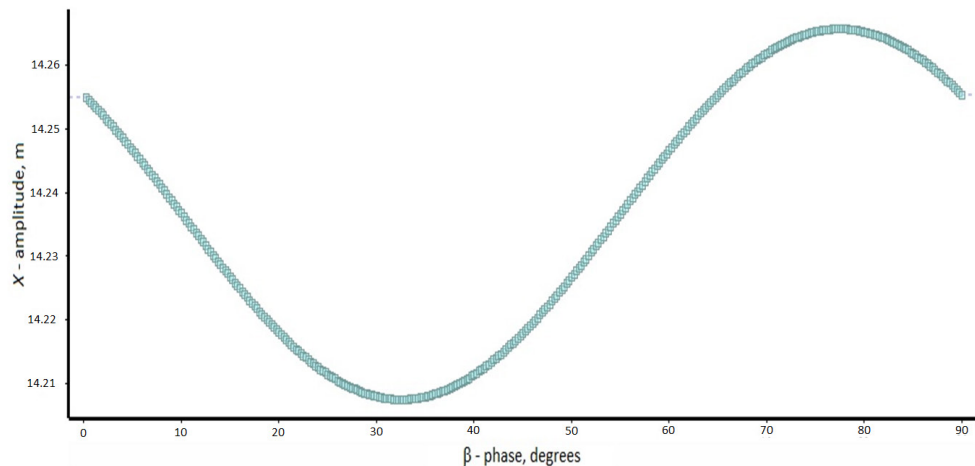
Fig. 7. Estimated dependence of the total operating frequency split
of the resonator on phase angle of the defect function

harmonic has the most influence on the split of resonator frequency, which corresponds to the elliptical mode shape. Sources [3, 19] describe the reason of the indicated influence in detail. At the same time, the harmonics different from the fourth one have one order less impact. Thus, to model the worst case of a defect affecting the frequency split, it is expedient to use the fourth harmonic of the defect distribution.

As it was mentioned before, when we employ FEM, a "mathematical" split occurs even in ideal geometry. It is important to note, that this "mathematical" split is a measurable (calculating) variable. The main reason of its emergence is the non-ideality of the finite element mesh. Therefore, when we are solving the eigenfrequency problem in the resonator model and introduce a defect $x(\alpha)$, we obtain a certain total split, with the "mathematical" split being one of its components.

Based on the assumption that the operating eigenfrequency under study is elliptical, and consequently, corresponds to the second harmonic, the "mathematical" split is represented in the form of the second harmonic as a component of the total split. Given the above, to determine the value of the split components, we need to find the phase shift of the harmonics with respect to each other. Note that if the harmonics representing the "mathematical" split and the defect distribution coincide, the total split is a sum of the values of the split of both of the defects, while in case of the antiphase, it a difference thereof. The indicated feature is apparent, for example, if we introduce the fourth harmonic of the defect with a change in the initial phase angle from 0° to 90° (Fig. 7).

In this figure, we plotted the total split value $\Sigma \Delta f$ along the vertical axis and the phase angle β along the horizontal axis. The phase angle of the extremums depends on the built mesh and is preserved with the change in the amplitude and the nature of the defect (the defect is caused by the manufacturing errors or heterogeneity of the material).

Calculation of the split value when adding a defect into the resonator FEM. One of the factors defining the eigenfrequency split effect in the resonator is mass unbalance of the sensory organ. In a real hemispherical resonator, the unbalanced mass is continuously distributed across the whole shell, which in case of excitation causes oscillations of its center of mass and leads to the split of the frequencies and reduction in the Q-factor due to the oscillation energies dissipation in supports. The mass unbalance itself is due to the above mentioned geometrical and physical errors, including circumferentially varying thickness and inhomogeneous density. Since applying FE models leads to emergence of the "mathematical" split, to calculate the component of the

introduced circumferentially varying thickness, we have to find the value of such split as well. It is possible, if we use a harmonic function as a defect (circumferentially varying thickness) distribution function:

$$h(\alpha) = h_0 + X_h \cdot \sin(m\alpha + \beta),$$

where h_0, m, is the nominal thickness of the resonator wall, X_h, m, is a half of the value of circumferentially varying thickness, α, deg, is an angular coordinate corresponding to the azimuth angle.

In this paper, to solve the problem of finding the resonator eigenvalues be means of ANSYS, the split of the operating frequency can be determined via the difference between two near frequencies corresponding to the elliptical mode shape. The calculation results in a certain total split of various defects, if they are introduced into the resonator FEM. In case of "ideal" geometry (absence of defects), the total split is equal to the "mathematical" split:

$$\sum \Delta f = \Delta f_m = f_{II}^{(2)} - f_{II}^{(1)},$$

where Δf_m, Hz, is the "mathematical" split; $f_{II}^{(2)}$, $f_{II}^{(1)}$, Hz, are the highest and lowest values of the eigenvalues defining the split.

If we introduce an additional defect into consideration, for example, circumferentially varying thickness, then the total split is determined as

$$\sum \Delta f = f_{II}^{(2)} - f_{II}^{(1)} =$$
$$= \Delta f_m \cdot \sin(2\alpha_1 + \beta_1) + \Delta f_h \cdot \sin(m\alpha_2 + \beta_2),$$

where Δf_h, Hz, is the split cause by circumferentially varying thickness; α_i, β_i, deg, are the angles and phases defining the defect distribution with respect to the azimuth angle.

The above relations show that unambiguous determination Δf_h required knowing the initial angles and phases of the harmonics corresponding to the defects. If we bear this in mind and use two extremal values of the total split value (when finding the harmonics in phase and antiphase), then we can compile a simple system of two equations allowing us to determine the splits from each defect:

$$\begin{cases} \sum \Delta f_{max} = \Delta f_h + \Delta f_m, \\ \sum \Delta f_{min} = \Delta f_h - \Delta f_m. \end{cases}$$

To automate the calculation of two extremal values of the total split in ANSYS, we can denote and as parameters, thus producing a diagram similar to the one presented in Fig. 7. Note that the found angle and phase corresponding to the "mathematical" split are maintained in the model even after a change in characteristics describing other defects, which excludes the need for additional calculation to provide the search for the extremal values of the total split. Therefore, using the block Lanczos method in ANSYS software allows us to determine the value of the split caused by circumferentially varying thickness by means of accounting for the "mathematical" split.

As an example of using the presented methodology of calculations, for the hemispherical resonator of the given design, we obtained numerical values of the splits caused by circumferentially varying thickness and inhomogeneous density (Table 1). Each effect was considered separately. The value of thickness variations amounted to 6 μm, the density of the fused quartz was ranging within 2200−2220 kg/cm³. The defects function is represented in a form of the fourth harmonic.

As a result, the obtained values are limited by the applied method of numerical calculation and simplifications accepted in the mathematical model of the shell for the SHELL281 type finite elements.

In the process of the study, we noted a number of features. For example, when adding a density defect into the FEM, we established that the value of the "mathematical" split changes in proportion to the average arithmetical value of frequencies $f_{II}^{(1)}$ and $f_{II}^{(2)}$, which allows calculating the "mathematical" split value not only in the course of the computations, when the harmonics are in phase/antiphase. This does not eliminate the need for finding the extremal values of the total split for a newly developed FEM. At the same time, we do not observe any similar

73

Table 3

Results of calculating the operating resonator frequency split

Set defect function	Split, Hz
$\rho(\alpha) = 2210 + 10 \cdot \sin 4\alpha$	7.7193
$h(\alpha) = 9 \cdot 10^{-4} + 3 \cdot 10^{-6} \cdot \sin 4\alpha$	6.4881

dependence for a change, for example, in the thickness of the hemisphere or the elastic modulus of the material. Thus, seeking the dependence of the split on the defects changing the generated stiffness matrix of the FEM requires finding the new value of the "mathematical" split at each change as well.

Conclusion

The presented research produced finite element models (FEMs) including various types of elements, which can be used in the studies of resonator operation dynamics. We established that to determine the eigenfrequencies of a hemispherical resonator with elliptical oscillations, the use of SHELL281 elements is preferable, as it provides an optimal computational time/accuracy ratio. In addition, FEMs using the indicated elements and the methods described and tested in this paper are handy in the studies on the influence various defects exert on the resonator operation.

Sensitivity of shell elements to the circumferentially varying thickness is apparently limited by the error of the numerical calculation method; its estimation transcends the scope of this article. The described methodology allows studying a frequency split caused by the uneven distribution of the material properties (density, elastic modulus, Poisson's ratio), as well as circumferentially varying thickness of the inside, outside, and middle surface of the hemisphere using standard functions of the ANSYS Mechanical software package.

The paper notes the importance of taking into account the phase of the functions describing the defects distribution due to the presence of the "mathematical" split in any FEM caused by the calculation method error and asymmetry of the finite element mesh.

REFERENCES

1. **Peshehonov V.G.,** Perspektivy giroskopii [The prospects for gyroscopy], In the book: Proceedings of the 13-th All-Russian Conference on the Management Problems "VSPU-2019", Publication of Institute of Control Sciences RAS, Moscow (2019) 36−38 (in Russian).

2. **Dzhashitov V.E., Pankratov V.M., Golikov A.V.,** Obshaya i prikladnaya teoriya giroskopov s primeneniem komputernih tehnologii [The general and applied theories of gyroscopes using computer technology], Edited by Peshehonov V.G., Publication of State Research Center of the Russian Concern CSRI "Electropribor", St. Petersburg, 2010 (in Russian).

3. **Zhuravlev V.F., Klimov D.M.,** Volnovoi tverdotelnii giroskop [The solid-state wave gyro], Moscow, "Nauka" Publ., 1985 (in Russian).

4. **Lunin B.S., Matveev V.A., Basarab M.A.,** Volnovoi tverdotelnii giroskop. Teoriya I tecnologiya [The solid-state wave gyro. The theory and technology], "Radiotechnika" Publ., Moscow, 2014 (in Russian).

5. **Naraykin O.S., Sorokin F.D., Kozubnyak S.A.,** Rasheplenie sobstvennih chastot kolcevogo resonarota tverdotelnogo volnovogo gyroscopa, vizvannoe vozmushcheniem formy [Splitting of natural frequencies of a ring resonator of the solid-state gyro due to form perturbation], Herald of the

Bauman Moscow State University, Machinery. (6) (2012) 176−185 (in Russian).

6. **Heidari A., Chan M., Yang H., et al.,** Hemispherical wineglass resonators fabricated from the microcrystalline diamond, Journal of Micromechanics and Microengineering. 23 (12) (2013) 125016−125023.

7. **Kozubnyak S.A.,** Splitting of natural frequencies of cylindrical resonator gyro due to non-ideal shape, Herald of the Bauman Moscow State University, Machinery. (3 (102)) (2015) 176−185 (in Russian).

8. **Vahlyarskiy D.S., Guskov A.M., Basarab M.A., Matveev V.A.,** Numerical study of differently shaped HRG resonators with various defects, Science & Education of the Bauman MGTU. Electronic Journal. (10) (2016) 1−22 (in Russian).

9. Ansys®MechanicalTM, Release 14.5, Help System, Mechanical APDL, Structural Analysis guide, Modal Analysis, ANSYS, Inc.

10. **Druskin V.L., Knizhnerman L.A.,** Error bounds in the simple Lanczos procedure for computing functions of symmetric matrices and eigenvalues, Computational Mathematics and Mathematical Physics. 31 (7) (1991) 20−30.

11. **Vahlyarskiy D.S.,** Optimizatsiya formy rezonatora volnovogo tvyordotelnogo giroskopa po kriteriyu minimuma rasshchepleniya sobstvennykh chastot [Optimizing the resonator shape of solid-state wave gyro according to the criterion of minimum splitting of eigenfrequency], PhD Thesis, Bauman State Technical University, Moscow, 2019 (in Russian).

12. Ansys®MechanicalTM, Release 14.5.

13. **Goldstein H.,** Classical mechanics, Addison-Wesley, USA, 1951.

14. **Novozhilov V.V., Radok J.M.R. (**Eds.), Thin shell theory, Springer Netherlands, 1964.

15. **Babakov I.M.,** Teoriya kolebaniy [The theory of vibrations], Nauka, Moscow, 1968 (in Russian).

16. **Kirchhoff G.,** Vorlesungen über mechanic, Publisher B.G. Teubner, Leipzig, 1824.

17. Ansys®MechanicalTM, Release 14.5, Help System, Mechanical APDL, Element Reference, ANSYS, Inc.

18. **Timoshenko S., Woinowky-Krieger S.,** Theory of plates and shells, 2nd Ed., McGraw-Hill Book Company, inc., New York, Toronto, London, 1959.

19. **Matveev V.A., Lipatnikov V.I., Alekhin A.V.,** Proektirovanie volnovogo tverdotelnogo gyroscopa [Design of a solid-state gyroscope], Bauman MSTU Publ., Moscow, 1997 (in Russian).

20. **Kireenkov A.A.,** Calculation of the spectrum of a hemisphere on a leg, Mechanics of Solids. A Journal of RAS. 33 (4) (1998) 19−24.

21. **Strutt J.W. (3**rd **Baron Rayleigh),** The theory of sound, Vol. II, Macmillan, London, 1896.

22. **Goldenweiser A.L.,** Theory of thin elastic shells, Int. Ser. of Monograph in Aeronautics and Astronautics, Pergamon Press, New York, 1961.

THE AUTHORS

SHEVCHENKO Sergei A.
JSC "Command Devices Research Institute"
16, Tramvaynyy Ave., St. Petersburg, 198216, Russian Federation
shevchenko.sergei.a@yandex.ru

KONOTOPOV Oleg I.
JSC "Command Devices Research Institute"
16, Tramvaynyy Ave., St. Petersburg, 198216, Russian Federation
konotopov96@gmail.com

СПИСОК ЛИТЕРАТУРЫ

1. **Пешехонов В.Г.** Перспективы гироскопии // Сборник трудов XIII Всероссийского совещания по проблемам управления ВСПУ-2019. М.: Изд. Института проблем управления им. В.А. Трапезникова РАН, 2019. С. 36−38.

2. **Джашитов В.Э., Панкратов В.М., Голиков А.В.** Общая и прикладная теория гироскопов с применением компьютерных технологий. Под ред. В.Г. Пешехонова. СПб.: Изд. ЦНИИ «Электроприбор», 2010. 154 с.

3. **Журавлев В.Ф., Климов Д.М.** Волновой твердотельный гироскоп. М.: Наука, 1985. 125 с.

4. **Лунин Б.С., Матвеев В.А., Басараб М.А.** Волновой твердотельный гироскоп. Теория и технология. М.: Радиотехника, 2014. 176 с.

5. **Нарайкин О.С., Сорокин Ф.Д., Козубняк С.А.** Расщепление собственных частот кольцевого резонатора твердотельного волнового гироскопа, вызванное возмущением формы // Вестник МГТУ им. Н.Э. Баумана. Сер. Машиностроение. 2012. Спец. выпуск № 6 «Современные проблемы прикладной механики, динамики и прочности машин». С. 176−185.

6. **Heidari A., Chan M., Yang H., Jaramillo G., Taheri-Tehrani P., Fonda P., Najar H., Yamazaki K., Lin L., Horsley D.** Hemispherical wineglass resonators fabricated from the microcrystalline diamond // Journal of Micromechanics and Microengineering. 2013. Vol. 23. No. 12. Pp. 125016−125023.

7. **Козубняк С.А.** Расщепление собственных частот колебаний цилиндрического резонатора волнового твердотельного гироскопа, вызванное возмущением формы // Вестник МГТУ им. Н.Э. Баумана. Сер. Приборостроение. 2015. № 3 (102). С. 39−49.

8. **Вахлярский Д.С., Гуськов А.М., Басараб М.А., Матвеев В.А.** Численное исследование резонаторов ВТГ различной формы при наличии дефектов различного типа // Наука и образование. Электронное научное издание МГТУ им. Н.Э. Баумана. 2016. № 10. С. 1−22.

9. Ansys®MechanicalTM, Release 14.5, Help System, Mechanical APDL, Structural Analysis guide, Modal Analysis, ANSYS, Inc.

10. **Друскин В.Л., Книжнерман Л.А.** Оценки ошибок в простом процессе Ланцоша при вычислении функции от симметричных матриц и собственных значений // Журнал вычислительной математики и математической физики 1991. Т. 31. № 7. С. 970−983.

11. **Вахлярский Д.С.** Оптимизация формы резонатора волнового твердотельного гироскопа по критерию минимума расщепления собственных частот. Дис. ... канд. физ.-мат. наук. Специальность 01.02.06: Динамика, прочность машин, приборов и аппаратуры. М.: Московский государственный технический университет имени Н.Э. Баумана, 2019. 197 с.

12. Ansys®MechanicalTM, Release 14.5.

13. **Голдстейн Г.** Классическая механика. Пер. с англ. М.: Наука. Гл. редакция физико-математической литературы, 1975. 413 с.

14. **Новожилов В.В.** Теория тонких оболочек. Ленинград: Судпромгиз, 1962. 431 с.

15. **Бабаков И.М.** Теория колебаний. М.: Гостехиздат, 1958. 628 с.

16. **Кирхгоф Г.** Механика. Лекции по математической физике. Пер. с нем. М.: Изд-во АН СССР, 1962. 392 с.

17. Ansys®MechanicalTM, Release 14.5, Help System, Mechanical APDL, Element Reference, ANSYS, Inc.

18. **Тимошенко С.П., Войновский-Кригер С.** Пластинки и оболочки. Пер. с англ. М.: Физматгиз, 1963. 635 с.

19. **Матвеев В.А., Липатников В.И., Алехин А.В.** Проектирование волнового твердотельного гироскопа. М.: Изд-во МГТУ им. Н.Э. Баумана, 1998. 168 с.

20. **Киреенков А.А.** Расчет спектра полусферы на ножке // Известия РАН. Механика твердого тела. 1998. № 4. С. 23−29.

21. **Дж.В. Стретт (Лорд Рэлей).** Теория звука. Т. 2. Пер. с англ. М.: ГТТЛ, 1955. 474 с.

22. **Гольденвейзер А.Л.** Теория упругих тонких оболочек. М.: Наука, 1976. 512 с.

СВЕДЕНИЯ ОБ АВТОРАХ

ШЕВЧЕНКО Сергей Александрович — *начальник сектора АО «НИИ командных приборов», Санкт-Петербург, Российская Федерация.*

198216, Российская Федерация, г. Санкт-Петербург, Трамвайный пр-т, 16

shevchenko.sergei.a@yandex.ru

КОНОТОПОВ Олег Игоревич — *инженер-конструктор АО «НИИ командных приборов», Санкт-Петербург, Российская Федерация.*

198216, Российская Федерация, г. Санкт-Петербург, Трамвайный пр-т, 16

konotopov96@gmail.com

Nuclear physics

OPTIMIZATION OF THE COPPER-64 PRODUCTION FROM NATURAL NICKEL TARGET AT A CYCLOTRON

A. Tiba, Ya.A. Berdnikov

Peter the Great St. Petersburg Polytechnic University,
St. Petersburg, Russian Federation

The paper is devoted to the problem of the copper-64 isotope production engineering that is important for application in the nuclear medicine. The production is carried out by proton irradiation of a nickel target (a natural mixture of isotopes). For this purpose, the energy dependence of the protons-nickel target interaction cross-sections, protons with initial kinetic energies of $10-15$ MeV in this case, has been analyzed. Besides, the half-lives of the resulting isotopes were considered. Based on the analysis, the optimal conditions (the proton beam energy and the waiting time after irradiation) for obtaining the ^{64}Cu isotope from natural nickel were found. It was established that under conditions close to ideal, it could be expected that ^{64}Cu radionuclide purity would be very high and reach at least 99 %. Ideal conditions mean complete separation of nickel and cobalt isotopes from the required copper one.

Keywords: copper-64 isotope, cyclotron irradiation, nickel target, radionuclide purity, yield calculation

ОПТИМИЗАЦИЯ ПОЛУЧЕНИЯ ИЗОТОПА МЕДИ-64 ИЗ ПРИРОДНОГО НИКЕЛЯ НА ЦИКЛОТРОНЕ

А. Тиба, Я.А. Бердников

Санкт-Петербургский политехнический университет Петра Великого,
Санкт-Петербург, Российская Федерация

Статья посвящена проблеме разработки технологии получения изотопа ^{64}Cu, важного для применения в ядерной медицине, путем циклотронного облучения протонами мишени из природного никеля. С этой целью проанализирована энергетическая зависимость сечений взаимодействия протонов, обладающих начальной кинетической энергией $10 - 15$ МэВ, с мишенью из никеля (природная смесь изотопов). Кроме того, рассмотрены величины периодов полураспада образующихся изотопов. На основе проведенного анализа определены оптимальные условия получения изотопа ^{64}Cu (энергия пучка протонов и время выдержки после облучения) из природного никеля. Установлено, что в условиях, близких к идеальным (случай полного отделения изотопов никеля и кобальта от требуемого изотопа меди) можно ожидать, что радионуклидная чистота изотопа ^{64}Cu будет очень высокой и достигать не менее 99 %.

Ключевые слова: изотоп меди-64, циклотронное облучение, никелевая мишень, радионуклидная чистота, расчет выхода

Introduction

It is well known that the ^{64}Cu isotope undergoes radioactive transformation as a result of three processes: positron and electron decay, and electron capture. This isotope emits β^+, β^- particles (their energies are 0.65 and 0.57 MeV, respectively, and the yields are 17.6 and 38.5%) with a half-life of 12.7 h. It plays an important role among bifunctional radioisotopes for both positron emission tomography (PET) and radionuclide therapy. The half-life of ^{64}Cu allows producing this isotope at regional or national cyclotron facilities, distributing it to local nuclear medicine departments with a loss of no more than one (approximately) half-life [1, 2].

Furthermore, the half-life of the ^{64}Cu isotope is compatible with the time scales required for administering a radiopharmaceutical (containing a molecular carrier: peptides, antibodies, nanoparticles, etc.), so that it is subsequently distributed and accumulated over the patient's body.

The ^{64}Cu isotope is better suited for high-resolution PET imaging than for therapy due to its low average energy of β^+ particles (278 keV) and very low intensity of accompanying gamma radiation (1345.77 keV, with the yield of 0.475%). At the same time, its average energy of β^- particles is convenient for radionuclide therapy of small tumors [1, 2].

The ^{64}Cu isotope has numerous advantages over such PET isotopes as ^{18}F (its half-life is $t_{1/2} = 109.8$ min) and ^{11}C ($t_{1/2} = 20.4$ min) currently used in clinical practice. Since the half-lives of both ^{18}F and ^{11}C are relatively short, these isotopes are usually prepared at cyclotrons located near clinics.

The ^{64}Cu isotope can be produced in the reactor by either the thermal neutron capture reaction ^{63}Cu$(n,\gamma)^{64}$Cu or the fast neutron reaction 64Zn$(n,\gamma)^{64}$Cu. However, the yields of the reactions producing ^{64}Cu in a nuclear reactor are low [3].

It should be noted that two cyclotron methods are currently used to produce ^{64}Cu isotope. One of them uses the ^{64}Ni isotope as a target, and the other the ^{68}Zn isotope.

Producing the ^{64}Cu isotope by the ^{68}Zn$(p,\alpha n)^{64}$Cu reaction using protons provides certain benefits, since in this case it is possible to simultaneously produce the

$$^{67}\text{Ga}(^{68}\text{Zn}(p,2n)^{67}\text{Ga})$$

and

$$^{64}\text{Cu}(^{68}\text{Zn}(p,\alpha n)^{64}\text{Cu}),$$
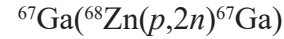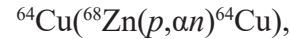
isotopes used in medicine from the same target [5].

However, this method comes with several drawbacks:

firstly, a cyclotron with a higher energy of 30 MeV is required;

secondly, complex radiochemical separation is necessary;

thirdly, production of the isotopes generates highly contaminated waste from several radionuclide impurities;

fourthly, the yield of ^{64}Cu isotopes is small, since the reaction cross section is low (about 20 mb at a proton energy of 30 MeV) [5, 6].

As noted above, ^{64}Cu isotope can be obtained by the ^{64}Ni$(p,n)^{64}$Cu reaction with both natural and nickel targets enriched with the ^{64}Ni isotope, using protons with a relatively low energy, 10 MeV (this is considerably below 30 MeV). The drawback of using a ^{64}Ni-enriched target is that the ^{64}Ni isotope is very expensive [4].

Relatively cheap targets made of natural nickel seem to be more attractive, but the disadvantage in this case is that the content of the ^{64}Ni isotope in the target is low, and, consequently, the production efficiency is insufficiently high; moreover, large amounts of other impurities are generated during irradiation, so complex chemical procedures are required for separating these impurities and isolating ^{64}Cu [5].

However, these difficulties can be largely overcome by selecting the correct initial proton energy corresponding to the maximum cross section for the ^{64}Ni$(p,n)^{64}$Cu reaction (647 mb at an energy of 10.5 MeV [11]) and optimizing the waiting time after irradiation.

The goal of this study consists in analysis and optimization of producing the ^{64}Cu isotope from natural nickel using protons with energies of

10 − 15 MeV at the MGC-20 cyclotron at Peter the Great St. Petersburg Polytechnic University.

Method for analyzing the yield of isotopes in a nickel target (natural mixture) irradiated with a proton beam at energies of 10−15 MeV

As noted above, a proton beam with energies of 10 − 15 MeV can be used to obtain the ^{64}Cu isotope. The target is a natural mixture of nickel isotopes: ^{58}Ni (68%), ^{60}Ni (26%), ^{61}Ni (1.14%), ^{62}Ni (3.71%) и ^{64}Ni (0.926%) [7].

Protons with energies of 10−15 MeV can induce various nuclear reactions in the target on different isotopes of nickel, generating different isotopes as by-products that can interfere with the process of separating the ^{64}Cu isotope from the resulting isotope mixture, and determining the amount of ^{64}Cu produced by spectroscopic methods.

It follows from the above that it is useful to know the total yield of each isotope produced in different reactions (see Table 1) and compare it with the yield of the ^{64}Cu isotope. The isotopes produced in the target through irradiating a natural mixture of nickel isotopes with protons are given in Table 1 [8 − 12].

Isotope yields for a natural mixture of nickel isotopes irradiated by protons can be determined accounting for the energy losses to excitation and ionization for protons passing through the target material [13]:

$$\left\langle -\frac{dE}{dx} \right\rangle = \frac{4\pi}{m_e c^2} \frac{nz^2}{\beta^2} \left(\frac{e^2}{4\pi\varepsilon_0} \right)^2 \left[\ln \left(\frac{2m_e c^2 \beta^2}{I} \right) \right], \quad (1)$$

where $-dE/dx$, MeV/cm, are specific ionization losses (x is the proton penetration depth); z is the charge number of the bombarding particle; m_e, g, is the electron mass; e, Cl, is the electron charge; c, cm/s, is the speed of light; β is the ratio of the speed of the bombarding particle to the speed of light ($\beta = v/c$); I, eV, is the mean ionization potential; ε_0, F/m, is the electrical constant; n, cm^{-3}, is the electron concentration of the target,

$$n = \frac{N_A Z \rho}{A M_u};$$

N_A, 1/mol, is the Avogadro constant; ρ, g/ m^3, is the target density; Z is the charge number of the target; A is the atomic mass; M_u, g/mol, is the molar mass.

The mean ionization potential of nickel is, like the mean ionization potential for other elements, $I = 328 \pm 10$ eV [14].

Eq. (1) is simplified in the nonrelativistic case $\beta^2 << 1$, where the proton is a bombarding particle ($z = 1$):

$$\left\langle -\frac{dE}{dx} \right\rangle = \left(\frac{144\rho Z z^2}{AE} \right) \ln \left[\frac{2179E}{I} \right]. \quad (2)$$

The solution to Eq. (2) gives the dependence $E(x)$ for the mean proton energy E on their penetration depth x.

The production of all isotopes at different depths in the target is found by the following formula [15]:

$$\frac{dN_i}{dx} = \left(\frac{Jn_f}{\lambda e} \right) \left(1 - \exp\left(-t_{rad}\lambda \right) \right) \sigma(x), \quad (3)$$

where N_i, cm^{-3}, is the number of atoms of type i of the radioisotope produced; J, A, is the cyclotron current; n_f is the concentration of nickel isotope nuclei in natural nickel; λ, s^{-1}, is the decay constant of the radionuclide produced; t_{rad}, s, is the target irradiation time.

Integrating distribution (3) from zero to target thickness τ, we obtain the dependence for the radioisotopes produced in target on thickness τ:

$$N_i\left(\tau, t_{rad} \right) = \int_0^\tau dx \left\{ \frac{dN_i}{dx} \right\}. \quad (4)$$

The decrease in proton flux with depth, as well as other processes removing protons from the

Table 1

**Characteristics of isotopes produced in the target
made of natural mixture of nickel isotopes irradiated
with protons _p_ as a result of nuclear reactions [8 − 12]**

Isotope	Half-life	Nuclear reaction	E_{thr}, MeV	σ, mb, at	
				15 MeV	10 MeV
^{55}Co	17.5 h	^{58}Ni(_p_,α)	1.36	35.7	8.7
^{57}Co	271.74 days	^{58}Ni(_p_,2_p_)	8.3	149.3	4.9
		^{58}Ni(_p_, _p_ + n)^{57}Ni→ ^{57}Co	12.3		
		^{60}Ni(_p_,α)	0.3		
		^{61}Ni(_p_, _n_ + α)	8.2		
		^{62}Ni(_p_, 2_n_ + α)	18.9		
		^{58}Ni(_p_,d)	10.0		
^{58}Co	70.86 days	^{61}Ni(p,α)	0.7	0.88	0.78
		^{62}Ni(p,α + _n_)	10.3		
^{57}Ni	35.6 h	^{58}Ni(_p_, _p_ + n)	12.4	8.8	–
		^{58}Ni(_p_,d)	10.1		
^{60}Cu	23.7 min	^{64}Ni(_p_,n)	7.0	58.8	79.8
^{61}Cu	3.3 h	^{61}Ni(_p_,n)	3.1	186	472
		^{62}Ni(_p_,2_n_)	13.0		
^{62}Cu	9.67 min	^{62}Ni(_p_,n)	5.0	359.3	498.9
^{64}Cu	12.7 h	^{64}Ni(_p_,n)	2.5	206.0	647.0

N o t a t i o n s: E_{thr} is the threshold reaction energy, σ is the reaction cross section (for two values of the initial kinetic energy of the proton beam).

beam can be neglected in this case.

Eqs. (2), (4) and the values of the reaction cross section σ (see Table 1) were used to determine the activity of each isotope for protons with initial kinetic energies of 15 (Fig. 1, _a,b_) and 10 MeV (Fig. 1, _c,d_), cyclotron current of 2 μA, and a target made of natural nickel. Fig. 1 shows the computational results for the activity of the ^{55}Co and ^{64}Cu isotopes for targets of various thicknesses and various irradiation times.

Considering Fig. 1, we can see that a sufficient target thickness for an initial proton energy of 15 MeV is 400 μm: the dependence of the activity accumulated on the target thickness disappears at this value. This value is 200 μm for an initial energy of 10 MeV.

The activity of each isotope after the end of irradiation and after different waiting times was calculated by the equation

$$A_t = A_0 \exp(-\lambda t), \qquad (5)$$

where A_0, s^{-1}, is the isotope activity at $t = 0$; A_t, s^{-1}, is the isotope activity after waiting time t, s; λ, s^{-1}, is the isotope decay constant.

The computed activities and ratios of the activities of the produced isotopes to the activities of the ^{64}Cu isotope produced for different waiting times after the end of irradiation are given in Table 2 (target irradiation time is 1.5 h, $E = 15$ and 10 MeV, cyclotron current is 2 μA).

After the nickel target (natural mixture of isotopes) was irradiated, the ^{64}Cu isotope had to be separated from the target. This is typically achieved by the well-known method of ion-exchange chromatography with a resin column (Dowex1-8X [1] or AG1-X8 [16]). Since some radioisotopes with a short half-life are produced in the target during irradiation (see Table 1), it is

**Comparison of the activity values of isotopes produced in the target
made of a natural mixture of nickel isotopes irradiated with protons as a result of nuclear reactions**

Isotope	Activity A_t, s^{-1} $\left(\text{Ratio } A_t \big/ A_t \, ^{64}\text{Cu}\right)$						
	$t = 0$	$t=9.67$ min	$t=23.7$ min	$t=3.3$ h	$t=12.7$ h	$t=17.5$ h	$t=50$ h
Initial kinetic energy of proton beam: 15 MeV							
^{55}Co	$2.5 \cdot 10^7$ (2.3)	$2.4 \cdot 10^7$ (2.4)	$2.4 \cdot 10^7$ (2.5)	$2.1 \cdot 10^7$ (2.3)	$1.5 \cdot 10^7$ (2.8)	$1.2 \cdot 10^7$ (2.85)	$3.4 \cdot 10^6$ (4.8)
^{57}Co	$2.3 \cdot 10^5$ (0.02)	229996 (0.02)	229990 (0.02)	229919 (0.02)	229698 (0.04)	229572 (0.05)	229781 (0.32)
^{58}Co	17500 (0,002)	17498 (0.002)	17497 (0.002)	17476 (0.001)	17409 (0.003)	17375 (0.004)	17147 (0.02)
^{57}Ni	$4.15 \cdot 10^5$ (0.04)	413699 (0.04)	413819 (0.038)	389166 (0.04)	324061 (0.06)	295139 (0.07)	156722 (0.22)
^{60}Cu	$6.0 \cdot 10^8$ (54.5)	$4.5 \cdot 10^8$ (45.0)	$3.0 \cdot 10^8$ (28.0)	$1.8 \cdot 10^6$ (0.19)	–	–	–
^{61}Cu	$3.7 \cdot 10^7$ (3.4)	$3.5 \cdot 10^7$ (3.5)	$3.4 \cdot 10^7$ (3.2)	$1.8 \cdot 10^7$ (1.9)	$2.5 \cdot 10^6$ (0.5)	$9.3 \cdot 10^5$ (0.2)	1024 (0.001)
^{62}Cu	$5.7 \cdot 10^8$ (51.8)	$2.8 \cdot 10^8$ (28)	$1.0 \cdot 10^8$ (9.3)	–	–	–	–
^{64}Cu	$1.1 \cdot 10^7$ (1.0)	$1.09 \cdot 10^7$ (1.0)	$1.07 \cdot 10^7$ (1.0)	$9.1 \cdot 10^7$ (1.0)	$5.4 \cdot 10^6$ (1.0)	$4.2 \cdot 10^6$ (1.0)	$7.0 \cdot 10^5$ (1.0)
Initial kinetic energy of proton beam: 10 MeV							
^{55}Co	$2.4 \cdot 10^6$ (0.30)	$2.4 \cdot 10^6$ (0.32)	$2.3 \cdot 10^6$ (0.30)	$2.1 \cdot 10^6$ (0.30)	$1.5 \cdot 10^6$ (0.40)	$1.2 \cdot 10^5$ (0.40)	$3.3 \cdot 10^5$ (0.66)
^{57}Co	12500 (0.001)	12499 (0.001)	12499 (0.001)	12495 (0.001)	12483 (0.003)	12476 (0.004)	12433 (0.02)
^{58}Co	5500 (0.0007)	5499 (0.0007)	5499 (0.0007)	5492 (0.0008)	5471 (0.001)	5460 (0.001)	5389 (0.01)
^{60}Cu	$1.8 \cdot 10^8$ (24.0)	$1.3 \cdot 10^8$ (17.5)	$9.0 \cdot 10^7$ (12.3)	$5.5 \cdot 10^5$ (0.08)	–	–	–
^{61}Cu	$2.2 \cdot 10^7$ (2.90)	$2.1 \cdot 10^7$ (2.83)	$2.0 \cdot 10^7$ (2.74)	$1.1 \cdot 10^7$ (1.70)	$1.5 \cdot 10^6$ (0.4)	$5.5 \cdot 10^5$ (0.2)	609 (0.001)
^{62}Cu	$2.9 \cdot 10^8$ (38.6)	$1.4 \cdot 10^8$ (19.0)	$5.3 \cdot 10^7$ (7.3)	–	–	–	–
^{64}Cu	$7.5 \cdot 10^6$ (1.0)	$7.4 \cdot 10^6$ (1.0)	$7.3 \cdot 10^6$ (1.0)	$6.3 \cdot 10^6$ (1.0)	$3.7 \cdot 10^6$ (1.0)	$2.8 \cdot 10^6$ (1.0)	$0.5 \cdot 10^6$ (1.0)

N o t e s. 1. The values are given for the activities A_t of the isotopes produced, as well as the ratios of A_t to the corresponding activities of the ^{64}Cu isotope produced (in brackets)) for different waiting times t after the end of irradiation. 2. The target irradiation time was 1.5 h, the cyclotron current was 2 μA. 3. Dashes indicate that the activity of the isotope is below 1 decay per second.
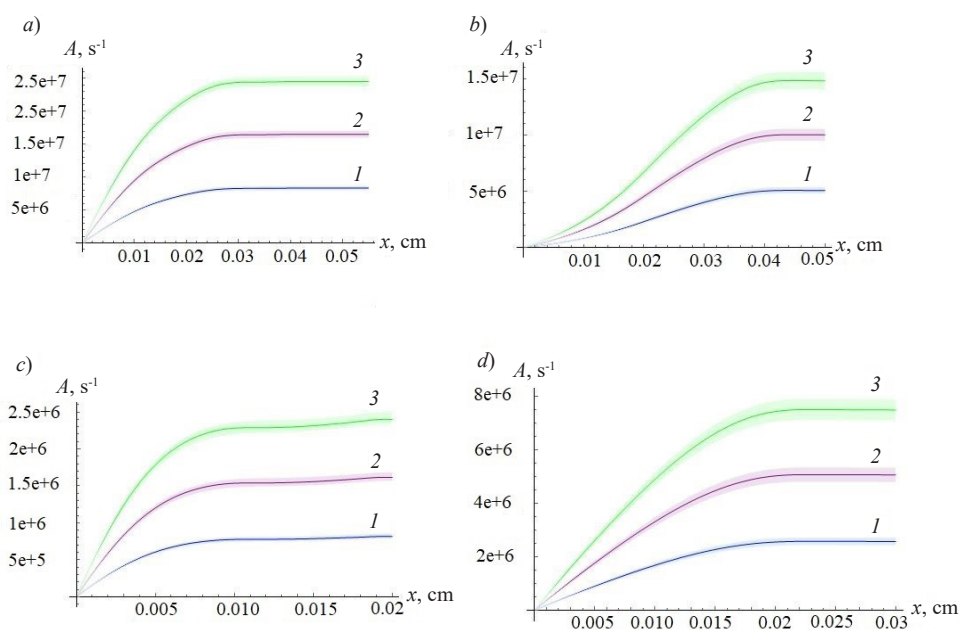
Fig. 1. Dependences of accumulated activity of ^{55}Co (*a,c*) and ^{64}Cu (*b,d*) radioisotopes on the thickness of natural nickel target for protons with an initial kinetic energy of 15 MeV (*a,b*) and 10 МэВ (*c,d*), for different irradiation times, h: 0.5 (*1*), 1.0 (*2*), 1.5 (*3*). The lines correspond to the dependence curves, and the bands to measurement uncertainty (associated with the errors in finding the reaction cross section)

preferable to wait 12−17 h before chromatography (as follows from the data in Table 2) in order to reduce the activity of the ^{60}Cu and ^{62}Cu isotopes. This gives a reduction of the activity by more than 1 million times. The chemical separation process takes about 20 h on average. As follows from the data in Table 2, a very high radionuclide purity of the ^{64}Cu isotope can be achieved, at least 99%, if it is completely separated (ideal case) from the nickel and cobalt isotopes).

Conclusion

The technology for producing the ^{64}Cu isotope has been analyzed, which has important applications in nuclear medicine, by cyclotron irradiation of a target made of natural nickel with protons (the initial kinetic energy of the proton beam is 10 and 15 MeV, the cyclotron current is 2 μA) for different irradiation times. It is established that the radionuclide purity of the ^{64}Cu isotope can be expected to be very high, reaching at least 99%, under conditions close to ideal (if nickel and cobalt isotopes are completely separated from the required copper isotope).

REFERENCES

1. **Szucs Z., Takacs S., Alirezapour B.,** Development of cost-effective method for production of ^{64}Cu from nat. Ni, Journal of Radioanalytical and Nuclear Chemistry. 302 (2) (2014) 1035−1038.

2. **Jalilian A.R., Jr J.O.,** The current status and future of theranostic copper-64 radiopharmaceuticals, Iran Journal of Nuclear Medicine. 25 (1) (2017) 1−10.

3. **Qaim S.M.,** The present and future of medical radionuclide production, Radiochimica Acta. 100 (9) (2012) 635−651.

4. **Ma M.T., Donnelly P.S.,** Peptide targeted copper-64 radiopharmaceuticals, Journal of Current Topics in Medicinal Chemistry. 11 (5) (2011) 500−520.

5. **Van So Le, Howse J., Zaw M., et al.,** Alternative method for ^{64}Cu radioisotope production, Journal of Applied Radiation and Isotopes. 67 (7) (2009) 1324−1331.

6. **Hilgers K., Stoll T., Skakun Y., et al.,** Cross-section measurements of the nuclear reactions nat. $Zn(d,x)^{64}Cu$, $^{66}Zn(d,a)^{64}Cu$ and $^{68}Zn(p,\alpha n)^{64}Cu$ for production of ^{64}Cu and technical developments for small-scale production of ^{67}Cu via the $^{70}Zn(p,a)^{67}Cu$ process, Journal of Applied Radiation and Isotopes. 59 (6) (2003) 343−351.

7. **Rosman K.J.R., Taylor P.D.P.,** Isotopic compositions of the elements, Pure and Applied Chemistry. 70 (1) (1998) 217−235.

8. **Amjed N., Hussain M., Aslam M.N., et al.,** Evaluation of nuclear reaction cross sections for optimization of production of the emerging diagnostic radionuclide ^{55}Co, Journal of Applied Radiation and Isotopes. 108 (February) (2016) 38−48.

9. **Tarkányi F.T., Ignatyuk A.V., Hermanne A., et al.,** Recommended nuclear data for medical radioisotope production: diagnostic positron emitters, Journal of Radioanalytical and Nuclear Chemistry. 319 (2) (2019) 533−666.

10. **Khandaker M.U., Kim K., Lee M., et al.,** Excitation functions of (p,x) reactions on natural nickel up to 40 MeV, Journal of Nuclear Instruments and Methods in Physics Research. Part B. 269 (10) (2011) 1140−1149.

11. **Aslam M.N., Sudár S., Hussain M., et al.,** Charged particle induced reaction cross section data for production of the emerging medically important positron emitter ^{64}Cu: A comprehensive evaluation, Radiochimica Acta. 97 (12) (2009) 669−686.

12. **Uddin M.S., Chakraborty A.K., Spellerberg San, et al.,** Experimental determination of proton induced reaction cross sections on nat. Ni near threshold energy, Radiochimica Acta. 104 (5) (2016) 305−314.

13. **Tanabashi M., Hagiwara K., Hikasa K., et al.** (Particle Data Group), Review of Particle Physics, Physical Review, D. 98 (3) (2018) 030001.

14. **Seltzer S.M., Berger M.J.,** Evaluation of the collision stopping power of elements and compounds for electrons and positrons, The International Journal of Applied Radiation and Isotopes. 33 (11) (1982) 1189−1218.

15. International Atomic Energy Agency, Cyclotron produced radionuclides: physical characteristics and production methods, Technical Reports Series. No. 468. IAEA, Vienna, 2009.

16. **Jeffery C.M., Smithc S.V., Asad A.H., et al.,** Routine production of copper-64 using 11.7 MeV protons, AIP (American Institute of Physics). Conference Proceedings. 1509 (84) (2012) 84−90.

THE AUTHORS

TIBA Ali
Peter the Great St. Petersburg Polytechnic University
29 Politechnicheskaya St., St. Petersburg, 195251, Russian Federation
alitiba1991@gmail.com

BERDNIKOV Yaroslav A.
Peter the Great St. Petersburg Polytechnic University
29 Politechnicheskaya St., St. Petersburg, 195251, Russian Federation
berdnikov@spbstu.ru

СПИСОК ЛИТЕРАТУРЫ

1. **Szucs Z., Takacs S., Alirezapour B.** Development of cost-effective method for production of ^{64}Cu from nat. Ni // Journal of Radioanalytical and Nuclear Chemistry. 2014. Vol. 302. No. 2. Pp. 1035−1038.

2. **Jalilian A.R., Jr J.O.** The current status and future of theranostic copper-64 radiopharmaceuticals // Iran Journal of Nuclear Medicine. 2017. Vol. 25. No. 1. Pp. 1−10.

3. **Qaim S.M.** The present and future of medical radionuclide production // Radiochimica Acta. 2012. Vol. 100. No. 9. Pp. 635−651.

4. **Ma M.T., Donnelly P.S.** Peptide targeted copper-64 radiopharmaceuticals // Journal of Current Topics in Medicinal Chemistry. 2011. Vol. 11. No. 5. Pp. 500−520.

5. **Van So Le., Howse J., Zaw M., Pellegrini P., Katsifis A., Greguric I., Weiner R.** Alternative method for ^{64}Cu radioisotope production // Journal of Applied Radiation and Isotopes. 2009. Vol. 67. No. 7. Pp. 1324−1331.

6. **Hilgers K., Stoll T., Skakun Y., Coenen H.H., Qaim S.M.** Cross-section measurements of the nuclear reactions nat. $Zn(d,x)^{64}$Cu, $^{66}Zn(d,a)^{64}$Cu and $^{68}Zn(p,\alpha n)^{64}$Cu for production of ^{64}Cu and technical developments for small-scale production of ^{67}Cu via the $^{70}Zn(p,\alpha)^{67}$Cu process // Journal of Applied Radiation and Isotopes. 2003. Vol. 59. No. 6. Pp. 343−351.

7. **Rosman K.J.R., Taylor P.D.P.** Isotopic compositions of the elements // Pure and Applied Chemistry. 1998. Vol. 70. No. 1. Pp. 217−235.

8. **Amjed N., Hussain M., Aslam M.N., Tarkanyi F., Qaim S.M.** Evaluation of nuclear reaction cross sections for optimization of production of the emerging diagnostic radionuclide ^{55}Co // Journal of Applied Radiation and Isotopes. 2016. Vol. 108. February. Pp. 38−48.

9. **Tarkányi F.T., Ignatyuk A.V., Hermanne A., et al.** Recommended nuclear data for medical radioisotope production: diagnostic positron emitters // Journal of Radioanalytical and Nuclear Chemistry. 2019. Vol. 319. No. 2. Pp. 533−666.

10. **Khandaker M.U., Kim K., Lee M., Kim K.S., Kim G.** Excitation functions of (p,x) reactions on natural nickel up to 40 MeV // Journal of Nuclear Instruments and Methods in Physics Research. Part B. 2011. Vol. 269. No. 10. Pp. 1140−1149.

11. **Aslam M.N., Sudár S., Hussain M., Malik A.A., Shah H.A., Qaim S.M.** Charged particle induced reaction cross section data for production of the emerging medically important positron emitter ^{64}Cu: A comprehensive evaluation // Radiochimica Acta. 2009. Vol. 97. No. 12. Pp. 669−686.

12. **Uddin M.S., Chakraborty A.K., Spellerberg San, Shariff M.A., Das S., Rashid M.A., Spahn I., Qaim S.M.** Experimental determination of proton induced reaction cross sections on nat. Ni near threshold energy // Radiochimica Acta. 2016. Vol. 104. No. 5. Pp. 305−314.

13. **Tanabashi M., Hagiwara K., Hikasa K., et al.** (Particle Data Group). Review of Particle Physics // Physical Review. D. 2018. Vol. 98. No. 3. P. 030001.

14. **Seltzer S.M., Berger M.J.** Evaluation of the collision stopping power of elements and compounds for electrons and positrons // The International Journal of Applied Radiation and Isotopes. 1982. Vol. 33. No. 11. Pp. 1189−1218.

15. International Atomic Energy Agency. Cyclotron produced radionuclides: physical characteristics and production methods. Technical Reports Series. No. 468. Vienna: IAEA, 2009. 266 p.

16. **Jeffery C.M., Smithc S.V., Asad A.H., Chana S., Price R.I.** Routine production of copper-64 using 11.7 MeV protons // AIP (American Institute of Physics). Conference Proceedings. 2012. Vol. 1509. No. 84. Pp. 84−90.

СВЕДЕНИЯ ОБ АВТОРАХ

ТИБА Али — *аспирант Высшей инженерно-физической школы Санкт-Петербургского политехнического университета Петра Великого, Санкт-Петербург, Российская Федерация.*

195251, Российская Федерация, г. Санкт-Петербург, Политехническая ул., 29

alitiba1991@gmail.com

БЕРДНИКОВ Ярослав Александрович — *доктор физико-математических наук, профессор Высшей инженерно-физической школы Санкт-Петербургского политехнического университета Петра Великого, Санкт-Петербург, Российская Федерация.*

195251, Российская Федерация, г. Санкт-Петербург, Политехническая ул., 29

berdnikov@spbstu.ru

DIQUARK PARTON DISTRIBUTION FUNCTIONS BASED ON THE LIGHT-FRONT AdS/QCD QUARK-DIQUARK NUCLEON MODEL

B. Rodriguez-Aguilar, Ya.A. Berdnikov

Peter the Great St. Petersburg Polytechnic University,
St. Petersburg, Russian Federation

In the paper, we present a phenomenological unpolarized parton distribution functions (PDFs) for diquarks based on the light front soft-wall AdS/QCD quark-diquark nucleon model. From a probed model consistent with the Drewll−Yan−West relation and quark counting rule, we have performed a fit of some free parameters using known phenomenological data of quark PDFs. The model considers the entire set of possible valence diquarks within the nucleon. In our investigation, we focused on the spin-0 $((ud)_0)$, spin-1 $((ud)_1)$ and spin-1 $((uu)_1)$ valence diquarks in the proton. The diquark PDFs obtained can be used in proton-proton collision simulations.

Keywords: diquark, parton distribution function, AdS/QCD, holography

ПАРТОННЫЕ ФУНКЦИИ РАСПРЕДЕЛЕНИЯ ДИКВАРКОВ, ОСНОВАННЫЕ НА (АдС/КХД)-МОДЕЛИ НУКЛОНА КВАРК-ДИКВАРК

Б. Родригес-Агилар, Я.А. Бердников

Санкт-Петербургский политехнический университет Петра Великого,
Санкт-Петербург, Российская Федерация

В работе представлены феноменологические неполяризованные партонные функции распределения для дикварков, основанные на модели с мягкой стеной на световом конусе AdS/QCD кварк-дикваркового нуклона. На основе проверенной модели, согласующейся с соотношением Дрелла − Яна − Веста и правилом счета кварков, в работе определен набор параметров с использованием известных феноменологических данных кварковых функций распределения партонов (ФРП). Модель рассматривает все возможные состояния валентных дикварков. В данном исследовании мы остановились на рассмотрении состояний валентных дикварков *ud* со спинами 0 $((ud)_0)$ и 1 $((ud)_1)$, а также *uu* со спином 1 $((uu)_1)$ в протоне. Полученные дикварковые ФРП могут быть использованы при моделировании протон-протонных столкновений.

Ключевые слова: дикварк, функция распределения партонов, АдС/КХД, голография

Introduction

Since the second half of the last decade of the 20th century, the AdS/CFT correspondence [1] between string theory in anti-de Sitter (AdS) space-time and conformal field theories (CFTs) in physical space-time has been a very active and interesting field of study. Among other things, the wealth of this correspondence stands in the possibility to perform calculations between opposite coupling regimes, strongly coupled theories can be mapped into weakly coupled ones and *vice versa*. CFTs are defined as scale invariant theories, so it is impossible to applicate the AdS/CFT correspondence to the quantum chromodynamics (QCD) itself directly.

It is worth noting that this is because the coupling constants change with the renormalization scale μ in QCD that we get the condition under which perturbation theory is valid [2].

Nevertheless, in the strong coupling regime of QCD, the couplings appear to be approximately constant. This is the basis for a light-front holography, an approximation of the AdS/CFT to QCD quantized on the light front (light-front AdS/QCD) [3] that has shown the ability to find analytic solutions in the non-perturbative regime of QCD, like improving predictions of hadron masses and structure properties (see e.g. Ref. [4]).

In this work, we are particularly interested in the fact that light-front AdS/QCD predicts a general form of two particle bound state wave function inside nucleons which cannot be derived simply from valence quarks [4, 5]. This has led to considerable progress in nucleon analytical results considering valence diquarks in their structure, just as light-front wave functions QCD matched with soft-wall AdS/QCD predictions [6 − 8].

Another recent result contemplates the scale evolution of the parton distribution functions (PDFs) for a quark-diquark nucleon model using scale-dependent parameters following the DGLAP (Dokshitzer − Gribov − Lipatov − Altarelli − Parisi) evolution [5], that are consistent with the quark counting rule and Drell − Yan − West relation [9, 10]. Based on these last two results, we have fitted the PDF parameters of the quark-diquark nucleon model to the available data from NNPDF2.3 QCD + QED NNLO [11] for *u* and *d* quarks, in order to get the unpolarized PDFs for the spin-0 $(ud)_0$, spin-1 $(ud)_1$ and spin-1 $(uu)_1$ diquarks. With such parameters available, the diquark PDFs can be used to simulations of proton (and neutron) collisions with participating diquarks.

To consider proton collisions based on a nucleon model with diquark structures inside, it is useful to inspect the properties of the parton model.

The parton model

The cross section for proton-proton collisions can be expressed by the so called improved parton model formula [12]:

$$\sigma_{(P_1,P_2)} = \sum_{i,j} dx_1 dx_2 f_i^1(x_1,\mu) f_j^2(x_2,\mu) \times$$
$$\times \hat{\sigma}_{ij}(x_1 P_1, x_2 P_2, \alpha_s(\mu), \mu), \qquad (1)$$

where the scripts 1 and 2 are labels to incoming proton beams carried momentum P.

In this scenario, the incoming proton beam is equivalent to a beam made of constituent partons. Typically, these partons are taken as the massless-pointlike elementary particles, quarks and gluons [12], with longitudinal momentum distribution characterized by the parton distribution functions $f_i(x, \mu)$.

This means, given some proton with momentum P, the probability to find in such parton i with momentum between xP and $(x + dx)P$ is precisely $dx f_i(x, \mu)$ being dependent as well of the renormalization scale μ.

While represents the parton cross sections, which can be computed with perturbative QCD (pQCD) for sufficiently small running coupling $\alpha_s(\mu)$ [2].

However, due to the fact that partons cannot be observed as free particles, the PDFs cannot be calculated using pQCD. Nowadays, the simplest way to obtain PDFs is fitting observables to experimental data, among other phenomenological tools (see e.g. Refs. [13, 14]).

Nevertheless, in order to work with a parton model using constituent diquarks, we must ex-

pand this picture beyond quarks and gluons. As we mentioned above, recent results from soft-wall AdS/QCD [4, 7] have shown a phenomenological approach to reproduce unpolarized PDFs of quark-diquark nucleons [5].

In the next section we show how this phenomenological approach has been constructed to finally obtain our parameters that allow us to exhibit our diquark PDFs.

The soft-wall light front AdS/QCD quark-diquark nucleon model

In this section we intend to outline how to obtain the PDF of a quark-diquark nucleon model using soft-wall light front holographic QCD (for a more detailed analysis see Ref. [5] and its references, from where this section is heavily based).

To construct such a PDF model, it is assumed that a virtual incoming photon interacts with a massless-valence quark. The other two valence quarks are then forming a spectator diquark. In this way, it is ensured that this model is in accordance with the traditional quark-interacting frameworks, from where it is possible to build reliable properties for the nucleon model, so for diquarks. The diquarks can have then either spin-0 (scalar diquark) or spin-1 (vector diquark).

The nucleon state is represented by a spin-flavor SU (4) symmetry. This implies that the possible states are the isoscalar-scalar diquark singlet state, the isoscalar-vector diquark state and the isovector-vector diquark state. Shortly, the diquark can be either scalar or axial-vector.

For the proton state we can write it as

$$|P;\pm\rangle = C_S |uS^0\rangle^{\pm} + C_V |uA^0\rangle^{\pm} + \\ + C_{VV} |dA^1\rangle^{\pm}, \tag{2}$$

where, following the original notation in Ref. [5], S and A represent the scalar and vector diquark having isospin at their superscript; the subscripts in the coefficients denote the isoscalar-scalar (S), the isoscalar-vector state (V) and the isovector-vector state (VV).

For the neutron, the state is given by the isospin symmetry $u \leftrightarrow d$.

Without losing the generality of the model, we will take the case for the proton, which is what we care about in this work.

Using the light-cone convention $x^{\pm} = x^0 \pm x^3$ [15] it is convenient to choose a frame where the proton transverse momentum vanishes, denoted as

$$P \equiv \left(P^+, \frac{M^2}{P^+}, \mathbf{0}_{\perp} \right),$$

where M is the proton mass.

So the momentum of the struck quark can be taken as

$$p \equiv \left(xP^+, \frac{p^2 + |p_{\perp}|^2}{xP^+}, \mathbf{p}_{\perp} \right)$$

and the diquark

$$P_X \equiv \left((1-x)P^+, P_X^-, -\mathbf{p}_{\perp} \right).$$

We can interpret from this notation that $x = p^+/P^+$ is the longitudinal momentum fraction carried by the struck quark.

Now, we can express the two particle Fock-state expansion.

For total angular momentum projection $J^z = \pm 1/2$ with spin-0 diquark is given by

$$|uS\rangle^{\pm} = \int \frac{dx d^2 \mathbf{p}_{\perp}}{2(2\pi)^3 \sqrt{x(1-x)}} \times \\ \times \left[\psi_+^{\pm(u)}(x, \mathbf{p}_{\perp}) \left| +\frac{1}{2} s; sP^+, \mathbf{p}_{\perp} \right\rangle + \\ + \psi_-^{\pm(u)}(x, \mathbf{p}_{\perp}) \left| -\frac{1}{2} s; sP^+, \mathbf{p}_{\perp} \right\rangle \right], \tag{3}$$

where

$$\left| \lambda_q \lambda_S; sP^+, \mathbf{p}_{\perp} \right\rangle$$

is the two-particle state having struck quark of helicity λ_q and a scalar diquark having helicity $\lambda_s = s$ (spin-0 singlet diquark helicity is denoted by s to distinguish from triplet diquark).

While, the spin-1 diquark state is given by the following expression [16]:

$$|\nu A\rangle^{\pm} = \int \frac{dx\,d^2\mathbf{p}_{\perp}}{2(2\pi)^3 \sqrt{x(1-x)}} \times$$

$$\times \left[\psi_{++}^{\pm(\nu)}(x,\mathbf{p}_{\perp}) \left| +\frac{1}{2}+1; xP^+,\mathbf{p}_{\perp} \right\rangle + \right.$$

$$+ \psi_{-+}^{\pm(\nu)}(x,\mathbf{p}_{\perp}) \left| -\frac{1}{2}+1; xP^+,\mathbf{p}_{\perp} \right\rangle +$$

$$+ \psi_{+0}^{\pm(\nu)}(x,\mathbf{p}_{\perp}) \left| +\frac{1}{2}0; xP^+,\mathbf{p}_{\perp} \right\rangle + \quad (4)$$

$$+ \psi_{-0}^{\pm(\nu)}(x,\mathbf{p}_{\perp}) \left| -\frac{1}{2}0; xP^+,\mathbf{p}_{\perp} \right\rangle +$$

$$+ \psi_{+-}^{\pm(\nu)}(x,\mathbf{p}_{\perp}) \left| +\frac{1}{2}-1; xP^+,\mathbf{p}_{\perp} \right\rangle +$$

$$+ \psi_{--}^{\pm(\nu)}(x,\mathbf{p}_{\perp}) \left| -\frac{1}{2}-1; xP^+,\mathbf{p}_{\perp} \right\rangle \right].$$

where $|\lambda_q \lambda_D; sP^+,\mathbf{p}_{\perp}\rangle$ represents a two-particle state with a quark of helicity $\lambda_q = \pm\frac{1}{2}$ and a vector diquark of helicity $\lambda_D = \pm 1, 0$ (triplet). Here $\nu = u, d$ is a flavor index.

The light-front (LF) wave functions with spin-0 diquark state, $\psi_{\pm}^{\pm(u)}$ at the initial scale μ_0 for $J = \pm\frac{1}{2}$ are given by expressions [8]:

$$J = +\frac{1}{2}: \begin{cases} \psi_+^{+(u)}(x,\mathbf{p}_{\perp}) = N_S \varphi_1^{(u)}(x,\mathbf{p}_{\perp}), \\ \psi_-^{+(u)}(x,\mathbf{p}_{\perp}) = \\ = N_S \left(-\frac{p^1+ip^2}{xM} \right) \varphi_2^{(u)}(x,\mathbf{p}_{\perp}); \end{cases} \quad (5)$$

$$J = -\frac{1}{2}: \begin{cases} \psi_+^{-(u)}(x,\mathbf{p}_{\perp}) = \\ = N_S \left(\frac{p^1-ip^2}{xM} \right) \varphi_2^{(u)}(x,\mathbf{p}_{\perp}), \\ \psi_-^{-(u)}(x,\mathbf{p}_{\perp}) = N_S \varphi_1^{(u)}(x,\mathbf{p}_{\perp}). \end{cases} \quad (6)$$

In a very similar way, for vector diquarks with $J = \pm\frac{1}{2}$ the LF wave functions $\psi_{\pm\pm}^{\pm(\nu)}$ at the initial scale μ_0 can be written as

$$J = +\frac{1}{2}: \begin{cases} \psi_{++}^{+(\nu)}(x,\mathbf{p}_{\perp}) = \\ = N_1^{\nu}\sqrt{\frac{2}{3}}\left(\frac{p^1-ip^2}{xM} \right)\varphi_2^{(\nu)}(x,\mathbf{p}_{\perp}), \\ \psi_{-+}^{+(\nu)}(x,\mathbf{p}_{\perp}) = N_1^{\nu}\sqrt{\frac{2}{3}}\varphi_1^{(\nu)}(x,\mathbf{p}_{\perp}), \\ \psi_{+0}^{+(\nu)}(x,\mathbf{p}_{\perp}) = N_0^{\nu}\sqrt{\frac{1}{3}}\varphi_1^{(\nu)}(x,\mathbf{p}_{\perp}), \\ \psi_{-0}^{+(\nu)}(x,\mathbf{p}_{\perp}) = \\ = N_0^{\nu}\sqrt{\frac{1}{3}}\left(\frac{p^1+ip^2}{xM} \right)\varphi_2^{(\nu)}(x,\mathbf{p}_{\perp}), \\ \psi_{+-}^{+(\nu)}(x,\mathbf{p}_{\perp}) = 0, \\ \psi_{--}^{+(\nu)}(x,\mathbf{p}_{\perp}) = 0; \end{cases} \quad (7)$$

$$J = -\frac{1}{2}: \begin{cases} \psi_{++}^{-(\nu)}(x,\mathbf{p}_{\perp}) = 0, \\ \psi_{-+}^{-(\nu)}(x,\mathbf{p}_{\perp}) = 0, \\ \psi_{+0}^{-(\nu)}(x,\mathbf{p}_{\perp}) = \\ = N_0^{\nu}\sqrt{\frac{1}{3}}\left(\frac{p^1-ip^2}{xM} \right)\varphi_2^{(\nu)}(x,\mathbf{p}_{\perp}), \\ \psi_{-0}^{-(\nu)}(x,\mathbf{p}_{\perp}) = N_0^{\nu}\sqrt{\frac{1}{3}}\varphi_1^{(\nu)}(x,\mathbf{p}_{\perp}), \\ \psi_{+-}^{-(\nu)}(x,\mathbf{p}_{\perp}) = N_1^{\nu}\sqrt{\frac{2}{3}}\varphi_1^{(\nu)}(x,\mathbf{p}_{\perp}), \\ \psi_{--}^{-(\nu)}(x,\mathbf{p}_{\perp}) = \\ = N_1^{\nu}\sqrt{\frac{2}{3}}\left(\frac{p^1+ip^2}{xM} \right)\varphi_2^{(\nu)}(x,\mathbf{p}_{\perp}). \end{cases} \quad (8)$$

The LF wave functions $\varphi_i^{(\nu)}$ ($i = 1, 2$) are the twist-3 LF wave functions. These functions can be derived in light-front QCD and in soft-wall AdS/QCD [4, 17 − 19, 6].

In Ref. [7] a generalized form to $\varphi_i^{(\nu)}$ was proposed by matching the electromagnetic form factors of the nucleon in soft-wall AdS/QCD and light-front QCD, getting that

Table 1

The fitted parameters for nucleon valence *u* and *d* quarks at the initial scale μ_0 [5]

Parameter	Value	
	u	*d*
a_1^v	0.280 ± 0.001	$0.5850 \pm 0,0003$
b_1^v	0.1716 ± 0.0051	0.7000 ± 0.0002
a_2^v	0.84 ± 0.02	$0.9434^{+0.0017}_{-0.0013}$
b_2^v	0.2284 ± 0.0035	$0.6400^{+0.0082}_{-0.0022}$
δ^v	1.0	1.0

N o t a t i o n: $v = u, d$ — quarks, while $a_1^v, b_1^v, a_2^v, b_2^v$, δ^v — parameters defined in Eq. (9).

$$\varphi_i^{(v)}\left(x,\mathbf{p}_\perp\right) = \frac{4\pi}{\kappa}\sqrt{\frac{\log(1/x)}{(1-x)}}x^{a_i^v}\left(1-x\right)^{b_i^v} \times$$

$$\times \exp\left[-\delta^v\,\frac{\mathbf{p}_\perp^2}{2\kappa^2}\frac{\log(1/x)}{(1-x)^2}\right], \quad (9)$$

where κ is a scale parameter coming from the soft-wall AdS/QCD model.

With this information, it is possible to write the Dirac and Pauli form factors for spin-1/2 composite particle systems [20].

In Ref. [21] it was found, by fitting the proton form factors from the soft-wall AdS/QCD model with experimental data [22 − 26], that the best agreement if given with $\kappa = 0.4066$ GeV. Furthermore, in Ref. [5] the flavor form factors for *u* and *d* in this light-front diquark model was fitted with experimental data [27, 28], obtaining the value of the parameters $a_i^{(v)}$ and $b_i^{(v)}$ at the initial scale μ_0 (see Table 1).

In the same way, using the Sachs form factors, the coefficients for the quark-diquark nucleon state (2) were obtained in Ref. [5]:

$$C_S^2 = 1.3872, \quad C_V^2 = 0.6128, \quad C_{VV}^2 = 1.0.$$

Besides, the normalized constants N_i were found to be

$$N_S = 2.0191, \quad N_0^{(u)} = 3.2050, \quad N_0^d = 5.9423,$$

$$N_1^{(u)} = 0.9895, \quad N_1^d = 1.1616.$$

Quark-diquark unpolarized PDF evolution

The unpolarized parton distribution function is defined as [8, 5]:

$$f^{(v)}\left(x,\mu_0\right) = \frac{1}{2}\int\frac{dz^-}{2(2\pi)}\exp\left(\frac{ip^+z^-}{2}\right)\times$$

$$\times\left\langle P;S\left|\overline{\psi}^{(v)}(0)\gamma^+\psi^{(v)}\left(z^-\right)\right|P;S\right\rangle\Big|_{z^+=z_T=0}, \quad (10)$$

which depends only on the light-cone momentum fraction $x = p^+/P^+$ where the proton state $\left|P;S\right\rangle$ with spin S is given as in Eq. (2).

Indeed, γ^+ is the light-cone representation of the usual γ^μ matrix, detailed definition is found in Ref. [15].

The leading order QCD evolution of the unpolarized PDF is given as the standard DGLAP expansion [29, 30, 5]:

$$\int_0^1 dx\,x^n f\left(x,\mu\right) =$$

$$= \left(\frac{\alpha_s(\mu)}{\alpha_s(\mu_0)}\right)^{\frac{\gamma_n^{(0)}}{2\beta_0}}\int_0^1 dx\,x^n f\left(x,\mu_0\right), \quad (11)$$

where the anomalous dimension is determined by

$$\gamma_n^{(0)} = -2C_F\left(3 + \frac{2}{(n+1)(n+2)} - 4\sum_{k=1}^{n+1}\frac{1}{k}\right) \quad (12)$$

and the running coupling constant is given as

$$\alpha_s(\mu) = \frac{4\pi}{\beta_0 \ln\left(\dfrac{\mu^2}{\Lambda_{QCD}^2}\right)}. \qquad (13)$$

In this work we take $C_F = 4/3$, $\beta_0 = 9$ and $\Lambda_{QCD} = 0.226$ GeV.

The initial scale in most of the works on which ours is based is taken to be $\mu_0 = 0.313$ GeV since it is a value available for pion phenomenology.

Thus, the light-front diquark unpolarized PDFs at scale μ are given by [5]:

$$f^{(S)}(x,\mu) = N_S^2(\mu) \times$$
$$\times \left[\frac{1}{\delta^u(\mu)} x^{2a_1^u(\mu)}(1-x)^{2b_1^u(\mu)+1} + \right.$$
$$+ x^{2a_2^u(\mu)-2}(1-x)^{2b_2^u(\mu)+3} \times \qquad (14)$$
$$\left. \times \frac{\kappa^2}{\left(\delta^u(\mu)\right)^2 M^2 \ln(1/x)} \right];$$

$$f^{(A)}(x,\mu) = \left(\frac{1}{3}N_0^{(v)2}(\mu) + \frac{2}{3}N_1^{(v)2}(\mu) \right) \times$$
$$\times \left[\frac{1}{\delta^v(\mu)} x^{2a_1^v(\mu)}(1-x)^{2b_1^v(\mu)+1} + \right.$$
$$+ x^{2a_2^v(\mu)-2}(1-x)^{2b_2^v(\mu)+3} \times \qquad (15)$$
$$\left. \times \frac{\kappa^2}{\left(\delta^v(\mu)\right)^2 M^2 \ln(1/x)} \right].$$

The parameters a_i^v, b_i^v, δ^v are now dependent on the scale μ such that the relation (11) holds, i. e. [5],

$$a_i^v(\mu) = a_i^v(\mu_0) + A_i^v(\mu), \qquad (16)$$

$$b_i^v(\mu) = b_i^v(\mu_0) - \qquad (17)$$
$$- B_i^v(\mu)\frac{4C_F}{\beta_0}\ln\left(\frac{\alpha_s(\mu^2)}{\alpha_s(\mu_0^2)}\right),$$

$$\delta^v(\mu) = \exp\left[\delta_1^v\left(\ln\left(\frac{\mu^2}{\mu_0^2}\right) \right)^{\delta_2^v} \right] \qquad (18)$$

where the quantities $A_i^v(\mu)$ and $b_i^v(\mu)$ are defined as

$$\Pi_i^v(\mu) = \alpha_{\Pi,i}^v \mu^{2\beta_{\Pi,i}^v}\left[\ln\left(\frac{\mu^2}{\mu_0^2}\right) \right]^{\gamma_{\Pi,i}^v}\Big|_{i=1,2} \qquad (19)$$

for $\Pi = A, B$.

The $a_i^v(\mu)$ and $b_i^v(\mu)$ are the parameters given in Table 1. It should be noted that the parameter δ^μ tends to unity while $\mu \to \mu_0$.

In order to find the evolution parameters $\alpha_{\Pi,i}^v, \beta_{\Pi,i}^v, \gamma_{\Pi,i}^v$ and δ^v it is useful to write the flavor decomposed PDFs $f^u(x, \mu)$ and $f^d(x, \mu)$. It was well discussed in Ref. [8] that for the relation between quark flavors and diquark states should have a linear behavior with free coefficients to be determinate with experimental data. Indeed, in the same way the proton state (2) has to be consistent with the real world under the same coefficients C_S, C_V and C_{VV}, which was how the flavored form factors were decomposed from the diquarks, and such parameters founded in Ref. [5].

So, the flavor decomposed PDFs are given as

$$f^u(x,\mu) = C_S^2 f^{(S)}(x,\mu) + C_V^2 f^{(V)}(x,\mu), \qquad (20)$$

$$f^d(x,\mu) = C_{VV}^2 f^{(VV)}(x,\mu). \qquad (21)$$

Then, the flavored PDF $f^v(x, \mu)$ in the light-front quark-diquark model can be written as

$$f^v(x,\mu) =$$
$$= N^{(v)}\left[\frac{1}{\delta^v(\mu)} x^{2a_1^v(\mu)}(1-x)^{2b_1^v(\mu)+1} + \right.$$
$$+ x^{2a_2^v(\mu)-2}(1-x)^{2b_2^v(\mu)+3} \times \qquad (22)$$
$$\left. \times \frac{\kappa^2}{\left(\delta^v(\mu)\right)^2 M^2 \ln(1/x)} \right],$$

where

$$N^{(u)} = \left(C_S^2 N_s^2 + C_V^2\left(\frac{1}{3}N_0^{(u)2} + \frac{2}{3}N_1^{(u)2} \right) \right) \qquad (23)$$

and

$$N^{(d)} = \left(C_{VV}^2 \left(\frac{1}{3} N_0^{(d)2} + \frac{2}{3} N_1^{(d)2} \right) \right), \quad (24)$$

for u and d quarks respectively.

In this work, we have followed the fashion of Ref. [5] and we have obtained the values of the evolution parameters by fitting the flavor PDFs (22) with data from NNPDF2.3 QCD + QED NNLO [11].

The fit was performed in gnuplot [31], an open source plotting tool using non-linear least-square theory, taking first a f^{ν} depending on parameters $\Pi_i^{\nu}(\mu)$ then getting the evolution parameters $\alpha_{\Pi,i}^{\nu}$, $\beta_{\Pi,i}^{\nu}, \gamma_{\Pi,i}^{\nu}$ and δ^{ν}.

The unpolarized PDF data was fitted for 100 equal-spaced data points for different $x \in (0, 1)$ and $\mu^2 = 2, 4, 8, 16, 32, 64, 128, 256$ GeV^2.

The fitted parameters for $\alpha_{\Pi,i}^{\nu}, \beta_{\Pi,i}^{\nu}, \gamma_{\Pi,i}^{\nu}$ are shown in Table 2 while the fitted δ^{ν} being shown in Table 3.

In appendix A we show the different fits performed for the scales mentioned above.

With this data applied to the PDFs (14) and (15), we have drawn the functions $x \cdot f(x)$ of the isoscalar-scalar diquark and isovector-vector diquark for energy scales $\mu^2 = 10, 10^2, 10^3$ and 10^4 GeV^2 shown in Fig. 1, a, b, c, d respectively. The smooth bands show the case of the scalar diquark, while the checkered bands are for the mentioned vector diquark. It is important to note that

$$\frac{1}{3} N_0^{(u)2} + \frac{2}{3} N_1^{(u)2} \approx N_S^2,$$

from values reported in Ref. [5], so the behavior of the $f^{(S)}$ (isoscalar-scalar) curve and the $f^{(V)}$ (isoscalar-vector) one is very similar.

Table 2

PDF evolution parameters with 95% confidence bounds

$\Pi_i^{\nu}(\mu)$	α_i^{ν}	β_i^{ν}	γ_i^{ν}	$\chi^2/d.o.f$
A_1^u	-0.196314 ± 0.002266	$-0.197209 \pm 0,010210$	0.927163 ± 0.036270	0.09
B_1^u	6.48940 ± 0.04592	0.161127 ± 0.006494	-0.910813 ± 0.021850	0.17
A_2^u	$-0.441651 \pm 0,002674$	$-0.0389503 \pm 0,0058020$	0.306214 ± 0.019020	0.995
B_2^u	2.58149 ± 0.26410	-0.0548368 ± 0.0780600	$-0.807298 \pm 0,277900$	1.54
A_1^d	-0.119059 ± 0.002517	-0.124819 ± 0.018800	0.952914 ± 0.060100	0.27
B_1^d	12.84810 ± 0.09134	0.0976609 ± 0.006134	-0.80035 ± 0.01510	0.53
A_2^d	-0.514816 ± 0.000724	-0.001555 ± 0.001244	0.171831 ± 0.003307	0.41
B_2^d	1.10727 ± 0.00703	0.0844447 ± 0.005591	-0.57190 ± 0.01486	0.03

Table 3

PDF evolution parameters δ_1^{ν} and δ_2^{ν} for $\nu = u, d$

$\delta^{\nu}(\mu)$	δ_1^{ν}	δ_2^{ν}	$\chi^2/d.o.f$
δ^u	0.035074 ± 0.03009	0.48314 ± 0.06732	10.50
δ^d	0.406762 ± 0.007024	0.46990 ± 0.01275	3.79

F o o t n o t e: in Tabs. 2 and 3 the data was used from NNPDF2.3 QCD+QED NNLO [11].

a)

b)

c)

d)
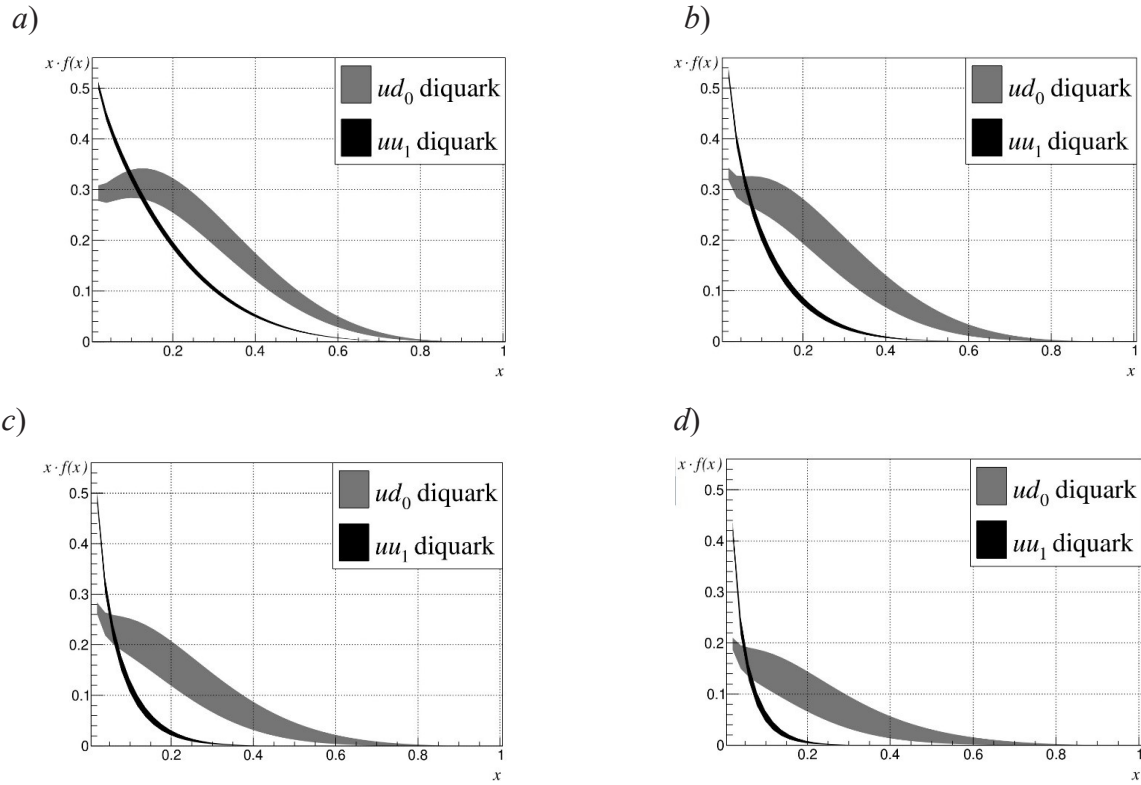
Fig. 1. Graphs of the $x \cdot f(x)$ functions (diquark PDFs)
at different scale energies μ^2, (GeV)^2: 10 (a), 10^2 (b), 10^3 (c), 10^4 (d).
The cases of the scalar ud_0 (gray bands) and vector uu_1 (black ones) diquarks are shown

Conclusions

The soft-wall light front AdS/QCD has allowed us to construct parton distribution functions (PDFs) for diquarks in agreement with the data obtained for quarks phenomenologically. We have particularly taken data from NNPDF2.3 QCD+QED NNLO [11], but the model can be adapted to desired experimental data with u and d quark PDF information.

Although the uncertainties for the values in $\Pi_i^v(\mu)$ reported here should be still improved, an acceptable fit for the functions (14) and (15) is shown in our parameters in Tabs. 2 and 3 looking at $\chi^2/d.o.f$.

In general terms, the behavior of diquark PDFs observed in Figs. 1 reveals a similarity to the quark PDFs. Such behavior goes in the sense that as the energy scale increases, a shift to $x = 0$ of the peak of the functions is visible; as well as, while x approaches 1, xf tends to vanish exponentially. This fact can be compared with the re-sults in Ref. [5], where using the same model with NNPDF21(NNLO) [32] data were fitted the u and d quark PDFs.

The phenomenological diquark PDFs reported here are intended to be tested within the framework of particle collisions.

Especially for us, it is expected to study the effect in the production of hadrons in collision simulations of the AdS/QCD quark-diquark nucleon model taking into account participant diquarks in hard processes.

Appendix

Parameter fitting for PDF evolution from NNPDF2.3 QCD+QED NNLO

The scale evolution of A_i^v and B_i^v is parameterized by α_i^v, β_i^v and γ_i^v. While δ^v is parameterized by δ_1^v and δ_2^v, $f(x, \mu)$ is given by Eq. (22) along with Eqs. (16) – (19). The $f(x, \mu)$ function depending on the parameters A_i^v, B_i^v and δ^v are fitted at 8 different energy scales μ^2 in Table 4 for u quark, while the fitted parameters for d quark are given in Table 5.

Each $\chi^2/d.o.f$ was evaluated for 100 equally-spaced points for different $x \in (0, 1)$. The fitting of the parameters at $\mu^2 = 2, 4, 8, 16, 32, 64, 128$ and 256 GeV^2 are shown in Fig. 2 and 3. The data points are extracted from NNPDF2.3 QCD + QED NNLO [11]. It should be noted that the $\chi^2/d.o.f$ values show that the uncertainty ranges found with the fit are overestimated, this is because for this first instance, uncertainties were not taken from the PDF data of Ref. [11]. An improvement in this fact is expected for future works.
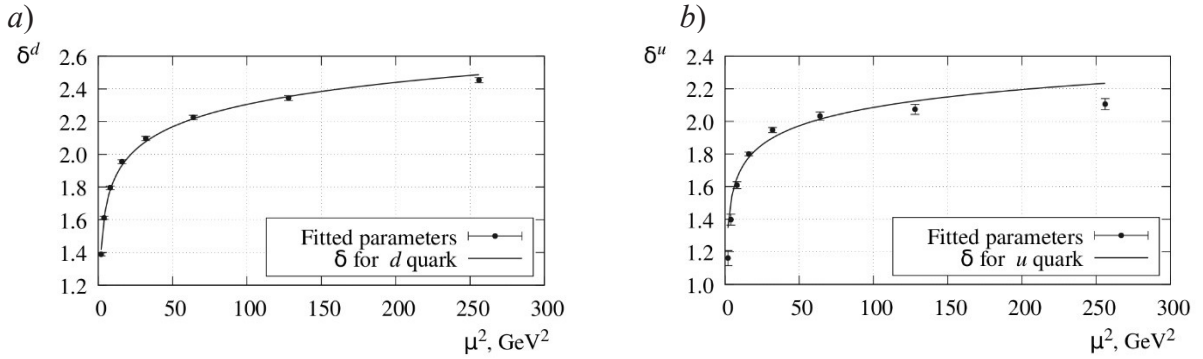
Fig. 2. Plots of δ^u (*a*) and δ^d (*b*) parameters vs. energy scales obtained by fitting the data of Table 3 through varying evolution parameters δ_1^v and δ_2^v or u (*a*) and d (*b*) quarks

Table 4

Fitting of the PDF $f_1(x)$ at various energy scales for the u quark

μ^2, GeV^2	A_1^u	B_1^u	A_2^u	B_2^u	δ^u	$\chi^2/d.o.f$
2.0	−0.133482± ±0.027630	9.88657± ±0.57650	−0,398994± ±0.008142	2.50897± ±0.82540	1.16148± ±0.04635	9.15238e −06
4.0	−0.206116± ±0.014570	5.97471± ±0.18860	−0.463197± ±0.004770	1.64702± ±0.29730	1.39743± ±0.03360	2.73019e −06
8.0	−0.257193± ±0.006954	4.63066± ±0.06874	−0.508357± ±0.002519	1.28388 ± ±0.10670	1.60899± ±0.02080	6.44055e −07
16.0	−0.294376± ±0.002982	3.97296± ±0.02359	−0.542694± ±0.001198	1.01137± ±0.03058	1.80059± ±0.01118	1.22395e −07
32.0	−0.316551± ±0.003503	3.63544± ±0.02254	−0.567223± ±0.001527	0.774017± ±0.020070	1.94722± ±0.01540	1.77367e − 07
64.0	−0.325091± ±0.005228	3.45959± ±0.02855	0.582866± ±0.002362	0.620872± ±0.018460	2.03299± ±0.02475	4.29130e − 07
128.0	−0.325202± ±0.006335	3.36176± ±0.03040	−0.592571± ±0.002883	0.504157± ±0.019470	2.07403± ±0.03057	7.16693e − 06
256.0	−0.324260± ±0.006969	3.28934± ±0.04935	−0.600304± ±0.003162	0.504157± ±0.019470	2.10605± ±0.03384	6.94007e − 06
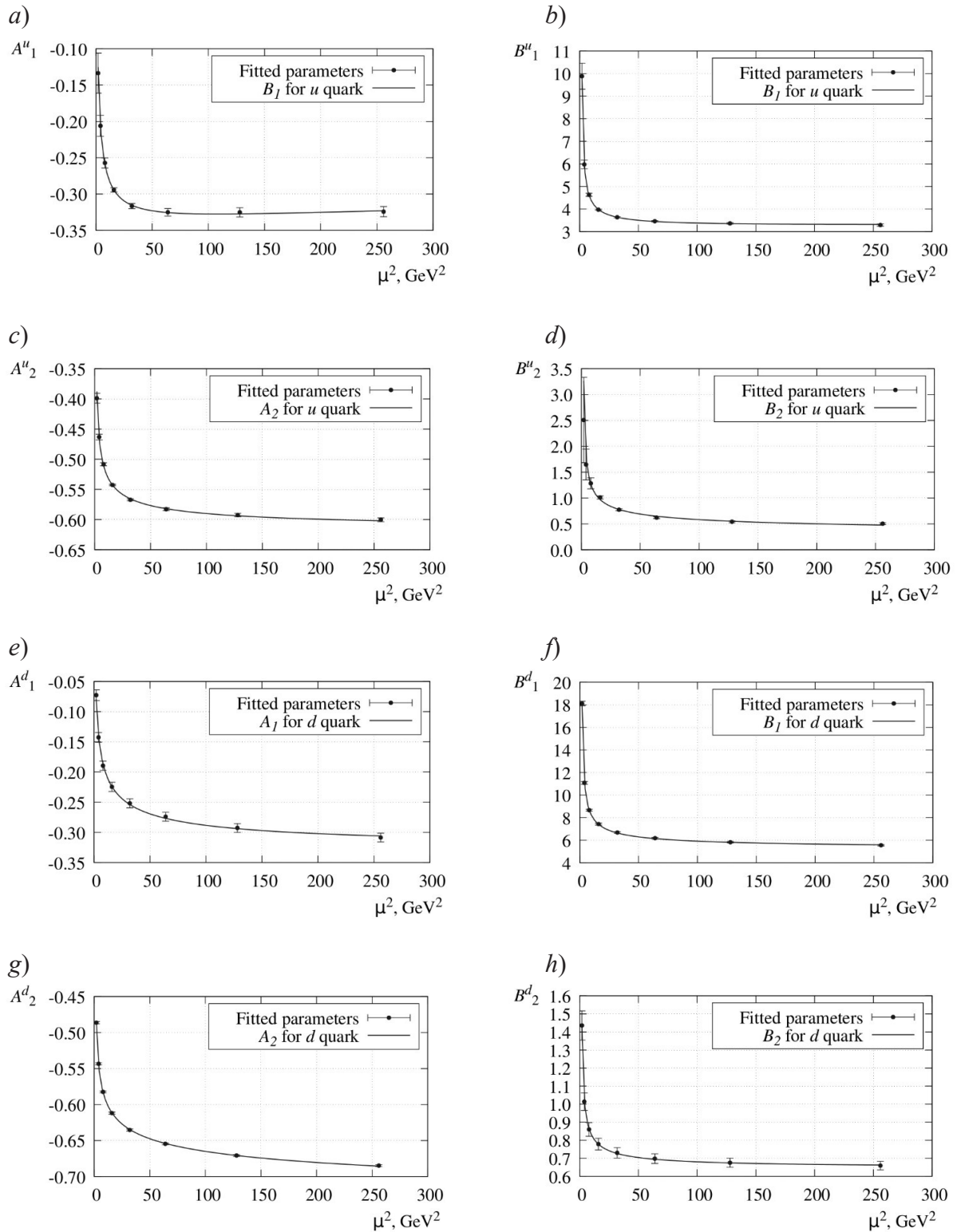
Fig. 3. Plots of A_1^u (a), B_1^u (b), A_2^u (c), B_2^u (d), A_1^d (e), B_1^d (f) and A_2^d (h) parameters vs. energy scales obtained by fitting the data of Tabs. 4, 5 through using Eq. (19) and varying evolution parameters $\alpha_{\Pi,i}^v$, $\beta_{\Pi,i}^v$ and $\gamma_{\Pi,i}^v$ for u ($a - d$) and d ($e - h$) quarks

Table 5

Fitting of the PDF $f_1(x)$ at various scales for the d quark

μ^2, GeV^2	A_1^d	B_1^d	A_2^d	B_2^d	δ^d	$\chi^2/d.o.f$
2.0	$-0.0726864\pm$ ±0.0088830	$18.11530\pm$ ±0.19740	$-0.486242\pm$ ±0.001573	$1.43562\pm$ ±0.08108	$1.388050\pm$ ±0.008694	1.54472e –06
4.0	$-0.142581\pm$ ±0.008094	$11.07900\pm$ ±0.11820	$-0.543380\pm$ ±0.001465	$1.01348\pm$ ±0.04888	$1.612030\pm$ ±0.009794	1.42185e –06
8.0	$-0.189572\pm$ ±0.007766	$8.65931\pm$ ±0.09223	$-0.582432\pm$ ±0.001427	$0.860135\pm$ ±0.037990	$1.79567\pm$ ±0.01090	1.35531e –06
16.0	$-0.224539\pm$ ±0.007578	$7.42345\pm$ ±0.07912	$-0.611889\pm$ ±0.001410	$0.778533\pm$ ±0.032410	$1.95505\pm$ ±0.01194	1.29922e –06
32.0	$-0.251850\pm$ ±0.007459	$6,67682\pm$ ±0.07126	$-0.635289\pm$ ±0.001402	$0.729967\pm$ ±0.028960	$2.09703\pm$ ±0.01291	1.24493e –06
64.0	$-0,274124\pm$ ±0.007376	$6.17642\pm$ ±0.06598	$-0.654558\pm$ ±0.001398	$0.697843\pm$ ±0.026600	$2.22594\pm$ ±0.01381	1.19305e –06
128.0	$-0.292732\pm$ ±0.007316	$5.81723\pm$ ±0.06219	$-0.654558\pm$ ±0.001398	$0.675414\pm$ ±0.024860	$2.34434\pm$ ±0.01466	1.14381e –06
256.0	$-0.308610\pm$ ±0.007272	$5.54758\pm$ ±0.05934	$-0.684823\pm$ ±0.001397	$0.659191\pm$ ±0.023530	$2.45415\pm$ ±0.01547	1.09728e –06

REFERENCES

1. **Maldacena J.M.,** The large N limit of superconformal field theories and supergravity, Adv. Theor. Math. Phys. 2 (2) (1998) 231−252.

2. **Peskin M.E., Schroeder D.V.,** An introduction to quantum field theory, Addison-Wesley Pub. Co., Reading, USA, 1995.

3. **De Teramond G.F., Brodsky S.J.,** Light-front holography: A first approximation to QCD, Phys. Rev. Lett. 102 (8) (2009) 081601.

4. **Brodsky S.J., de Teramond G.F.,** Light-front dynamics and AdS/QCD correspondence: The pion form factor in the space- and time-like regions, Phys. Rev. D. 77 (5) (2008) 056007.

5. **Maji T., Chakrabarti D.,** Light front quark-diquark model for the nucleons, Phys. Rev. D. 94 (9) (2016) 094020.

6. **Gutsche T., Lyubovitskij V.E., Schmidt I., Vega A.,** Nucleon resonances in AdS/QCD, Phys. Rev. D. 87 (1) (2013) 016917.

7. **Gutsche T., Lyubovitskij V.E., Schmidt I., Vega A.,** Light-front quark model consistent with Drell−Yan−West duality and quark counting rules, Phys. Rev. D. 89 (5) (2014) 054033 [Erratum: Phys. Rev. D. 92 (1) (2015) 019902].

8. **Bacchetta A., Conti F., Radici M.,** Transverse-momentum distributions in a diquark spectator model, Phys. Rev. D. 78 (7) (2008) 074010.

9. **Drell S.D., Yan T.M.,** Connection of elastic electromagnetic nucleon form-factors at large Q^2 and deep inelastic structure functions near threshold, Phys. Rev. Lett. 24 (4) (1970) 181−185.

10. **West G.B.,** Phenomenological model for the electromagnetic structure of the proton, Phys. Rev. Lett. 24 (21) (1970) 1206−1209.

11. **Ball R.D., Bertone V., Carrazza S., et al.,** Parton distributions with QED corrections, Nucl. Phys. B. 877 (2) (2013) 290−320.

12. **Nason P.,** Introduction to perturbative QCD, Lecture notes for the 11th Jorge Andre Swieca Summer School on Particle and Fields, January 14−27, 2001, Campos do Jordao, SP, Brazil (2002) 409−486.

13. **Pumplin J., Stump D.R., Huston J., et al.,** New generation of parton distributions with uncertainties from global QCD analysis, JHEP. 2002 (7) (2002) 12.

14. **Ball R.D., Bertone V., Carrazza S., et al.,** Parton distributions for the LHC run II, JHEP. 2015 (4) (2015) 40.

15. **Lepage G.P., Brodsky S.J.,** Exclusive processes in perturbative quantum chromodynamics, Phys. Rev. D. 22 (9) (1980) 2157.

16. **Ellis J.R., Hwang D. S., Kotzinian A.,** Sivers asymmetries for inclusive pion and kaon production in deep-inelastic scattering, Phys. Rev. D. 80 (7) (2009). 074033.

17. **Brodsky S.J., Cao F.-G., de Teramond G.F.,** Meson transition form factors in light-front holographic QCD, Phys. Rev. D. 84 (7) (2011) 075012.

18. **Abidin Z., Carlson C.E.,** Nucleon electromagnetic and gravitational form factors from holography, Phys. Rev. D. 79 (11) (2009) 115003.

19. **Gutsche T., Lyubovitskij V.E., Schmidt I., Vega A.**, Chiral symmetry breaking and meson wave functions in soft-wall AdS/QCD, Phys. Rev. D. 87 (5) (2013) 056001.

20. **Brodsky S.J., Drell S.D.,** The anomalous magnetic moment and limits on fermion substructure, Phys. Rev. D. 22 (8) (1980) 2236.

21. **Chakrabarti D., Mondal C.,** Generalized parton distributions for the proton in AdS/QCD, Phys. Rev. D. 88 (7) (2013) 073006.

22. **Gayou O., Wijesooriya K., Afanasev A., et al.,** Measurements of the elastic electromagnetic form-factor ratio $\mu_p G_{Ep}/G_{Mp}$ via polarization transfer, Phys. Rev. C. 64 (3) (2001) 038202.

23. **Gayou O., Aniol K.A., Averett T., et al.,** Measurement of G_{Ep}/G_{Mp} in $\mathbf{e}p \rightarrow e\mathbf{p}$ to $Q^2 = 5.6$ GeV^2, Phys. Rev. Lett. 88 (9) (2002) 092301.

24. **Arrington J., Melnitchouk W., Tjon J.A.,** Global analysis of proton elastic form factor data with two-photon exchange corrections, Phys. Rev. C. 76 (3) (2007) 035205.

25. **Punjabi V., Perdrisat C.F., Aniol K.A., et al.,** Proton elastic form-factor ratios to $Q^2 = 3.5$ GeV^2 by polarization transfer, Phys. Rev. C. 71 (5) (2005) 055202 [Erratum: Phys. Rev. C. 71 (6) (2005) 069902].

26. **Puckett A.J.R., Brash E.J., Jones M.K., et al.,** Recoil polarization measurements of the proton electromagnetic form factor ratio $Q^2 = 8.5$ GeV^2, Phys. Rev. Lett. 104 (24) (2010) 242301.

27. **Cates G.D., de Jager C.W., Riordan S., Wojtsekhowski B.,** Flavor decomposition of the elastic nucleon electromagnetic form factors, Phys. Rev. Lett. 106 (25) (2011) 252003.

28. **Diehl M., Kroll P.,** Nucleon form factors, generalized parton distributions and quark angular momentum, Eur. Phys. J. C. 73 (4) (2013) 2397.

29. **Altarelli G., Parisi G.,** Asymptotic freedom in parton language, Nucl. Phys. B. 126 (2) (1977) 298−318.

30. **Broniowski W., Arriola E.R., Golec-Biernat K.,** Generalized parton distributions of the pion in chiral quark models and their QCD evolution, Phys. Rev. D. 77 (3) (2008) 034023.

31. **Williams T., Kelley C.,** gnuplot 5.4. An interactive plotting program. Version 5.4. December, 2020, www.gnuplot.sourceforge.net. Accessed February 28, 2021.

32. **Del Debbio L., Forte S., Latorre J.I., et al.,** Neural network determination of parton distributions: the nonsinglet case, JHEP. 2007 (3) (2007) 39.

THE AUTHORS

RODRIGUEZ-AGUILAR Benjamin
Peter the Great St. Petersburg Polytechnic University
29 Politechnicheskaya St., St. Petersburg, 195251, Russian Federation
rodrigesagilar.l@edu.spbstu.ru

BERDNIKOV Yaroslav A.
Peter the Great St. Petersburg Polytechnic University
29 Politechnicheskaya St., St. Petersburg, 195251, Russian Federation
berdnikov@spbstu.ru

СПИСОК ЛИТЕРАТУРЫ

1. **Maldacena J.M.** The large N limit of super-conformal field theories and supergravity // Advances in Theoretical and Mathematical Physics. 1998. Vol. 2. No. 2. Pp. 231−252.

2. **Peskin M.E., Schroeder D.V.** An introduction to quantum field theory. Reading, USA: Addison-Wesley Pub. Co., 1995. 842 p.

3. **De Teramond G.F., Brodsky S.J.** Light-front holography: A first approximation to QCD // Physical Review Letters. 2009. Vol. 102. No. 8. P. 081601.

4. **Brodsky S.J., de Teramond G.F.** Light-front dynamics and AdS/QCD correspondence: The pion form factor in the space- and time-like regions // Physical Review. D. 2008. Vol. 77. No. 5. P. 056007.

5. **Maji T., Chakrabarti D.** Light front quark-diquark model for the nucleons // Physical Review. D. 2016. Vol. 94. No. 9. P. 094020.

6. **Gutsche T., Lyubovitskij V.E., Schmidt I., Vega A.** Nucleon resonances in AdS/QCD // Physical Review. D. 2013. Vol. 87. No. 1. P. 016917.

7. **Gutsche T., Lyubovitskij V.E., Schmidt I., Vega A.** Light-front quark model consistent with Drell − Yan − West duality and quark counting rules // Physical Review. D. 2014. Vol. 89. No. 5. P. 054033 [Erratum: Physical Review. D. 2015. Vol. 92. No. 1. P. 019902].

8. **Bacchetta A., Conti F., Radici M.** Transverse-momentum distributions in a diquark spectator model // Physical Review. D. 2008. Vol. 78. No. 7. P. 074010.

9. **Drell S.D., Yan T.M.** Connection of elastic electromagnetic nucleon form-factors at large Q^2 and deep inelastic structure functions near threshold // Physical Review Letters. 1970. Vol. 24. No. 4. Pp. 181−185.

10. **West G.B.** Phenomenological model for the electromagnetic structure of the proton // Physical Review Letters. 1970. Vol. 24. No. 21. Pp. 1206−1209.

11. **Ball R.D., Bertone V., Carrazza S., Del Debbio L., Forte S., Guffanti A., Hartland N.P., Rojo J.** Parton distributions with QED corrections // Nuclear Physics. B. 2013. Vol. 877. No. 2. Pp. 290−320.

12. **Nason P.** Introduction to perturbative QCD // Lecture notes for the 11th Jorge Andre Swieca Summer School on Particle and Fields. January 14 − 27, 2001, Campos do Jordao, SP, Brazil. 2002. Pp. 409−486.

13. **Pumplin J., Stump D.R., Huston J., Lai H.L., Nadolsky P.M., Tung W.K.** New generation of parton distributions with uncertainties from global QCD analysis // Journal of High Energy Physics. 2002. Vol. 2002. No. 7. P. 12.

14. **Ball R.D., Bertone V., Carrazza S., Deans C.S., Del Debbio L., Forte S., Guffanti A., Hartland N.P., Latorre J.I., Rojo J., Ubiali M.** Parton distributions for the LHC run II // Journal of High Energy Physics. 2015. Vol. 2015. No. 4. P. 40.

15. **Lepage G.P., Brodsky S.J.** Exclusive processes in perturbative quantum chromodynamics // Physical Review. D. 1980. Vol. 22. No. 9. P. 2157.

16. **Ellis J.R., Hwang D.S., Kotzinian A.** Sivers asymmetries for inclusive pion and kaon production in deep-inelastic scattering // Physical Review. D. 2009. Vol. 80. No. 7. P. 074033.

17. **Brodsky S.J., Cao F.-G., de Teramond G.F.** Meson transition form factors in light-front holographic QCD // Physical Review. D. 2011. Vol. 84. No. 7. P. 075012.

18. **Abidin Z., Carlson C.E.** Nucleon electromagnetic and gravitational form factors from holography // Physical Review. D. 2009. Vol. 79. No. 11. P. 115003.

19. **Gutsche T., Lyubovitskij V.E., Schmidt I., Vega A.** Chiral symmetry breaking and meson wave functions in soft-wall AdS/QCD // Physical Review. D. 2013. Vol. 87. No. 5. P. 056001.

20. **Brodsky S.J., Drell S.D.** The anomalous magnetic moment and limits on fermion substructure // Physical Review. D. 1980. Vol. 22. No. 9. P. 2236.

21. **Chakrabarti D., Mondal C.** Generalized parton distributions for the proton in AdS/QCD // Physical Review. D. 2013. Vol. 88. No. 7. P. 073006.

22. **Gayou O., Wijesooriya K., Afanasev A., et al.** Measurements of the elastic electromagnetic form-factor ratio $\mu_p G_{Ep}/G_{Mp}$ via polarization transfer // Physical Review. C. 2001. Vol. 64. No. 3. P. 038202.

23. **Gayou O., Aniol K.A., Averett T., et al.** Meas-

urement of G_{Mp}/G_{Ep} in e$p \rightarrow e\mathbf{p}$ to $Q^2 = 5.6$ GeV^2// Physical Review Letters. 2002. Vol. 88. No. 9. P. 092301.

24. **Arrington J., Melnitchouk W., Tjon J.A.** Global analysis of proton elastic form factor data with two-photon exchange corrections // Physical Review. C. 2007. Vol. 76. No. 3. P. 035205.

25. **Punjabi V., Perdrisat C.F., Aniol K.A., et al.** Proton elastic form-factor ratios to $Q^2 = 3.5$ GeV^2 by polarization transfer // Physical Review. C. 2005. Vol. 71. No. 5. P. 055202 [Erratum: Physical Review. C. 2005. Vol. 71. No. 6. P. 069902].

26. **Puckett A.J.R., Brash E.J., Jones M.K., et al.** Recoil polarization measurements of the proton electromagnetic form factor ratio $Q^2 = 8.5$ GeV^2 // Physical Review Letters. 2010. Vol. 104. No. 24. P. 242301.

27. **Cates G.D., de Jager C.W., Riordan S., Wojtsekhowski B.** Flavor decomposition of the elastic nucleon electromagnetic form factors // Physical Review Letters. 2011. Vol. 106. No. 25. P. 252003.

28. **Diehl M., Kroll P.** Nucleon form factors, generalized parton distributions and quark angular momentum // European Physical Journal. C. 2013. Vol. 73. No. 4. P. 2397.

29. **Altarelli G., Parisi G.** Asymptotic freedom in parton language // Nuclear Physics. B. 1977. Vol. 126. No. 2. Pp. 298−318.

30. **Broniowski W., Arriola E.R., Golec-Biernat K.** Generalized parton distributions of the pion in chiral quark models and their QCD evolution // Physical Review. D. 2008. Vol. 77. No. 3. P. 034023.

31. **Williams T., Kelley C.** gnuplot 5.4. An interactive plotting program. Version 5.4. December, 2020 // www.gnuplot.sourceforge.net. Accessed February 28, 2021.

32. **Del Debbio L., Forte S., Latorre J.I., Piccione A., J. Rojo J.** Neural network determination of parton distributions: the nonsinglet case // Journal of High Energy Physics. 2007. Vol. 2007. No. 3. P. 39.

СВЕДЕНИЯ ОБ АВТОРАХ

РОДРИГЕС-АГИЛАР Бенджамин — *студент магистратуры Высшей инженерно-физической школы Санкт-Петербургского политехнического университета Петра Великого, Санкт-Петербург, Российская Федерация.*

195251, Российская Федерация, г. Санкт-Петербург, Политехническая ул., 29
rodrigesagilar.l@edu.spbstu.ru

БЕРДНИКОВ Ярослав Александрович — *доктор физико-математических наук, профессор Высшей инженерно-физической школы Санкт-Петербургского политехнического университета Петра Великого, Санкт-Петербург, Российская Федерация.*

195251, Российская Федерация, г. Санкт-Петербург, Политехническая ул., 29
berdnikov@spbstu.ru

Radiophysics

AN ANALYSIS OF CORRECTIONS TO THE PROPAGATION CONSTANTS OF A MULTIMODE PARABOLIC OPTICAL FIBER UNDER BENDING

A.A. Markvart, L.B. Liokumovich, N.A. Ushakov

Peter the Great St. Petersburg Polytechnic University,
St. Petersburg, Russian Federation

The goal of our work was to study a circularly bent, weakly guiding, multimode optical fiber with a parabolic refractive index profile. With this in mind, the second-order corrections to propagation constants of longitudinally perturbed arbitrary dielectric waveguide's modes were found using the perturbation theory. Based on that general result, a simple analytic equation describing the corrections to the propagation constants of the modes in the bent parabolic optical fiber was derived. It was shown that the increments of squares of mode propagation constants were the same for all modes. Moreover, the increments of mode propagation constants' differences in the bent fiber were proportional to those in the straight fiber. The proportionality coefficient was independent of the mode number. The obtained results are of high importance for development of optical fiber sensors, in which fiber bending is possible.

Keywords: fiber, curvature, graded index, bent waveguide, perturbation analysis, propagation constant

АНАЛИЗ ПОПРАВОК К ПОСТОЯННЫМ РАСПРОСТРАНЕНИЯ В ИЗОГНУТОМ МНОГОМОДОВОМ ПАРАБОЛИЧЕСКОМ ОПТИЧЕСКОМ ВОЛОКНЕ

А.А. Маркварт, Л.Б. Лиокумович, Н.А. Ушаков

Санкт-Петербургский политехнический университет Петра Великого,
Санкт-Петербург, Российская Федерация

Работа посвящена исследованию равномерно изогнутого слабонаправляющего оптического многомодового волокна с параболическим профилем показателя преломления. В рамках формализма малых возмущений записана формула для поправок второго порядка малости к постоянным распространения мод равномерно возмущенного диэлектрического волновода. На этой основе получено простое аналитическое выражение для поправок к постоянным распространения мод изогнутого параболического многомодового волокна. Показано, что поправки к квадратам постоянных распространения мод одинаковы для всех мод. При этом поправки к разности постоянных распространения мод в изогнутом волокне пропорциональны разности постоянных распространения мод прямолинейного волокна с коэффициентом, не зависящим от номеров мод. Результат особенно важен для анализа интерферометрических оптоволоконных датчиков на основе изгиба чувствительного волокна.

Ключевые слова: оптическое волокно, градиентный профиль, изогнутый волновод, метод возмущений, постоянная распространения

Introduction

The fiber in any extended fiber optic paths has some degree of bending. This is undesirable in some systems, for instance, leading to optical losses in communication devices. Conversely, the operating principles of other types of systems are actually based on bending, for example, in optical modulators [1], multiplexers [2], splitters [3]; bending can also be measured using fiber optic sensors. In particular, fiber optic sensors allow tracking the state of buildings, structures and mechanical assemblies [4 − 6], monitoring human health [7 − 9] by monitoring the bending of the fiber; such sensors are used to fabricate medical devices [10], equipment in robotics [11], and for other purposes.

In view of the above, it is essential to develop an array of convenient analytical tools making it possible to calculate the effect of fiber bending on the parameters of light propagation in it. Recent studies have focused closely on analytical [12, 13] and numerical [14, 15] calculations of optical losses in bent fibers. However, the change in phase progression or propagation constants (PC) of the waveguide modes of optical fiber under bending is an equally important factor. For example, this change plays a decisive role in interferometric fiber optic sensors, where the interference signal directly depends on the difference in propagation constants (PCD) of the interfering modes [16 − 26]. Even though this issue is crucial for fiber optic bending sensors, scarce attention has been given in the literature to calculation of the corrections to mode PC under fiber bending, in particular, for the most common fiber with a parabolic refractive index. The well-known studies calculating the changes in the phase progression or propagation constants of waveguide modes under fiber bending [27 − 33] have failed to yield simple expressions for the corrections to the PC and PCD of the modes in a parabolic fiber. A general expression was introduced in [34] for the changes in the mode PC for the case of

uniform fiber perturbation, obtained from a system of differential equations for coupled modes. However, this expression does not allow formulating an explicit analytical expression for the case of a parabolic fiber, which would be convenient for computational estimates. Appendix 1 of this study contains this expression and its brief analysis.

The goal of this paper consists in analyzing the propagation constants and their difference for the case of a weakly guiding multimode optical fiber with a parabolic refractive index profile, uniformly bent in a circle.

In view of the goal set, we first derived a general formula for calculating the corrections to the PC of the modes of a dielectric waveguide uniformly perturbed along the axis (the method of small perturbations was used); the case of a parabolic optical fiber was analyzed in detail based on this formula.

Calculation of corrections to the PC of the mth mode of a perturbed dielectric waveguide

To apply the method of small perturbations to solving the problem, we rely on the approach used in monograph [35] for obtaining a first-order correction to the PC of the modes of a perturbed waveguide. We are going to establish below that the first-order correction vanishes in the case of uniform bending of the fiber. For this reason, we determined a correction for the second-order mode PC to account for the bending.

Based on this approach, let us formulate the statement of a specific problem. Suppose an unperturbed dielectric waveguide has a relative permittivity profile

$$\varepsilon_0\left(r,\varphi\right)=n_0^2\left(r,\varphi\right),$$

where n_0 is the refractive index profile; r, φ are the coordinates in a cylindrical coordinate system where the axis z coincides with the fiber axis.

If perturbation that is uniform along the axis is introduced, the relative permittivity profile of the perturbed waveguide can be written in the form

$$\varepsilon(r, \varphi) = \varepsilon_0(r, \varphi) + \Delta\varepsilon(r, \varphi). \quad (1)$$

Let the unperturbed modes have the form

$$\mathbf{E}'_m = \mathbf{E}_m(r, \varphi)\exp\left[i(\omega t - \beta_m z)\right],$$
$$m = 0, 1, 2, \ldots, \quad (2)$$

where the transverse mode functions $\mathbf{E}_m(r, \varphi)$ satisfy the unperturbed wave equation

$$\left[\nabla_t^2 + k_0^2\varepsilon_0\right]\cdot\mathbf{E}_m(r, \varphi) = \beta_m^2\mathbf{E}_m(r, \varphi). \quad (3)$$

Here we omitted the term $\nabla(\nabla\cdot\mathbf{E}'_m)$, which is justified for linearly polarized modes of optical fiber [36].

These modes are mutually orthogonal and satisfy the following orthogonality condition:

$$\int\mathbf{E}_m^*\cdot\mathbf{E}_l\, dS = N_m\delta_{ml}. \quad (4)$$

Consider the influence from the perturbation of relative permittivity $\Delta\varepsilon(r, \varphi)$, which is small compared with the magnitude of $\varepsilon(r, \varphi)$. Let us assume that such a small perturbation only causes small changes in mode functions and propagation constants.

Let the mode functions change by $\delta\mathbf{E}_m^{(1)}$, and the squares of the propagation constants by $\delta\beta_m^{2(1)}$. In this case, the wave equation takes the form

$$\left[\nabla_t^2 + k_0^2\varepsilon_0 + k_0^2\Delta\varepsilon\right]\cdot\left(\mathbf{E}_m + \delta\mathbf{E}_m^{(1)}\right) =$$
$$= \left(\beta_m^2 + \delta\beta_m^{2(1)}\right)\cdot\left(\mathbf{E}_m + \delta\mathbf{E}_m^{(1)}\right). \quad (5)$$

If we neglect the second-order terms $\Delta\varepsilon\cdot\delta\mathbf{E}_m^{(1)}$ and $\delta\beta_m^{2(1)}\cdot\delta\mathbf{E}_m^{(1)}$ and use relation (3), Eq. (5) can be written in a simpler form:

$$\left[\nabla_t^2 + k_0^2\varepsilon_0\right]\cdot\delta\mathbf{E}_m^{(1)} + k_0^2\Delta\varepsilon\cdot\mathbf{E}_m =$$
$$= \beta_m^2\cdot\delta\mathbf{E}_m^{(1)} + \delta\beta_m^{2(1)}\cdot\mathbf{E}_m. \quad (6)$$

To solve this equation, we expand $\delta\mathbf{E}_m^{(1)}$ in terms of the unperturbed mode functions:

$$\delta\mathbf{E}_m^{(1)} = \sum a_{ml}\mathbf{E}_l, \quad (7)$$

where a_{ml} are constant coefficients.

Substituting expression (7) for $\delta\mathbf{E}_m^{(1)}$ into Eq. (6) and using (3), we obtain the following relation:

$$\sum_l a_{ml}\left(\beta_l^2 - \beta_m^2\right)\cdot\mathbf{E}_l =$$
$$= \left(\delta\beta_m^{2(1)} - k_0^2\Delta\varepsilon\right)\cdot\mathbf{E}_m. \quad (8)$$

If relation (8) is scalarly multiplied by the complex conjugate quantity $\mathbf{E}_m^*$ and this product is integrated over the entire transverse plane, then the expression on the left-hand side will be equal to zero by virtue of orthogonality relation (4). Thus, we have the following expression:

$$\int\mathbf{E}_m^*\cdot\left(\delta\beta_m^{2(1)} - k_0^2\Delta\varepsilon\right)\cdot\mathbf{E}_m\, dS = 0. \quad (9)$$

Since $\delta\beta_m^{2(1)}$ is a constant, it follows from expression (9) that

$$\delta\beta_m^{2(1)} = \frac{k_0^2\int\mathbf{E}_m^*\cdot\Delta\varepsilon\cdot\mathbf{E}_m\, dS}{N_m}. \quad (10)$$

This expression gives the first-order correction to the square of the propagation constant β_m^2. Since the correction to the PC square is small, we can write the actual correction to the PC [35]:

$$\delta\beta_m = \delta\beta_m^2\big/2\beta_m.$$

As a result, we obtain the following expression:

$$\delta\beta_m^{(1)} = \frac{k_0^2\int\mathbf{E}_m^*\cdot\Delta\varepsilon\cdot\mathbf{E}_m\, dS}{2\beta_m N_m}. \quad (11)$$

To calculate the coefficients aml $a_{ml}(m \neq l)$, we scalarly multiply the left and right-hand sides of Eq. (8) by $\mathbf{E}_l^*$, $(m \neq l)$ and integrate over the entire transverse plane. Then the following expression can be written:

$$a_{ml} = \frac{k_0^2}{\left(\beta_m^2 - \beta_l^2\right) N_l} \int \mathbf{E}_m \cdot \Delta\varepsilon \cdot \mathbf{E}_l^* dS, \qquad (12)$$
$$l \neq m.$$

Thus, we obtained (with an accuracy up to notations) expressions for the first-order correction to the PC and coefficients $a_{ml}(m \neq l)$, similar to those given in monograph [35], except for the normalization parameter N_m introduced.

Similarly, we derive the second-order corrections to the mode PC. For this purpose, we consider the wave equation in the form

$$\left[\nabla_t^2 + k_0^2\varepsilon_0 + k_0^2\Delta\varepsilon\right] \times$$
$$\times\left(\mathbf{E}_m + \delta\mathbf{E}_m^{(1)} + \delta\mathbf{E}_m^{(2)}\right) =$$
$$= \left(\beta_m^2 + \delta\beta_m^{2\,(1)} + \delta\beta_m^{2\,(2)}\right) \times \qquad (13)$$
$$\times\left(\mathbf{E}_m + \delta\mathbf{E}_m^{(1)} + \delta\mathbf{E}_m^{(2)}\right),$$

where $\delta\mathbf{E}_m^{(2)}, \delta\beta_m^{2\,(2)}$ are the second-order corrections to the mode function and the PC square, respectively.

If we use relation (3) and further assumptions, such as neglecting the third and fourth-order terms and taking (6) as an initial approximation, Eq. (13) can be reduced to the following form:

$$\left[\nabla_t^2 + k_0^2\varepsilon_0\right] \cdot \delta\mathbf{E}_m^{(2)} + k_0^2\Delta\varepsilon\delta\mathbf{E}_m^{(1)} =$$
$$\beta_m^2\delta\mathbf{E}_m^{(2)} + \delta\beta_m^{2\,(1)}\delta\mathbf{E}_m^{(1)} + \delta\beta_m^{2\,(2)}\mathbf{E}_m. \qquad (14)$$

To solve this equation, we expand $\delta\mathbf{E}_m^{(2)}$ in terms of the unperturbed mode functions:

$$\delta\mathbf{E}_m^{(2)} = \sum_l b_{ml}\mathbf{E}_l, \qquad (15)$$

where b_{ml} are constant coefficients.

Substituting expressions (7) for $\delta\mathbf{E}_m^{(1)}$ and (15) for $\delta\mathbf{E}_m^{(2)}$ into Eq. (14), and using (3), we obtain the following relation:

$$\sum_l b_{ml}\left(\beta_l^2 - \beta_m^2\right) \cdot \mathbf{E}_l +$$
$$+ k_0^2\Delta\varepsilon\sum_l a_{ml}\mathbf{E}_l = \qquad (16)$$

$$= \delta\beta_m^{2\,(1)}\sum_l a_{ml}\mathbf{E}_l + \delta\beta_m^{2\,(2)} \cdot \mathbf{E}_m. \qquad (16)$$

If this ratio is scalarly multiplied by $\mathbf{E}_m^*$ and integrated over the entire transverse plane, then the first term on the left-hand side and all terms of the sum, except for the term with $l = m$, are equal to zero by virtue of orthogonality relation (4).

If we also use expression (10), then we can write the following ratio:

$$k_0^2\sum_l a_{ml}\int \mathbf{E}_m^* \cdot \Delta\varepsilon \cdot \mathbf{E}_l dS =$$
$$= k_0^2 a_{mm}\int \mathbf{E}_m^* \cdot \Delta\varepsilon \cdot \mathbf{E}_m dS + \qquad (17)$$
$$+ \delta\beta_m^{2\,(2)}N_m.$$

Then, keeping in mind that the first term on the right-hand side of this expression is mutually canceled out with the summation term $l = m$ in its left-hand side, and using expression (12), the second-order correction to the PC square of the mth mode can be written in the following form in the case when the waveguide is perturbed uniformly along the axis:

$$\delta\beta_m^{2\,(2)} = \sum_{l \neq m}\left(\beta_l^2 - \beta_m^2\right) a_{ml}a_{lm}, \qquad (18)$$

or

$$\delta\beta_m^{2\,(2)} = \sum_{l \neq m}\frac{k_0^4}{\left(\beta_m^2 - \beta_l^2\right) N_m N_l} \times$$
$$\times\left|\int \mathbf{E}_m \cdot \Delta\varepsilon \cdot \mathbf{E}_l^* dS\right|^2. \qquad (19)$$

Given that $\delta\beta_m^{2\,(2)}$ is the correction to the PC square, and the actual correction to the PC is

$$\delta\beta_m^{(2)} = \delta\beta_m^{2\,(2)}\big/2\beta_m,$$

we obtain the following expression:

$$\delta\beta_m^{(2)} = \sum_{l \neq m}\frac{k_0^4}{2\beta_m\left(\beta_m^2 - \beta_l^2\right) N_m N_l} \times$$
$$\times\left|\int \mathbf{E}_m \cdot \Delta\varepsilon \cdot \mathbf{E}_l^* dS\right|^2. \qquad (20)$$

Expressions (19) and (20) are the desired ex-

pressions for the second-order correction to the PC of the optical fiber mode.

Notably, expressions (19) and (20) hold true for any dielectric waveguides where the term $\nabla(\nabla \cdot \mathbf{E}'_m)$ can be neglected in formulating the wave equation.

Appendix 2 of this paper compares Eq. (20) with the formula obtained by the approach used in [34].

Case of uniform bending of optical fiber with a parabolic refractive index profile

Expressions (11) and (20) describe the general form of corrections to the mode PC under perturbation of the dielectric waveguide. Let us consider their specific form for the case of a uniformly bent parabolic fiber.

The relative permittivity profile of parabolic optical fiber is described by the following expression:

$$\varepsilon(r) = n^2(r) =$$
$$= n_1^2 \begin{cases} 1 - 2\Delta \cdot (r^2/a^2), & r < a, \\ 1 - 2\Delta, & r > a, \end{cases} \quad (21)$$

where a is the radius of the core; n_1 is the maximum value of the refractive index in the cross section; Δ is the relative difference of refractive indices,

$$\Delta = \left(n_1^2 - n_2^2\right)\big/2n_1^2$$

(n_2 is the refractive index in the cladding region).

The eigenmodes are described as linearly polarized LP_{lp}-modes within the model of weakly guiding fiber with an unlimited parabolic profile [37]. The scalar component of the mode has the form

$$E'_{lp} = E_{lp}(r,\varphi)\exp\left[j\left(\omega t - \beta_{lp} z\right)\right], \quad (22)$$

where $E_{lp}(r, \varphi)$ are the scalar transverse mode functions, l is the azimuthal order of the mode, and the index p is the radial order of the mode.

Transverse mode functions are given by the following expressions:

$$E_{lp}(r,\varphi) = \Psi(r) \cdot \begin{pmatrix} \cos l\varphi \\ \sin l\varphi \end{pmatrix}, \quad (23)$$

$$\Psi(r) = \left(\sqrt{2}\,\frac{r}{w}\right)^l L_q^{(l)}\left(2\frac{r^2}{w^2}\right)\exp\left[-\frac{r^2}{w^2}\right]. \quad (24)$$

Here $L_q^{(l)}$ are the generalized Laguerre polynomials of order l and degree q ($q = p - 1$); they have the form

$$L_q^{(l)}(u) = \sum_{\nu=0}^{q}\binom{q+l}{q-\nu}\frac{(-u)^{\nu}}{\nu!}. \quad (25)$$

The parameter w gives the boundaries where the field exists in the radial direction and is defined by the following expression:

$$w = \sqrt{\frac{2a}{n_1 k_0 \sqrt{2\cdot\Delta}}}. \quad (26)$$

The propagation constant β_{lp} of the LP_{lp}-mode, taking into account expression (26) and the data from monograph [37], is found by the expression

$$\beta_{lp} = n_1 k_0 \sqrt{1 - \frac{4}{w^2}(2p + l - 1)}. \quad (27)$$

To calculate the corrections to the PC of the LP_{lp}-mode, we use the normalized mode functions:

$$E_{lpN} = \frac{E_{lp}}{\sqrt{\int E_{lp}E_{lp}dS}}. \quad (28)$$

In this case, the normalization parameter Nlp introduced in condition (4) is equal to unity. Then relations (10), (11), (19), and (20) can be rewritten in the following form:

$$\delta\beta_{lp}^{2\,(1)} = k_0^2 \int E_{lpN} \cdot \Delta\varepsilon \cdot E_{\eta\mu N}dS, \quad (29)$$

$$\delta\beta_{lp}^{(1)} = \frac{k_0^2}{2\beta_{lp}}\int E_{lpN} \cdot \Delta\varepsilon \cdot E_{\eta\mu N}dS, \quad (30)$$

105

$$\delta\beta_{lp}^{2\,(2)} = \sum_{lp \ne \eta\mu} \frac{k_0^4}{\left(\beta_{lp}^2 - \beta_{\eta\mu}^2\right)} \times$$

$$\times\left(\int E_{lpN} \cdot \Delta\varepsilon \cdot E_{\eta\mu N} dS\right)^2, \qquad (31)$$

$$\delta\beta_{lp}^{(2)} = \sum_{lp \ne \eta\mu} \frac{k_0^4}{2\beta_{lp}\left(\beta_{lp}^2 - \beta_{\eta\mu}^2\right)} \times$$

$$\times\left(\int E_{lpN} \cdot \Delta\varepsilon \cdot E_{\eta\mu N} dS\right)^2. \qquad (32)$$

The following common approach can be applied to analyze the bending of a fiber with the radius R (see Figure) [37]: instead of a fiber uniformly bent around the circumference of the fiber, we introduce an equivalent straight fiber with a relative dielectric permittivity profile $\varepsilon(r, \varphi)$ of the form (1). In this case, $\varepsilon_0(r, \varphi)$ is the relative permittivity profile of an unbent straight fiber, and the perturbation $\Delta\varepsilon(r, \varphi)$ is described by the expression

$$\Delta\varepsilon = \frac{2n_1^2 r \cos\varphi}{R}. \qquad (33)$$

In this case, the distributions of the transverse fields coincide for the bent and equivalent straight fibers [37].

Within the framework of the model for the equivalent straight fiber, the first-order correction to the PC of the LP_{lp}-mode for bent fiber can be obtained by substituting expression (33) into expression (30). However, it is easy to prove that it is equal to zero due to the antisymmetric nature of the perturbation. Therefore, it is insufficient to confine the consideration with only the first correction in the bending case.

Substituting expression (33) into expression (31), we obtain a second-order correction to the PC square of the LP_{lp}-mode:

$$\delta\beta_{lp}^{2\,(2)} = \sum_{lp \ne \eta\mu} \frac{4k_0^4 n_1^4}{\left(\beta_{lp}^2 - \beta_{\eta\mu}^2\right)R^2} I_{lp,\eta\mu}^2; \qquad (34)$$

here we have introduced the following notation for the integral characterizing the relationship between the LP_{lp}-mode and the $LP_{\eta\mu}$-mode:

$$I_{lp,\eta\mu} = \iint E_{lpN} \cdot r^2 \cos\varphi \cdot E_{\eta\mu N} dr d\varphi. \qquad (35)$$

This integral can be calculated explicitly for all combinations of LP_{lp}-modes [37]. The following integrals (35) are nonzero in this case:

1. Integral characterizing the relationship of the LP_{lp}-mode with the $LP_{l+1,p}$-mode, i.e.,
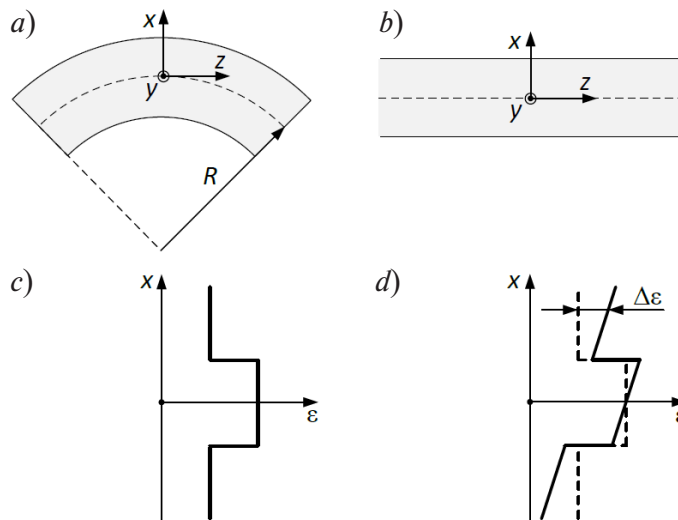
Schematic diagrams for bending analysis for fiber with the radius R: *a, b* are the bent and equivalent straight fiber; *c, d* are the profiles of relative permittivity for fibers *a* and *b*, respectively

$$I_{lp,(l+1)p} = \frac{w}{2}\sqrt{\frac{p+l}{\sigma_l}}; \qquad (36)$$

2. Integral characterizing the relationship of the LP_{lp}-mode with the $LP_{l-1,p+1}$-mode, i.e.,

$$I_{lp,(l-1)(p+1)} = \frac{w}{2}\sqrt{\frac{p}{\sigma_{l-1}}}; \qquad (37)$$

3. Integral characterizing the relationship of the LP_{lp}-mode with the $LP_{l-1,p}$-mode, i.e.,

$$I_{lp,(l-1)p} = \frac{w}{2}\sqrt{\frac{p+l-1}{\sigma_{l-1}}}; \qquad (38)$$

4. Integral characterizing the relationship of the LP_{lp}-mode with the $LP_{l+1,p-1}$-mode, i.e.,

$$I_{lp,(l+1)(p-1)} = \frac{w}{2}\sqrt{\frac{p-1}{\sigma_l}}, \qquad (39)$$

at the same time, $\sigma_l = 1$ if $l = 0$, and $\sigma_l = 2$ if $l \neq 0$.

The remaining modes turned out to be unrelated to the LP_{lp}-mode. We should note that all coupled modes differ by unity in their composite mode number $m = 2p + l - 1$.

Thus, the absolute value of the difference between the PC squares of the coupled modes does not depend on the values of l and p and follows the expression

$$\left|\beta_{lp}^2 - \beta_{\eta\mu}^2\right| = \frac{4}{w^2}. \qquad (40)$$

Therefore, the factor in front of the integral in expression (34) can be simplified and taken outside the sum sign (accounting for the plus or minus signs). Then expression (34) can be rewritten as follows:

$$\delta\beta_{lp}^{2\,(2)} = \frac{k_0^4 n_1^4 w^2}{R^2} \times$$
$$\times\left(I_{lp,(l+1)p}^2 + I_{lp,(l-1)(p+1)}^2 - I_{lp,(l-1)p}^2 - I_{lp,(l+1)(p-1)}^2\right). \qquad (41)$$

By enumerating all possible combinations of the indices l and p, it is easy to prove that the

expression in brackets in relation (41) is equal to $w^2/4$ regardless of the values of the indices and the orientation of the mode function LP_{lp} ($\cos(l\varphi)$ or $\sin(l\varphi)$).

Thus, the desired increment of the propagation constant square of the LP_{lp}-mode in a parabolic optical fiber takes on a relatively simple form:

$$\delta\beta_{lp}^2 = \delta\beta_{lp}^{2\,(2)} = \frac{k_0^4 n_1^4 w^4}{4R^2} = \frac{k_0^2 n_1^2 a^2}{2\Delta \cdot R^2} \qquad (42)$$

and, importantly, does not depend on the mode number.

The actual increment of the PC $\delta\beta_{lp} = \delta\beta_{lp}^2\big/2\beta_{lp}$ is written as

$$\delta\beta_{lp} = \frac{k_0^2 n_1^2 a^2}{4\beta_{lp} \cdot \Delta \cdot R^2}. \qquad (43)$$

Now we can proceed to calculating the difference

$$\Delta\beta_{lp,\eta\mu}^b = \beta_{lp}^b - \beta_{\eta\mu}^b$$

that is the difference in the mode propagation constants under fiber bending, which is important for calculations of interferometric sensors:

$$\Delta\beta_{lp,\eta\mu}^b =$$
$$= \Delta\beta_{lp,\eta\mu}^s - \frac{k_0^2 n_1^2 a^2}{4\cdot\Delta\cdot\beta_{lp}^s\beta_{\eta\mu}^s R^2}\Delta\beta_{lp,\eta\mu}^s, \qquad (44)$$

where $\Delta\beta_{lp,\eta\mu}^b$, $\Delta\beta_{lp,\eta\mu}^s$ are the mode PCD of bent and straight fibers, respectively.

The resulting expression can be simplified taking into account that $\beta_{lp}^s\beta_{\eta\mu}^s \approx k_0^2 n_1^2$:

$$\Delta\beta_{lp,\eta\mu}^b = \Delta\beta_{lp,\eta\mu}^s\left(1 - \frac{a^2}{4\Delta \cdot R^2}\right). \qquad (45)$$

Thus, the change in mode PCD in a bent parabolic optical fiber is proportional to the mode PCD in a straight fiber $\Delta\beta_{lp,\eta\mu}^s$ with the proportionality coefficient $a^2/(4\Delta)$ independent of mode numbers. It is important for assessing the efficiency of fiber optic sensors that detect bend-

ing to obtain an estimate of the sensitivity of the change in mode PCD to the inverse square of the bending radius, which, according to expression (45), has the form

$$\frac{\partial\left(\Delta\beta_{lp,\eta\mu}^{b}\right)}{\partial\left(\dfrac{1}{R^{2}}\right)} = \frac{a^{2}}{4\Delta}\Delta\beta_{lp,\eta\mu}^{s}. \qquad (46)$$

It should be borne in mind that both the theoretical formulas (22) − (27) for the mode functions and the mode PC of a parabolic fiber, and the formulas (42) − (46) that we derived for the corrections to the PC and PCD of the mode were obtained in the approximation of an unlimited parabolic profile of the fiber's refractive index. For this reason, strictly speaking, they cannot be used to describe the behavior of modes close to cutoff, whose field appears to largely extend beyond the fiber core.

The elasto-optical effect should be taken into account in the formulation of expression (33) for the perturbed profile of relative permittivity to use the expressions obtained for analysis of real fibers. The following approach can be used for approximate account of this effect: the real curvature radius of the bend is replaced with an effective one, for example, $R_{eff} = 1.27\,R$ for glass fiber [30].

Conclusion

To analyze the influence of bending of a parabolic multimode fiber on the propagation constants of the modes and their differences, we have obtained analytical expressions for second-order corrections using the method of small perturbations. We have established that the increments to the squares of mode propagation constants are the same for all modes. Furthermore, we have confirmed that the change in the difference between the mode propagation constants in a bent fiber is proportional to the difference in the mode propagation constants in a straight fiber with a proportionality factor that does not depend on the mode numbers. In this case, the magnitude of the changes depends on the ratio between the radius of the fiber core and the relative difference between the refractive indices of the core and the

cladding. The result obtained has major importance for developing interferometric fiber optic sensors with fiber bending detection, as well as in analysis of phase effects in fiber optic systems with multimode fibers. The generalized expression derived for the second-order correction (20) to the mode propagation constant presents interest not only for analysis of optical fibers but also arbitrary dielectric waveguides with uniform perturbation.

Appendix 1

Known estimate of the correction to the PC of the mth mode of optical fiber with a parabolic profile under uniform perturbation

The influence of fiber bending on the PC of fiber modes is analyzed in [34] but since the first-order correction vanishes in the perturbation method, the authors suggested using, instead of the perturbation method, a more specific approach to analyzing the system of differential equations of coupled modes.

As a result, the following estimate for the PC increment was obtained in [34]:

$$\delta\beta_{m} = -\sum_{l}\frac{\kappa_{ml}\kappa_{lm}}{\beta_{m}-\beta_{l}}, \qquad (A1)$$

where $\delta\beta_{m}$ is the correction to the PC of an mth mode due to fiber perturbation leading to mode coupling; β_{m} is the PC of an mth mode without perturbation; κ_{mn} is the coupling coefficient between the mth and n^{th} mode.

The expression for the coupling coefficients can be found, for example, in [36, 37]:

$$\kappa_{ml} = \frac{k_{0}^{2}}{2\beta_{m}}\int\int E_{mN}\left(r,\varphi\right)\cdot\Delta\varepsilon\left(r,\varphi\right)\times$$
$$\times E_{lN}\left(r,\varphi\right)\cdot r dr d\varphi, \qquad (A2)$$

where k_{0} is the wavenumber; $\Delta\varepsilon(r,\varphi)$ is the perturbation of the profile of the relative permittivity of the fiber, in particular, under bending; $E_{mN}(r,\varphi)$ is the normalized mode function; r,φ are the coordinates in a cylindrical coordinate system where the z axis coincides with the fiber axis. In this case, the mode functions satisfy the

normalization condition:

$$\iint E_{mN}^2 r dr d\varphi = 1. \qquad (A3)$$

If we substitute the expression (A2) to (A1), we can obtain an estimate for the increment of the mode PC:

$$\delta\beta_m = \sum_{l \neq m} \frac{k_0^4}{4\beta_m\beta_l\left(\beta_m - \beta_l\right)} \times \\ \times \left(\iint E_{mN} \cdot \Delta\varepsilon \cdot E_{lN} r dr d\varphi\right)^2. \qquad (A4)$$

In the case of an optical parabolic fiber in the formalism LP_{lp}, the mode PC can be found using expression (27). The integrals in estimate (A4) for the given fiber are also known (see Eqs. (35) − (39)). However, the expression obtained based on (A4) still remains cumbersome, complicating analysis of the physical meaning.

Appendix 2

Comparison of expressions for the PC increment under fiber bending

Let us compare expression (20) that we obtained to expression (A4). Notice that estimate (20) differs from estimate (A4) in the denominator of the factor in front of the integral. The denominator in expression (20) can be written in the following form:

$$2\beta_m\left(\beta_m^2 - \beta_l^2\right) = 2\beta_m\left(\beta_m + \beta_l\right)\left(\beta_m - \beta_l\right).$$

For a weakly guiding optical fiber, when the relative difference in refractive indices tends to zero, $\beta_m \approx \beta_l$, therefore the following relation holds true:

$$2\beta_m\left(\beta_m + \beta_l\right)\left(\beta_m - \beta_l\right) \approx 4\beta_m\beta_l\left(\beta_m - \beta_l\right)$$

and the formulas converge asymptotically.

However, Eq. (20) seems to be more appropriate for use for three reasons:

firstly, it was obtained by method of small perturbations generally accepted for such analysis, yielding simple and understandable approximations; on the contrary, a number of approximations made in [34] do not allow clearly assessing the order of smallness of the correction to the PC and the conditions for the applicability of the obtained estimate;

secondly, we obtained a simple and convenient expression for the PC increments under bending of a parabolic fiber from Eq. (20), while expression (A4) is a complex sum where the PC has to be written out for all modes associated with the calculated one;

thirdly, the expression that we obtained allowed drawing important physical conclusions about the increment of the mode PC under bending (they are discussed in Conclusion), while it is difficult to draw such conclusions based on expression (A4).

REFERENCES

1. **Bösch M., Liakatas I., Jäger M., et al.,** Polymer based electro-optic inline fiber modulator, Ferroelectrics. 223 (1) (1999) 405−412.

2. **Diemeer J., Spiekman L.H., Ramsamoedj R., Smit M.K.,** Polymeric phased array wavelength multiplexer operating around 1550 nm, Electron. Lett. 32 (12) (1996) 1132−1133.

3. **Li X.-Y., Sun B., Yu Y.-Y., He K.-P.,** Bending dual-core photonic crystal fiber coupler, Optik (Stuttg.). 125 (21) (2014) 6478−6482.

4. **Inaudi D., Vurpillot S., Casanova N., Kronenberg P.,** Structural monitoring by curvature analysis using interferometric fiber optic sensors, Smart Mater. Struct. 7 (2) (1998) 199−208.

5. **Liu M.Y., Zhou Sh.-G., Song H., et al.,** A novel fibre Bragg grating curvature sensor for structure deformation monitoring, Metrol. Meas. Syst. 25 (3) (2018) 577−587.

6. **Zhi G., Di H.,** Wind speed monitoring system based on optical fiber curvature sensor, Opt. Fiber

Technol. 62 (March) (2021) 102467.

7. **Ushakov N., Markvart A., Kulik D., Liokumovich L.,** Comparison of pulse wave signal monitoring techniques with different fiber-optic interferometric sensing elements, Photonics. 8 (5) (2021) 142.

8. **Li X., Liu D., Kumar R., et al.,** A simple optical fiber interferometer based breathing sensor, Meas. Sci. Technol. 28 (3) (2017) 035105.

9. **Irawati N., Hatta A.M., Yhuwana Y.G.Y.,** Sekartedjo, Heart rate monitoring sensor based on singlemode-multimode-singlemode fiber, Photonic Sensors. 10 (2) (2020) 186−193.

10. **Novais S., Silva S.O., Frazão O.,** Curvature detection in a medical needle using a Fabry-Perot cavity as an intensity sensor, Measurement. 151 (February) (2020). 107160.

11. **He Y., Zhang X., Zhu L., et al.,** Curvature and force measurement of soft manipulator based on stretchable helical optic fibre, Opt. Fiber Technol. 53 (December) (2019) 102010.

12. **Savović S., Djordjevich A., Savović I.,** Theoretical investigation of bending loss in step-index plastic optical fibers, Opt. Commun. 475 (15 November) (2020) 126200.

13. **Marcuse D.,** Field deformation and loss caused by curvature of optical fibers, J. Opt. Soc. Am. 66 (4) (1976) 311−320.

14. **Schermer R., Cole M.,** Improved bend loss formula verified for optical fiber by simulation and experiment, IEEE J. Quant. Electron. 43 (10) (2007) 899−909.

15. **Velamuri A.V., Patel K., Sharma I., et al.,** Investigation of planar and helical bend losses in single- and few-mode optical fibers, J. Light. Technol. 37 (14) (2019) 3544−3556.

16. **Silva S., Frazão O., Viegas J., et al.,** Temperature and strain-independent curvature sensor based on a singlemode/multimode fiber optic structure, Meas. Sci. Technol. 22 (8) (2011) 085201.

17. **Wu Q., Semenova Y., Wang P., et al.,** Experimental demonstration of a simple displacement sensor based on a bent single-mode-multimode-single-mode fiber structure, Meas. Sci. Technol. 22 (2) (2011) 025203.

18. **Yang B., Niu Y., Yang B., et al.,** High sensitivity curvature sensor with intensity demodulation based on single-mode-tapered multi-

mode-single-mode fiber, IEEE Sens. J. 18 (3) (2018) 1094−1099.

19. **Su J., Dong X., Lu C.,** Property of bent few-mode fiber and its application in displacement sensor, IEEE Photonics Technol. Lett. 28 (13) (2016) 1387−1390.

20. **Ivanov O.V.,** Mode interaction in a structure based on optical fiber with depressed inner cladding, J. Commun. Technol. Electron. 63 (10) (2018) 1143−1151.

21. **Chen J., Lu P., Liu D., et al.,** Optical fiber curvature sensor based on few mode fiber, Optik (Stuttg.). 125 (17) (2014) 4776−4778.

22. **Dong S., Pu S., Huang J.,** Highly sensitive curvature sensor based on singlemode-multimode-singlemode fiber structures, J. Optoelectron. Adv. Mater. 16 (11−12) (2014) 1247−1251.

23. **Gong Y., Zhao T., Rao Y.-J. Wu Y.,** All-fiber curvature sensor based on multimode interference, IEEE Photonics Technol. Lett. 23 (11) (2011) 679−681.

24. **Tian K., Xin Y., Yang W., et al.,** A curvature sensor based on twisted single-mode-multimode-single-mode hybrid optical fiber structure, J. Light. Technol. 35 (9) (2017) 1725−1731.

25. **Petrov A.V., Chapalo I.E., Bisyarin M.A., Kotov O.I.,** Intermodal fiber interferometer with frequency scanning laser for sensor application, Applied Optics. 59 (33) (2020) 10422−10431.

26. **Kosareva L.I., Kotov O.I., Liokumovich L.B., et al.,** Two mechanisms of phase modulation in multimode fiber-optic interferometers, Tech. Phys. Lett. 26 (1) (2000) 70−74.

27. **Oksanen M.I.,** Perturbational analysis of curved anisotropic optical fibers, J. Opt. Soc. Am. A. 6 (2) (1989) 180−189.

28. **Shemirani M.B., Mao W., Panicker R.A., Kahn J.M.,** Errata to "Principal modes in graded-index multimode fiber in presence of spatial- and polarization-mode coupling", J. Light. Technol. 29 (12) (2011) 1900−1900.

29. **Garth S.J.,** Modes and propagation constants on bent depressed inner cladding optical fibers, J. Light. Technol. 7 (12) (1989) 1889−1894.

30. **Schermer R.T.,** Mode scalability in bent optical fibers, Opt. Express. 15 (24) (2007) 15674−15701.

31. **Garth S.J.,** Modes on a bent optical waveguide, IEEE Proc. J.: Optoelectronics. 134 (4)

(1987) 221−229.

32. **Kumar A., Goyal I.C., Ghatak A.K.,** Effect of curvature on dispersion in multimode parabolic index fibres, Opt. Acta: Internat. J. Opt. 22 (11) (1975) 947−953.

33. **Malik D.P.S., Gupta A., Ghatak A.K.,** Propagation of a Gaussian beam through a circularly curved selfoc fiber, Appl. Opt. 12 (12) (1973) 2923−2926.

34. **Taylor H.,** Bending effects in optical fibers, J. Light. Technol. 2 (5) (1984) 617−628.

35. **Yariv A., Yeh P.,** Optical waves in crystals. Willey, New York, 1984.

36. **Yariv A., Yeh P.,** Photonics: optical electronics in modern communications. Oxford University Press, New York, 2007.

37. **Unger H.-G.,** Planar optical waveguides and fibres. Clarendon Press, Oxford, 1977.

THE AUTHORS

MARKVART Aleksandr A.
Peter the Great St. Petersburg Polytechnic University
29 Politechnicheskaya St., St. Petersburg, 195251, Russian Federation
markvart_aa@spbstu.ru

LIOKUMOVICH Leonid B.
Peter the Great St. Petersburg Polytechnic University
29 Politechnicheskaya St., St. Petersburg, 195251, Russian Federation
leonid@spbstu.ru

USHAKOV Nikolai A.
Peter the Great St. Petersburg Polytechnic University
29 Politechnicheskaya St., St. Petersburg, 195251, Russian Federation
n.ushakoff@spbstu.ru

СПИСОК ЛИТЕРАТУРЫ

1. **Bösch M., Liakatas I., Jäger M., Bosshard Ch., Günter P.** Polymer based electro-optic inline fiber modulator // Ferroelectrics. 1999. Vol. 223. No. 1. Pp. 405−412.

2. **Diemeer J., Spiekman L.H., Ramsamoedj R., Smit M.K.** Polymeric phased array wavelength multiplexer operating around 1550 nm // Electronics Letters. 1996. Vol. 32. No. 12. Pp. 1132−1133.

3. **Li X.-Y., Sun B., Yu Y.-Y., He K.-P.** Bending dual-core photonic crystal fiber coupler // Optik (Stuttgart). 2014. Vol. 125. No. 21. Pp. 6478−6482.

4. **Inaudi D., Vurpillot S., Casanova N., Kronenberg P.** Structural monitoring by curvature analysis using interferometric fiber optic sensors // Smart Materials and Structures. 1998. Vol. 7. No. 2. Pp. 199−208.

5. **Liu M.Y., Zhou Sh.-G., Song H., Zhou W.-J., Zhang X.** A novel fibre Bragg grating curvature sensor for structure deformation monitoring // Metrology and Measurement Systems. 2018. Vol. 25. No. 3. Pp. 577−587.

6. **Zhi G., Di H.** Wind speed monitoring system based on optical fiber curvature sensor // Optical Fiber Technology. 2021. Vol. 62. March. P. 102467.

7. **Ushakov N., Markvart A., Kulik D., Liokumovich L.** Comparison of pulse wave signal monitoring techniques with different fiber-optic interferometric sensing elements // Photonics. 2021. Vol. 8. No. 5. P. 142.

8. **Li X., Liu D., Kumar R., Ng W.P., Fu Y.-q., Yuan J., Yu Ch.** A simple optical fiber interferometer based breathing sensor // Measurement Science

and Technology. 2017. Vol. 28. No. 3. P. 035105.

9. **Irawati N., Hatta A.M., Yhuwana Y.G.Y., Sekartedjo.** Heart rate monitoring sensor based on singlemode-multimode-singlemode fiber // Photonic Sensors. 2020. Vol. 10. No. 2. Pp. 186−193.

10. **Novais S., Silva S.O., Frazão O.** Curvature detection in a medical needle using a Fabry-Perot cavity as an intensity sensor // Measurement. 2020. Vol. 151. February. P. 107160.

11. **He Y., Zhang X., Zhu L., Sun G., Lou X., Dong M.** Curvature and force measurement of soft manipulator based on stretchable helical optic fibre // Optical Fiber Technology. 2019. Vol. 53. December. P. 102010.

12. **Savović S., Djordjevich A., Savović I.** Theoretical investigation of bending loss in step-index plastic optical fibers // Optics Communications. 2020. Vol. 475. 15 November. P. 126200.

13. **Marcuse D.** Field deformation and loss caused by curvature of optical fibers // Journal of the Optical Society of America. 1976. Vol. 66. No. 4. Pp. 311−320.

14. **Schermer R., Cole M.** Improved bend loss formula verified for optical fiber by simulation and experiment // IEEE Journal of Quantum Electronics. 2007. Vol. 43. No. 10. Pp. 899−909.

15. **Velamuri A.V., Patel K., Sharma I., Gupta S.S, Gaikwad S., Krishnamurthy P.K.** Investigation of planar and helical bend losses in single- and few-mode optical fibers // Journal of Lightwave Technology. 2019. Vol. 37. No. 14. Pp. 3544−3556.

16. **Silva S., Frazão O., Viegas J., Ferreira L.A., Araújo F.M., Malcata F.X., Santos J.L.** Temperature and strain-independent curvature sensor based on a singlemode/multimode fiber optic structure // Measurement Science and Technology. 2011. Vol. 22. No. 8. P. 085201.

17. **Wu Q., Semenova Y., Wang P., Hatta A.M., Farrell G.** Experimental demonstration of a simple displacement sensor based on a bent single-mode-multimode-single-mode fiber structure // Measurement Science and Technology. 2011. Vol. 22. No. 2. P. 025203.

18. **Yang B., Niu Y., Yang B., Hu Y., Dai L., Yin Y., Ding M.** High sensitivity curvature sensor with intensity demodulation based on single-mode-tapered multimode-single-mode fiber // IEEE Sensors Journal. 2018. Vol. 18. No. 3. Pp. 1094−1099.

19. **Su J., Dong X., Lu C.** Property of bent few-mode fiber and its application in displacement sensor // IEEE Photonics Technology Letters. 2016. Vol. 28. No. 13. Pp. 1387−1390.

20. **Ivanov O.V.** Mode interaction in a structure based on optical fiber with depressed inner cladding // Journal of Communications Technology and Electronics. 2018. Vol. 63. No. 10. Pp. 1143−1151.

21. **Chen J., Lu P., Liu D., Zhang J., Wang Sh., Chen D.** Optical fiber curvature sensor based on few mode fiber // Optik (Stuttgart). 2014. Vol. 125. No. 17. Pp. 4776−4778.

22. **Dong S., Pu S., Huang J.** Highly sensitive curvature sensor based on singlemode-multimode-singlemode fiber structures // Journal of Optoelectronics and Advanced Materials. 2014. Vol. 16. No. 11−12. Pp. 1247−1251.

23. **Gong Y., Zhao T., Rao Y.-J., Wu Y.** All-fiber curvature sensor based on multimode interference // IEEE Photonics Technology Letters. 2011. Vol. 23. No. 11. Pp. 679−681.

24. **Tian K., Xin Y., Yang W., Geng T., Ren J., Fan Y.-X., Farrell G., Lewis E., Wang P.** A curvature sensor based on twisted single-mode-multi-mode-single-mode hybrid optical fiber structure // Journal of Lightwave Technology. 2017. Vol. 35. No. 9. Pp. 1725−1731.

25. **Petrov A.V., Chapalo I.E., Bisyarin M.A., Kotov O.I.** Intermodal fiber interferometer with frequency scanning laser for sensor application // Applied Optics. 2020. Vol. 59. No. 33. Pp. 10422−10431.

26. **Косарева Л.И., Котов О.И., Лиокумович Л.Б., Марков С.И., Медведев А.В., Николаев В.М.** Два механизма модуляции фазы в многомодовых волоконных интерферометрах // Письма в Журнал технической физики. 2000. Т. 26. № 2. С. 53−58.

27. **Oksanen M.I.** Perturbational analysis of curved anisotropic optical fibers // Journal of the Optical Society of America. A. 1989. Vol. 6. No. 2. Pp. 180−189.

28. **Shemirani M.B., Mao W., Panicker R.A., Kahn J.M.** Errata to "Principal modes in graded-index multimode fiber in presence of spatial- and polarization-mode coupling" // Journal of Lightwave Technology. 2011. Vol. 29. No. 12. Pp. 1900−1900.

29. **Garth S.J.** Modes and propagation constants on bent depressed inner cladding optical fibers // Journal of Lightwave Technology. 1989. Vol. 7. No. 12. Pp. 1889−1894.

30. **Schermer R.T.** Mode scalability in bent optical fibers // Optics Express. 2007. Vol. 15. No. 24. Pp. 15674−15701.

31. **Garth S.J.** Modes on a bent optical waveguide // IEEE Proceedings Journal: Optoelectronics. 1987. Vol. 134. No. 4. Pp. 221−229.

32. **Kumar A., Goyal I.C., Ghatak A.K.** Effect of curvature on dispersion in multimode parabolic index fibres // Optica Acta: International Journal of Optics. 1975. Vol. 22. No. 11. Pp. 947−953.

33. **Malik D.P.S., Gupta A., Ghatak A.K.** Propagation of a Gaussian beam through a circularly curved selfoc fiber // Applied Optics. 1973. Vol. 12. No. 12. Pp. 2923−2926.

34. **Taylor H.** Bending effects in optical fibers // Journal of Lightwave Technology. 1984. Vol. 2. No. 5. Pp. 617−628.

35. **Yariv A., Yeh P.** Optical waves in crystals. New York: Willey, 1984. 589 p.

36. **Yariv A., Yeh P.** Photonics: optical electronics in modern communications. New York: Oxford University Press, 2007. 849 p.

37. **Unger H.-G.** Planar optical waveguides and fibres. Oxford: Clarendon Press Oxford, 1977. 751 p.

СВЕДЕНИЯ ОБ АВТОРАХ

МАРКВАРТ Александр Александрович — *ассистент Высшей школы прикладной физики и космических технологий Санкт-Петербургского политехнического университета Петра Великого, Санкт-Петербург, Российская Федерация.*

195251, Российская Федерация, г. Санкт-Петербург, Политехническая ул., 29
markvart_aa@spbstu.ru

ЛИОКУМОВИЧ Леонид Борисович — *доктор физико-математических наук, профессор Высшей школы прикладной физики и космических технологий Санкт-Петербургского политехнического университета Петра Великого, Санкт-Петербург, Российская Федерация.*

195251, Российская Федерация, г. Санкт-Петербург, Политехническая ул., 29
leonid@spbstu.ru

УШАКОВ Николай Александрович — *научный сотрудник Высшей школы прикладной физики и космических технологий Санкт-Петербургского политехнического университета Петра Великого, Санкт-Петербург, Российская Федерация.*

195251, Российская Федерация, г. Санкт-Петербург, Политехническая ул., 29
n.ushakoff@spbstu.ru

Theoretical physics

ABOUT THE PROPER TIME AND THE MASS OF THE UNIVERSE

N.N. Gorobey[1], A.S. Lukyanenko[1], A.V. Goltsev[2]

[1] Peter the Great St. Petersburg Polytechnic University,
St. Petersburg, Russian Federation;

[2] Ioffe Institute of the Russian Academy of Sciences,
St. Petersburg, Russian Federation

For a closed universe, a modification of the quantum gravity where the dynamics is reduced to the motion in the orbit of a general covariance groups has been proposed. To connect these motion parameters, namely, proper time and spatial shifts, to observations, classical equations of motion were introduced into the quantum theory as additional conditions. The equations account for differential conservation laws for additional dynamical variables, which form the spatial density of distribution and motion of the universe's proper mass in the representation of Arnovitt, Deser and Misner (ADM). This made it possible to determine the average values of the parameters of proper time and spatial shifts in the evolutionary history of the universe. In order to preserve the homogeneity and isotropy of space, the proper mass of the universe should next be set equal to zero. Nonzero values of its proper mass (mass spectrum) were allowed in the operator canonical representation of the quantum gravity, which was also introduced instead of the ADM representation.

Keywords: universe, proper time, proper mass, quantization, Hermitian operator, Dirac spinor

О СОБСТВЕННОМ ВРЕМЕНИ И МАССЕ ВСЕЛЕННОЙ

Н.Н. Горобей[1], А.С. Лукьяненко[1], А.В. Гольцев[2]

[1] Санкт-Петербургский политехнический университет Петра Великого,
Санкт-Петербург, Российская Федерация;

[2] Физико-технический институт им. А.Ф. Иоффе РАН,
Санкт-Петербург, Российская Федерация

Для случая замкнутой Вселенной предложена модификация квантовой теории гравитации, в которой динамика сводится к движению по орбите групп общей ковариантности. Чтобы связать с наблюдениями параметры этого движения, а именно собственное время и пространственные сдвиги, в качестве дополнительных условий в квантовую теорию вводятся классические уравнения движения указанных параметров. Эти уравнения отражают дифференциальные законы сохранения дополнительных динамических переменных, которые в представлении Арновитта, Дезера и Мизнера (АДМ) образуют пространственную плотность распределения и движения собственной массы Вселенной. Определены средние значения параметров собственного времени и пространственных сдвигов в истории эволюции Вселенной. Инвариантное определение собственной массы (спектра масс) сформулировано в операторном каноническом представлении теории гравитации, которое также вводится вместо представления АДМ.

Ключевые слова: Вселенная, собственное время, собственная масса, квантование, Эрмитов оператор, спинор Дирака

Introduction

For a closed universecase, the following Wheeler − DeWitt equation (a system of wave equations) is the heart of quantum gravity:

$$\hat{H}^{\mu}\Psi = 0. \qquad (1)$$

According to this equation, the wave function of the universe Ψ does not depend from any external parameter of time. Albeit adopting this concept, we, nonetheless, assume that time is required for interpretation and description of the observation results, and thus it should be introduced in the quantum cosmology as well. This calls for a modification of the canonical procedure for quantizing the theory.

This paper proposes a variant of such a modification in case of a closed universe, which allows introducing the time parameter (parameters). The modification is simultaneously a variant of the quasiclassical approximation and presents no changes into the dynamical content of the theory at the classical level.

As a model for our constructions, let us consider the mechanics of a relativistic particle. In relativistic mechanics, mass particle Hamiltonian m is proportional to the Hamiltonian constraint, i.e.

$$h = NH, \, H \equiv p^2 - m^2c^2, \qquad (2)$$

which expresses the known condition imposed on a particle's four-momentum.

We use a simplified notation for a four-vector square $p^2 = p^{\mu}p_{\mu}$. Let us base our constructions on the formal symmetry of relativistic mechanics: the reparametrization-invariance of action which has geometrical meaning of a particle's world line in Minkowski space. The arbitrary function N of the parameter τ on the world line provides this invariance. This symmetry is the simplest analog of the general covariance principle in Einstein's theory of gravity.

The most universal tool of quantizing covariant theories is Batalin − Fradkin − Vilkovisky formalism (BFV-formalism) which prescribes the way to constructing Becchi − Rouet − Stora − Tyutin propagator (BRST-propagator) [1, 2]. In the simplest case of a relativistic particle, this formalism gives a simple result as well: functional-integral representation of the Green's function for the Klein − Gordon equation [3], which contains an additional integral over particles proper time within $[0, \infty)$. This representation was first proposed by V.A. Fock [4] and J. Schwinger [5]. The problem of interpretation of this covariant quantum theory consists in the fact that proper time here is not a parameter of the evolution, while the Green's function itself has no dynamical meaning. We obtain the same result for homogenous models of the universe in the quantum theory.

For the proper time in the quantum theory to obtain the meaning of an evolution parameter, we need additional constructions allowing proper time integration in the propagator. The authors of Ref. [6] propose a modification of the original theory for the homogenous anisotropic model of the universe which allows removing the proper time integral without changing its dynamical content at the classical level.

Let us conditionally divide the modification into two stages. At the first one, the proper time is introduced into the initial action of the classical theory as a new dynamical variable using a relation

$$N = \dot{s}. \qquad (3)$$

At the second stage, we add Euler − Lagrange (EL) to the initial action for the new dynamical variable as an additional condition. It is equivalent to adding to the initial action its variation generated by an infinitesimal shift of the proper time:

$$\delta s = -\varepsilon. \qquad (4)$$

In the simplest homogenous model of the universe [6], this EL equation is reduced to the law of conservation of Hamiltonian constraint which in the original theory was a consequence of equations of physical dynamical variables motion. Such a modification obviously does not change dynamical content at the classical level, but in this case, it already leads to some additions.

Consider the consequences of the theory under consideration on the example of relativistic mechanics. As an initial system, let us take a massless particle ($m = 0$ in relation (2)) with Lagrangian

$$L = \frac{1}{2}\frac{\dot{x}^2}{N}. \qquad (5)$$

After two stages of modification move on to the Lagrange function:

$$\hat{L} = \frac{1}{2}\frac{\dot{x}^2}{\dot{s}}\left(1 + \frac{\dot{\varepsilon}}{\dot{s}}\right), \qquad (6)$$

where the infinitesimal shift of the proper time ε should also be considered as an independent dynamical variable.

Pass on to the canonical form of the modified theory. Its Hamiltonian equals zero as Lagrangian (6) is a homogenous function of velocities of the first order, while the constraint equation takes the form

$$p_s = P_\varepsilon - \sqrt{2P_\varepsilon}\sqrt{p^2}, \qquad (7)$$

where

$$P_\varepsilon = \frac{1}{2}\frac{\dot{x}^2}{\dot{s}^2} \qquad (8)$$

is a canonical momentum conjugated to ε.

Another canonical equation of motion is the conservation law for the additional dynamical variable $\dot{P} = 0$. Bearing in mind Eq. (7), this means the conservation law of the initial theory constraint. However, the particle's mass can be not equal to zero now, if we set

$$P_\varepsilon = 2m^2c^2. \qquad (9)$$

Thus, the proposed modification leads to appearance of the additional parameter P_ε in the theory, which in this case serves as the constant of motion. This could also be understood as an expansion of the admissible initial values of the particle's velocity due to its "gained" mass. Note that the initial constraint (2) is an invariant of the Lorentz transformations acting in Minkowski space and phase space of the relativistic particle. The proper mass obtained in this construction is an invariant as well.

There is another significant result of the modification: a square root of the 4-momentum square p_μ in Eq. (7). In the quantum theory, it is a source of an additional conditional in the form of δ, a function in the functional integral which defines the proper time on the world line of the particle as integral Eq. (8):

$$s = \int \frac{\sqrt{dx_\mu dx^\mu}}{\sqrt{2P_\varepsilon}}. \qquad (10)$$

This exact equation allows eliminating proper time integration in the propagator for the relativistic particle. A generalization of this modification of the covariant quantum theory for a case of a system with two Hamiltonian constraints and two proper time parameters is considered in paper [7].

In this paper, the authors proposed a modification of the gravity theory in the general case of an inhomogeneous universe. It is based on the representation of the action obtained by Arnovitt, Deser and Misner (ADM) [8, 9] using a (3 + 1)-split of 4D-metric. A part of elements of this metric (N, N_i), which are called successor and shift functions, play a role of Lagrange multipliers in the canonical representation of the ADM action. The modification of the theory in this representation leads to occurrence of additional dynamical variables, which form scalar and vector densities with respect to transformations of space coordinates. Similar to the relativistic particle, they can be called density and flux density distribution of the proper mass

of the universe. Assumption of non-zero values of these variables in the ADM representation means a breach of homogeneity and isotropy of the space. Generalization of the theory be means of introducing invariant non-zero values of the additional dynamical variables is possible in the operator representation of gravitational constraints [10], which is also considered in this paper.

In the operator representation, additional variables are invariants of $3D$-diffeomorphisms and form a spectrum of proper mode masses of the universe.

Proper time and mass of the universe in the ADM representation

The action of the gravity theory in ADM representation obtained by means of $(3 + 1)$-split of $4D$-metric has the form of [9]:

$$I_{ADM} = \int N dt \int_{\Sigma} \sqrt{g} d^3 x \times$$
$$\times \left[R + \mathrm{Tr} K^2 - \left(\mathrm{Tr} K \right)^2 \right], \tag{11}$$

where

$$K_{ik} = \frac{1}{2N} \left[\nabla_i N_k + \nabla_k N_i - \dot{g}_{ik} \right] \tag{12}$$

is the tensor of the hypersurface extrinsic curvature of the constant time Σ.

To simplify, we exclude the action of matter fields from action (11). The addition of the matter does not change the main conclusions of the article. Here, N, N_i are successor and shift functions which are the elements of the $4D$-metric. Time derivatives of these functions are absent in the ADM action, so they play the role of Lagrange multipliers in the canonical representation of the action.

EL equations for N, N_i are essentially classic constraint equations expressed via time derivatives from $3D$-metric:

$$\frac{\delta I_{ADM}}{\delta N} = H =$$
$$= \sqrt{g} \left[R + \left(\mathrm{Tr} K \right)^2 - \mathrm{Tr} K^2 \right] = 0, \tag{13}$$

$$\frac{\delta I_{ADM}}{\delta N_i} = H^i =$$
$$= -2 \nabla_k \left[\sqrt{g} \left(g^{ik} K - K^{ik} \right) \right] = 0. \tag{14}$$

The Hamiltonian in the case of the closed universe has the form of a linear combination

$$h_{ADM} = \int d^3 x N_{\mu} \Pi^{\mu}, \tag{15}$$

where Π^{μ} are ADM constraints expressed via canonical momenta

$$\pi^{ik} = \sqrt{g} \left(g^{ik} K - K^{ik} \right), \tag{16}$$

conjugated to $3D$-metric elements.

Momentum quadratic Hamiltonian constraints are canonical generators of shifts normal to the space cross-section Σ, while the linear momentum constraints serve as canonical generators of $3D$-space diffeomorphisms.

Here, we have no need for explicit form of these constraints in the ADM representation. Although, let us note that they form scalar and vector densities with respect to transformations of space coordinates on Σ. Further, we follow general notations [11] sufficient for any covariant theories. Summation over repeated indices implies integration if the range of the possible index values forms continuum.

In the gravity theory, the variation range of the Latin index is as follows:

$$\alpha = \left(\mu, x \right); \ \ \mu = 0; \ \ i, x \in \Sigma.$$

In these general notations, the infinitesimal shifts of the proper (multipoint) time are united with the infinitesimal space shifts on the hypersurface by means of a united symbol ε_{α}, so that the infinitesimal variations of the canonical variables generated by these shifts are written in the form

$$\delta q_{\alpha} = \varepsilon_b \left\{ q_{\alpha}, \varphi_b \right\},$$
$$\delta p_{\alpha} = \varepsilon_b \left\{ p_{\alpha}, \varphi_b \right\}. \tag{17}$$

The constraints form closed algebra with respect to Poisson brackets, i.e.

$$\{\varphi_\alpha, \varphi_b\} = C_{abd}\varphi_d, \qquad (18)$$

and we will not need its structural functions in the explicit form here as well.

Transformations (17) in this case act as symmetry transformations of the theory only in so far as the action written in the canonical form

$$I = \int dt L(q_i, \dot{q}_i, \lambda_\alpha) = \\ = \int dt [p_i \dot{q}_i - \lambda_\alpha \varphi_\alpha] \qquad (19)$$

is an invariant of the transformations with an additional Lagrange multipliers transformation:

$$\delta\lambda_\alpha = \dot{\varepsilon}_\alpha - C_{bd\alpha}\lambda_b \varepsilon_d. \qquad (20)$$

Take Eq. (20) as the basis of our further constructs. Let us consider them as functional differential equations in the form

$$\frac{\delta\lambda_\alpha(t)}{\delta s_b(t')} = \\ = \delta_{\alpha b}\frac{d}{dt}\delta(t-t') - C_{db\alpha}\lambda_b(t)(t-t') \qquad (21)$$

with respect to λ_α, and here, we assume them to be functionals of the proper time s_α parameters.

Solution to these equations at additional initial conditions $\lambda_\alpha[0] = 0$ has the following form:

$$\lambda_\alpha = \dot{s}_b \Lambda_{b\alpha}. \qquad (22)$$

It can be obtained using iterations in the form of functional Taylor series, in which with the accuracy of up to second order of smallness with respect to s_α

$$\Lambda_{b\alpha}. = \delta_{b\alpha} - \frac{1}{2!}C_{bd\alpha}s_d + \\ + \frac{1}{3!}C_{b'd'\alpha'}C_{bdb'}s'_d s_d - .... \qquad (23)$$

We will also need a variation of Lagrange multipliers (22) at the infinitesimal shift of the proper time ε_α parameters:

$$\delta\lambda_\alpha = \dot{\varepsilon}_b \Lambda_{b\alpha} + \dot{s}_b \frac{\partial\Lambda_{b\alpha}}{\partial s_d}\varepsilon_d. \qquad (24)$$

Eqs. (22) and (24) are a generalization of Eqs. (3) and (4) for the general case of an inhomogeneous universe. Using an analogy with relativistic mechanics, let us write Lagrange function of the modified gravity theory at once in the general case:

$$\tilde{L}(q, \dot{q}, s, \dot{s}, \varepsilon, \dot{\varepsilon}) = L(q, \dot{q}, \lambda(s, \dot{s})) + \\ + \frac{\partial L(q, \dot{q}, \lambda(s, \dot{s}))}{\partial\lambda_d}\delta\lambda_d(s, \dot{s}, \varepsilon, \dot{\varepsilon}). \qquad (25)$$

The peculiarities connected with the time problem and possible solutions to it in the modified theory reveal themselves after a transition to the canonical form of the action (25). Modified Lagrange function (25) is a homogenous first order function of all generalized velocities. For this reason, the Hamiltonian of the modified theory equals zero.

Taking this into account, we deviate here from the standard formalism of covariant dynamics quantization in terms of the external time parameter [1, 2]. Such a description remains possible in the island universe model, the energy of which is equal to zero, and the time is measured in hours at infinity [12]. Instead, in a closed universe, we can talk about symmetry transformations or motion of general covariance groups in the orbit generated by constraints, while the parameters of this motion form the proper (multipoint) time s_α.

In the modified theory, this intrinsic dynamics consists in the equations that determine the canonical momenta conjugated to the proper time:

$$p_{s_\alpha} = \frac{\partial\tilde{L}}{\partial\dot{s}_\alpha} = -\tilde{h}_\alpha. \qquad (26)$$

These equations will play a role of constraints in the modified theory after the transition to its canonical form. For this purpose, we should exclude all velocities from the right-hand side of Eq. (26) by expressing them through the corre-

sponding canonical momenta.

In the quantum theory, the constraints of Eq. (26) transform into a system of self-consistent wave equations of Schrödinger equation type

$$i\hbar \frac{\partial \Psi}{\partial s_\alpha} = \hat{\tilde{h}} \Psi \qquad (27)$$

for the universe wave function Ψ.

The general covariance principle demands excluding the dependence of the universe wave function on the additional dynamical variables s_α.

Obtain the invariant propagator by additional integration of solution to system (27) along the whole orbit of the general covariance groups with a simple measure:

$$\tilde{K} = \int \prod_\alpha ds_\alpha \Psi(s_\alpha,...). \qquad (28)$$

We will not develop the modified quantum theory here, but focus on those aspects of the canonical form of the classical theory, which lead to eliminating the integrals in propagator (28). One of such aspects is excluding the infinitesimal shift velocities of the proper time $\dot{s}_\alpha$ as a result of which there are square roots in Eq. (26) which are similar to those contained in constraints Eq. (7). To exclude them, there are equations determining the corresponding canonical conjugated momenta in the form

$$P_{\varepsilon_\alpha} = \frac{\partial L(q,\dot{q},\lambda(s,\dot{s}))}{\partial \lambda_d} \Lambda_{ad} = $$
$$= \Lambda_{ad} \varphi_d, \qquad (29)$$

which we will further require in explicit form.

Eqs. (29) allow obtaining a generalization of simplest Eq. (10) for the proper time of the relativistic particle in a form of a system of equations for the proper (multipoint) time of the universe.

Let us write off this system in explicit form keeping in mind our agreement on the condensed Latin index:

$$\frac{\sqrt{N^2(x)\left[\mathrm{Tr}K^2(x)-\left(\mathrm{Tr}K(x)\right)^2\right]}}{\sqrt{P_{\varepsilon_\alpha}\Lambda_{\alpha 0}^{-1}(x)+R(x)}} = $$
$$= N(x), \qquad (30)$$

$$\sqrt{g(x)}P_{\varepsilon_\alpha}\Lambda_{\alpha i}^{-1}(x) = $$
$$= -2\nabla_k\left[\sqrt{g(x)}\left(g^{ik}(x)K(x)-K^{ik}(x)\right)\right]. \qquad (31)$$

Here, successor and shift functions are determined by Eqs. (22). Both sides of Eqs. (30) and (31) are homogenous functions of the first and zero degrees of velocities, respectively. The integrals of these equations define the proper time of the universe as a trajectory function in its configuration space. This time also acts as a functional of the additional dynamical variables $P_{\varepsilon\alpha}$, therefore, Eqs. (30), (31) should be solved together with their motion equations. They are obtained as EL equations for infinitesimal shifts of the proper time in the modified time and have the form

$$\frac{d}{dt}P_{\varepsilon_\alpha} + P_q\Lambda_{qd}^{-1}\dot{s}_b\frac{\partial \Lambda_{bd}}{\partial s_\alpha} = 0. \qquad (32)$$

According to expressions (29), the additional dynamical variables $P_{\varepsilon\alpha}$, as well as the constraints in the ADM representation, form spatial densities. Permission of their non zero values violates the covariance of the modified theory with respect to $3D$-diffeomorphisms. There is no breach of the covariance, if we assume the additional dynamical variables to be identically equal to zero. Moreover, the result of the modification in the form of the system of Eqs. (30), (31) defining the proper time of the universe in the ADM representation is maintained. The invariant definition of the proper time and mass of the universe can be achieved by using $3D$-invariant representation of the gravitational constraints.

Operator representation of gravitational constraints

The $3D$-invariant representation of the gravitational constraints is based on the operator equality

$$H = D^2 + \frac{1}{2}\Delta = 0, \qquad (33)$$

which is equivalent to a complete set of gravitational constraints in the ADM-representation [9]. Here, D is the Dirac $3D$-operator, while Δ is Laplace − Beltrami $3D$-operator in Dirac

bispinor space at the compact space cross-section $\sum$ with the given scalar product

$$\left(\psi_1, \psi_2\right) = \int \sqrt{g} \, d^3 x \psi_1^+ \psi_2. \tag{34}$$

Both operators Δ and D are Hermitian with respect to product (34), their coefficients are the essence of the function of canonical variables of the gravitational field (g_{ik}, π^{ik}).

To introduce a new canonical representation, let us consider the fact the proper functions of the Hermitian operator H form a complete set in Dirac bispinor space, while the necessary and sufficient conditions of its equality to zero is the equality to zero of all of its proper values defined by a secular equation.

$$H\psi_\alpha = h_\alpha \psi_\alpha. \tag{35}$$

In its turn, this means that the proper values of H form closed algebra with respect to Poisson brackets with the previous canonical variables:

$$\left\{h_\alpha, h_\beta\right\} = \tilde{C}_{\alpha\beta\gamma} h_\gamma. \tag{36}$$

Operator Eq. (33) allows us to transform the Hamiltonian of the gravity theory from the initial representation in the form of integral (15) of the ADM local constraints distribution at the space cross-section $\sum$ into a linear combination of mode Hamiltonians:

$$h_H = \lambda_\alpha h_\alpha\left(g, \pi\right). \tag{37}$$

Here, modes are understood as proper states of the operator H.

Secular Eq. (35) can be represented in a matrix form based on spectral decomposition for each Hermitian and elliptical operator in equality (33).

Write the secular equation for the Dirac operator square:

$$D^2 \psi_n = d_n^2 \psi_n. \tag{38}$$

Assuming the set of proper functions ψ_n is orthonormal, we will seek a solution to Eq. (35) in a form of decomposition

$$\psi_\alpha = \sum_n c_{\alpha n} \psi_n, \tag{39}$$

for the coefficients of which we obtain a system of equations

$$\sum_n \Delta_{mn} c_{\alpha n} = \left(h_\alpha - d_m^2\right) c_{\alpha m} \Delta_{mn} = $$
$$= \left(\psi_m, \Delta \psi_n\right). \tag{40}$$

Now, let us write the secular equation for the Hermitian matrix Δ_{mn} in the form:

$$\sum_n \Delta_{mn} f_n^p = \delta_p f_m^p \tag{41}$$

and look for a solution to system (40) as a decomposition

$$c_{\alpha n} = \sum_p a_{\alpha p} f_n^p. \tag{42}$$

Assuming again the set of vector-sequences f_n^p orthonormal with respect to a common Hermitian scalar product in the space of sequences, for the coefficients of this decomposition and the proper values of operator H of interest, we obtain:

$$\sum_m d_m^2 f_m^{+p'} f_m^p a_{\alpha p} = \left(h_\alpha + \delta_{p'}\right) a_{\alpha p'}. \tag{43}$$

In this form, the system of equations defining mode Hamiltonians of the universe h_α, can be useful, in particular, to formulate finite-dimensional approximations. Thus, for a homogenous universe, obviously, we have the sole mode with Hamiltonian

$$h = d_1^2 - \delta_1, \tag{44}$$

which coincides with the Hamiltonian of the homogenous anisotropic universe considered in paper [6].

Mode Hamiltonians of h_α are invariants of $3D$-transformations of the coordinates in the space cross-section. Consequently, all variables appearing in the constructs of the previous chapter are also invariants. Mode parameters of the proper time and the proper mass spectrum are invariant as well from direct analogy of relativistic mechanics. This allows us to consider the evolution of the universe in the modified quantum the-

ory without violating the general covariance principle even at non-zero values of the proper mass. For the wave function of the universe origin, we postulate the conditional principle of minimum space energy defined by the functional

$$W = \frac{\left\langle \Psi_0 \left| d_1^2 \right| \Psi_0 \right\rangle}{\left\langle \Psi_0 \middle| \Psi_0 \right\rangle}. \qquad (45)$$

Equal-zero Hamiltonian of the universe (37) here serves as an additional condition, while the wave function Ψ_0 and Lagrange multipliers λ_n are the variational parameters. To calculate this energy defined by the elliptical operator d_1^2, we take its minimal proper value. Further, we solve the system of wave equations (27) (written now in the operator representation). The propagator (28) obtained in this fashion has additional dependence on the spectrum of invariant mode mass. This, in turn, allows us to define observable mode parameters of the proper time as average values of the corresponding observables:

$$\left\langle \hat{\varepsilon}_\alpha \right\rangle_\Psi = \left\langle \frac{\hbar}{i} \frac{\delta}{\delta P_\alpha} \right\rangle_\Psi. \qquad (46)$$

These parameters of time or the corresponding spatial scale, obviously, can be associated with the hierarchy of the spatial structures emerging in the process of the universe evolution. After calculating mean values (46), in the frame of the original theory, the mode mass should be set equal to zero. However, the general covariance principle now does not exclude the non-zero values of these parameters as well. The presence of absence of the proper mass of the universe is a question of observations and their interpretation we leave open here.

The new canonical representation of the gravity theory allows us to modify original Wheeler – DeWitt form (1) as well. The system of local (for each point of the space) wave equations superimposed on the physical state of the universe should now be replaced by non-local mode conditions. In case of strict adherence to the conventional formulation of the quantum constraints, the operator representation leads to the following

system of wave equations for the physical state of the universe Ψ:

$$\hat{h}_\alpha \Psi = 0. \qquad (47)$$

Nonetheless, direct form of operator representation (33) as a self-consistent definition of the modes themselves with the wave equation for the universe wave function in the frame of the functional differential equation seems more natural:

$$\hat{H}\psi_\alpha \Psi_\alpha = 0. \qquad (48)$$

In this formulation of the quantum cosmology, the solutions should be grouped in sequences with increasing mode index α, which by that takes the meaning of a quantum parameter of the proper time in this sequence of the physical states of the universe Ψ_α.

Conclusion

The absence of the traditional view of time in the quantum cosmology is one of the consequences of the general covariance principle, which excludes any external numbering of the universe structure. This means that the universe evolution should be defined in the intrinsic terms. In fact, the structure of the covariance group itself, after additional constructs, defines the intrinsic dynamics of the universe. The constructs proposed in this paper are based on the structure of the general covariance group in the canonical ADM-representation obtained by means of (3+1)-split of the time-space geometry. The proper time and the spatial shifts as the natural parameters of the symmetry transformations are introduced in the initial action as independent dynamical variables. In this case, the dynamics of the closed universe is reduced to the motion of the general covariance group in the orbit. In quantum theory, such a motion is described by a system of wave equations of Schrödinger type. However, the general covariance principle demands independence of the wave function on the parameters of this motion: symmetry transformation. The independence is achieved by means

of averaging the wave function on the symmetry group orbit. The task of the second stage of modification consists in eliminating additional averaging on the orbit using a correlation of the intrinsic dynamics with the classical motion integrals. In the original theory, these integrals play a role of constraints, i.e. become zero due to the general covariance principle. In the modified theory, these values can differ from zero and become additional dynamical variables. Their motion is described by EL equations for the parameters of the general covariance transformations. Introducing additional dynamical variables associated with the motion integrals in quantum theory is a variant of the quasiclassical approximation. In this case, the approximation requires no substantiation by corresponding estimates. There is only one requirement left, which is the compliance with the observations. "Exact" quantum theory in the absence of the time parameter has no connection to the observations.

The additional dynamical parameters P_ε act as observable ones in the modified theory. In the ADM-representation, they form space distribution of the universe proper mass, as well as the space-time shifts canonically subjugated to them. For the latter, average (along the whole history of the universe) values can be determined in the original theory as well, where the universe proper mass should be taken as equal to zero. Non-zero proper mass of the universe (mass spectrum) is admissible in the operator canonical representation of the gravity theory for a closed universe. In this representation, the mass spectrum is associated with the hierarchy of the spatial structures emerging in the process of the universe evolution. The sequence of formation of the spatial structures of various scale itself may serve as a material basis for the definition of the proper time of the universe.

REFERENCES

1. **Fradkin E.S., Vilkovisky G.A.,** Quantization of relativistic systems with constraints, Phys. Lett. B. 55 (2) (1975) 224−226.

2. **Batalin I.A., Vilkovisky G.A.,** Relativistic *S*-matrix of dynamical systems with boson and fermion constraints, Phys. Lett. B. 69 (3) (1977) 309−312.

3. **Govaerts J.,** A note on the Fradkin − Vilkovisky theorem, International Journal of Modern Physics. A. 4 (17) (1989) 4487−4504.

4. **Fock V.A.,** The eigen-time in classical and quantum mechanics, Phys. Zs. Sowjet. 12 (4) (1937) 404−425 (in German).

5. **Schwinger J.,** On gauge invariance and vacuum polarization, Phys. Rev. 82 (5) (1951) 664−679.

6. **Gorobey N., Lukyanenko A., Drozdov P.,** Energy conservation law in the closed universe and a concept of the proper time, Universe. 6 (10) (2020) universe6100174.

7. **Gorobey N.N., Lukyanenko A.S., Goltsev A.V.,** The proper mass of the universe, St. Petersburg Polytechnical State University Journal. Physics and Mathematics. 14 (1) (2021) 147−154.

8. **Arnowitt R., Deser S., Misner C.W.,** Dynamical structure and definition of energy in general relativity, Phys. Rev. 116 (5) (1959) 1322−1330.

9. **Misner C.W., Thorne K.S., Wheeler J.A.,** Gravitation, Princeton University Press, New Jersey, USA, 2017.

10. **Gorobey N.N., Lukyanenko A.S.,** Operator representation of gravitational constraints for the case of the closed universe, Theoretical and Mathematical Physics. 105 (3) (1995) 1603−1606.

11. **Faddeev L.D., Slavnov A.A.,** Gauge fields: An introduction to quantum theory, 2nd edition, Westview Press, 1993.

12. **Faddeev L.D., Popov V.N.,** Covariant quantization of the gravitational field, Sov. Phys. Usp. 16 (6) (1974) 777−788.

THE AUTHORS

GOROBEY Natalia N.
Peter the Great St. Petersburg Polytechnic University
29 Politechnicheskaya St., St. Petersburg, 195251, Russian Federation
n.gorobey@mail.ru

LUKYANENKO Alexander S.
Peter the Great St. Petersburg Polytechnic University
29 Politechnicheskaya St., St. Petersburg, 195251, Russian Federation
alex.lukyan@rambler.ru

GOLTSEV Alexander V.
Ioffe Institute of RAS
26, Politekhnicheskaya, St. Petersburg, 195251, Russian Federation
gorobej_nn@spbstu.ru

СПИСОК ЛИТЕРАТУРЫ

1. **Fradkin E.S., Vilkovisky G.A.** Quantization of relativistic systems with constraints // Physics Letters. B. 1975. Vol. 55. No. 2. Pp. 224−226.

2. **Batalin I.A., Vilkovisky G.A.** Relativistic *S*-matrix of dynamical systems with boson and fermion constraints // Physics Letters. B. 1977. Vol. 69. No. 3. Pp. 309−312.

3. **Govaerts J.** A note on the Fradkin − Vilkovisky theorem // International Journal of Modern Physics. A. 1989. Vol. 4. No. 17. Pp. 4487−4504.

4. **Фок В.А.** Собственное время в классической и квантовой механике // Известия АН СССР. Серия физическая. 1937. № 4−5. С. 551−568.

5. **Schwinger J.** On gauge invariance and vacuum polarization // Phys. Rev. 1951. Vol. 82. No. 5. Pp. 664− 679.

6. **Gorobey N., Lukyanenko A., Drozdov P.** Energy conservation law in the closed universe and a concept of the proper time // Universe. 2020. Vol. 6. No. 10. P. universe6100174.

7. **Gorobey N.N., Lukyanenko A.S., Goltsev A.V.** The proper mass of the universe // St. Petersburg Polytechnical State University Journal. Physics and Mathematics. 2021. Vol. 14. No. 1. Pp. 147−154.

8. **Arnowitt R., Deser S., Misner C.W.** Dynamical structure and definition of energy in general relativity // Phys. Rev. 1959. Vol. 116. No. 5. Pp. 1322−1330.

9. **Misner C.W., Thorne K.S., Wheeler J.A.** Gravitation. New Jersey, USA: Princeton University Press, 2017. 1279 p.

10. **Горобей Н.Н., Лукьяненко А.С.** Операторное представление гравитационных связей в случае замкнутой Вселенной // Теоретическая и математическая физика. 1995. Т. 105. № 3. С. 503−507.

11. **Славнов А.А., Фаддеев Л.Д.** Введение в квантовую теорию калибровочных полей. 2-е изд. М.: Наука, 1988. 272 с.

12. **Фаддеев Л.Д., Попов В.Н.** Ковариантное квантование гравитационного поля // Успехи физических наук. 1973. Т. 111. Вып. 3. С. 427−450.

СВЕДЕНИЯ ОБ АВТОРАХ

ГОРОБЕЙ Наталья Николаевна — *доктор физико-математических наук, профессор кафедры физики Санкт-Петербургского политехнического университета Петра Великого, Санкт-Петербург, Российская Федерация.*

195251, Российская Федерация, г. Санкт-Петербург, Политехническая ул., 29

n.gorobey@mail.ru

ЛУКЬЯНЕНКО Александр Сергеевич — *доктор физико-математических наук, профессор кафедры физики Санкт-Петербургского политехнического университета Петра Великого, Санкт-Петербург, Российская Федерация.*

195251, Российская Федерация, г. Санкт-Петербург, Политехническая ул., 29

alex.lukyan@rambler.ru

ГОЛЬЦЕВ Александр Викторович — *доктор физико-математических наук, профессор, старший научный сотрудник Физико-технического института им. А.Ф. Иоффе, Санкт-Петербург, Российская Федерация.*

195251, Российская Федерация, г. Санкт-Петербург, Политехническая ул., 26.

golysev@ua.pt

Mechanics

DEFLECTION OF AN INTERFACE CRACK FROM THE STRAIGHT-LINE GROWTH DUE TO THE UNSTRAIGHTNESS OF THE MATERIAL INTERFACE

V.V. Tikhomirov

Peter the Great St. Petersburg Polytechnic University,
St. Petersburg, Russian Federation

An antiplane semi-infinite interface crack propagation problem has been considered, the crack tip coinciding with the angular point of the materials interface. The exact solution of the problem was obtained using the Mellin integral transformation. Asymptotic formulas for stresses near the crack tip were constructed, and they could contain one or two singular terms. To analyze the crack growth, the Novozhilov force criterion of fracture was used. Based on the obtained exact solution, the calculation accuracy of the crack angle and the destructive load, determined using asymptotics, was estimated. The dependences of these fracture characteristics on the composition parameters were investigated.

Keywords: antiplane interface crack, corner point, crack deflection angle, breaking load

ОТКЛОНЕНИЕ ИНТЕРФЕЙСНОЙ ТРЕЩИНЫ ОТ ПРЯМОЛИНЕЙНОГО РОСТА ВСЛЕДСТВИЕ НЕПРЯМОЛИНЕЙНОСТИ ГРАНИЦЫ РАЗДЕЛА МАТЕРИАЛОВ

В.В. Тихомиров

Санкт-Петербургский политехнический университет Петра Великого,
Санкт-Петербург, Российская Федерация

Рассматривается задача о поведении антиплоской полубесконечной интерфейсной трещины, вершина которой совпадает с угловой точкой границы раздела материалов. С помощью интегрального преобразования Меллина получено точное решение рассмотренной задачи. Для напряжений вблизи указанной угловой точки построены асимптотические выражения, которые могут содержать одно или два сингулярных слагаемых. Для анализа роста трещины использован силовой критерий разрушения (критерий Новожилова). На основе полученного точного решения проведена оценка точности вычислений угла отклонения трещины и разрушающей нагрузки, определяемых с помощью асимптотик. Исследованы зависимости этих характеристик разрушения от параметров композиции материалов.

Ключевые слова: антиплоская интерфейсная трещина, угловая точка, угол отклонения трещины, разрушающая нагрузка

Introduction

Special points (singularities/singular points) of stress fields, which initiate the fracture process, play an important role in linear fracture mechanics, the results of which are based on the equations of the linear elasticity theory. Tips of cracks, sharp notches or inclusions in a material can serve as such singular points. A crack tip located in a homogenous material has a classical singularity, i.e. the singularity equals 0.5. In other cases, generally speaking, singularity differs from the indicated value. The singularity is determined by finding the roots of transcendental characteristic equations located in the range of (0, 1). A review of the results associated with this statement is presented in papers [1 − 3].

Among many problems of fracture mechanics, a class of problems connected with the crack/materials interface interaction attracts particular attention. In plane and antiplane statements, this class of problems was studied in papers [4 − 7]. There, the interface was taken to be straight-line. Note that in these cases the classical Griffith − Irwin fracture criteria is not applicable, as the singularity in the crack tip differs from 0.5 and thus we require other criteria approaches. A short review of such approaches is given in article [8].

If the interface between the materials has a breakpoint, then, as it is shown in [9], this point in the antiplane problem is essentially singular. In other words, in this case, the characteristic equation at some composition parameter values has two different roots less than one and defining two singular summands in the stress field asymptotic behavior of the crack tip.

This paper studies a deflection of the initially straight interface crack from the straight-line growth caused by piecewise-rectilinear interface between two materials.

As the fracture criterion, we used Novozhilov's force criterion [10]. Based on the obtained exact solution, the paper focuses on the possibility of using the asymptotic behavior of stress field to find the deflection angle and failure load, as well as on the analysis of these fracture characteristics dependences on the material composition parameters. Paper [11] considered a similar problem in the plane statement. However, its results were based on applying asymptotic solutions and the numerical finite element method.

Problem statement and finding exact solution

Consider semi-infinite interface shear crack, the tip of which coincides with the angular point of two connected wedge-shaped regions Ω_1 and Ω_2 with corner angles α and $(2\pi - \alpha)$ respectively (Fig. 1). The materials of the regions are considered homogenous and isotropic with shear moduli μ_1 and μ_2. Self-balanced concentrated forces of T value are applied to the crack ends at the distance of r_0 from the tip. The contact at the interface is assumed to be ideal.

Displacement and stress fields in each of the regions are constructed in the form of Mellin integrals:

$$w_k(r,\theta) = \frac{1}{2\pi i}\int_L W_k(p,\theta)r^{-p}dp,$$

$$\tau_{\theta z k}(r,\theta) =$$
$$= \frac{1}{2\pi i}\int_L T_{\theta z k}(p,\theta)r^{-p-1}dp \quad (k=1,2),$$

(1)

where the displacement and stress transformants are determined as

$$W_k(p,\theta) = A_k(p)\sin p\theta + + B_k(p)\cos p\theta,$$

$$T_{\theta z k}(p,\theta) = \mu_k p\left[A_k(p)\cos p\theta - - B_k(p)\sin p\theta\right].$$

(2)

Here, r, θ are polar coordinates.

Resulting from the regularity conditions of the solution at $r \to 0$ and $r \to \infty$, the contour of integration L is parallel to the imaginary axis in the range of

$$-\delta_1 < \operatorname{Re} p < \delta_2 \quad (\delta_1, \delta_2 > 0).$$

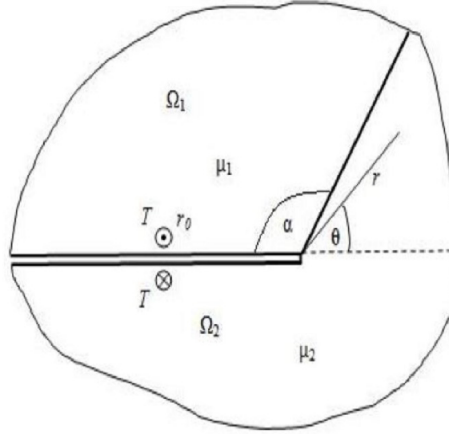Making functions (1) subject to the conditions of the ideal contact at $\theta = \pi - \alpha$ and the con-

Figure. 1. Semi-infinite interface crack, crack tip coinciding with the angular point of the materials interface:
μ_1, μ_2 — materials shear moduli in regions Ω_1 and Ω_2; α — corner angle of the region Ω_1;
T — self-balanced concentrated forces applied at the distance of r_0 from the tip; r, θ — polar coordinates

ditions of crack ends loading at $\theta = \pm\pi$, we find variables $A_k(p)$ и $B_k(p)$, included in Eq. (2). As a result, the stress representation has the form

$$\tau_{\theta zk} = \frac{T}{\pi i r_0} \int_L \frac{\Phi_k(p,\theta,\alpha,m)}{\Delta(p,\alpha,m)} \left(\frac{r_0}{r}\right)^{p+1} dp$$

$$(k = 1, 2)$$

(3)

$$\Phi_k(p,\theta,\alpha,m) = \varphi_{k1}(p,\alpha,m)\sin p\theta +$$

$$+ \varphi_{k2}(p,\alpha,m)\cos p\theta,$$

(4)

$$\varphi_{11}(p,\alpha,m) = \sin \pi p -$$

$$- m\sin(\pi-\alpha)p\cos(2\pi-\alpha)p,$$

$$\varphi_{12}(p,\alpha,m) = m\sin(\pi-\alpha)p\sin(2\pi-\alpha)p,$$

$$\varphi_{21}(p,\alpha,m) = \sin \pi p -$$

$$- m\cos\alpha p\sin(\pi-\alpha)p,$$

(5)

$$\varphi_{22}(p,\alpha,m) = -m\sin\alpha p\sin(\pi-\alpha)p,$$

$$\Delta(p,\alpha,m) = \sin 2\pi p - m\sin 2(\pi-\alpha)p.$$

Elastic properties of the composition are reflected in these formulas via one bielastic constant

$$m = (\mu_1 - \mu_2)/(\mu_1 + \mu_2).$$

At all combinations of the materials shear moduli, this variable satisfies an inequality $|m| \le 1$. If the inclusion material (region Ω_1) is more rigid than the matrix material, then $0 < m < 1$; if not (in case of a soft inclusion) the value of m belongs to the range $-1 < m < 0$. Value $m = 0$ corresponds to the homogenous medium, while values $m \pm 1$ define an ideally rigid inclusion and a wedge-shaped notch.

The poles of the subintegral function in Eq. (3) are defined by the roots of the characteristic equation

$$\Delta(p,\alpha,\beta,m) = 0.$$

(6)

Function (5) is an entire uneven function of the integral of the integral transformation parameter p, which has no zeroes on the imaginary axis except for the single zero $p = 0$. However, according to Eq. (4) this point is a removable singularity. Therefore, the the contour of integration L in Eq. (3) can be superposed onto the imagi-

nary axis. We can show that Eq. (5) has no complex zeroes belonging to the range of $|\mathrm{Re}\ p| \leq 1$.

Due to unevenness of function (5), each root of Eq. (6) $p_- < 0$ has a respective root $p_+ > 0$, in addition, $p_- = -p_+$. Since for the purpose of investigating stress singularity (3) in the crack tip, we are only interested in the roots that do not exceed one, let us consider the real roots of the characteristic equation located in the range of (0, 1) for convenience.

Function (5) has the following property:

$$\Delta(p, \alpha, m) = \Delta(p, 2\pi - \alpha, -m).$$

It follows from this, that it is sufficient to consider such a system configuration that $0 < \alpha < \pi$ at positive and negative values of the bielastic constant m.

A detailed analysis shows that in case of a more rigid medium 1, when $\mu_1 > \mu_2$ and, consequently $m > 0$, at $\pi/2 \leq \alpha < \pi$ the characteristic equation has one root $p_1 \in (1/4, 1/2)$, while at $0 < \alpha < \pi/2$ it has two: $p_1 \in (1/4, 1/2)$ and $p_2 \in (3/4, 1)$.

If $m < 0$, i.e. $\mu_1 < \mu_2$, Eq. (6) at $0 < \alpha \leq \pi/2$ has one root $p_1 \in (1/2, 3/4)$ generating a weak singularity $\lambda = 1 - p_1 < 1/2$ of stresses (3), while at $\pi/2 < \alpha < \pi$ it has two roots in the range of (1/2, 1).

The case of $\alpha = \pi/2$ is singular, as with such a geometry the characteristic equation has only one root in the range of (0, 1) at any $m \in (-1, 1)$. Moreover, the roots of Eq. (6) split into two sets, because

$$\Delta(p, \pi/2, m) =$$
$$= 2(\cos \pi p - m/2)\sin \pi p.$$

The first positive zero of function $\cos \pi p - m/2$ is a monotone decreasing variable of the m parameter taking values equal to 2/3 at $m = -1$ and to 1/3 at $m = 1$.

Similar splitting of the roots in Eq. (6) is also incident, for example, at $\alpha = \pi/3$ and $\alpha = 2\pi/3$.

Fracture criterion

To calculate the stress in the composite medium at $r < r_0$, let us close the contour of integration L in Eq. (3) on the left by a semicircle of long radius and use the Cauchy theorem on residues in the poles of the subintegral function. As a result, the stress in each of the regions has the form

$$\tau_{\theta z k} = \frac{2T}{r_0} \sum_{n=1}^{\infty} \frac{\Phi_k(-p_n, \theta, \alpha, m)}{\Delta'(p_n, \alpha, m)} \left(\frac{r_0}{r}\right)^{-p_n+1}$$
$$(k = 1, 2). \tag{7}$$

As the fracture criterion, we use the force criterion proposed by V.V. Novozhilov [10], according to which the fracture by crack growth occurs when mean stress calculated at some distance from its tip d reaches a critical value equal to the shear strength of the material τ_c:

$$\bar{\tau}_{\theta z k} = \frac{1}{d_k} \int_0^{d_k} \tau_{\theta z k}(r, \theta) dr = \tau_{ck}. \tag{8}$$

This criterion in the plane and antiplane problems was applied, for example, in papers [8, 11, 12].

Using representation (7), for the mean stress we obtain:

$$\bar{\tau}_{\theta z k}(\theta) =$$
$$= \frac{2T}{r_0} \sum_{n=1}^{\infty} \frac{\Phi_k(-p_n, \theta, \alpha, m)}{p_n \Delta'(p_n, \alpha, m)} \left(\frac{d_k}{r_0}\right)^{p_n-1}. \tag{9}$$

Angles $\theta_1(\alpha, m)$ and $\theta_2(\alpha, m)$ defining the growth direction of the crack are found from the conditions of function (9) extremum in the regions Ω_1 and Ω_2. Using Eq. (4) we can show that the derivative $\partial \Phi_1/\partial \theta < 0$ at $\pi - \alpha < \theta < \pi$ and any permissible values of the parameter $|m| \leq 1$. In other words, function $\bar{\tau}_{\theta z 1}(\theta)$ in the region Ω_1 is monotone decreasing and takes the largest value at the boundary of $\theta = \pi - \alpha$. Since the crack cannot propagate in the region Ω_1, we further consider only the necessary condition of the mean stress extremum $\bar{\tau}_{\theta z 2}(\theta)$ in the region Ω_2:

$$\partial \bar{\tau}_{\theta z 2}(\theta)/\partial \theta = 0$$
$$\text{at } -\pi < \theta < \pi - \alpha, \tag{10}$$

which due to inequality (9) has the form

$$\sum_{n=1}^{\infty} \frac{\partial \Phi_2(-p_n, \theta, \alpha, m)/\partial \theta}{p_n \Delta'(p_n, \alpha, m)} \left(\frac{d_2}{r_0}\right)^{p_n-1} = 0. \tag{11}$$

Asymptotic approach

If Eq. (6) has only one positive root $p_1 \in (0, 1)$, then stress asymptote (7) at $r \to 0$ is mononomial:

$$\tau_{\theta z 2} =$$
$$= \frac{2T}{r_0} \frac{\Phi_2\left(-p_1, \theta, \alpha, m\right)}{\Delta'\left(p_1, \alpha, m\right)} \left(\frac{r_0}{r}\right)^{-p_1+1}, \quad (12)$$

and fracture condition (8) on beam $\theta = \theta_2$ takes the form

$$\frac{2T}{r_0} \frac{\Phi_2\left(-p_1, \theta_2, \alpha, m\right)}{p_1\Delta'\left(p_1, \alpha, m\right)} \left(\frac{d_2}{r_0}\right)^{p_1-1} =$$
$$= \tau_{c2}. \quad (13)$$

This formula is true at ant values of the parameters α and m. When considering the case of homogenous medium, let us set $m = 0$ in equality (13) and, consequently, $p_1 = 1/2$, while $\theta_2 = 0$. Then, using Eqs. (4) and (5), for the relative critical distance d_2 we obtain the following representation:

$$\frac{d_2}{r_0} = \gamma^2, \gamma^2 = \frac{2}{\pi r_0}\left(\frac{K_{3c}^{(2)}}{\tau_{c2}}\right)^2,$$

where γ is the dimensionless geometric parameter, $K_{3c}^{(2)}$ is the material fracture toughness in the region Ω_2.

Note that the same representation for the critical distance was obtained for a sharp notch in papers [8, 13].

Equality (11) defining the crack deflection angle θ_2 (α, m) in the considered case takes the form

$$\frac{\partial \Phi_2\left(-p_1, \theta, \alpha, m\right)}{\partial \theta} = 0.$$

Then, using Eq. (4), for the deflection angle we obtain the representation

$$\theta_2 = \frac{1}{p_1}\text{arctg}\left[-\frac{\varphi_{22}\left(p_1, \alpha, m\right)}{\varphi_{21}\left(p_1, \alpha, m\right)}\right]. \quad (14)$$

Therefore, we conclude that if we use mononomial asymptote (12), the critical distance d_2 exerts no influence on the deflection angle of the crack.

Dependence of the deflection angle on the parameters. Based on the properties of function (4) we can show that at $m > 0$ ($\mu_1 > \mu_2$) and $\pi/2 \le \alpha < \pi$ the angle $\theta_2 > 0$ is in fact the monotone increasing function of the parameter m. In other words, the crack deflects in the direction of the interface with the more rigid material. In the limiting case, when the material in the region Ω_1 is ideally rigid, i.e. $m \to 1$, the deflection angle $\theta_2 = \pi - \alpha$. Moreover, at the considered values of the parameters, the derivative $\partial\theta_2/\partial\alpha < 0$ and, consequently, the angle θ_2, is a decreasing function of the parameter α which approaches zero at $\alpha \to \pi$. This corresponds to the growth of the crack across the interface between two heterogeneous semiplanes.

If the material in the region Ω_2 is relatively more rigid ($m < 0$) and $0 < \alpha \le \pi/2$, then it follows from Eqs. (4) and (14) that $\theta_2 < 0$. In this case, the crack grows in the direction from the interface. The greatest deflection of the crack in the negative direction from the polar angle origin occurs at $m \to -1$. Due to the monotonicity of the function of θ_2 with respect to the parameter α, the deflection achieves its maximum at $\alpha = \pi/2$, when $\theta_2 \to -\pi/4$ for $m \to -1$.

Note that dependence (14) has an especially simple form, when $\alpha = \pi/2$:

$$\theta_2 = \frac{1}{p_1}\text{arctg}\frac{m}{\sqrt{4 - m^2}},$$

where p_1 is the first positive zero of the function $\cos \pi p - m/2$.

Using the obtained value of deflection angle (14), from equality (13) we obtain critical load causing the crack growth:

$$T = \frac{p_1\Delta'\left(p_1, \alpha, m\right)}{2\Phi_2\left(-p_1, \theta_2, \alpha, m\right)}\gamma^{2(1-p_1)}r_0\tau_{c2}.$$

Bearing in mind that the critical loaf for the semi-infinite crack in the homogenous material

is defined by the formula $T_0 = 0{,}5\pi\gamma r_0\tau_{c2}$, let us introduce reduced critical load T^* into consideration for the composition:

$$T^* = \frac{T}{T_0} = \frac{p_1\Delta'(p_1,\alpha,m)}{\pi\Phi_2(-p_1,\theta_2,\alpha,m)}\gamma^{1-2p_1}. \quad (15)$$

At other values of the parameters, the characteristic equation has two roots: p_1 and p_2 in the range of (0, 1), and the stress asymptote contains two singular summands:

$$\tau_{\theta z2} =$$
$$= \frac{2T}{r_0}\left[\frac{\Phi_2(-p_1,\theta,\alpha,m)}{\Delta'(p_1,\alpha,m)}\left(\frac{r_0}{r}\right)^{-p_1+1} + \right.$$
$$\left. + \frac{\Phi_2(-p_2,\theta,\alpha,m)}{\Delta'(p_2,\alpha,m)}\left(\frac{r_0}{r}\right)^{-p_2+1}\right]. \quad (16)$$

In this case the fracture condition has the form

$$\frac{2T}{r_0}\left[\frac{\Phi_2(-p_1,\theta_2,\alpha,m)}{p_1\Delta'(p_1,\alpha,m)}\left(\frac{d_2}{r_0}\right)^{p_1-1} + \right.$$
$$\left. + \frac{\Phi_2(-p_2,\theta_2,\alpha,m)}{p_1\Delta'(p_2,\alpha,m)}\left(\frac{d_2}{r_0}\right)^{p_2-1}\right] = \tau_{c2}. \quad (17)$$

At the same time, the critical distance is defined by the formula

$$\frac{d_2}{r_0} = \frac{9}{4\gamma^2}\left(\sqrt{1+\frac{4}{3}\gamma^2}-1\right)^2.$$

If $\gamma \ll 1$, то $d_2/r_0 \sim \gamma^2$ and, consequently, at sufficiently small values of γ we can use the result obtained with the mononomial asymptote for the critical distance.

The crack deflection angle θ_2 in this case is a root of the equation

$$\varphi_{21}(p_1)\sin p_1\theta + \varphi_{22}(p_1)\cos p_1\theta +$$
$$+ \frac{\Delta'(p_1)}{\Delta'(p_2)}\Big[\varphi_{21}(p_2)\sin p_2\theta +$$
$$+ \varphi_{22}(p_2)\cos p_2\theta\Big]\left(\frac{d_2}{r_0}\right)^{p_2-p_1} = 0. \quad (18)$$

In contrast to the mononomial asymptote, here the angle θ_2 depends on the critical distance.

After finding the deflection angle using fracture criterion (17), we calculate the critical load and then its reduced value based on definition (15).

Numerical results and their discussion

Based on exact solution (7) and fracture criterion (8), (9), using the same approach we find that the relative critical distance satisfies the following equation

$$\frac{d_2}{r_0} = \gamma\,\mathrm{arctg}\sqrt{\frac{d_2}{r_0}},$$

while the reduced failure load is found on the basis of the formula

$$T^* =$$
$$= \frac{1}{\pi\gamma}\left[\sum_{n=1}^{\infty}\frac{\Phi_k(-p_n,\theta_2,\alpha,m)}{p_n\Delta'(p_n,\alpha,m)}\left(\frac{d_k}{r_0}\right)^{p_n-1}\right]^{-1}. \quad (19)$$

In addition, the direction of the crack growth is defined by the angle θ_2, which is the root of Eq. (11).

To estimate the accuracy of the asymptotic approach, the author calculated the fracture characteristics θ_2 and T^* based on the exact solution at different values of the parameters α, m and γ. Fig. 2 shows the dependence of the crack deflection angle θ_2 on the bielastic constant m calculated on the basis of asymptote (14) and the exact solution at $\alpha = \pi/2$ and $\gamma = 0.25$. At these parameters values, the asymptote give an upper bound of the deflection angle at $m > 0$ and the lower bound at $m < 0$. The highest error of the asymptotic estimate equals 25.7% in case of the soft material in the region Ω_2 and is approximately 69% in the case of a relatively rigid material of this region. When the Ω_1 region material becomes more rigid ($m \to 1$), the accuracy of asymptotic Eq. (14) increases and the crack grows in the neighborhood of the interface.

A similar situation also takes place at other values of the parameters α, m and γ, including the case of binomial asymptote (16), when the crack deflection angle is defined as the root of Eq. (18).
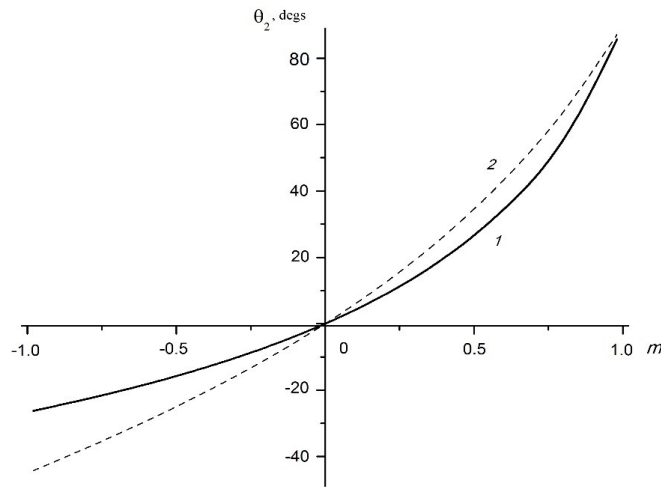
Fig. 2. Dependences of the interface crack deflection angle θ_2 on the bielastic constant m obtained on the basis of exact solution (*1*) and based on mononomial stress asymptote (*2*); $\alpha = \pi/2$, $\gamma = 0.25$
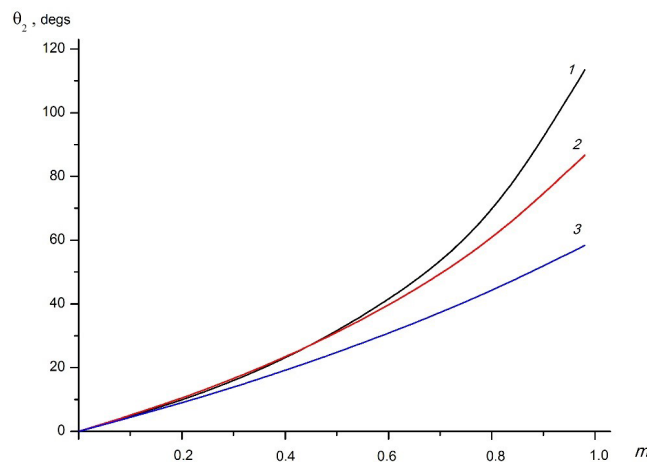

Fig. 3. Dependence of the interface crack deflection θ_2 calculated on the basis of the exact solution on the bielastic constant $m > 0$ at $\gamma = 0.1$ and different values of the angle α: $\pi/3$ (*1*), $\pi/2$ (*2*), $2\pi/3$ (*3*)

The only difference from the case of $\alpha = \pi/2$ consists in the fact that the error of the asymptotic approach considerably drops at negative values of the bielastic constant.

The calculations show that the accuracy of the deflection angle increases as the parameter γ grows for all possible values of α and m. Note that accounting only for the first summand in binomial asymptote (16) leads to extremely high errors (more than 100%) when seeking the deflection angle and, consequently, is unacceptable.

Thus, the use of the stress field asymptotes in the neighborhood of the crack tip at sufficiently small values of the parameter γ determines the deflection angle of the crack well qualitatively, but may result in significant inaccuracies in a quantitative sense.

Fig. 3 indicates the dependence of the angle θ_2 calculated on the basis of the exact solution in case of a relatively more rigid material of the region Ω_1 at different values of its corner angle. According to the conclusions of the asymptotic
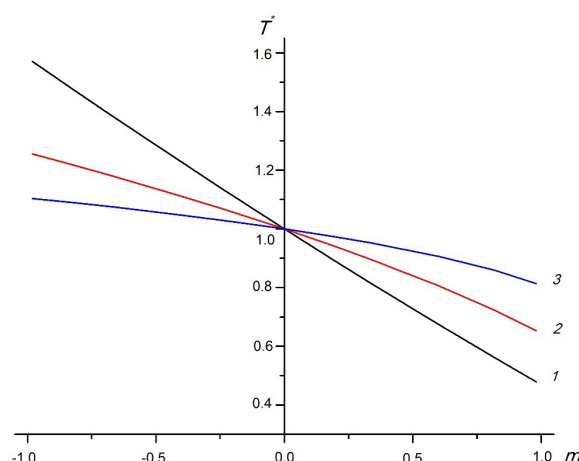
131

Fig. 4. Dependence of the reduced failure load T^*,
calculated on the basis of the exact solution on the bielastic constant m at $\alpha = \pi/2$
and different values of the parameter γ: 0.10 (*1*), 0.25 (*2*), 0.50 (*3*)

approach, in this case, the crack deflects in the direction of the interface between the materials, while at $m \to 1$ its growth occurs in the neighborhood of this boundary. At $m < 0$ the difference in the deflection angles for various values of the angle α is insignificant (less than 6%) and the dependence of θ_2 on m is close to curve *1* in Fig. 2.

The accuracy of the reduced failure load T^* calculated on the basis of the asymptotes is rather high and is within 5% at the values of γ not exceeding 0.5 for all possible values of the variables α and m. In addition, taking into account only the singular terms of the stress fields define the lower-bound estimate of the failure load. The accuracy of this estimate increases as γ drops. Fig. 4 presents the dependence of T^* calculated on the basis of exact solution (19), at $\alpha = \pi/2$ and various values of γ. Similar dependences take place for other values of α as well. The given curves show that at $m > 0$ the value of the reduced load is below one, while at $m < 0$ they exceed one. This means that for the crack propagation in case of a relatively rigid material 1, less force applied to its ends is required compared to the case of a homogenous medium. The situation of a softer material in the region Ω_1 is reversed: the forces needed to be applied to the ends of the cracks to cause its growth in the composite medium exceed the forces applied in the homogenous case.

Conclusion

Based on the Novozhilov's force criterion (fracture criterion), we obtained asymptotic and exact relations for the characteristics of an interface crack fracture the tip of which coincides with the angular point of the materials interface. The fracture characteristics include such macroscopic parameters of the material as fracture toughness and shear strength. The asymptotic formulas for sufficiently small values of the dimensionless geometric parameter γ provide a qualitatively accurate upper and lower bound estimates for the deflection angle of the initially straight-line interface crack. The crack deflects in the direction of the interface with the more rigid material and in the opposite direction in case of the softer material. However, in the quantitative sense, the asymptotic formulas produce considerable inaccuracies. Nonetheless, the critical load values calculated with the use of the asymptotic formulas possess sufficient accuracy and can be applied to estimate these loads.

REFERENCES

1. **Eischen J.W.,** Fracture of nonhomogeneous materials, International Journal of Fracture. 34 (1) (1987) 3–22.

2. **Carpinteri A., Paggi M.,** On the asymptotic stress field in angularly nonhomogeneous materials, International Journal of Fracture. 135 (1-4) (2005) 267–283.

3. **Paggi M., Carpinteri A.,** On the stress singularities at multimaterial interfaces and related analogies with fluid dynamics and diffusion, Applied Mechanical Review. 61 (2) (2008) 020801.

4. **Erdogan F., Gupta G.D.,** Bonded wedges with an interface crack under anti-plane shear loading, International Journal of Fracture. 11 (4) (1975) 583–593.

5. **Fenner D.N.,** Stress singularities in composite materials with an arbitrarily oriented crack meeting an interface, International Journal of Fracture. 12 (5) (1976) 705–721.

6. **He M-Y., Hutchinson J.W.,** Crack deflection at an interface between dissimilar elastic materials, International Journal of Solids and Structures. 25 (9) (1989) 1053–1067.

7. **Misuris G., Kuhn G.,** Comparative study of an interface crack for different wedge-interface models, Archive of Applied Mechanics. 71 (11) (2001) 764–780.

8. **Tikhomirov V.V.,** Sharp V-notch fracture criteria under antiplane deformation, St. Petersburg State Polytechnical University Journal. Physics and Mathematics. 11 (3) (2018) 99–107.

9. **Tikhomirov V.V.,** Longitudinal shear crack terminating at a wedge-shaped elastic inclusion, St. Petersburg State Polytechnical University Journal. Physics and Mathematics. 2 (194) (2014) 110–119.

10. **Novozhilov V.V.,** O neobkhodimom i dostatochnom kriterii khrupkoy prochnosti [On the necessary and sufficient test of brittle strength], Prikladnaya Matematika & Mekhanika. 33 (2) (1969) 212–222 (in Russian).

11. **Klusák J., Krepl O., Profant T.,** Behaviour of a crack in a corner or at a tip of a polygon-like particle, Procedia Structural Integrity. 2 (2016) 1912–1919.

12. **Knesl Z.,** A criterion of V-notch stability, International Journal of Fracture. 48 (4) (1991) R79–R83.

13. **Carpinteri A., Cornetti P., Pugno N., Sapora A.,** On the most dangerous V-notch, International Journal of Solids and Structures. 47 (7–8) (2010) 887–893.

THE AUTHOR

TIKHOMIROV Victor V.
Peter the Great St. Petersburg Polytechnic University
29 Politechnicheskaya St., St. Petersburg, 195251, Russian Federation
victikh@mail.ru

СПИСОК ЛИТЕРАТУРЫ

1. **Eischen J.W.** Fracture of nonhomogeneous materials // International Journal of Fracture. 1987. Vol. 34. No. 1. Pp. 3–22.

2. **Carpinteri A., Paggi M.** On the asymptotic stress field in angularly nonhomogeneous materials // International Journal of Fracture. 2005. Vol. 135. No. 1-4. Pp. 267–283.

3. **Paggi M., Carpinteri A.** On the stress singularities at multimaterial interfaces and related analogies with fluid dynamics and diffusion // Applied Mechanical Review. 2008. Vol. 61. No. 2. P. 020801.

4. **Erdogan F., Gupta G.D.** Bonded wedges with an interface crack under anti-plane shear loading // International Journal of Fracture. 1975. Vol. 11. No. 4. Pp. 583–593.

5. **Fenner D.N.** Stress singularities in composite

materials with an arbitrarily oriented crack meeting an interface // International Journal of Fracture. 1976. Vol. 12. No. 5. Pp. 705−721.

6. **He M-Y., Hutchinson J.W.** Crack deflection at an interface between dissimilar elastic materials // International Journal of Solids and Structures. 1989. Vol. 25. No. 9. Pp. 1053−1067.

7. **Misuris G., Kuhn G.** Comparative study of an interface crack for different wedge-interface models // Archive of Applied Mechanics. 2001. Vol. 71. No. 11. Pp. 764−780.

8. **Тихомиров В.В.** Критерии разрушения острого выреза в условиях антиплоской деформации // Научно-технические ведомости СПбГПУ. Физико-математические науки. 2018. Т. 11. № 3. С. 99−107.

9. **Тихомиров В.В.** Трещина продольного сдвига, упирающаяся в клиновидное упругое включение // Научно-технические ведомости СПбГПУ. Физико-математические науки. 2014. № 2 (194). С. 110−119.

10. **Новожилов В.В.** О необходимом и достаточном критерии хрупкой прочности // Прикладная математика и механика. 1969. Т. 33. № 2. С. 212−222.

11. **Klusák J., Krepl O., Profant T.** Behaviour of a crack in a corner or at a tip of a polygon-like particle // Procedia Structural Integrity. 2016. Vol. 2. Pp. 1912−1919.

12. **Knesl Z.** A criterion of V-notch stability // International Journal of Fracture. 1991. Vol. 48. No. 4. Pp. R79−R83.

13. **Carpinteri A., Cornetti P., Pugno N., Sapora A.** On the most dangerous V-notch // International Journal of Solids and Structures. 2010. Vol. 47. No. 7−8. Pp. 887−893.

СВЕДЕНИЯ ОБ АВТОРЕ

ТИХОМИРОВ Виктор Васильевич *— кандидат физико-математических наук, доцент Высшей школы теоретической механики, заместитель директора по учебной работе Института прикладной математики и механики Санкт-Петербургского политехнического университета Петра Великого, Санкт-Петербург, Российская Федерация.*

195251, Российская Федерация, г. Санкт-Петербург, Политехническая ул., 29
victikh@mail.ru